Gamma-ray production in the Be-type Star–Pulsar Binary System PSR B1259-63

Brian van Soelen

Submitted in fulfilment of the requirements for the degree
Philosophiae Doctor
in the Faculty of Natural and Agricultural Sciences,
Department of Physics,
University of the Free State,
South Africa

Date of submission: 30 January 2012

Supervised by: Prof P.J. Meintjes, Department of Physics

Abstract

The high-mass binary system PSR B1259-63/LS 2883 is one of only six known gamma-ray binaries, and the only one where the compact object is known from the direct observation of a pulsed radio signal to be a 48 ms pulsar. During it's eccentric 3.4 year orbit, the pulsar moves through the circumstellar disc of the optical companion, approximately twenty days before and after periastron. This results in conditions for complicated interactions between the material in the disc, the fast rotating pulsar, the pulsar wind, and the radiation field from the star and disc. The system has been the object of multi-wavelength campaigns with telescopes such as the VLT, H.E.S.S. and *Fermi*. The interaction between the stellar and pulsar wind results in the formation of a radiating pulsar wind nebula within the binary system, which has been detected from radio to TeV gamma-ray energies. The spectral energy distribution is dominated by the emission at gamma-ray energies, classifying this system as a gamma-ray binary. The interaction between the stars is greater near periastron where the pulsar passes closest to the optical companion. Approximately twenty days from periastron the pulsar passes through or behind the Be star's circumstellar disc, obscuring the pulsed radio signal. During this period there is a corresponding increase in the unpulsed emission from the system. The TeV gamma-rays are believed to be produced by electrons in the pulsar wind which cool via the inverse Compton up-scattering of stellar photons from the optical companion. The circumstellar disc associated with the Be star produces an infrared flux below $\sim 10^{15}$ Hz, which is greater than that expected from the blackbody distribution associated with star, providing additional target photons which could increase the inverse Compton scattering rate. The scattering of infrared photons can occur in the Thomson limit with its significantly larger cross-section and should produce GeV energy gamma-rays in the energy range observed by the *Fermi* telescope. A curve of growth method is presented to model the infrared free-free and free-bound emission from the circumstellar disc, taking into account the changing viewing angle as observed from the pulsar. The curve of growth model is fitted to archive near-infrared and optical data and mid-infrared data obtained with the Very Large Telescope during January 2011. The effect of this infrared excess on the inverse Compton scattering rate is considered for an isotropic and anisotropic photon distribution, considering pre– and post–shock electron distributions. The anisotropic modelling considers the effects of the changing size and orientation of the circumstellar disc relative to the pulsar, as well as the change in the inverse Compton scattering angle during the orbit. The inverse Compton scattering rate for three disc orientations is modelled over a period of approximately 160 days around periastron, including the disc crossing epochs before and after periastron. The maximum disc contribution is found to occur close to periastron and not near the disc–crossing where the low infrared flux from the disc, at a radius of ~ 45 stellar radii, has a less significant effect. It is found that the inclusion of the infrared flux from the circumstellar disc can increase the GeV flux from the system by a factor $\gtrsim 2$ near periastron, for favourable disc orientations. The predicted increase is, however, less than was detected with *Fermi* during the 2011 periastron passage. The observations showed a flare which cannot be explained by this, or any current model.

Key words: radiation mechanisms: thermal – radiation mechanisms: non-thermal – techniques: photometric –stars: emission-line, Be –stars: individual: LS 2883 – pulsars: individual: PSR B1259-63 – infrared: stars –gamma-rays: general – X-rays: binaries

Opsomming

Die hoë-massa binêre sisteem PSR B1259-63/LS 2883 is een van slegs ses bekende gamma-straal binêre stelsels, en is die enigste sisteem waar die kompakte voorwerp bekend is, naamlik as 'n 48 ms pulsar, soos afgelei vanuit die direkte waarneming van 'n pulserende radio-sein. Tydens die eksentrieke 3.4-jaar baan, beweeg die pulsar deur die sirkumstellêre skyf van die optiese ster, ongeveer twintig dae voor en na periastron. Dit lei tot gunstige toestande vir ingewikkelde interaksies tussen die materiaal in die skyf, die vinnig-roterende pulsar, die pulsarwind en die stralingsveld van die ster en skyf. Die stelsel is die voorwerp van multi-golflengte veldtogte met teleskope soos VLT, HESS en Fermi. Die interaksie tussen die ster en pulsar winde het 'n pulsar-wind newel tot gevolg binne die binêre stelsel, wat waargeneem word van radio tot TeV gammastraal energieë. Die spektraalenergie verspreiding word gedomineer deur die uitstraling van gammastraal-energie fotone, wat hierdie sisteem klassifiseer as 'n gammastraal binêre sisteem. Die interaksie tussen die sterre is mees intens naby periastron, d.i waar die pulsar die naaste verbybeweeg aan die optiese ster. Ongeveer twintig dae vanaf periastron beweeg die pulsar deur of agter die Be ster se sirkumstellêre skyf, waar die gepulseerde radiosein versper word. Gedurende hierdie periode is daar 'n ooreenstemmende toename in die nie-gepulseerde radio uitstraling vanaf die sisteem. Die TeV gammastrale word vermoedelik geproduseer deur elektrone in die pulsarwind, wat deur die inverse Compton proses, ster en skyf fotone opwaarts verstrooi tot baie hoë-energie. Die sirkumstellêre skyf wat geassosieer word met die B-tipe ster, produseer 'n surplus infrarooi vloed, wat groter is as die swartstraling vloed wat geassosieer word met die ster alleen onder die frekwensiegebied $\sim 10^{15}$ Hz, wat addisionele teikenfotone verskaf wat die inverse Compton verstrooiingstempo versnel. Hierdie verstrooiing van infrarooi fotone vind hoofsaaklik plaas in die Thomson-grens met sy aansienlik groter botsingsdeursnit (produksiewaarskynlikheid). Dit veroorsaak dat GeV energie gammastrale meer geredelik geproduseer word in die GeV energie gebied wat moontlik deur die *Fermi* teleskoop waargeneem kan word. 'n Groeikurwe metode word voorgestel om die infrarooi vry-vry en vry-gebonde emissie van die sirkumstellêre skyf te modelleer, met inagname van die wisselende besigtigingshoek soos waargeneem vanaf die pulsar. Die groeikurwe model is begrens met beulp van infrarooi en optiese waarnemings, met onder andere die sogenaamde "Very Large Telescope (VLT)" gedurende Januarie 2011. Die effek van hierdie infrarooi surplus op die inverse Compton verstrooiingstempo is in aanmerking geneem vir 'n isotropiese en nie-isotropiese foton verspreiding, inagenome van voor en na-skok elektron versdelings. Die nie-isotropiese modellering neem effekte in ag soos die veranderende grootte en oriëntasie van die sirkumstellêre skyf relatief tot die pulsar, sowel as die verandering in inverse Compton verstrooiingshoek gedurende die wentelbaan, veral naby periastron. Die inverse Compton verstrooingstempo vir drie skyf oriëntasies is gemodelleer oor 'n tydperk van ongeveer 160 dae rondom periastron, insluitend die skyf oorkruising episodes voor en na periastron. Dit is bevind dat die maksimum inverse Compton verstrooiingstempo naby aan periastron plaasvind en nie naby die skyf oorkruising waar die lae infrarooi intensiteit vanaf die skyf, op afstande van ~ 45 ster radiusse, nie 'n betekenisvolle effek op die inverse Compton gamma-straal produksietempo het nie. Daar is bevind dat die insluiting van die infrarooi vloed vanaf die sirkumstellêre skyf die GeV produksietempo vanaf die sisteem met faktor $\gtrsim 2$ verhoog naby periastron vir gunstige skyf oriëntasies. Die voorspelde verhoging is egter minder as wat deur Fermi waargeneem is gedurende die 2011 periastron. Die waarnemings toon 'n opvlamming wat nie deur hierdie model of enige huidige model verklaar kan word nie.

Sleutelwoorde: uitstralingsmeganismes: termies – uitstralingsmeganismes: nie-termies – tegnieke: fotomeriese – sterre: emissielyn, Be – sterre: individuele: LS 2883 – pulsars: individuele: PSR B1259-63 – infrarooi: sterre – gammastrale: gewone – X-strale: binêre sterre.

This thesis is dedicated to Peter,
Who lived and died a hero,
And will not be forgotten.

Contents

Chapter 1

Introduction

The *Fermi* gamma-ray space telescope was launched in June 2008 and observes the universe in the GeV energy gamma-ray range. The telescope has detected an immense number of source, a large proportion of which have not been previously detected. The recently published Second *Fermi*/LAT[i] catalogue (2FGL) lists 1873 sources detected by the *Fermi* gamma-ray telescope between 100 MeV and 100 GeV. The counterpart of only 127 of these sources have been "firmly identified" as they match the *Fermi* defined criteria of periodic variability, spatial morphology and/or correlated variability between the *Fermi* source and the proposed counterpart. A further 1170 sources have possible associations that do not meet the requirements for "firm identification" but in many cases it is highly probable that the proposed association is correct.

Included in the list of firmly identified sources are 83 pulsars, four high mass binaries and three Pulsar Wind Nebula (PWN). The fast rotating neutron stars associated with these sources possess a huge reservoir of rotational kinetic energy which can be channelled into non-thermal emission through a plethora of processes, e.g. synchrotron radiation, bremsstrahlung and inverse Compton scattering. The four binary systems which have been firmly associated with *Fermi* detections are LSI+61 303, LS 5039, Cygnus X-3 and 1FGL J1018.65856. Not included in this list is PSR B1259-63 which has been detected by *Fermi* (Abdo et al., 2011), but is not included in the catalogue as it was only detected after the 2FGL source inclusion cut-off date. All of these systems comprise of a massive non-degenerate star and a compact object (neutron star or black hole), and emit non-thermal radiation from radio to gamma-ray energies. The multi-wavelength emission, including the gamma-ray emission, is often transient and shows a modulation which follows the orbital period (e.g. TeV modulation in PSR B1259-63; Aharonian et al., 2005).

A new binary classification can be made, namely gamma-ray binaries, which are defined to be dominant emitters at gamma-ray energies (Dubus, 2006a). While Cygnus X-3 is not included in this category, since its emission is dominant at X-ray energies, there are two other gamma-ray binary systems; HESS J0632+057, which has only been detected at TeV energies

[i]Large Area Telescope

with the High Energy Stereoscopic System (H.E.S.S.), in Namibia (Aharonian et al., 2007) and AGL J2241+4454 which has been detected by AGILE[ii] (Lucarelli et al., 2010). This makes a total of only six known gamma-ray binary systems.

Of particular interest is the system PSR B1259-63 which consists of a rapidly rotating pulsar ($\sim$ 48 ms) orbiting a Be star (LS 2883). The system was originally detected as part of a radio pulsar survey that took place between November 1989 and September 1991 at the Parkes radio telescope (Johnston et al., 1992a,b) and became the first discovered radio pulsar in orbit around a main-sequence star. It is also the only one of the gamma-ray binaries where the nature of the compact object is determined from direct observation. In the other systems, the compact object cannot be directly observed and its nature must be inferred from other observational results and from the shape of the spectral energy distribution (SED).

The optical companion in PSR B1259-63 also presents its own set of challenges as it is a Be-type star (Johnston et al., 1992a). Be stars show uncharacteristic emission lines instead of absorptions lines and it was originally proposed by Struve (1931) that the stars are surrounded by a nebulous ring of material. Optical interferometry observations have since confirmed the presence of an extended circumstellar envelope which is symmetrical around the rotation axis (see e.g. Quirrenbach et al., 1994).

Observations of Be stars at infrared (IR) wavelengths show a higher flux than is predicted by the Kurucz stellar atmosphere models (Kurucz, 1979) which is the result of IR emission through free-free and free-bound scattering in the circumstellar disc. This IR excess provides a huge reservoir of soft target photons for inverse Compton (IC) scattering in the Thomson limit where the scattering cross-section is significantly larger than the cross-section of blackbody photons from the B type star which scatter in the Klein-Nishina regime. While previous modelling has taken into account the increased density structure around the Be star, and the effect this will have on cooling effects (e.g. Sierpowska-Bartosik and Bednarek, 2008), the influence of the disc's IR excess on IC scattering has not been considered. The large disc size, believed to extend to a few tens of stellar radii, and the excess of soft IR photons, may have a significant influence on the high energy emission in PSR B1259-63. This could be particularly significant near the periastron passages when the pulsar passes close to and through the circumstellar disc of the Be star.

The aim of this study is to investigate the IR excess of the circumstellar disc and the effect this will have on the IC gamma-ray production in PSR B1259-63/LS 2883. Another reason for the investigation of this particular source was the periastron passage of the pulsar during December 2010, which made it the focus of several international multi-wavelength campaigns as well as high energy and very high energy observations, with *Fermi* and H.E.S.S.

In this thesis I have modelled gamma-ray production in PSR B1259-63/LS 2883 through the inverse Compton scattering. I have taking into account both the blackbody distribution associated with the star and the IR emission associated with the circumstellar disc. I have constrained

[ii] Astrorivelatore Gamma a Immagini LEggero

the IR emission from the disc using the curve of growth method proposed by Waters (1986), which models the IR excess as observed from Earth. I have fitted the curve of growth method to archive optical and IR data available in the literature and VLT[iii] observations taken during January 2011. From the point of view of the pulsar, the circumstellar disc will change dramatically in orientation and angular size near periastron and I have modified the curve of growth method to take into account the change in the IR emission as observed from this point of view. The modification allows me to calculate the IR emission from a disc of any orientation. I have calculated the inverse Compton scattering for the system using both an isotropic and an anisotropic model. The isotropic scattering was calculated using the method outlined in Blumenthal and Gould (1970) and the anisotropic scattering from the kernel developed by Fargion et al. (1997) and Dubus et al. (2008). The anisotropic model considers the orientation of the binary system, the anisotropic target photon distribution, and the direction of the inverse Compton scattering.

This thesis is structured as follows: Chapter 2 outlines the previous observations of PSR B1259-63/LS 2883 and the conclusions that have been drawn from this system thus far; Chapters 3 and 4 discuss the properties of Be stars/binary systems and pulsars and pulsar wind nebulae respectively, which are important for the modelling of gamma-ray binaries; the isotropic and anisotropic Compton scattering formulae which I used to model the Compton scattering rate are considered in Chapter 5; in Chapter 6 I discuss the curve of growth method, first purposed by Waters (1986), for predicting the IR excess from Be stars, along with the modifications that I have made to the model; the modelling of the Compton spectrum of PSR B1259-63/LS 2883 is presented in detail in Chapter 7 and the results thereof are considered in Chapter 8; the conclusions of this study are summarised in Chapter 9. Appendixes A–C present additional derivations that are not included in the main body of the text. Appendix D presents the conference proceedings for *IAU Symposium 272* where the isotropic results were presented in part (which were later included in van Soelen and Meintjes, 2011). Appendix E presents the peer-reviewed conference proceedings of the High Energy Phenomena in Relativistic Outflows III (HEPRO III) conference, which will appear in the International Journal of Modern Physics: Conference Series.

[iii] Very Large Telescope

Chapter 2

PSR B1259-63/LS 2883

The aim of this study is to investigate the multi-wavelength nature of PSR B1259-63/LS 2883 and in particular the influence of the IR excess on the gamma-ray production. This chapter presents a brief summary of the observations of this system, including the initial detection of the pulsar, up to the recent *Fermi* observations around the December 2010 periastron passage. This chapter is structured as follows, sections 2.1 to 2.5 present the reported radio, optical, infrared, X-ray and TeV energy gamma-ray observations of the system before the 2010 periastron passage. Section 2.6 briefly discusses how the system was understood based on the multi-wavelength observations before this event. The 2010/2011 *Fermi* observations are discussed in section 2.7. The chapter concludes with a short description of observations of PSR B1259-63 and other Be X-ray binary systems undertaken at the South African Astronomical Observatory (SAAO) and at the European Southern Observatory (ESO) with the Very Large Telescope (VLT).

2.1 Radio observations

2.1.1 Discovery of the pulsar PSR B1259-63

The pulsar PSR B1259-63 was originally detected as part of a southern sky survey undertaken to search for short-period pulsars at 640 and 1500 MHz with the Parkes 64-m radio telescope situated near Parkes, New South Wales, Australia (Johnston et al., 1992a). The initial search covered a 50 day period in mid 1988, while further follow up observations of potential pulsars were undertaken in 1989 and 1990. A total of 46 new pulsars were detected during the survey, including the 48 ms pulsar PSR B1259-63.

Following its discovery, Johnston et al. (1992b) undertook more detailed observations of the system. Ninety three (93) timing observations were performed over 24 observation sessions at 430, 660 and 1520 MHz on the Parkes telescope and the pulsar was detected at 660 and 1520 MHz, but could not be detected at 430 MHz. Table 2.1 shows the measured parameters for PSR 1259-63 obtained during these observations. Fig. 2.1 shows the mean pulse profiles at 660 and 1520 MHz

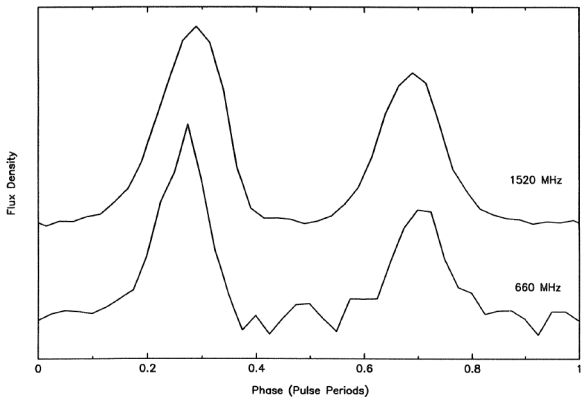

Figure 2.1: The mean pulse profile for PSR B1259-63 for two frequencies 660 and 1520 MHz (Johnston et al., 1992b).

Table 2.1: Parameters of PSR 1259-63 from the radio observation reported by Johnston et al. (1992b).

Parameter	**Value**	
Pulsar radio position (J2000)	$13^{\rm h}02^{\rm m}47\overset{\rm s}{.}72 \pm 0\overset{\rm s}{.}03$	$-63°50'08\overset{''}{.}5 \pm 0\overset{''}{.}2$
LS 2883 optical position (J2000)	$13^{\rm h}02^{\rm m}47\overset{\rm s}{.}65 \pm 0\overset{\rm s}{.}10$	$-63°50'09\overset{''}{.}5 \pm 0\overset{''}{.}7$
Dispersion measure ($\rm cm^{-3}$ pc)	146.7 ± 0.2	
Pulsar distance (kpc)	2.3	
Flux density at 660 MHz (mJy)	4 ± 1	
Flux density at 1520 MHz (mJy)	4.6 ± 0.3	

respectively. These exhibit a pulse and an interpulse at both observed frequencies. At 660 MHz the pulse-interpulse separation is $\sim 160°$, while at 1520 MHz it is slightly less at $\sim 145°$. On average the interpulse flux was 40% of the pulse flux, though, in some observations, the interpulse flux was larger than the pulse flux. The period offset and mean flux detected from the pulsar over $\sim$ 700 days (Fig. 2.2) is consistent with the pulsar being part of a binary system. The curved line in the upper section of Fig. 2.2 is the best fit to the binary system, using a pulsar period derivative of $\dot{P} = 2 \times 10^{-14}$ s s^{-1}.

In order to constrain better the position of the pulsar, two observations were undertaken using the Australia Telescope Compact Array (ATCA), which revealed a point source with a flux density of 6 mJy and 9 mJy in the first and second observation (Johnston et al., 1992b). Optical searches showed that the position and distance of the Be star LS 2883[i] agreed very well with the pulsar position and proposed distance (see Table 2.1). This system became the first

[i]The star was initially called SS 2883 in Johnston et al. (1992b) and, subsequently, papers have referred to the star as such. It has, however, recently been indicated by Negueruela et al. (2011) that this is erroneous as *SS* generally refers to the Stephenson and Sanduleak (1977) catalogue which only contains 455 stars, none of which are the optical companion LS 2883. The optical companion should instead be referred to as LS 2883 as it is found in the Southern Hemisphere extension to the *Luminous Star* catalogue (Hardop et al., 1959; Stephenson and Sanduleak, 1971). This new naming convention has since been adopted and this study will follow the convention of referring to the optical star as LS 2883.

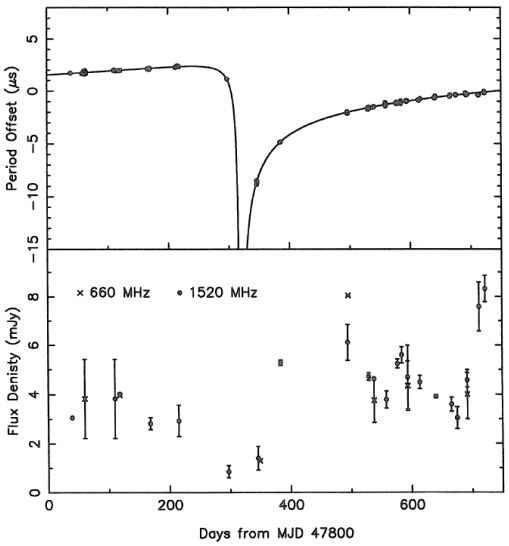

Figure 2.2: The pulsed radio emission from PSR B1259-63. **Upper:** The change in the pulsar period (from 47.662 ms) with respect to time. The error in the measurement is smaller than the size of the plotted point. The curved line is fitted by assuming that the variation is due to orbital motion. A period derivative of $\dot{P} = 2 \times 10^{-14}$ s s^{-1} is used to fit the curve. **Lower:** The mean flux density of the pulsar observed at 660 and 1520 MHz for the same time period (Johnston et al., 1992b).

known radio pulsar with a main sequence companion.

Long term monitoring of the system shows that the orbit is highly eccentric, $e \approx 0.87$ with a ≈ 3.4 year orbital period. The best system parameters, based on 13 years of observations of the system by Wang, Johnston, and Manchester (2004), are given in Table 2.2.

The peak interaction between the pulsar and the optical companion occurs near the periastron passage, every 3.4 years. Most of the non-thermal radiation is observed during this period.

2.1.2 Observations during periastron

During the 1994 and 1997 periastron passages PSR B1259-63 was observed with the Parkes telescope, ATCA and the Molonglo Observatory Synthesis Telescope (MOST) (Johnston et al., 1996, 1999, 2001). As the pulsar approached periastron there was an increase (and a variability) in the dispersion measurement (DM) of the pulsed signal, followed by a disappearance of the pulsed signal ~ 20 days either side of periastron. However, around periastron an unpulsed and variable radio component was detected with a flux density of $10 - 30$ mJy, significantly higher than the flux density of the pulsed emission of $2 - 3$ mJy detected away from periastron. These observations are explained by the conjecture that the pulsar passing through the circumstellar disc of the Be star, leading to an eclipse of the pulsed signal. The unpulsed signal is believed to be synchrotron emission originating from an extended pulsar wind nebula (Moldón et al., 2011a) which forms from the interaction between the pulsar and stellar wind. As is discussed later, the

Table 2.2: Binary parameters of PSR B1259-63 based on radio observations of the system over 13 years. Data from Wang et al. (2004).

Parameter	Value
RA	13h02m47.65s
Dec	-63°50'08.7"
P	47.76250678 ms
$\dot{P}$	2.27655×10^{-15}
$P_{\rm orb}$	1236.7243 days
e	0.869887

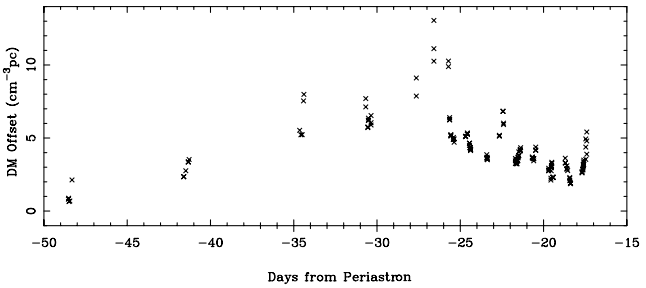

Figure 2.3: The offset of the dispersion measure (DM) from 147.6 cm^{-3} pc for PSR B1259-63 during the 1997 periastron passage (Johnston et al., 2001).

unpulsed emission region extends well beyond the binary orbit.

During the 1994 periastron passage the pulsar was undetectable between $\tau - 19$ and $\tau + 14$ days (Johnston et al., 1996) and during 1997 there was a similar disappearance between $\tau - 16$ and $\tau + 16$ days (Johnston et al., 2001), where τ is the epoch of periastron. During the 1997 observations the DM away from periastron was found to be 147.6 cm^{-3} pc. This value is assumed to be due to the interstellar medium (ISM). The offset from this value as the pulsar approaches periastron is shown in Fig. 2.3. The DM offset is variable on short time scales. This is interpreted as due to the pulsar passing through the inhomogeneous stellar wind, but not the circumstellar disc of LS 2883 (Johnston et al., 2001). Johnston et al. (2001) considered the DM offset (ΔDM $\approx$ 4 cm^{-3} pc) at $\tau - 20$ days, just before the pulsar eclipse, and showed that the electron number density was $n_{\rm e} \sim 7.3 \times 10^5$ cm^{-3} at this point, if the assumed additional distance through the stellar wind is $\sim 1.7 \times 10^{13}$ cm. Assuming the density scales with distance as $n_{\rm e} \propto r^{-2}$, this implies that the number density at the surface of the star is $n_{\rm e} \sim 1.7 \times 10^9$ cm^{-3}.

The disappearance of the pulsed signal at all radio frequencies ~ 20 days before periastron is interpreted as due to the pulsar passing through the circumstellar disc, which then obscures the pulsar. The curve of growth (COG) method used to model the infrared flux from the circumstellar disc in Chapter 6 (p. 127) assumes the disc has a finite size, a half-opening angle $\theta_{\rm disc}$ and a density profile given by

$$\rho \propto \rho_0 (r/R_*)^{-n},$$

where ρ_0 is the density at the base of the disc and n is a parameter of the COG method. From the fit found in Chapter 6 it can be shown that the electron number density at the inner edge of the disc, near the stellar surface, is of the order of $n_0 \sim 6.22 \times 10^{13}$ cm^{-3}. The binary separation is $\approx 45R_*$ at 20 days from periastron and the electron number density at the disc crossing is therefore (equation 6.9, p. 105)

$$\begin{aligned} n_{\rm e} &= n_0 \left(\frac{r}{R_*}\right)^{-n} \\ &\sim 5.53 \times 10^8 \text{ cm}^{-3} \end{aligned}$$

where $n = 3.055$ is fit by the COG method. The optical depth of the disc at a frequency ν due to free-free scattering can be approximated by (e.g. Lang, 1974, p. 47)

$$\tau_\nu \approx 8.235 \times 10^{-2}\, T^{-1.35} \left(\frac{\nu}{10^9 \text{ Hz}}\right)^{-2.1} \int_0^d n_{\rm e}^2 \, dl, \tag{2.1}$$

where T is the disc temperature and d is the path length along the line-of-sight, measured in parsecs. From equation (2.1) it can be shown that the optical depth at 8.4 GHz will be $\tau_\nu \approx 1$ after a path length of $d \sim 6.78 \times 10^9$ cm, while the height of the disc is of the order of 1.0×10^{12} cm at $45R_*$ (for $\theta_{\rm disc} = 1°$), which shows that the disc will completely eclipse the pulsed signal. Since the orbital separation is $\sim 50R_*$ at 20 days from periastron, this implies that the circumstellar disc extends to a radius of $R_{\rm disc} \gtrsim 50R_*$ and, therefore, $50R_*$ is adopted as the radius of the circumstellar disc in this study.

Further observations over subsequent periastron passages showed results similar to those observed during 1994 and 1997. Fig. 2.4 shows the observed unpulsed radio signal from PSR B1259-63 during the 1994, 1997, 2000 and 2004 periastron passages. The basic shape of the light curve remains similar during each periastron passage and is characterised by an increase in the unpulsed emission at $\sim \tau - 20$ days (where τ is the epoch of periastron). The emission rises to a peak a few days before periastron, decreases around periastron, and shows a second peak at $\sim \tau + 20$ days, with a subsequent slower decrease in the radio emission. However, there are differences in the radio data collected at different crossings. For example, in 1997 and 2004, the second peak is higher than the first by a factor $\sim 2 - 3$, while in 2000 the peaks are nearly symmetrical. This variability is attributed to changes in the circumstellar material between periastron passages (Johnston et al., 2005). The shape of the unpulsed radio light curve is consistent with the pulsar wind interacting with the high density circumstellar disc and creating a synchrotron emitting outflow. The slow decay of the unpulsed radio emission after the second disc crossing is then due to adiabatic expansion (Connors et al., 2002).

An extended radio structure around PSR B1259-63 was detected at 2.3 GHz with the Australian Long Baseline Array (LBA) around the 2007 periastron passage (Fig. 2.5; Moldón et al., 2011a). Three observations took place at $\tau + 1$, $\tau + 21$ and $\tau + 315$ days, referred to as Run A, B and C as in that author's paper. Runs A and B showed an extended, variable radio source

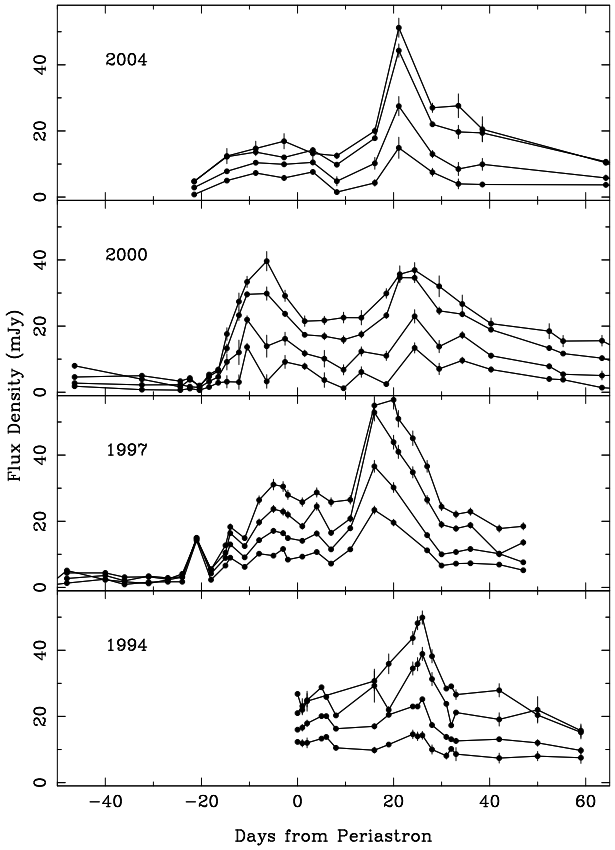

Figure 2.4: Radio observations of the unpulsed emission from PSR B1259-63 over the 1994 to 2004 periastron passages at (from top down) 1.384, 2.496, 4.800 and 8.640 GHz. The image is taken from Johnston et al. (2005) and combines data from Johnston et al. (1999) and Connors et al. (2002).

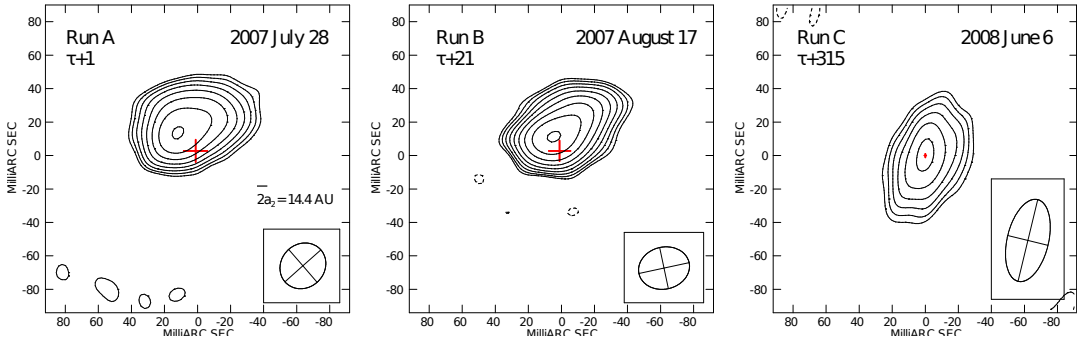

Figure 2.5: Observations of PSR B1259-63 at 2.3 GHz with the LBA around the 2007 periastron passage. The crosses show the computed position of the pulsar in each figure if it is assumed that the point-like source detected during Run C is the pulsar. The corresponding length of the bars shows the uncertainty in the pulsar's position. Run A also includes the size of the major axis, calculated using the newer stellar mass estimate of the $M_* = 31 \pm 5$ M$_\odot$(Negueruela et al., 2011). Figure taken from Moldón et al. (2011a).

extending out to $50 - 55$ mas (milli-arcseconds) with a total flux of 19.9 ± 1.4 and 46.7 ± 1.0 mJy respectively, while Run C only detected a point-like source with a total flux of 3.0 ± 0.4 mJy. These flux measurements are consistent with previous observations of pulsed and unpulsed emission from the system. For an assumed distance to the source of 2.3 ± 0.4 kpc this corresponds to a size of $(120 - 130) \pm 20$ AU for the extended radio source (Moldón et al., 2011a). The binary system has a major axis of ~ 14.4 AU, which implies that this structure extends well beyond the binary orbit. Similar large scale structures have also been observed in other gamma-ray binary systems, namely LS 5039 (e.g. Ribó et al., 2008) and LS I+61 303 (e.g. Albert et al., 2008).

2.2 Optical observations

LS 2883, the main-sequence optical companion of PSR B1259-63, is a V~ 10 magnitude star, in the Centaurus constellation. Photometric data for LS 2883 has been included in a few bright star catalogues (Table 2.3), and a comparison between the archive data shows little variability in the optical magnitude. Johnston et al. (1994) confined the spectral type to a O9 - B2 type star, proposing that the star has spectral type B2e, with $M_* \simeq 10$ M$_\odot$ and $R_* \simeq 6$ R$_\odot$. Spectroscopic observations of the system undertaken by the authors showed Hα (single peak) and Hβ, Hγ, Hδ and He I 5876 (double peak) emission lines. Assuming a Keplerian circumstellar disc, the double peak of the Hβ line indicates an emission region at a radius of $8.5R_*$, which implies that the circumstellar disc has a radius $R_{\rm disc} > 8.5R_*$ (Johnston et al., 1994).

Negueruela et al. (2011) recently reported on high resolution ($R \sim 80\,000$) observations of LS 2883, made on the 29$^{\rm th}$ August 2009, with the UVES[ii] on the VLT[iii] between 373–499 nm and 565–946 nm. Those authors propose an O9.5 Ve stellar classification and a mass of $M_* = 31$ M$_\odot$

[ii] Ultraviolet and Visula Echelle Spectrograph
[iii] Very Large Telescope

Table 2.3: Optical magnitudes and colours for LS 2883.

Catalogue	V	B-V	U-B	$(U-B)_0$	A_ν	$M_\nu(U-B)_0$
Westerlund and Garnier (1989)	10.01	0.754	-0.506	-1.261	3.25	-4.6
Klare and Neckel (1977)	10.04	0.74	-0.44			
Schild et al. (1983)	10.05	0.72	-0.47			
Drilling (1991)	10.07	0.73	-0.47			

Table 2.4: The new stellar parameters for LS 2883 from Negueruela et al. (2011).

non-rotating		rotating	
$T^0_{\rm eff}$	33 500 K	i	33°
$\log g^0$	4.0	$\Omega_*/\Omega_{\rm crit}$	0.88
M^0_V	-4.47	$T_{\rm eff}$ (eq)	27 500 K
R^0_*	9.2 $R_\odot$	$T_{\rm eff}$ (pole)	34 000 K
$\log(L^0_*/L_\odot)$	4.98	$\log g$ (eq)	3.7
M^0_*	31 $M_\odot$	$\log g$ (eq)	4.1
		$R_{\rm eq}$	9.7 $R_\odot$
		$\log g$ (pole)	8.1 $R_\odot$
		$\log(L_*/L_\odot)$	4.79

with a radius of $R_* = 9.2$ $R_\odot$. From an analysis of the observed interstellar absorption lines seen in the spectrum those authors suggest that the star belongs to the stellar association Cen OB1 at a distance of $d = 2.3$ kpc. From earlier observations on the 8$^{\rm th}$ May 2006 with the SAAO 1.9m telescope, these authors determined the distance to two nearby stars, LS 2882 and LS 2888, which from standard extinction curves suggested a similar distance and association as proposed for the pulsar by Johnston et al. (1992b). Due to the high rotational velocity of LS 2883, gravitational darkening effects are important and Table 2.4 lists the parameters the star would have, were it not rotating (left column) and the modification to these parameters under the assumption that the star is rotating at 88% of its critical velocity (right column). While the more recent Negueruela et al. (2011) parameters are believed to be more accurate than those of Johnston et al. (1994), both stellar parameters have been considered in this study.

2.3 Infrared observations

As for the optical observations, there are limited infrared (IR) data of LS 2883 available in IR catalogues. Table 2.5 lists near IR measurements available from *2MASS* (Skrutskie et al., 2006) observations of the system at J, H and K_s, and at 8.28 μm and 12.13 μm from *Midcourse Space Experiment* (*MSX*) (Price et al., 2001) observations. Data from *2MASS* and *MSX* are available on-line through the NASA/IPAC Infrared Science Archive.[iv]

These archive observations at IR wavelengths are of particular importance to this study for

[iv] *http://irsa.ipac.caltech.edu/*

Table 2.5: IR data for PSR B1259-63 from *2MASS* (J,H,Ks) and *MSX* (A,C).

Filter	Wavelength μm	Magnitude	Flux Jy
J	1.235	8.026 ± 0.027	
H	1.662	7.699 ± 0.055	
Ks	2.159	7.248 ± 0.020	
A	8.28		0.2675 ± 0.0136
C	12.13		1.087 ± 0.5859

determining the flux that arises from the circumstellar disc associated with the Be star LS 2883. The emission from the disc is constrained by determining the IR excess from the system, which is the difference between the measured IR flux and the flux predicted by Kurucz stellar atmosphere models. The application of a curve of growth method to determine the IR excess in LS 2883 is discussed in Chapter 6, along with new observations obtained with the Very Large Telescope (section 2.8.4) in January 2011.

2.4 X-ray observations

PSR B1259-63 was first detected at X-ray energies with the Röntgen satellite (ROSAT) near apastron in two "multiday" observation periods roughly 5 months apart (Cominsky et al., 1994). An increase in the flux by a factor ~ 10 was detected between the two observations and the authors suggested that the flux may continue to rise towards periastron. Later, ASCA[v] X-ray observations two weeks before and after periastron showed a luminosity of the order of 10^{34} erg s^{-1} (Kaspi et al., 1995). The observations also showed that the flux two weeks after periastron was a factor ~ 2 higher than at periastron. This increase in the X-ray emission a few tens of days before and after periastron coincides with the disc crossing epoch. Similarly, ASCA detected a luminosity of $(9 \pm 3) \times 10^{32}$ erg s^{-1} near apastron (Hirayama et al., 1999).

Chernyakova et al. (2006) reported on XMM-Newton[vi] observations near the 2004 periastron passage combined with previously unreported BeppoSAX[vii] observations undertaken in 1997. The combined ASCA, XMM-Newton and BeppoSAX datasets presented a much more detailed X-ray light curve, with particular coverage focused on the disc crossing epochs. The observations show that the X-ray emission peaks within two narrow time bands that the authors suggested are the disc crossing positions. This would imply that the mid-plane of the disc is rotated by $\sim 70^\circ$ to the semi-major axis of the orbit with a half-opening angle $\theta_{\rm disc} = 18.5^\circ$ (Fig. 2.6) and folding the X-ray data around the presumed disc crossing phase showed a very good fit (Fig. 2.7). In addition the TeV gamma-ray emission detected by the High Energy Stereoscopic System (H.E.S.S.) in Namibia during the 2004 periastron passage also showed a good match

[v] Advanced Satellite for Cosmology and Astrophysics
[vi] X-ray Multi-mirror Mission–Newton
[vii] Satellite per Astronomia X

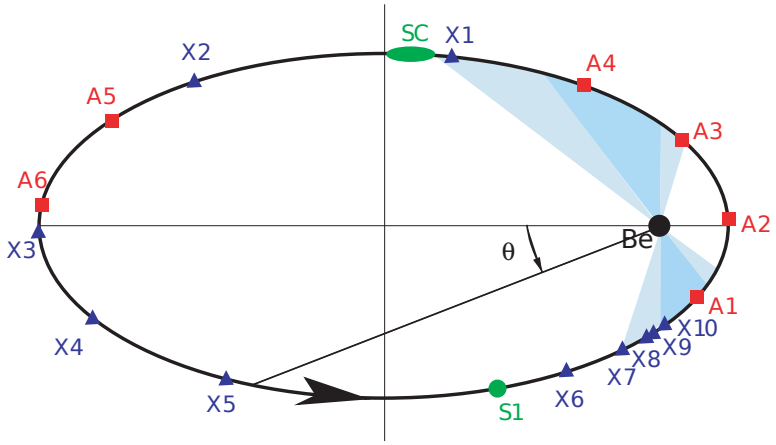

Figure 2.6: Positions of XMM-Newton (X1-X10), BeppoSAX (S1 & SC) and ASCA (A1-A5) observations of PSR B1259-63. The position of the disc in the orbital plane is inferred from the X-ray observations and is shown as the shaded section (Chernyakova et al., 2006).

when folded around this proposed disc position (Fig. 2.7).

X-ray observations during the next periastron passage in 2007, were in very good agreement with the previous observations (Chernyakova et al., 2009). The full X-ray combined light curve is shown in Fig. 2.8 along with the change in spectral index and hydrogen column density. The combination of 13 years of X-ray observations is very consistent, and the system appears very stable at X-ray energies.

An extended X-ray structure has also been detected by Chandra near apastron (Pavlov et al., 2011). The observations in the 0.5–8 keV energy band showed an elongated structure with an angular size of $\sim 4''$ and a luminosity of $\sim 10^{32}$ erg s^{-1} assuming a distance of 3 kpc. It is likely that this is associated with the PWN outflow from the pulsar.

2.5 Very high energy gamma-rays

A number of authors predicted gamma-ray emission through various production mechanisms for PSR B1259-63 (see e.g. Kawachi et al., 2004; Kirk et al., 1999; Tavani and Arons, 1997), but an initial search for gamma-ray emission undertaken with the CANGAROO-II telescope[viii] (Kawachi et al., 2004) $\sim$ 47 and $\sim$ 157 days after the October 2000 periastron passage was not able to detect the source. The first detection of PSR B1259-63 at Very High Energy (VHE, $>$ 100 GeV) gamma-rays was made around the next periastron passage in 2004 with the H.E.S.S. telescope with a 13σ significance (Aharonian et al., 2005). The observations showed a variable light curve with an inferred maximum flux a few days before and after periastron (Fig. 2.9). The

[viii] Collaboration between Australia and Nippon for a Gamma Ray Observatory in the Outback.

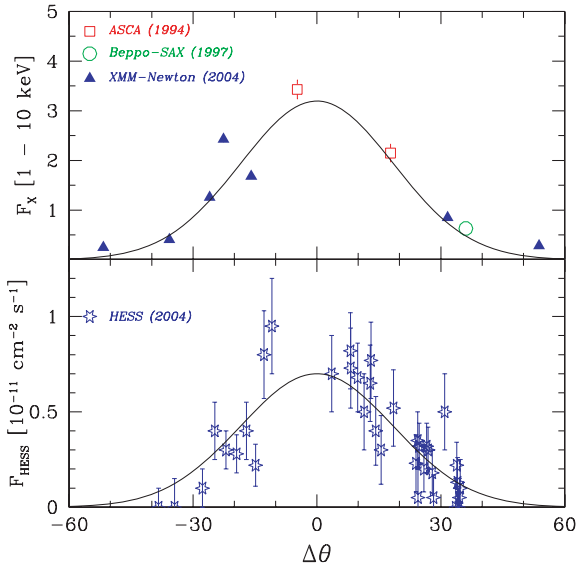

Figure 2.7: The X-ray (top) and H.E.S.S. (bottom) fluxes folded around the proposed disc crossing phase, $\Delta\theta$, where $\Delta\theta$ is defined as the difference between the angular position of the pulsar (θ in Fig. 2.6) and the proposed position of the mid-plane of the circumstellar disc. Therefore, $\Delta\theta = 0$ corresponds to the pulsar passing through the disc mid-plane (Chernyakova et al., 2006).

spectrum was fitted with a single powerlaw

$$F = F_0 \left(\frac{E}{1\mathrm{TeV}} \right)^{-\Gamma},$$

with $F_0 = (1.3 \pm 0.1_{\mathrm{stat}} \pm 0.3_{\mathrm{sys}}) \times 10^{-12}$ cm^{-2} s^{-1} TeV^{-1} and a photon index of $\Gamma = 2.7 \pm 0.2_{\mathrm{stat}} \pm 0.2_{\mathrm{sys}}$ (within statistical and systematic errors) which showed no significant variation during the observations. This infers a luminosity for the system of $L_\gamma \approx 8 \times 10^{32}$ erg s^{-1} for an assumed distance of 1.5 kpc (Aharonian et al., 2005).

Two observations during 2005 and 2006, monitoring the source away from periastron, showed no significant detection while monthly observations around periastron (April - August 2007) again detected PSR B1259-63 at VHE gamma-rays with a 9.5σ significance (Aharonian et al., 2009). The average energy flux was $F_E \approx 2 \times 10^{-12}$ erg cm^{-2} s^{-1}, with a best fit photon index of $\Gamma = 2.8 \pm 0.2_{\mathrm{stat}} \pm 0.2_{\mathrm{sys}}$. This infers a luminosity of $L_\gamma \approx 6 \times 10^{32}$ erg s^{-1} (assuming a distance of 1.5 kpc), consistent with the previous H.E.S.S. observation. While there was a possible suggestion of a change in the photon index between the May and June 2007 observations, a 1σ and 2σ comparison shows that there is no statistically significant change. The VHE light curve (combining all H.E.S.S. data) is shown in Fig. 2.10. A comparison between the 2004 and 2007 light curves would appear to show a change between the two periastron passages, but as is noted by the authors, due to the lower significance of the 2009 observations and the lower time resolution (monthly not daily observations) the 2007 data cannot be considered to be significantly

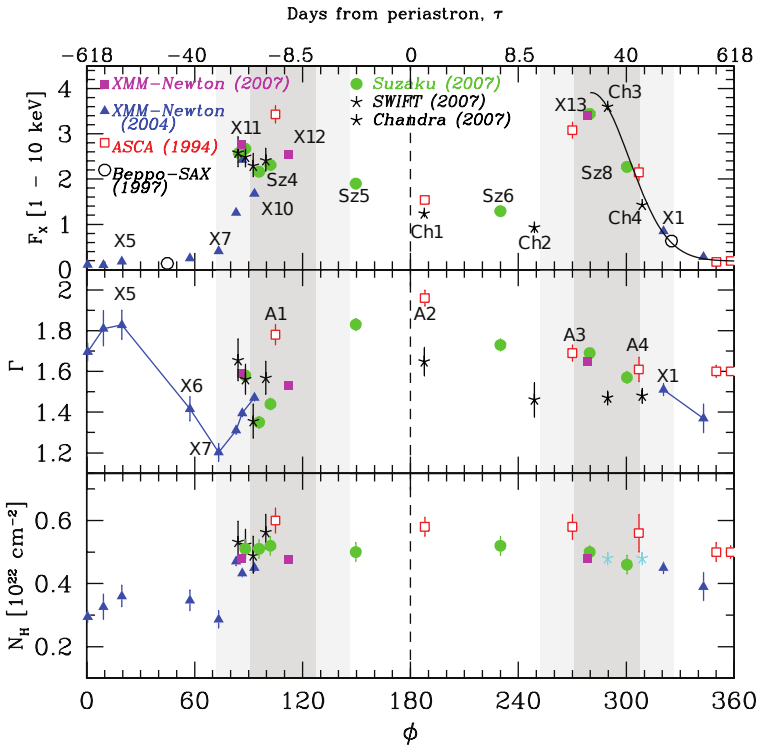

Figure 2.8: Combined X-ray light curve from PSR B1259-63 around different periastron passages. Shown is the change in flux (top) along with the variation of the spectral index (middle) and the hydrogen column density (bottom) observed during the observations (Chernyakova et al., 2009).

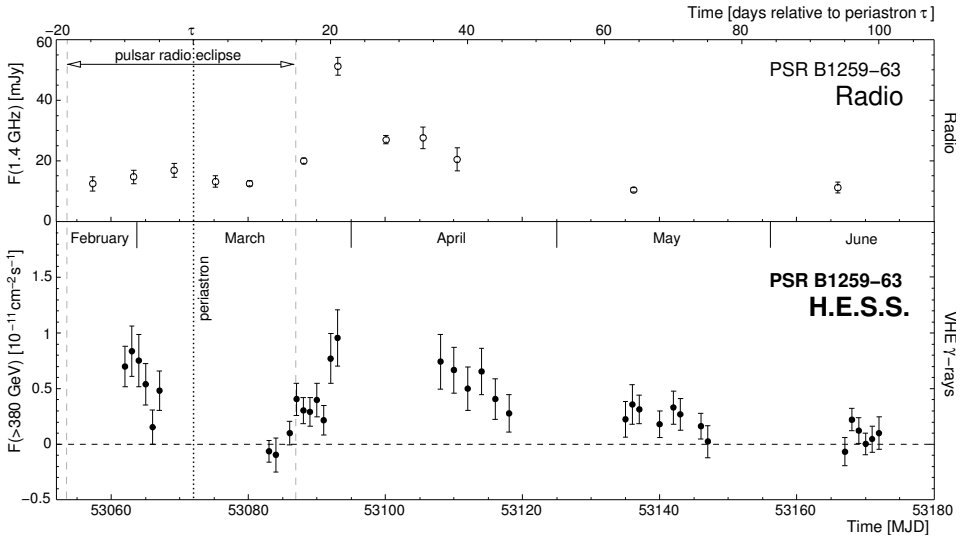

Figure 2.9: The H.E.S.S. light curve during the 2004 periastron passage (bottom panel) and the radio light curve (top panel) shown for comparison. The H.E.S.S. observations were performed daily, except when the moon prevented observations, resulting in the gaps in the H.E.S.S. light curve (Aharonian et al., 2005).

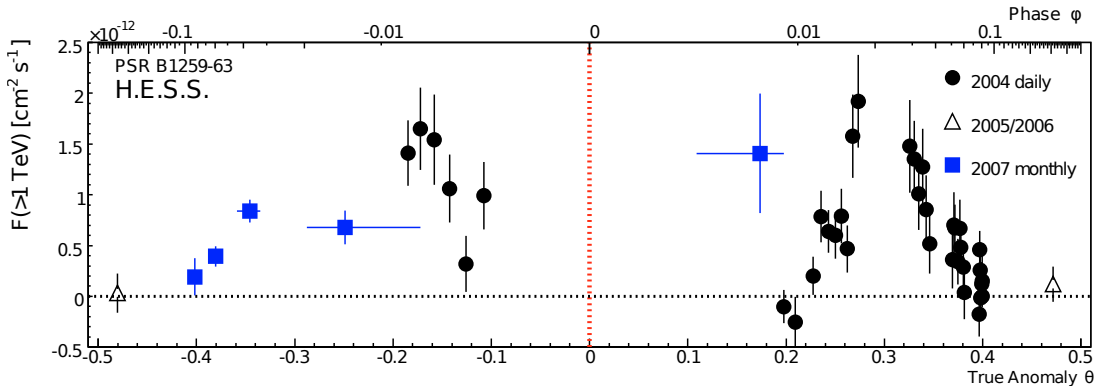

Figure 2.10: The H.E.S.S. light curve of PSR B1259-63 combining the 2004, 2005, 2006 and 2007 data (Aharonian et al., 2009).

different from the 2004 data.

2.6 A multi-wavelength view of PSR B1259-63

The discussion above has given a very brief overview of the observations of PSR B1259-63 since the original detection of the pulsar in 1992. The overview has attempted to highlight only those results which are believed to be most significant for this study. Before discussing the recent *Fermi* observations around the 2010 periastron passage it will be useful to consider the overall picture that is implied by the multi-wavelength observations.

PSR B1259-63 is unique among the gamma-ray binaries since the compact object is directly observed as a ~ 48 ms pulsar. This allows for a direct measurement of the energy output from the pulsar. The pulsar has a spin period of $P = 47.7625$ ms and a spin-down rate of 2.277×10^{-15} s s^{-1} (Wang et al., 2004), giving a spin-down luminosity of (equation 4.1)

$$L = 4\pi^2 I \frac{\dot{P}}{P^3} = 8.25 \times 10^{35} \text{ erg s}^{-1},$$

and therefore the observed X-ray and VHE gamma-ray luminosities near periastron are of the order of 0.1% of the available spin-down power. This is the same ratio as is observed for other young spin-down powered pulsars (Becker and Truemper, 1997). In addition there is a marked similarity between the radio, X-ray and gamma-ray light curves as shown in Fig. 2.11.

As shown in Fig. 2.7, there was a good agreement between both the X-ray and gamma-ray light curves if folded around the proposed disc position which lead Chernyakova et al. (2006) to suggest that IC scattering was not the dominant production mechanism for the TeV energy gamma-rays. There are, however, a few problems with this proposed disc position. Firstly, the proposed position is in conflict with the region of the pulsar eclipse (e.g. Khangulyan et al., 2007). The radio eclipse lasts roughly $\tau \pm 20$ days around periastron while for the proposed

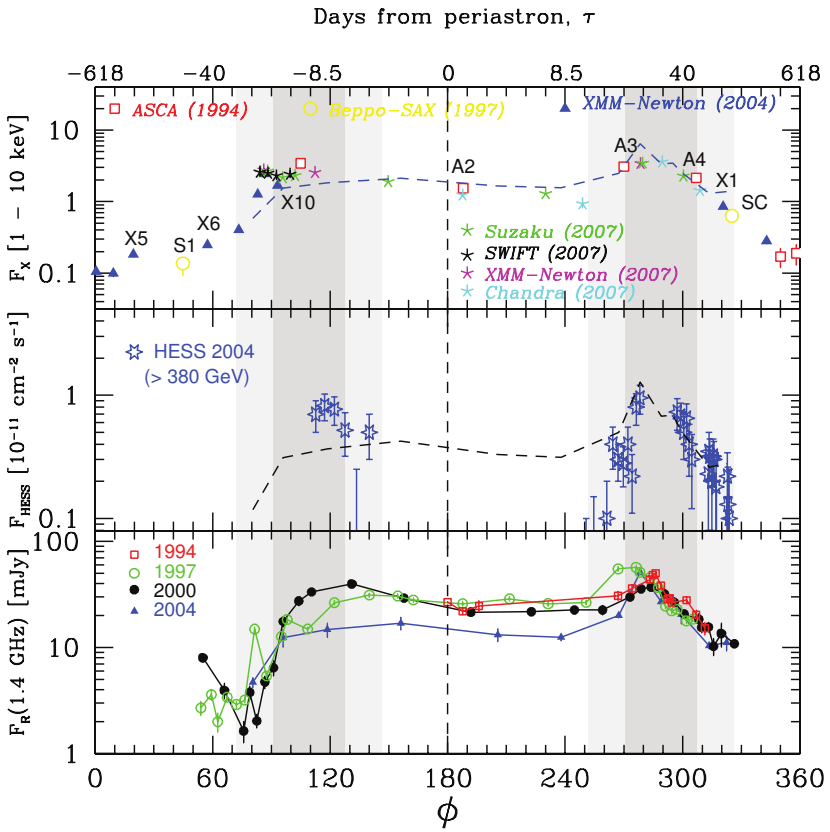

Figure 2.11: Comparison of the X-ray(top), VHE gamma-ray (middle) and radio (bottom) light curves of PSR B1259-63. Also shown is the disc position (shaded blue section) that was suggested by Chernyakova et al. (2006) (see section 2.4 p. 13). The dashed line plotted on the X-ray and H.E.S.S. light curves is the scaled radio light curve from 2004, which is shown for comparison (Chernyakova et al., 2009).

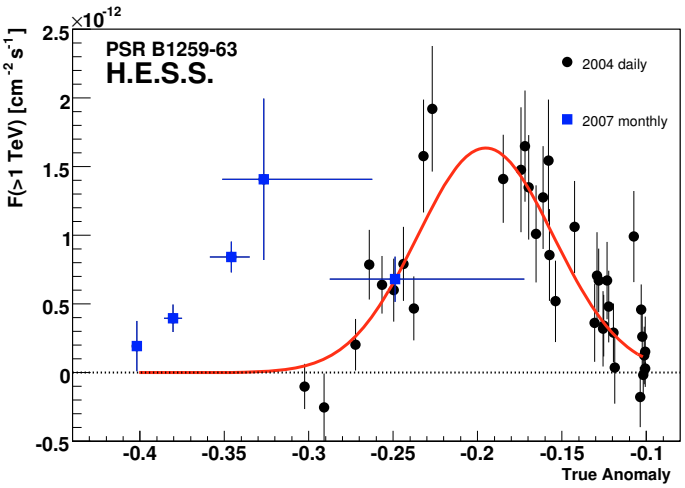

Figure 2.12: H.E.S.S. data (2004 and 2007) folded around the proposed disc position in Chernyakova et al. (2006). The 2007 data do not agree with the proposed disc position (Aharonian et al., 2009).

disc position the pulsar would emerge from the disc only after $\tau + 40$ days (see shaded region in Fig. 2.11). Secondly, while the 2004 H.E.S.S. observations agree with the proposed disc position (Fig. 2.7), the 2007 observations do not (Fig. 2.12; Aharonian et al., 2009). And lastly, the 9.3σ detection of TeV gamma-ray 46 days before periastron suggests IC scattering remains a viable gamma-ray production mechanism.

Chernyakova et al. (2009) discussed two competing IC models for the X-ray and gamma-ray production (Fig. 2.13). The two possibilities are a broad electron injection spectrum (dashed line) that would result in a single IC spectrum which would fit the X-ray and gamma-ray emission, or an electron spectrum peaked at high energies (e.g. 10 TeV) which would require both a synchrotron and IC spectrum to match the X-ray and gamma-ray emission respectively. The authors suggested that the possible detection of PSR B1259-63 with *Fermi* (between 20 MeV – 300 GeV) during the 2010 periastron passage could prove a vital test as it would provide coverage around GeV energies, where the two models show significant deviation in the predicted flux (Fig. 2.13). However, it was noted that the point source detection limit for LAT[ix] is 3×10^{-9} ph cm^{-2} s^{-1} (> 100 MeV) $\approx 5 \times 10^{-12}$ erg cm^{-2} s^{-1} (Atwood et al., 2009) could be too high to detect PSR B1259-63, especially in the case of the second model where the flux at GeV energies from IC scattering would almost certainly fall below the LAT detection threshold.

The *Fermi* detection or non-detection around the 2010 periastron passage was then of particular interest and a number of research groups organized multi-wavelength campaigns to observe the system during periastron.

[ix]Large Area Telescope: the LAT is the imaging instrument on-board *Fermi*.

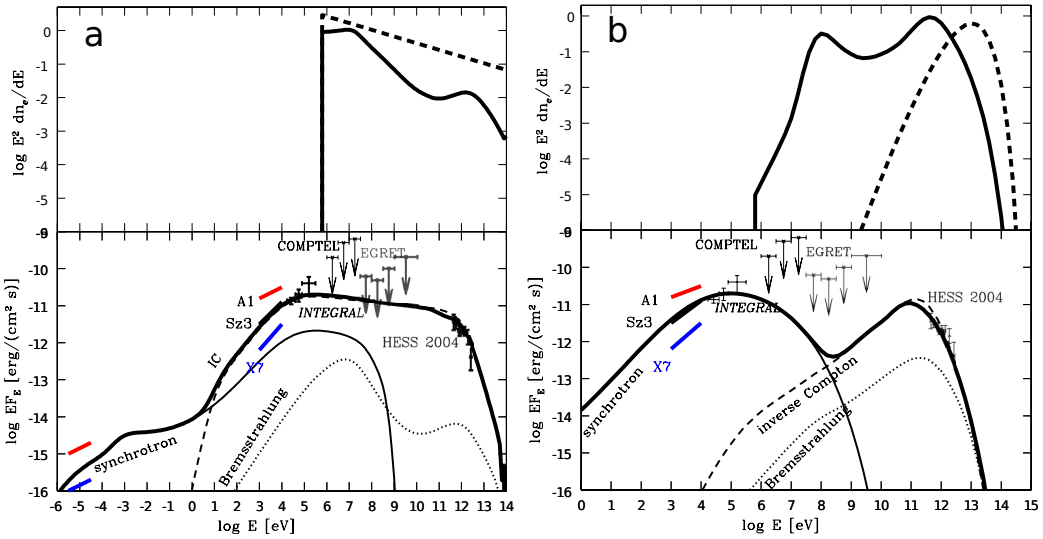

Figure 2.13: Possible X-ray and gamma-ray production mechanisms as discussed in Chernyakova et al. (2009). The top panel shows the initial electron injection spectrum (dashed line) and the resulting spectrum from the cooling and escaping of electrons (solid line). In (a) the injection spectrum in broad while in (b) the spectrum is peaked around 10 TeV. The bottom panel shows the resulting emission processes and the total emission. The most important feature is that for the broad spectrum (a) the X-ray and gamma-ray emission is the result of a single broad IC emission while in (b) the X-rays and gamma-rays are best fit by a synchrotron and IC process respectively.

2.7 Fermi detection

PSR B1259-63 was detected around the 2010 periastron with unexpected results (Abdo et al., 2011; Tam et al., 2011). Abdo et al. (2011) reported on the GeV energy activity and preliminary radio and X-ray observations during the periastron passage, and the results from this discussion are summarized below. During the period leading up to periastron, PSR B1259-63 was not detected by *Fermi* on a daily or weekly timescale and was only detected between 0.1–1 GeV during the first disc crossing by integrating over the period $\tau - 28$ to $\tau - 0$ days from periastron, leading to a 5σ detection (Abdo et al., 2011). This "brightening" phase, as it is referred to by the authors, lasted until ~ 18 days after periastron with a best fit photon index of $\Gamma = 2.4 \pm 0.2_{\rm stat} \pm 0.5_{\rm sys}$ and an energy flux of $F = (0.9 \pm 0.3_{\rm stat} \pm 0.4_{\rm sys}) \times 10^{-10}$ erg cm^{-2} s^{-1} (within statistical and systematic errors). This faint detection near the disc crossing is predicted by previous models.

However, ~ 30 days after periastron, the source became very active and was much brighter than during the brightening phase, showing an average flux of $F(> 100$ MeV$) = (4.4 \pm 0.3_{\rm stat} \pm 0.7_{\rm sys}) \times 10^{-10}$ erg cm^{-2} s^{-1}, with a photon index of $\Gamma = (1.4 \pm 0.6_{\rm stat} \pm 0.2_{\rm sys})$ and a cutoff energy $E_c = (0.3 \pm 0.1_{\rm stat} \pm_{\rm sys})$ GeV. This "flare" and accompanying spectral hardening was unexpected as it was assumed that the system would show fairly symmetric emission around periastron. The observed *Fermi* spectral energy distribution (SED) during the brightening phase and flare is shown in Fig. 2.14. Radio and X-ray observations around periastron showed no unusual or

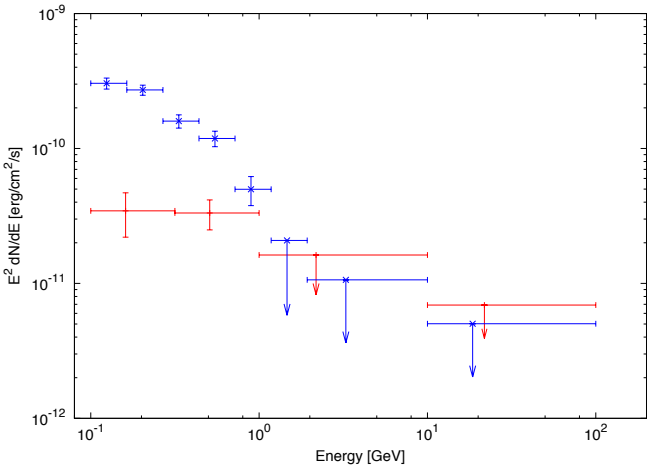

Figure 2.14: The observed *Fermi* SED observed during the brightening phase (red points), and post-periastron flare. Figure plotted using the data released with Abdo et al. (2011).

flaring events, and were consistent with previous observations. The *Fermi* light curve is shown in Fig. 2.15 along with radio, X-ray and TeV gamma-ray observations. Significantly, the peak luminosity detected was $L_\gamma \approx 8 \times 10^{35}$ erg s^{-1} (for an assumed distance of 2.3 kpc), which corresponds to $\approx 100\%$ of the spin-down power of the pulsar. This unexpected flaring behaviour cannot be explained by current models of gamma-ray binaries.

2.8 Observational campaigns

As part of this study an observational campaign was undertaken to observe Be-XRBs in the Small and Large Magellanic Clouds (SMC & LMC), and to observe PSR B1259-63/LS 2883 during the December 2010 periastron passage. A brief summary of this campaign is presented below, beginning with a short description of the telescopes used.

2.8.1 SAAO - 1.9m and 1.0m telescopes

Optical photometry and spectroscopic observations were undertaken at the South African Astronomical Observatory (SAAO) located near Sutherland, in the Northern Cape, using the 1.9 m and 1.0 m telescopes. The technical details presented here are based on the observations manuals available at the observatory and details from the observatory website.[x] The 1.9 m telescope was originally situated at the Radcliffe Observatory in Pretoria and the 1.0 m was originally stationed at Cape Town before being moved to the current site in Sutherland after the establishment of SAAO.

Photometric and spectroscopic observations were carried out with the 1.9 m using the SAAO

[x] *www.saao.ac.za*

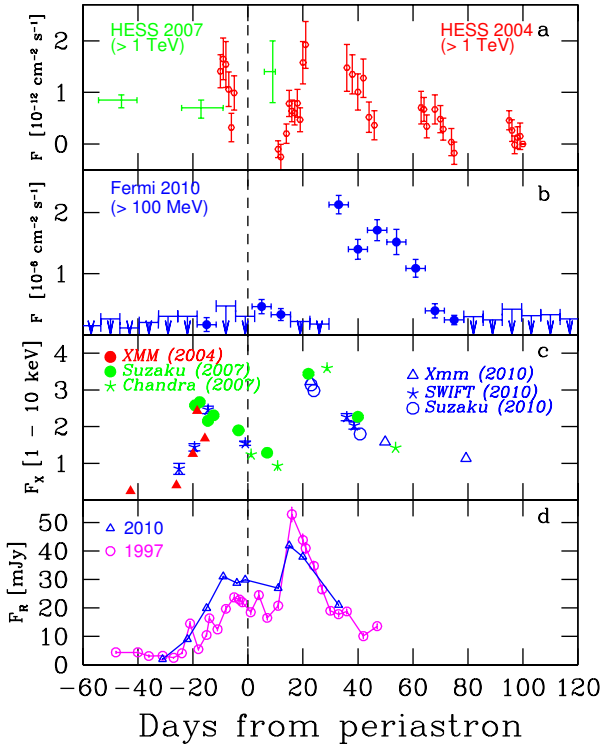

Figure 2.15: Mulit-wavelength light curves of PSR B1259-63. From top to bottom: (a) H.E.S.S. observations during 2004 and 2007, (b) *Fermi* 2010 observations, (c) X-ray flux in units of 10^{-11} erg cm^{-2} s^{-1}, and (d) 2.4 GHz radio observations. The light curves combine observations undertaken over different periastron passages. The 2010 observations are included for the *Fermi*, X-ray and radio light curves. (Abdo et al., 2011).

CCD (charge-coupled device) and grating spectrograph respectively, which are mounted at the telescope's Cassegrain focus and only photometric observations were performed with the 1.0 m telescope. The appropriate optical diagrams of each telescope are shown in Fig. 2.16. Both telescopes use an off-axis self guider which is used for source acquisition and computer assisted tracking correction.

With the SAAO CCD, the 1.9 m has a field of view of 146×146 arcsec, while the 1.0 m has a field of view of 317×317 arcsec. The wider field of view on the 1.0 m makes it ideal for observing crowded fields in the SMC and LMC, as a large number of stars are visible around the science target which allows for self-calibration of each frame.

SAAO CCD

The SAAO CCD can refer to one of two instruments, either the STE3 or STE4, with the STE4 being used during the observations. The SAAO CCD (STE4) is a back-illuminated CCD with a 1024×1024 pixel resolution and is cooled with liquid nitrogen during observations. The CCD has a gain of 2.8 electrons per ADU, a linear count limit of 65535 ADU and produces a readout noise of 6.5 electrons. Dark current effects are negligible due to the liquid nitrogen cooling. The CCD images are saved using the FITS format (Wells et al., 1981) on local data reduction computers. The local data reduction software corrects the science frame using standard optical data reduction techniques, correcting for readout noise and non-uniform CCD sensitivity, as well as known bad pixels.

Both the 1.9 m and the 1.0 m are fitted with the standard Johnston (U, B and V) and Cousin (R and I) filters and additional Hα, BG38, and Z filters are available.

Grating spectrograph

The grating spectrograph is mounted at the Cassegrain focus of the 1.9 m telescope and records the spectrum on a SITe CCD chip. The slit width of the spectrograph is 1.2 to 1.5 arcseconds and the desired spectral range and resolution is obtained by selecting the appropriate grating. Table 2.6 lists the available gratings and associated properties.

2.8.2 IRSF

The InfraRed Survey Facility (IRSF) 1.4 m telescope is a near IR telescope that observes in an altitude-azimuth configuration.[xi] The telescope is located at SAAO near Sutherland and was built as a collaboration between SAAO and the Nagoya University in Japan. Using the SIRIUS[xii] camera, which consists of three 1024×1024 CCDS, the IRSF takes simultaneous J, H and K_s filter observations. The primary science object of the telescope is to perform Magellanic Cloud

[xi] Technical details of this telescope are based on the available operation manuals, and information provided on the telescope website accessed via http://www.saao.ac.za/facilities/telescopes/.

[xii] Simultaneous-3color InfraRed Imager for Unbiased Survey

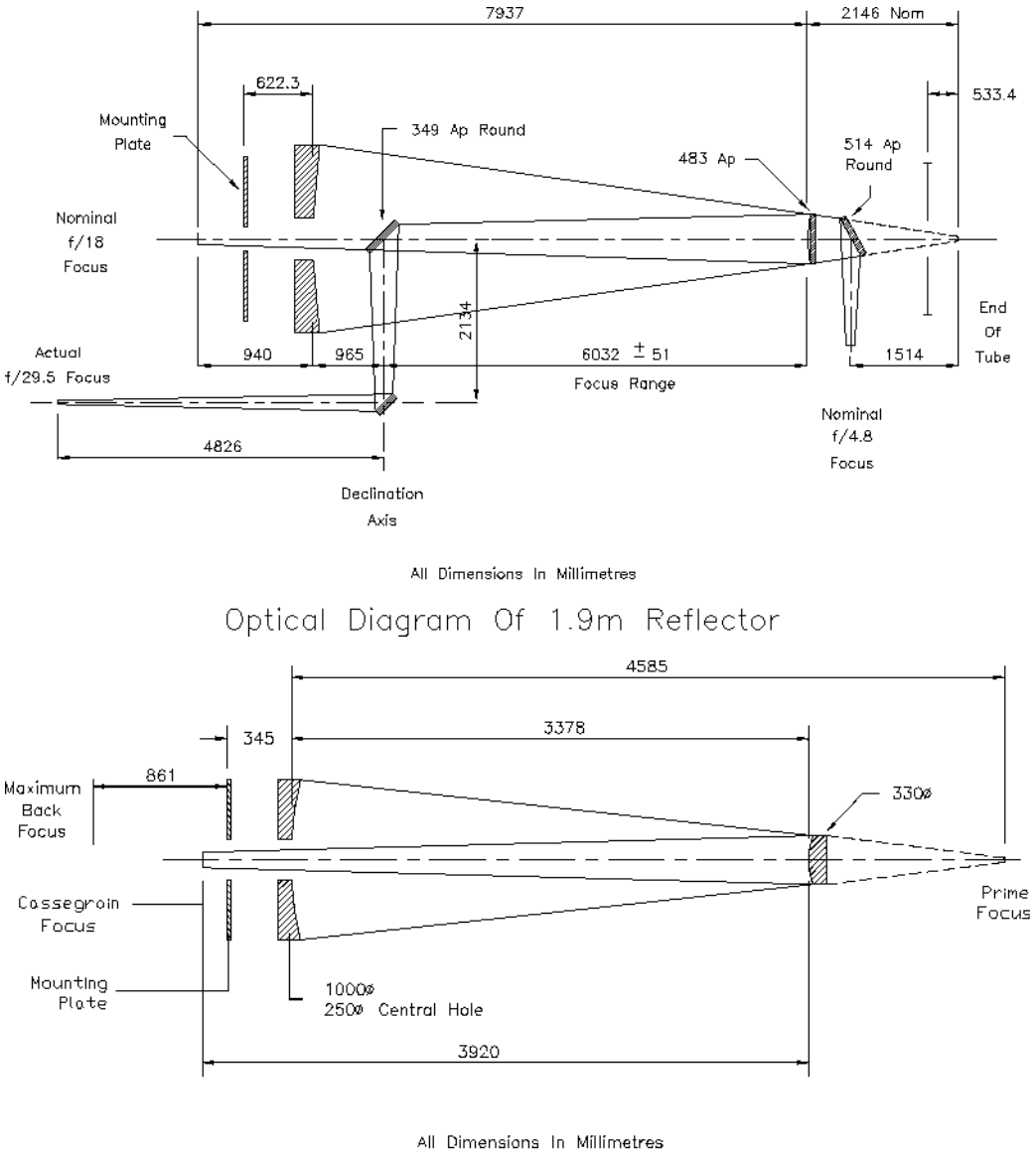

Figure 2.16: Diagram of the optics of the 1.9 m and 1.0 m telescopes at SAAO, Sutherland (http://www.saao.ac.za/facilities/telescopes/).

Table 2.6: Available grating for the SAAO grating spectrograph on the SAAO 1.9m telescope (www.saao.ac.za/facilities/instruments/grating-spectrograph/).

Grating No.	Lines mm^{-1}	Å Range	Useful Range	Blaze (1st order)	Resolition (Å) (Slit 250 μm)
7	300	210	3200	4600	5
8	400	155, 75	2300, 1150	7800	4, 2
9	830	65, 30	960, 480	7800	4, 2
4	1200	50	800	4600	1
6	600	100	1600	4600	2
5	1200	50, 20	800, 350	6800	1, 0.5
10	1200	50	800	10 000	1
11	600	100	1600	10 000	2

surveys, making it the ideal instrument for near IR observations of Be/X-ray binaries in the SMC/LMC.

In order to compensate for the IR flux associated with the night sky, multiple images are taken, each slightly offset from the centre of the science target position, but still overlapping with the central position (Nagata et al., 2003). Each offset position or "dither" is created by a combination of moving the telescope and rotating the SIRIUS camera. The number of dithers, the offset distance of each dither and the integration time per dither is defined by the observer. A typical observation of a Be/X-ray binary in the SMC would consist of 15 dithers with a 15 to 20 second integration time per dither within a 15 arcsec radius. In addition, a clear section of the sky, containing no or few stars, must also be observed to subtract the sky emission from the science observation. The sky observations must be taken using the same dither configuration as the target observation, for a region of sky close to the science target.

Each individual dither is saved as a separate FITS file and the final data image is obtained by reducing the data using the SIRIUS and SIRPOL software packages.[xiii] The software pipeline corrects for flat field, dark current and sky effects, realigns each image to the correct orientation using the SExtractor software package, and combines the corrected images to create the final science frame.

2.8.3 SALT & RSS

The Southern African Large Telescope[xiv] (also situated at SAAO) is a $\sim 10 \times 11$ metre optical telescope, with a primary mirror consisting of 91 individual hexagonal pieces. The telescope is designed to operate from 320 to 1700 nm and is one of the larger optical telescopes in the Southern Hemisphere. The limitation on the telescope is that it operates in a fixed altitude

[xiii] The software packages are available (on 16 January 2012) from *http://www.z.phys.nagoya-u.ac.jp/ nakajima/sirius/software/software.html*

[xiv] Technical details of this telescope are based on the available operation manuals which can be accessed via the SAAO website (www.saao.ac.za).

angle (37° to zenith) and sources can only be observed when they lie within the observable altitudes of 47° to 59°. Targets are tracked by moving the observation payload which lies at the primary focus above the telescope and not by moving the primary mirror in the azimuthal angle. The primary mirror is only moved to acquire new sources. Sources can be tracked for an average period of ~ 2 hours, depending on the altitude of the sources, with a maximum tracking time of ~ 3.5 hours.

Spectroscopic observations are performed using the Robert Stobie Spectrograph (RSS) which is mounted at the primary focus of the telescope and provides a resolution up to ~ 5500, with a maximum wavelength coverage between 320 to 900 nm.

2.8.4 VLT & VISIR

The European Southern Observatory (ESO) Very Large Telescope (VLT), situated at Paranal Observatory in the Atacama Desert, consists of four unit telescopes each with a 8.2 m mirror, that can operate, individually or as an optical interferometer, from the ultra-violet to the mid-IR (~ 300 nm to 25 μm). Mid-IR photometric observation were obtained with the VLT Imager and Spectrometer of the mid Infrared (VISIR; Lagage et al., 2004) mounted on Unit Telescope 3 (UT3), which is sensitive to the broad N and Q mid-IR bands, which correspond to the appropriate atmospheric windows. The instrument operates between 8 – 13 μm (N band) and 16.5 – 24.5 μm (Q band) with a maximum field of view of 32.3×32.3 arcsec depending on the system configuration (Smette and Vanzi, 2007).

The IR emission from the atmosphere is compensated for by a process of chopping, nodding and jittering the observations (Smette and Vanzi, 2007). During each observation the secondary mirror is rotated, allowing for an on-source and off-source observation; this processing is known as chopping. This observes the target and an appropriate region off-target of empty sky to compensate for the IR sky emission. The chopping process is then repeated by moving the telescope off source and repeating the observation to compensate for the light path difference between the on-source and off-source chops. This process of moving the telescope on-source and off-source is known as nodding. Observations of sources go through a cycle of chopping and nodding which removes the effect of the IR sky emission. In addition to the chopping-nodding cycle, an additional random offset or jitter can be added. This means that each observation will not occur on exactly the same spot on the CCD and this offset is added to compensate for bad pixels.

Observations also consist of a number of different “dithers” taken at each chopping and nodding position, each having a maximum observation time of 5 ms. These dithers are not stored, but are combined during the observation.

2.8.5 SMC/LMC campaign

As part of this study it was decided to undertake observations of other known Be/X-ray binary systems in the SMC/LMC. The advantage of such a survey is that sources are in close proximity and can be observed at the same time of the year, which makes it possible to observe a number of sources within a short time period. The observations were undertaken at optical and infrared wavelengths in order to determine the infrared excess of each Be star. The infrared excess is determined by the difference between the observed infrared flux of the star and flux which is predicted by the Kurucz model for the given spectral type (fitted to the observed optical magnitudes). These observations contribute to the understanding of the variability of Be stars in infrared and may allow for an ensemble estimation of the variability expected in the disc structure (and infrared excess) for systems such as PSR B1259-63. Since Be systems are extremely variable, optical and infrared observations must be taken nearly simultaneously. For this reason observation time was requested on the IRSF and either the 1.9 m/1.0 m telescopes during the same week. The observation campaign consisted of approximately 60 sources in the SMC. Data were obtained during three separate observation runs and remains an ongoing project. Results from the observations have contributed towards a study of the orbital parameters and spectral classification of IGR J010547253 (Townsend et al., 2011).

2.8.6 PSR B1259-63/LS 2883 December 2010 campaign

PSR B1259-63/LS 2883 went through periastron passage during December 2010. For this reason a multi-wavelength observation campaign was proposed to observe the source from Sutherland using the 1.9 m (spectroscopy), 1.0 m (photometry) and IRSF during the critical week of the periastron passage. Proposals were also submitted to observe the source with SALT and VLT in service mode.

Due to the hour angle, PSR B1259-63 was only observable from SAAO at a low altitude, and was only observable with the 1.9 m and 1.0 m during approximately the last hour of the observing night. Due to poor conditions it was not possible to obtain observations with either telescope as the observation week coincided with very poor weather. On nights when observations were possible, the weather tended to deteriorate during the night due to increasing humidity. The IRSF, with its altitude-azimuthal mount had much greater observing freedom and was able to observe the source during the week.

The proposal for SALT was submitted with the intention that observations would take place if the telescope was in the re-commissioning phase (after the upgrade and repair of the RSS). Unfortunately the re-commissioning phase had not begun by this period and the source was not observed.

The VLT observed the source in January 2011, slightly after periastron. The detected flux is closely inline with previous observations of the source and results of the VLT observations are presented in Chapter 6.

This chapter has presented the observed properties of the gamma-ray binary system PSR B1259-63/LS 2883. In order to model this system it is necessary to consider the properties of both the Be star and the pulsar. The following chapter (Chapter 3) presents a general discussion of the properties of Be stars and other Be binary systems, while the properties of pulsars and pulsar wind nebulae systems are presented in Chapter 4.

Chapter 3

Be stars and Be binary systems

Research into Be stars and active OB stars has progressed rapidly in the last few years, particularly with the development of interferometry techniques which have allowed for a more direct observation of OB stars and the circumstellar environment. OB star research is an active and rapidly progressing field of research and readers are referred to a detailed review on classical Be stars given by Porter and Rivinius (2003) and more recent reviews included in the proceedings of the IAU Symposium 272: *Active OB stars: Structure, Evolution, Mass-Loss, and Critical Limits* (Neiner et al., 2011).

OB stars are subdivided into multiple categories, from Luminous Blue Variable giants, to Be stars, B[e] stars, and Bp stars etc. This chapter will focus on "classic" Be stars and the Be star phenomena which generally affects B-type stars, and also late O-type and early A-type stars. This is the case for PSR B1259-63/LS 2883 where the main sequence companion is a O9.5 Ve type star. A brief summary of recent models, results and open questions surrounding Be stars which are pertinent to this study, will be presented.

3.1 Be stars

The most common definition for a Be star is a B-type star that shows or has shown emission lines instead of absorption lines in the Balmer spectrum (Collins, 1987). The discovery of Be stars was reported by Secchi (1866) who detected a bright emission line from γ Cassiopeiae. These observed emission lines are produced in a circumstellar disc that surrounds Be stars, as was first suggested by Struve (1931). Despite being studied and observed for nearly 150 years the key question surrounding Be stars remains how and why the star develops a circumstellar disc. Currently, the most promising model is that the discs are viscous driven, Keplerian, "decretion" discs, as will be discussed in section 3.2, since this model has been able to match a number of observational properties. This section will discuss some of the observational properties of Be stars, and the mechanisms that are believed to produce them.

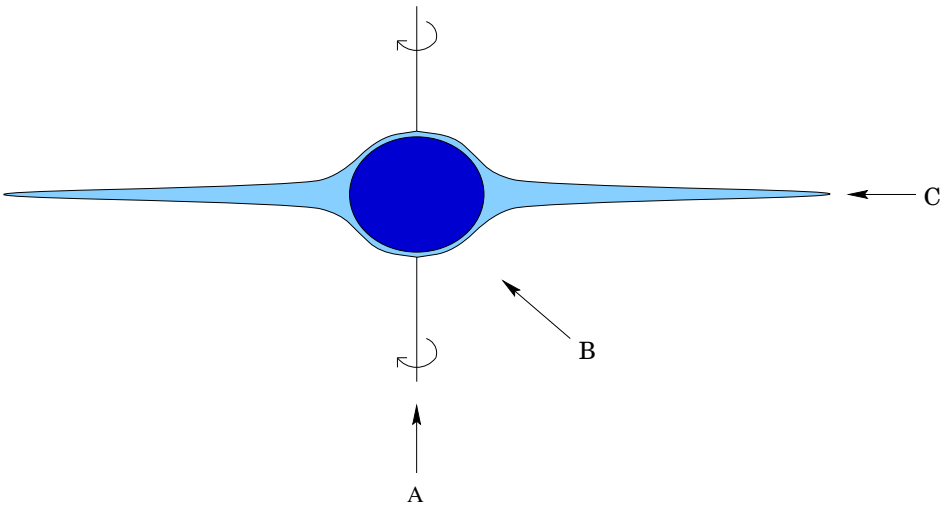

Figure 3.1: Illustration of how the viewing angle of a Be star can affect the observed emission lines. Observations from direction A will produce a single peak emission line, observations from direction B will show double peaked, Doppler shifted emission lines, while observations from direction C can produce shell star observations as discussed in the text (Howells, 2002).

3.1.1 Emission lines

Since Be stars are defined by the presence of emission lines which originate from the circumstellar disc, it is appropriate to begin by discussing the emission line properties.

Doppler shifting and shell stars

The properties of the observed spectral emission lines depend on the size and orientation of the Be star's circumstellar disc. Larger circumstellar discs, with more material, show bright emission lines, while smaller discs show fainter, less prominent lines. Because the discs are variable in nature, growing and shrinking in time, the emission lines are also variable and vanish if the circumstellar disc is depleted.

Depending on the orientation of the disc relative to the observer, as shown in Fig. 3.1, the observed emission lines may be a single peak if the disc is viewed predominantly face-on (A), or can show a double peak, due to Doppler shifting, with increasing inclination (B) (Struve, 1931). If the disc is observed edge on (C), the observation through the disc creates an additional absorption feature, which obscures light from the star and is observed as a narrow absorption component superimposed onto the stellar absorption feature. Such stars are known as shell stars. The standard definition of a shell star is given by Hanuschik (1996), and states that a Be star is defined as a shell star if the observed central FeII line flux is less than the flux from the star, i.e. $F_{\rm cen}/F_\star < 1$.

Fig. 3.2 shows three examples of Be stars that are observed from face-on (left) to edge-on (right) corresponding to observations at positions A, B and C in Fig. 3.1. Thus BD+46 0275

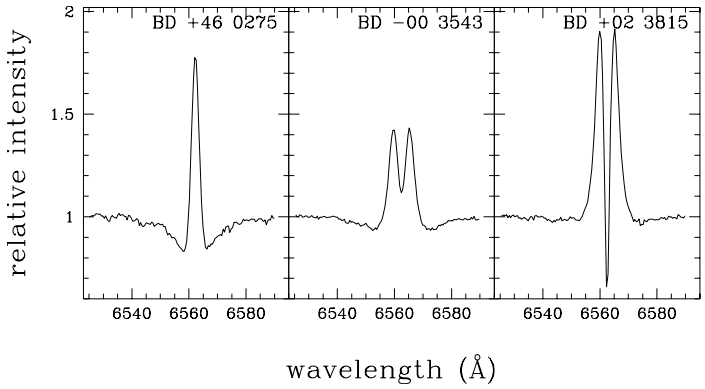

Figure 3.2: Observations of three Be stars which correspond from left to right to observations from direction A, B and C as shown in Fig. 3.1 (Howells, 2002).

is observed nearly face-on and shows a clear single emission line while BD+02 3815 is a typical shell star with a central absorption feature superimposed on the emission line.

An example of the variability observed from Be stars is shown for *o* Andromedae in Fig. 3.3, which shows the change in the Hα line due to the growth and decay of the circumstellar disc. The observation on the 26$^{\text{th}}$ of August 1986 shows the star in a discless state, with only the intrinsic stellar Hα absorption feature present. The dotted line fitted to this intrinsic feature is then shown on all other observations. The two observations before the 26$^{\text{th}}$ of August 1986 showed the disc decaying, while observations after this date show the subsequent growth of the circumstellar disc and the modification of the observed spectral line. Since *o* Andromedae is a shell type star, the disc is observed edge on (direction C in Fig. 3.1) and shows an enhanced Doppler shifted emission line and an additional absorption feature. Therefore, as the disc grows the Hα absorption line shows higher emission on the outer wings, due to the Doppler shifted emission from the disc, while the central flux begins to decrease below the intrinsic stellar line flux as additional absorption through the disc decreases the observed stellar contribution.

V/R variation

Observations of Be stars show that there can be a change over time in the relative amplitude of the "violet" and "red" edge of an observed double peak emission line, known as V/R variation. This variation occurs over a timescale of a few years and is observed in approximately two thirds of Be stars (e.g. Carciofi, 2011); an example is shown for X Persei in Fig. 3.4. The V/R variation is explained by a region of denser material in the circumstellar disc which orbits around the Be stars, known as one-arm oscillation.

It was shown by Kato (1983) that such a region could exist in a Keplerian disc, and Telting et al. (1994) used this model to explain the observed variations in β^1 Monoceros, as illustrated in Fig. 3.5. The denser material shown in the disc, orbits around the star in an anti-clockwise direction from top to bottom (I to IV) while the observer is to the left of the figure. At I the

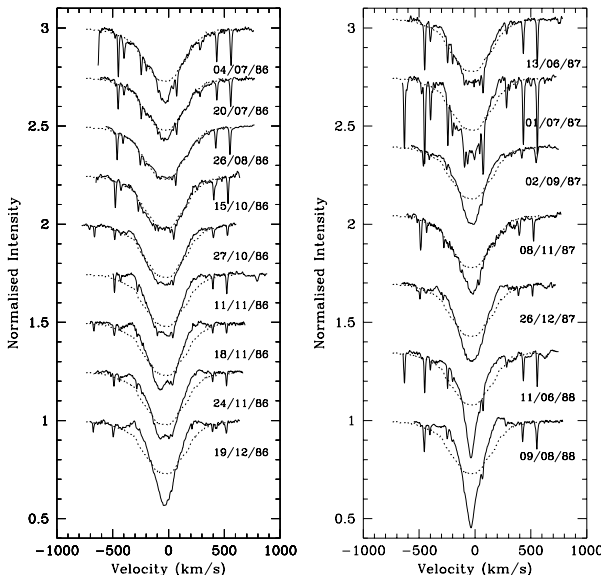

Figure 3.3: Hα observations of *o* Andromedae observed during the disc decay and subsequent re-growth. The dashed line indicates the stellar flux without any disc contribution, as observed around 26 August 1986. Since this is a shell star the central trough decreases below the intrinsic stellar flux; see text for discussion (Clark et al., 2003).

denser material is moving towards the observer, resulting in more emission being Doppler shifted towards the violet arm. At II the denser region lies between the observer and the star which creates an additional absorption features. At III the region is Doppler shifted away from the observer and enhances the red edge of the emission line, while at IV the region is behind the star and does not influence the emission lines.

Detailed modelling of this process has been continued for Be stars (by e.g. Okazaki, 1991, 1997) and Carciofi et al. (2009) has shown how the one-arm oscillation model in a Keplerian disc can be fitted to the V/R variation in ζ Tauri (Figs. 3.6 & 3.7).

3.1.2 Infrared excess

As was shown by Johnson (1967), five emission line stars (which included Be stars) in the *Bright Star Catalogue* showed an intrinsic colour index $(K\text{-}L)_0$,[i] after correction for interstellar reddening, which did not agree with the expected colour from a blackbody emitter. Fig. 3.8 shows the colour index plotted against spectral type for stars in the catalogue, and the emission line stars (marked with an E) lie above the predicted position for a blackbody emitter (solid line). As was soon shown by Woolf et al. (1970), this infrared excess could be fitted by a free-free spectrum added to the blackbody component of the star. The IR excess is associated with the circumstellar disc and is the most important property of Be stars concerning this study.

[i]The effective wavelengths for the filters are K = 2.2 μm and L = 3.4 μm.

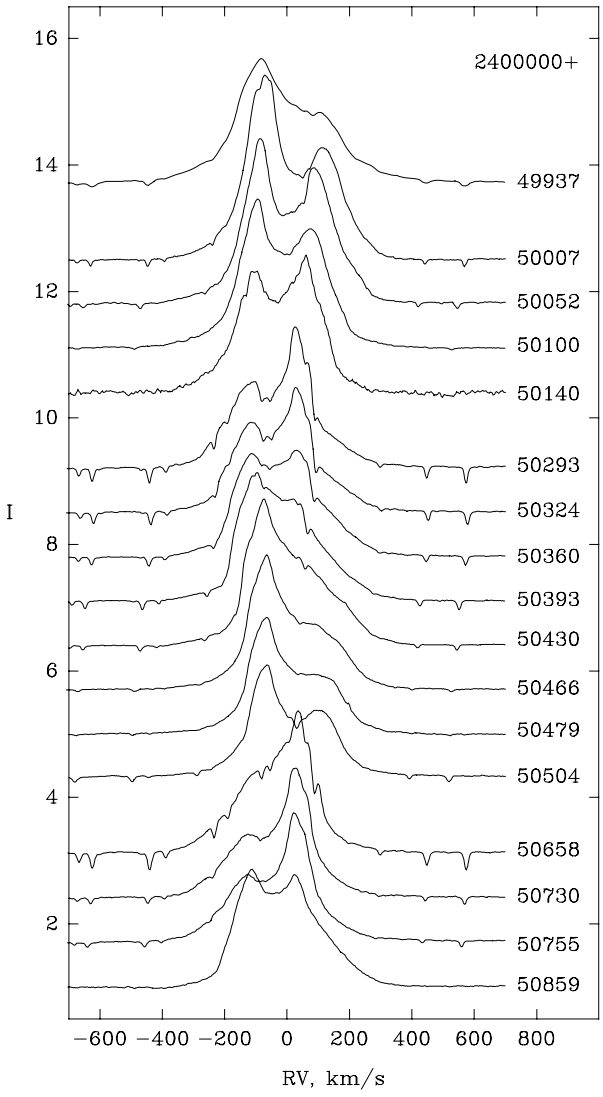

Figure 3.4: V/R variation of the Hα line observed from X Persei. The flux has been re-scaled to show the spectral lines and the numbers on the right indicate the Julian date (Clark et al., 2001).

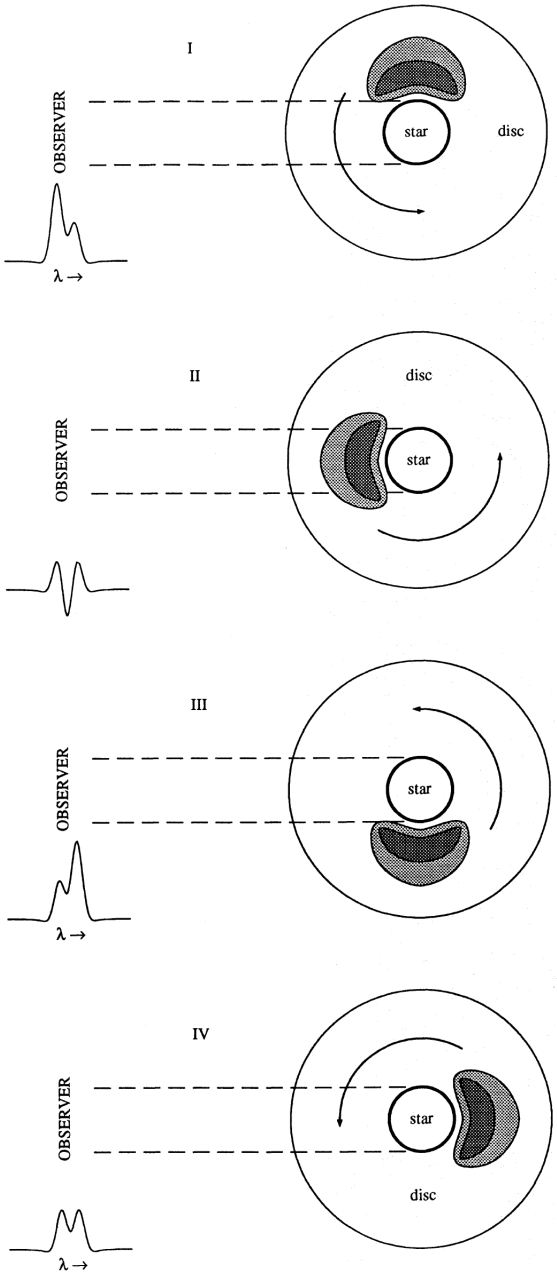

Figure 3.5: Diagram explaining the motion of a one-armed density structure in the circumstellar disc around a Be star. The denser region (shaded region) orbits the star in an anti-clockwise direction, creating the observed V/R variation See the text for a detailed discussion (Telting et al., 1994).

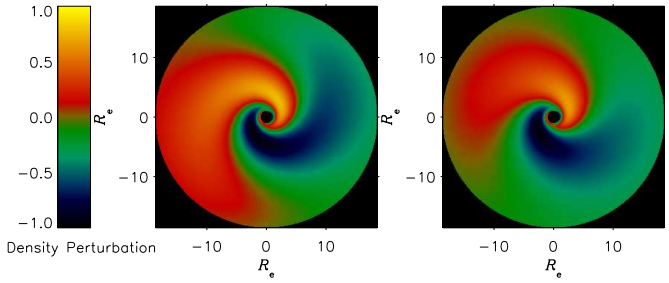

Figure 3.6: Two examples of a numerical model for the density profiles in Keplerian circumstellar discs shown as observed from above. The density disturbance moves in an anti-clockwise direction and can model the V/R variations discussed in the text (Carciofi et al., 2009).

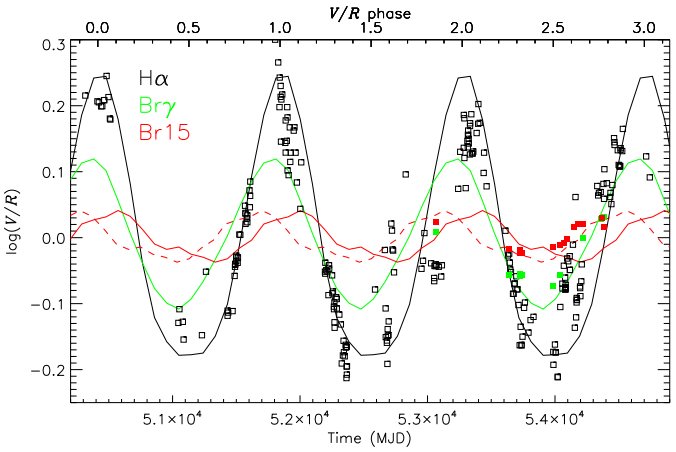

Figure 3.7: Modelling of the V/R variation in ζ Tauri. The open squares correspond to the observed data points and the solid lines to the best fit models. The colours shown in the figure correspond to the indicated emission lines and are Hα, Brγ and Br15, for black, green and red respectively. To produce a better fit to the observations a -0.2 phase shift has been applied to the Br15 line (dashed red line) (Carciofi et al., 2009).

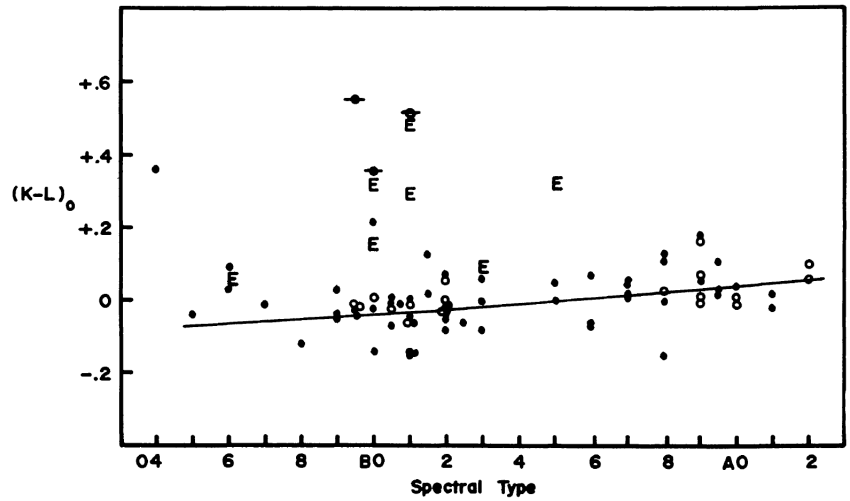

Figure 3.8: Plot of the intrinsic colour $(K\text{-}L)_0$ against spectral type for stars included in the *Bright Star Catalogue*. The solid black line shows where the colour index should lie if the stars radiate as blackbodies. Emission line stars are marked with an "E", and lie above the expected model curve, indicating that these stars appear redder than expected (Johnson et al., 1966).

The IR excess is believed to originate from (mainly) free-free emission in the Be stars' circumstellar discs. Waters (1986) developed an empirical model to predict this IR excess, using a curve of growth (COG) method and this method (and its application to PSR B1259-63/LS 2883) is discussed in Chapter 6. The IR excess is a variable phenomena as it is linked to the size of the circumstellar disc. As the disc grows and shrinks over periods of $\sim 100 - 1000$ days, there is a corresponding change in the IR excess. A good example is shown for X Persei in Fig. 6.6 (p. 114), where observations during disc and discless phases show a clear change in the flux at IR wavelengths (Telting et al., 1998). Similarly the IR excess associated with LS 2883 is shown in Chapter 6 (Figs. 6.11 & 6.12). The ongoing variability of Be stars is attested to by Rajoelimanana, Charles, and Udalski (2011) who analysed long-term light curves of a sample of Be X-ray binaries in the Small Magellanic Cloud (SMC) using data from MACHO[ii] and OGLE[iii]. The authors found superobital periods in 19 systems, which they propose are the result of variability in the circumstellar disc.

3.1.3 Interferometry

The development of optical interferometry has made it possible to image the asymmetry of the Be star environment more directly. Quirrenbach et al. (1994) used the MkIII optical interferometer at Mt. Wilson, to construct a map of the maximum-entropy of the Hα spectral line (656.3 nm) and 550 nm continuum around ζ Tauri. Fig. 3.9 shows the observations centred on 550 nm (left)

[ii] MAssive Compact Halo Objects
[iii] Optical Gravitational Lensing Experiment

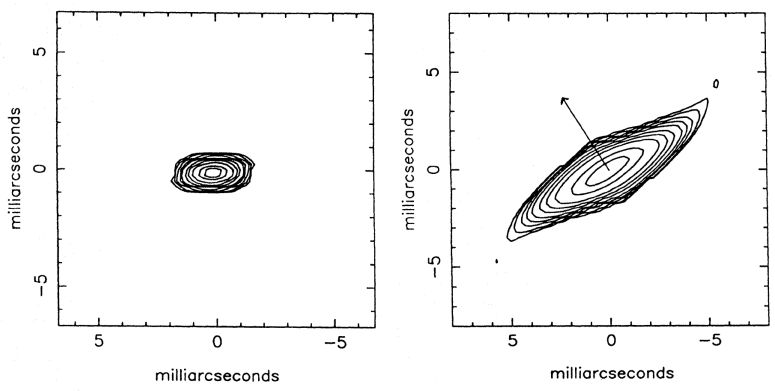

Figure 3.9: Observations of the 550 nm continuum (left) and the Hα (656.3 nm) emission (right) around ζ Tauri. Left: Maximum entropy around 550 nm. Right: maximum entropy around the Hα emission line. The entropy around 550 nm is an unresolved point source and appears flattened due to a higher resolution in the North-South direction, while the Hα emission shows an extended disc-like structure around the star (Quirrenbach et al., 1994).

and on the Hα line (right). The entropy map around 550 nm is an unresolved point source, while the Hα emission is clearly non-spherical and extends in a disc-like structure around the star. This is a clear indication that the emission region around Be stars is confined to a disc or disc-like region.

3.2 Modelling the circumstellar disc

Despite more than a hundred years of research on Be stars, the key question of how the circumstellar discs form remains. There has been rapid progress in the last few years and the current favoured model of a viscous decretion disc is able to explain a number of observed properties. This section will briefly discuss some aspects of the circumstellar disc modelling, beginning with an earlier wind compression model.

3.2.1 Wind compression and magnetically compressed discs

The first, initially viable, model to explain the circumstellar disc formation was the compression of discs due to radial outflow from the stellar wind, introduced by Bjorkman and Cassinelli (1993). The basic model was that material leaving the surface of the rapidly rotating star would follow orbital paths that intercept the equatorial plane of the star, where the collision between different streams of material would create a shock and a region of enhanced density. At first the model appeared viable, and Owocki, Cranmer, and Blondin (1994) showed that purely radial line-driven winds would create the proposed discs. However, this model was shown to fail once the effects of non-radial line forces, which must occur, were included in the calculation (Owocki et al., 1996).

The presence of magnetic field lines was also considered as a mechanism to provide the directional component to drive the wind outflow to the star's equatorial plane and form a disc through the same method as the wind compression model (e.g. Cassinelli et al., 2002). However, this method does not produce the correct disc formation and is unable to explain the observational properties of Be stars as was shown by 2D Magnetohydrodynamic (MHD) simulations presented by Owocki and Ud-Doula (2003). A different model is needed to explain the disc formation.

3.2.2 Viscous discs

The current favoured model for the circumstellar discs is the creation of viscous "decretion" discs around the stars, originally proposed by Lee et al. (1991). This model is particularly favoured as it would require the discs to be Keplerian, a property that has been detected in some Be stars (see e.g. Meilland et al., 2007). The model is similar to accretion disc theory, with the important difference that material is transferred away from and not towards the star via viscosity. The basic equations of viscous "decretion" discs are similar to those of accretion discs and are summarized, for example, by Carciofi (2011).

Model results from viscous discs

In the COG method (Chapter 6), the circumstellar disc is assumed to be isothermal and have a mass density that decays with radius as $\rho \propto r^{-n}$. Simulations of viscous discs show, however, that they would be non-isothermal and would not follow a steady density decay. Fig. 3.10 shows an example of a viscous disc solution from non-LTE (Local Thermodynamic Equilibrium) Monte Carlo simulations (Carciofi and Bjorkman, 2008). The left hand side of the figure shows that the decrease in mass density, ρ, with distance along the disc mid-plane from the centre of the disc/star,[iv] does not follow a constant power law but changes dynamically with distance, while the right hand side of the figure shows how the temperature, which has been averaged vertically through the disc, changes with distance from the centre of the disc as measured along the mid-plane.

The strength of the viscous model is that it has been able to match a number of the observed disc properties, including the V/R variation and emission lines. As was mentioned earlier, the viscous model is able to produce the one-arm oscillation required to explain the V/R variation (Fig. 3.7). Also shown by Carciofi et al. (2009) is how the viscous model can be fitted to the SED of the star (Fig. 3.11). It is the success of such fits which strengthens the case for viscous discs.

An interesting result of the viscous disc model is that most of the emitted flux occurs close to the centre of the disc/star. Fig. 3.12 plots the ratio of the flux emitted within a radial distance r from the centre of the disc in units of the maximum total flux emitted from the disc

[iv] The centre of disc mentioned here, and through the rest of this study, refers to the centre of the disc which would coincide with the centre of the star, since the disc is assumed to be symmetric around the star. Distances measured from the centre of the star/disc are measured from this point outwards towards the edge of the disc.

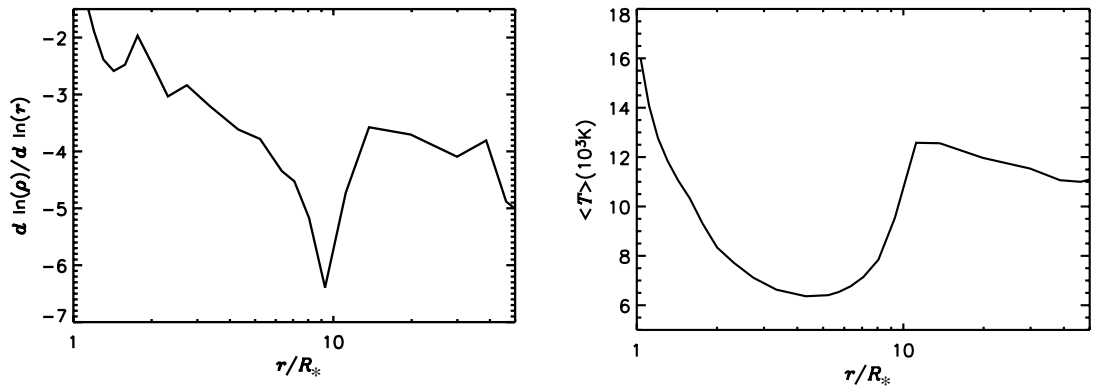

Figure 3.10: Non-LTE Monte Carlo model predictions for a Keplerian circumstellar disc. Left: change in the density with radial distance. Right: the vertically averaged temperature of the disc, plotted against distance along the disc mid-plane. See text for discussion (adapted from Carciofi and Bjorkman, 2008).

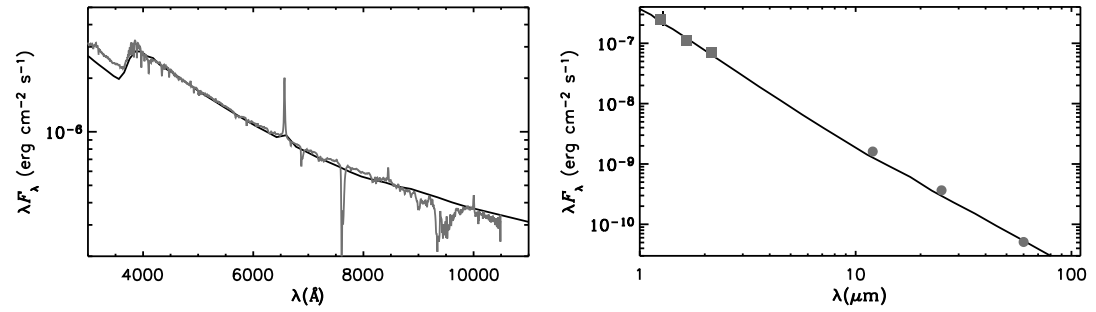

Figure 3.11: Optical (left) and IR (right) spectral energy distribution of ζ Tauri. The dark grey line/points are the observed data while the solid black line is the fitted Keplerian disc model (adapted from Carciofi et al., 2009).

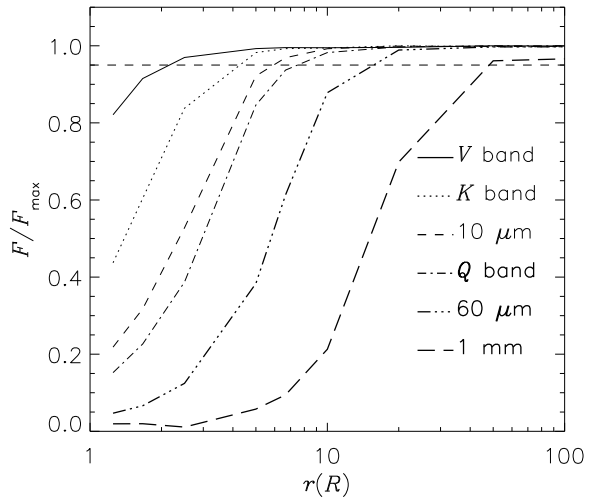

Figure 3.12: Plot of the percentage of the total maximum emission which is emitted within a radial distance r (in units of the stellar radius R) from the centre of the disc. The horizontal dashed line marks the 90% level and the radial distance is measured in stellar radii (Carciofi, 2011).

(i.e. $F/F_{\max}$) for various emission bands. This shows that most of the optical and near IR red emission is emitted within ~ 10 stellar radii from the star. For example, 90% of all the K flux is emitted within ~ 3 stellar radii, from the centre of the disc. As is shown later, the COG method presents a similar, quantitative result.

Disc formation

The, not insignificant, problem with the viscous disc mechanism, is the explanation of how the discs are created. Accretion discs form around compact objects when material attempts to accrete onto the surface of the compact object, but still possess a significant amount of angular momentum. The result is that the material must first spiral around the compact object, forming a ring of material, before viscous effects spread the ring into a disc. Material then loses angular momentum while moving through the disc until it loses sufficient angular momentum that it can accrete onto the surface of the compact object. Additional material and angular momentum is added to the outer edge of the disc, by the mass donor, sustaining the accretion disc. As such, accretion of material leads naturally to the formation of an accretion disc around compact objects. For a detailed study of accretion discs and accretion disc physics, see e.g. Frank, King, and Raine (2002).

The formation of "decretion" discs around a Be star is different. Material leaving the surface of a star in e.g. the stellar wind does not need to lose angular momentum like material attempting to accrete onto a compact object. Therefore, to create a viscous circumstellar disc in Be stars requires a launch mechanism which will place material into a Keplerian, or near Keplerian, orbit around the star. As material is placed into this orbit, the supply of material and its associated

angular momentum will then cause the material to spread out into a disc structure due to viscous effects, creating the observed Be disc. Some ideas related to the launching of an decretion disc are discussed below.

Disc launching

Recent reviews by Rivinius (2007) and Stee (2011) discuss some of the possibilities and problems surrounding the disc production and launching mechanisms. There are some observational links between the non-radial pulsation (NRP) mechanisms in Be stars and flares associated with the circumstellar disc, particularly in the case of μ Centauri where there is an observed correlation between the NRPs and increased disc activity (Rivinius et al., 1998). As outlined in Rivinius (2007, and references therein) spectroscopic observations around outburst stages are consistent with matter being transferred to the inner edge of the disc, as after the outburst there is more material near the star surface as is evident in the increased separation of the spectral line's double peaks. However, Owocki (2005) shows that Be stars must be rotating at $\sim 95\%$ of the critical velocity for NRPs to be able to launch material into a Keplerian orbit. The often quoted value for Be stars is that they rotate between 75% to 80% of their critical velocity, too low to create the disc through this process. This velocity range may, however, be too low and Townsend et al. (2004) discussed how equatorial gravitational darkening can affect observations and that the "measured" rotational velocity may under-predict the true rotational velocity of Be stars. Therefore, Be stars might be rotating at nearly the critical velocity which could allow non-radial pulsations to launch material to form circumstellar discs (Owocki, 2005). A discussion by Cranmer (2009) has also suggested that NRPs may produce resonance waves that will transport additional angular momentum to the surface of the star, which could be fed to the disc. The result is that a star rotating at only 60% of the critical velocity will be able to launch a circumstellar disc through NRPs.

Open questions

As discussed in the review by Baade et al. (2011), there remain a number of open questions regarding Be stars and OB stars in general. For example, the launch mechanism of the circumstellar disc remains an open question. As mentioned Be stars are known to be very fast rotators, and this seems to be linked to the circumstellar discs. However, there is a group of stars, Bn stars, that are also very fast rotators that do not show evidence of circumstellar discs. If Be stars produce discs, in part due to rapid rotation, why do Bn stars not produce discs?

The other issue that has not been discussed is that of the possible correlation between metallicity and the Be star phenomena. It has been discussed, by e.g. Vink et al. (2001) and Dray (2006), that metallicity can affect the mass lost from stars through their stellar wind. A higher mass loss will lead to a higher loss of angular momentum and, therefore, stars that have a lower metallicity and hence a lower mass loss rate should have a higher rotation rate. This may be one possible reason for the higher ratio of Be stars in the SMC, as the lower metallicity in the

SMC could lead to higher spin velocities and hence more Be stars. However, as shown by the observations of Bn stars, fast rotation does not lead directly to disc formation, and this may not be the direct cause for the higher ratio of Be stars in the SMC.

3.3 Be binary systems

A large number of Be stars form part of binary systems. For example the SMC is known to have a large number of Be/X-ray binaries (Be-XRBs). Of the detected gamma-ray binary systems, four are known to have a Be main sequence star in the system. It is important therefore to discuss briefly some aspects of Be binary systems.

3.3.1 Be-XRBs

Most Be binary systems are X-ray binaries, and are powered by accretion onto the compact object, normally a neutron star (NS). Coe (2000) reviewed accretion driven Be X-ray binary systems and the reader is referred to this and to the references therein for a detailed review of these systems.

circumstellar disc.

In Be-XRBs, material from the stellar wind or the circumstellar disc accretes onto the NS, producing X-ray emission. Because of the binary nature of the systems and the variability of the Be stars, Be-XRBs show periods of enhanced X-ray emission or outbursts. Two such types of outbursts are defined. Type I outbursts are regular, and are linked to the orbital period of the binary. Type II outbursts are much larger events, and are linked to periods of enhanced accretion and circumstellar disc activity.

The Type I outbursts can be understood in terms of the motion of the NS through the circumstellar disc of the Be star during its orbit. As the NS passes through the disc there is a period of enhanced accretion which results in a period of bright X-ray emission. The X-ray emission also shows a pulsed signal from the spin of the NS. As shown by Corbet (1984), there is a natural correlation between spin period observed in the X-ray emission and the binary period of the system, which can be explained as follows. Material attempting to accrete onto the surface of a NS will be influenced by the neuron star magnetic field. If the accreting material is trapped by the magnetic field lines it will rotate with the same spin velocity as the NS (e.g. Frank et al., 2002, pp. 158–174). If the rotational velocity of the trapped material is higher than the Keplerian velocity at this point, the material will not be able to accreted onto the surface of the compact object and will be "flung" out of the system; this is known as the "propeller effect". The distance where the rotation velocity of the magnetic field is equal to the Keplerian velocity is known as the corotation radius and is given by (e.g. Frank et al., 2002, p. 163)

$$R_\Omega = \left(\frac{GMP_{\rm spin}^2}{4\pi^2} \right)^{1/3},$$

where $P_{\rm spin}$ is the spin period of the NS. For material to accrete onto the surface of a pulsar, the radius at which the magnetic field begins to influence the flow of the accreting material must be less than the corotation radius. The radius at which the magnetic field begins to regulate the flow of material is determined by the point where the magnetic pressure of the NS is equal to the ram pressure of the accreting material. For a dipolar field configuration

$$B(r) \sim B_* \left(\frac{R_*}{r}\right)^3 \sim \frac{\mu}{r^3},$$

where B_* is the magnetic field at the surface of the star and $\mu = B_* R_*^3$ is the magnetic dipole moment, the magnetic pressure is given by

$$P_{\rm mag} = \frac{B^2}{8\pi} = \frac{B_*^2 R_*^6}{8\pi r^6} = \frac{\mu^2}{8\pi r^6}.$$

Therefore, equating the magnetic pressure to the ram pressure of a gas in free-fall it can be shown that the radius at which the magnetic field begins to control the accreting material is given by (e.g. Frank et al., 2002, p. 158)

$$r_m = 5.1 \times 10^8 \left(\frac{\dot{M}}{10^{16}\ \mathrm{g\ s^{-1}}}\right)^{-2/7} \left(\frac{M_1}{M_\odot}\right)^{-1/7} \left(\frac{\mu}{10^{30}\ \mathrm{G\ cm^3}}\right)^{4/7}\ \mathrm{cm}.$$

This is known as the Alfvén radius and accretion onto the NS will only be possible if the corotation radius is larger than the Alfvén radius. A NS that is observable through accretion driven X-ray emission, therefore, must first have spun down until this conditional was met.[v] As shown by Corbet (1984), since the Alfvén radius is dependent on the density of the material attempting to accrete onto the NS, and the density of this material depends on the binary separation (and therefore on the orbital period), there is an observed correlation between the spin period of the NS and the orbital period in HMXBs (Fig. 3.13).

The second kind of periodic outbursts, Type II outbursts, appear to be correlated to periods of enhanced disc size, as is evident from observations of the Hα line and optical/IR emission from the circumstellar disc. Fig. 3.14 shows the observed I magnitude of SXP11.5 in the period leading up to a Type II outburst, indicated by the vertical dashed lines. When the circumstellar disc grows to a large size, rapid accretion occurs, resulting in the observed X-ray outburst. The disc also appears to decrease rapidly in size after the outburst, as is seen by the fast drop in the I magnitude (open square in Fig. 3.14), or the change in the Hα intensity (Fig. 3.15).

[v] Spin down is the phenomenon by which a rotating compact object like a NS loses angular momentum and consequently its angular velocity decrease with time. A compact object can also gain angular moment when material with additional angular momentum accretes onto its surface. The transfer of additional angular momentum leads to the star spinning faster, and is said to spin-up.

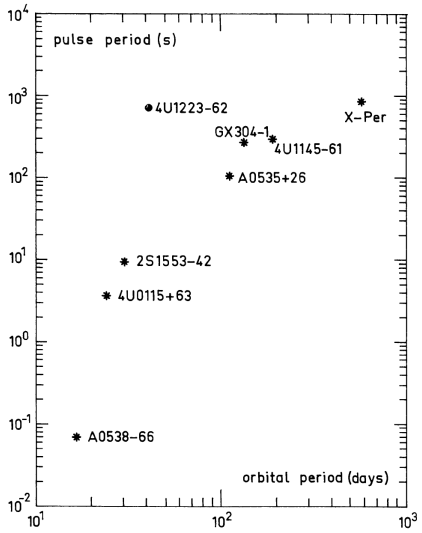

Figure 3.13: Observed correlation between the orbital period and the spin period of the pulsar which is observed in accretion driven high-mass X-ray binaries (Corbet, 1984).

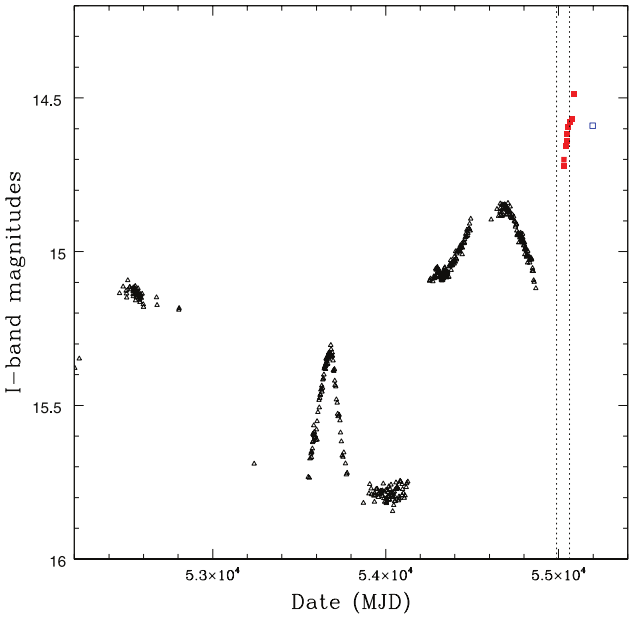

Figure 3.14: Oservations of SXP11.5 using the I filter, including a period of a Type II outburst, indicated by the vertical dashed lines. The I magnitude is a combined data set from OGLE III (open triangles), the Faulkes Telescope (closed squares), and SAAO 1.9m (open square) (Townsend et al., 2011).

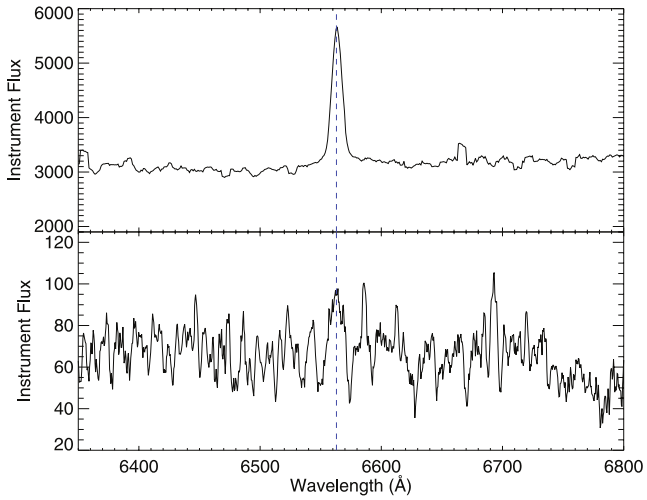

Figure 3.15: VLT (top) and SAAO 1.9m (bottom) observations of the Hα line of SXP11.5. The top spectrum was taken on the 12$^{\text{th}}$ of August 2009 during the X-ray burst phase (Fig. 3.14) while the lower spectrum was taken on the 12$^{\text{th}}$ of December 2009, after the X-ray burst had ended. (Townsend et al., 2011).

3.3.2 Effect on the circumstellar disc

As is seen by the rapid drop in the I magnitude intensity (Fig. 3.14) and the decrease in the Hα line (Fig. 3.15) associated with Type II outbursts, the compact objects in binary systems have a direct effect on the circumstellar discs surrounding Be stars. Reig, Fabregat, and Coe (1997) have shown that Be-XRBs with smaller orbits have correspondingly smaller Hα emission lines. This has led to the conclusion that the NS is confining the size of the circumstellar disc. This has also been shown by Okazaki et al. (2002) using smoothed-particle hydrodynamics (SPH) modelling. Okazaki et al. (2011) have recently modelled PSR B1259-63/LS 2883 using SPH and predicted that the disc should become truncated after the periastron passage.

3.4 Gamma-ray binaries

There are currently[vi] only six known gamma-ray binary systems, and they are listed in Table 3.1 together with the spectral types of their optical companions. Of the six systems only PSR B1259-63/LS 2883, which has a highly eccentric orbit ($P_{\text{orb}} = 3.4$ yr, $e \sim 0.8$), is known to contain a millisecond pulsar as the compact object. The other binary systems all have shorter orbital periods and are believed to contain a pulsar which is obscured by the circumstellar environment. Four of the binary systems also have an Oe/Be star as the optical companion. Chapter 2 presented a summary of the observations of PSR B1259-63/LS 2883. Here only a short summary of the other gamma-ray binary systems is presented.

[vi] As of 10$^{\text{th}}$ of January 2012: The binary nature of AGL J2241+4454/MWC 656 is reported by Casares et al. (2012) on this date.

Table 3.1: Summary of the position and observed spectral type of the six known gamma-ray binary systems.

Name	RA	Dec.	Spectral Type
PSR B1259-63	13 02 47.655	-63 50 08.67	O9.5Ve
LS 5039	18 26 15.057	-14 50 54.26	O6.5V
LSI+61 303	02 40 31.66516	+61 13 45.6115	B0Ve
HESS J0632+057	06 32 59.2545	+05 48 01.178	B0pe
1FGL J1018.6-5856	10 18 55.6	-58 56 46.2	O6V((f))
AGL J2241+4454	22 42 57.30295	+44 43 18.2525	B3 IVne+sh

3.4.1 LS 5039

LS 5039[vii] was originally identified as an X-ray binary source before its detection by H.E.S.S. at very high energies (VHE; > 100 GeV), and was proposed as the optical counterpart to the ROSAT all sky survey source RX J1826.2-1450 by Motch et al. (1997). The system's association with a possible X-ray source is based on a comparison of the ROSAT All Sky Survey with the compiled SIMBAD Catalogue[viii] for OB type stars (Motch et al., 1997). Clark et al. (2001) reported on spectroscopic observations that were made between 1995 and 2000 in optical (4100-7400 Å) and in near IR (1.5-2.2 μ m) wavelengths. The ratio of the He II 4541 and He I 4471 lines measured by optical spectroscopy indicates that the system is an O6.5 type star. The strong absorption of He II 4686 in LS 5039 showed that it is a main-sequence star, while the strong He II absorption in combination with the weak N III λ 4634-40-42 emission classified the star as an O6.5((f)) type giant. Casares et al. (2005) combined observations made between 23–31 July 2002, and 1–10 July 2003, with observations reported by McSwain et al. (2001, 2004), and found an orbital period of 3.90603 ± 0.00017 days, an eccentricity of $e = 0.35 \pm 0.04$ and a revised mass function of $f(M) = 0.0053 \pm 0.0009$ $M_\odot$. The new spectral analysis gave revised values of $T_{\rm eff} = 39000 \pm 1000$ K and $\log g = 3.85 \pm 0.10$ for the temperature and gravity of the star respectively. A later study by Aragona et al. (2009) found a similar orbital period $P_{\rm orb} = 3.90608 \pm .00010$ days, with eccentricity $e = 0.337 \pm 0.036$. Recently, Sarty et al. (2011) have proposed a smaller eccentricity of $e = 0.24 \pm 0.08$ and the possibility of orbital modulation of the photometric light curve on the milli-magnitude level. These authors also suggest a minimum mass of 1.8 $M_\odot$ for the compact object in the binary system.

As part of a search for Radio Emitting X-ray Binaries, Martí, Paredes, and Ribó (1998), observed LS 5039 with the Very Large Array (VLA) and found that the system was associated with an unresolved radio source. Observations with the Very Long Baseline Array (VLBA) by Paredes et al. (2000) revealed radio "jet" images (Fig. 3.16). From these radio jet observations, the authors estimated a 2 milliarcsecond size for the core of the system, with jets extending

[vii] This summary is adapted from Chapter 1 of van Soelen (2007).
[viii] Set of Identifications, Measurements, and Bibliography for Astronomical Data (SIMBAD) catalogue is managed by the Centre de Donnes astronomiques de Strasbourg (CDS).

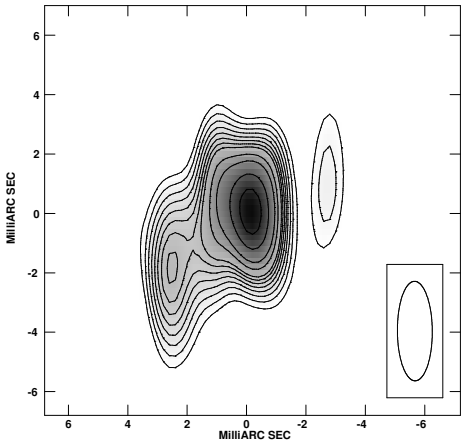

Figure 3.16: Observation of LS 5039 taken at 5 GHz with the VLBA on the 8$^{\text{th}}$ of May 1999 (Paredes et al., 2000).

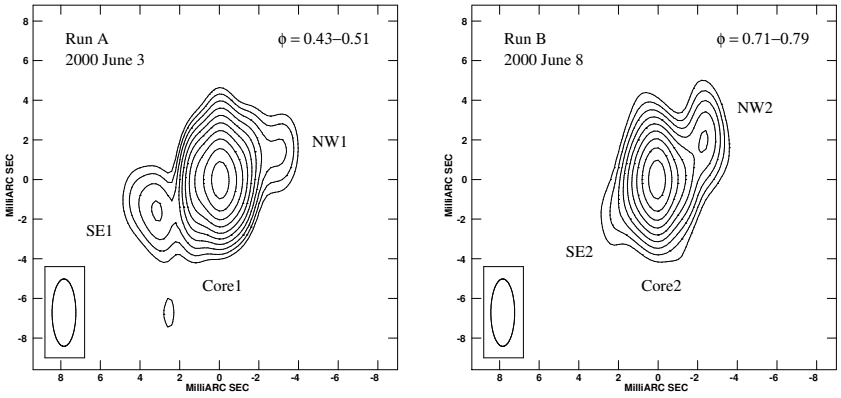

Figure 3.17: Observation of LS 5039 taken at 5 GHz with the VLBA on the 3$^{\text{rd}}$ and 8$^{\text{th}}$ of June 2000 (Ribó et al., 2008).

beyond 6 milliarcseconds with a position angle of 125°. Paredes et al. (2002) reported on follow up radio observations of LS 5039, made simultaneously with the European VLBI Network (EVN) and Multi-Element Radio-Linked Interferometer Network (MERLIN). The radio images show apparently clear jet structures that extend North West and South East, with the South East jet longer in both of the EVN and MERLIN images. However, as reported in Ribó et al. (2008), observations of LS 5039 made on the 3rd and 8th of June 2000 show variability in the morphology of the observations (Fig 3.17).

Ribó et al. (1999) analysed data from the Proportional Counter Array (PCA), located on the Rossi X-ray Timing Explorer (RXTE) satellite for X-ray pulsations, but found no pulsations between $\sim$ 0.02 to $\sim$ 2000 seconds. Later RXTE observations by Bosch-Ramon et al. (2005) are significant because they detection a possible orbital modulation in the X-ray flux. The observations took place over 17 runs between the 4$^{\text{th}}$ and 8$^{\text{th}}$ of July 2003. They found a measured

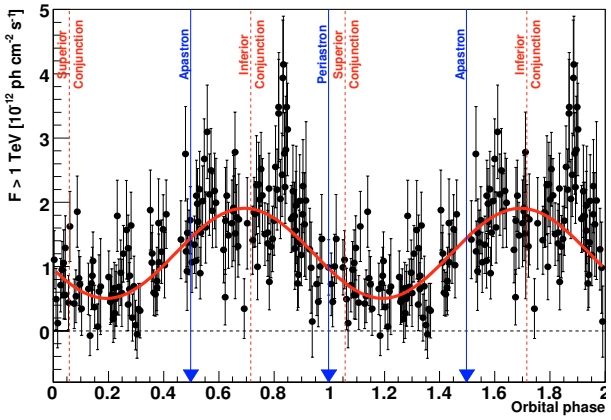

Figure 3.18: H.E.S.S. observations of LS 5039 folded with the 3.9 day orbital period (Aharonian et al., 2006).

flux between $(4.32^{+0.30}_{-0.41} - 6.95^{+0.29}_{-0.40}) \times 10^{-11}$ ergs cm^{-2} sec^{-1}, and a photon index between $1.69^{+0.08}_{-0.08}$ – $2.18^{+0.14}_{-0.13}$ for the energy band 3-30 keV. These authors reported on time variations in the X-ray flux when the data was folded with a period of ~ 3.9 days (Casares et al., 2005) which showed an orbital modulation and a one hour "mini-flare". More recent observations with *Suzaku* X-ray observatory, undertaken by Takahashi et al. (2009), show a clear orbital modulation of the X-ray light curve and a non-thermal spectrum.

Paredes et al. (2000) proposed that LS 5039 might be a gamma-ray source, and might be associated with 3EG J1824-1514 because it lies within the 95% confidence contour and is the only X-ray emitter within 1°. Subsequent observations of LS 5039 with H.E.S.S. revealed not only VHE gamma-ray emission from the system, but also found a 3.9 day modulation in the flux (Fig. 3.18; Aharonian et al., 2006). The counts fluctuate between $(0.46 \pm 0.21 - 2.96 \pm 0.17) \times 10^{-12}$ ph cm^{-2}s^{-1}TeV^{-1}. The spectral index varies between $(1.84 \pm 0.25) - (3.08 \pm 0.47)$, and is in anti-correlation to the luminosity. The source has an average luminosity of 7.8×10^{33} erg s^{-1}, and a spectral index of 2.06 ± 0.05. As discussed in Aharonian et al. (2006), the change in the spectral index could arise from pair-cascades, variation in radiative cooling if synchrotron losses become significant, or anisotropic IC scattering effects. The maximum flux appears to occur around inferior conjunction ($\phi = 0.716$) and the flux minimum at $\phi \sim 0.2$ (superior conjunction occurs at $\phi = 0.058$).

3.4.2 LSI+61 303

LSI+61 303 has, like PSR B1259-63, a Be star as its optical companion and, as in the case of LS 5039, was observed as an X-ray binary system before being detected at VHE gamma-ray energies with MAGIC[ix] (Albert et al., 2006). LSI+61 303 was originally detected as a variable radio source by Gregory and Taylor (1978), while the first X-ray detection was reported by

[ix] Major Atmospheric Gamma-ray Imaging Cherenkov

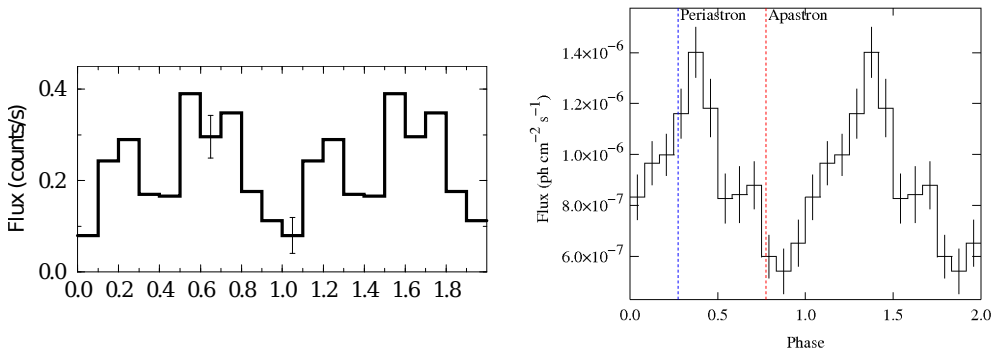

Figure 3.19: **Left**: ASM/RXTE observation of LSI+61 303 between 2-10 keV, folded with a 26.7 day period and a bin size corresponding to 0.1 phase (adapted from Paredes et al., 1997). **Right**: *Fermi* observations folded with a 26.4960 day period with a bin size of 1 day (Abdo et al., 2009).

Bignami et al. (1981) with *Einstein*. These authors, however, found no evidence for variability in the X-ray emission. Later observations with *ROSAT* detected the source with an X-ray luminosity of $5.9 \pm 2.9 \times 10^{33}$ erg s^{-1} between 0.1 and 2.4 keV, assuming a distance of 2.3 kpc to the source (Goldoni and Mereghetti, 1995). The observations showed variability with a modulation of the flux by a factor $\sim$ 3 over a $\sim$ 3 day period. Paredes et al. (1997) found a 26.7 ± 0.2 day modulation in ASM/RXTE[x] observations of the source (Fig. 3.19), with a minimum and maximum luminosity of $\sim 1 \times 10^{34}$ and $\sim 5 \times 10^{34}$ erg s^{-1} between 2 to 10 keV (assuming a distance of 2.0 kpc).

Due to observations of apparently fast precessing radio jets, e.g. at 5 GHz on the 22$^{\rm nd}$ and 23$^{\rm rd}$ of April 2001 with MERLIN[xi], LSI+61 303 was originally classified as a microquasar. However, Dhawan et al. (2006) presented VLBA observations of the source at 3.6 cm, taken every three days and covering slightly more than one orbital period, which showed that the radio outflow is directed away from the Be star. This implies that the system is more likely to be a PWN than a microquasar (Fig. 3.20).

LSI+61 303 also coincides with a known EGRET[xii] source (Kniffen et al., 1997) and the association was confirmed by the TeV gamma-ray detections with MAGIC (Albert et al., 2006). The VHE gamma-ray flux was later found to be modulated with a 26.8 ± 0.2 day orbital period (Albert et al., 2009). The system was also detected by *Fermi*, and is one of the brightest high energy (HE; $0.1 - 100$ GeV) sources. The *Fermi* data show an orbital period of $26.6 \pm .05$ days (Fig. 3.19; Abdo et al., 2009), similar to the orbital period of 26.4960 ± 0.0028 days that was detected in the radio (Gregory, 2002). Fig. 3.21 shows the *Fermi*, MAGIC and VERITAS spectral energy distribution.

[x] The All Sky Monitor (ASM) is an X-ray telescope on-board the Rossi X-ray Timing Explorer (RXTE) satellite.
[xi] Multi-Element Radio-Linked Interferometer Network
[xii] Energetic Gamma-Ray Experiment Telescope

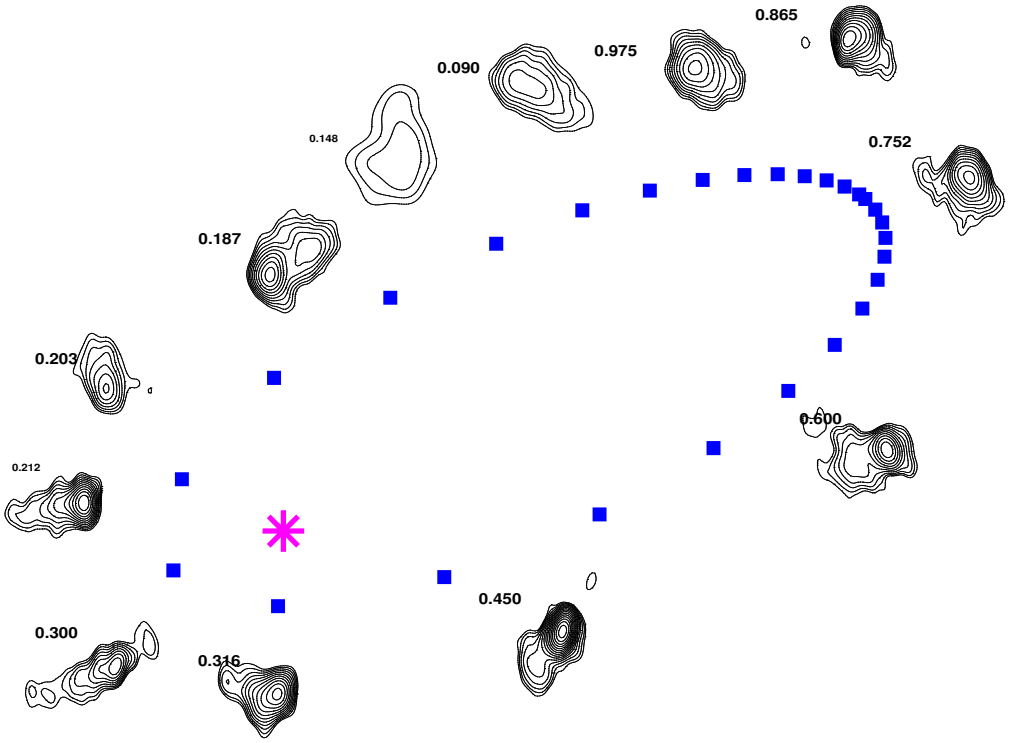

Figure 3.20: Observations of LSI+61 303 at 3.6 cm using the VLBA over the orbital period of the system (Dhawan et al., 2006).

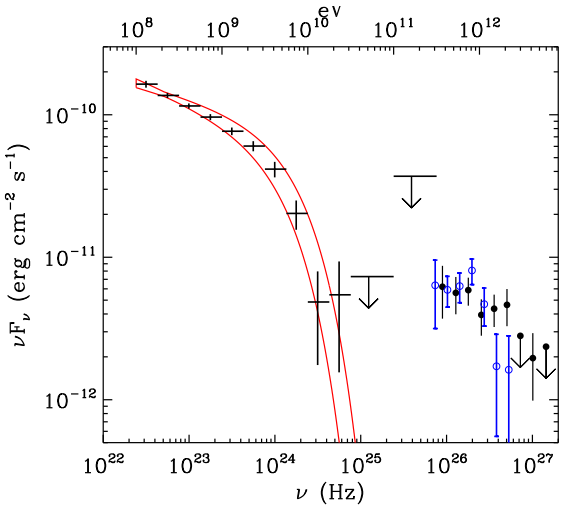

Figure 3.21: Spectral energy distribution for LSI+61 303, as observed with *Fermi* (crosses), MAGIC (open circles) and VERITAS (closed circles). The MAGIC and VERITAS observations are from the higher energy phase of the orbital period. The spectral energy distribution is clearly dominated by the Fermi spectrum. Also indicated on the graph is the $\pm 1\sigma$ limits on the fitted spectrum (curved lines). Figure from Abdo et al. (2009).

The X-ray and VHE flux light curves show an orbital correlation, while the HE emission is in anti-correlation to the X-ray/VHE energy flux (Abdo et al., 2009). This could imply a single particle distribution for the X-ray and VHE emission and a separate population for the HE emission as discussed by e.g. Zabalza et al. (2011). One of the most interesting discoveries made with the *Fermi* telescope is that the HE flux from LSI+61 303 has shown a change in the orbital modulation phase and a decrease in the modulation (Hadasch, 2010).

While the exact nature of the compact object in LSI+61 303 is unknown, a reported magnetar-like event in the direction of the system has led to recent speculation that the system may contain a magnetar (Barthelmy et al., 2008; de Pasquale et al., 2008; Dubus and Giebels, 2008; Evans et al., 2008; Rea and Torres, 2008; Torres et al., 2012). If this is true, LSI+61 303 will be the only known magnetar in a binary system.

3.4.3 HESS J0632+057

HESS J0632+057 was discovered serendipitously during a H.E.S.S. observation of the Monoceros supernova remnant (Aharonian et al., 2007). The detected point-like source coincides with a Be star, MWC 148, and is close to previously detected EGRET and X-ray sources. An observation of the region with *XMM-Newton* by Hinton et al. (2009) showed an X-ray source, XMMU J063259.3+054801, centred 0.6″ from MWC 148 and lying inside the HESS J0632+057 error box. The authors also found the source to be variable over the observation period of ~ 7 hours. VLA observations have also detected a point radio source (~ 0.3 mJy) with significant

variability (Skilton et al., 2009). The binary nature of the system was confirmed by the detection of a 320 ± 5 day orbital period by Bongiorno et al. (2011) using more than 2 years of *Swift* X-ray data. Subsequently two observations of the source with the VLBI (15 February 2011 and 17 March 2011) have shown extended radio structures around the binary system with a changing morphology (Moldón et al., 2011b). Surprisingly, this system has not been detected by *Fermi*.

Casares et al. (2012) have very recently reported on optical observations of the MWC 148 and confirm the binary nature of the system. The authors found a binary period of 321 days.

3.4.4 1FGL J1018.6-5856

1FGL J1018.6-5856 is one of the most recently discovered gamma-ray binaries. It was reported by the *Fermi* collaboration (Corbet et al., 2011). The *Fermi* flux has a 16.58 ± 0.04 day modulation period, associated with the orbital period. The authors also propose an association with a *Swift* X-ray source, coincident with the *Fermi* detection which also shows variability, and an O6V((f)) star located at R.A. = $10^{\rm h}\ 18^{\rm m}\ 55\overset{\rm s}{.}6$, Dec. = -58° 56' 46$\overset{''}{.}$2. The source has currently no confirmed TeV emission but there may be an association with a H.E.S.S. source reported by de Ona Wilhelmi et al. (2010).

3.4.5 AGL J2241+4454

Casares et al. (2012) have recently confirmed the binary nature of AGL J2241+4454 by optical observations of the Be star MWC 656, the proposed optical companion in the system. The system was detected by AGILE[xiii] (Lucarelli et al., 2010) as a possible new gamma-ray binary system, and Williams et al. (2010) proposed the possible gamma-ray binary nature of the system with an orbital period of 60.37 ± 0.04 days. Casares et al. (2012) found the Hα line is variable with a period of 60.37 ± 0.04 days, and propose that this confirms the binary nature of the system.

[xiii] Astrorivelatore Gamma a Immagini LEggero

Chapter 4

Pulsars, pulsar wind nebula and gamma-ray binaries

PSR B1259-63 consists of a young pulsar in orbit around a Be main sequence star. A shock forms between the pulsar and stellar winds, resulting in the acceleration and thermalization of leptons (electrons and positrons) to relativistic energies. In the post-shock region, the leptons cool through synchrotron and Inverse Compton (IC) processes to produce the observed non-thermal radiation from the system. For isolated pulsars the pulsar wind interacts with the supernova remnant, forming pulsar wind nebulae (PWNe). For PSR B1259-63 the observed TeV gamma-ray radiation is produced when the leptons in the pulsar wind "up-scatter" low energy photons from the Be star to gamma-ray energies via IC scattering, as discussed in Chapter 5. Since the energetics behind the observed high energy emission is determined by the particle acceleration processes associated with the pulsar and the PWN, a brief discussion of the most relevant aspects related to this study will be presented.

4.1 Pulsars

Pulsars were first discovered by J. Bell and A. Hewish as a rapidly "pulsating" radio source (Hewish et al., 1968). The suggestion that this pulsing radio source was powered by a neutron star (NS) was made by Gold (1968) who proposed that what were originally thought to be pulsations were in fact due to rapid rotation combined with a lighthouse effect. The observed radio "pulsations" are due to radio emission from the poles of the NS. This emission is observed as short pulses which are detected when the polar cap region rotates through the line-of-sight. The pulsating radio emission is then not due to any pulsation of the surface of the star, but to its rotation. In spite of this, NSs are still referred to as pulsars.

NSs are one of three possible outcomes for a star that has exhausted all nuclear fuel and collapses under self gravitation. The possible outcomes are a white dwarf, which is supported by

electron degeneracy pressure, a NS, which is supported mainly by neutron degeneracy pressure and a black hole, which is unable to support itself against gravitational collapse and forms a singularity surrounded by an event horizon from within which not even light is able to escape.

It was shown by Chandrasekhar (1931) that a white dwarf supported by the degenerate electron gas pressure has a maximum mass, known as the Chandrasekhar limit (e.g. Lipunov, 1987, p. 2) given by

$$M_{\rm Ch} \approx \frac{3.1}{\mu_{\rm e}^2}\left(\frac{hc}{G}\right)^{3/2} \approx 1.46 M_{\odot},$$

where $\mu_{\rm e}$ is the average number of nucleons per electron and it is assumed that $\mu_{\rm e} \rightarrow 2$. Stars with a core mass greater than 1.46 $M_{\odot}$ collapse further, forming either a NS or a black hole.

The maximum mass of a NS is determined by the Oppenheimer-Volkoff limit, beyond which the neutron degeneracy pressure is unable to resist gravity and the star collapses to form a black hole. Due to uncertainties in the exact equation of state for matter at the extremely high pressures present in NSs, the mass limit is not as accurately known as it is for white dwarfs. The maximum mass is believed to be approximately 3 $M_{\odot}$. Most NSs have masses below this limit and average at a mass of ≈ 1.4 $M_{\odot}$ (e.g. Thorsett and Chakrabarty, 1999). The most massive NS discovered to date has a mass of 1.97 ± 0.04 $M_{\odot}$ (Demorest et al., 2010).

NSs are very rapid rotators with spin periods ranging from milliseconds to a few hundred seconds (e.g. Fig. 4.1). They also have strong magnetic fields. Pulsars are also observed to be slowly spinning down and the energy released in spin-down powers the non-thermal radiation seen in systems like the Crab Nebula and PSR B1259-63. The pulsar spin-down power or luminosity ($L = \dot{E} = dE/dt$) is given by (e.g. Gaensler and Slane, 2006)

$$\dot{E} = 4\pi^2 I \frac{\dot{P}}{P^3}, \tag{4.1}$$

where $I \approx 10^{45}$ g cm^2 is the moment of inertia, P is the pulsar spin period and $\dot{P} = dP/dt$ is the rate of change of the spin period (or the period derivative). One of the most studied systems is the Crab Nebula and its associated pulsar which has a spin period of $P = 3.3 \times 10^{-2}$ s and a spin-down rate of $\dot{P} = 4 \times 10^{-13}$ s s^{-1}, implying a spin-down luminosity of $\dot{E} \approx 4 \times 10^{38}$ erg s^{-1}. Similarly, PSR B1259-63 has a spin period of $P = 47.7625$ ms and spin-down rate of $\dot{P} = 2.277 \times 10^{-15}$ s s^{-1} (Wang et al., 2004), which gives a spin-down luminosity of $\dot{E} = 8.25 \times 10^{35}$ erg s^{-1}.

The observed "pulsed" emission from pulsars is associated with the NS's strong magnetic field. If it is assumed that a pulsar has a dipole magnetic field, the surface equatorial field strength is determined by the spin period and period derivative and is given by (e.g. Bhattacharya and van den Heuvel, 1991, and references therein)

$$\begin{aligned} B &= \left(\frac{3c^3 I}{8\pi^2 R^6} P\dot{P}\right)^{1/2} \\ &= 3.2 \times 10^{19} \left(P\dot{P}\right)^{1/2} \left(\frac{R}{10^6 \text{ cm}}\right)^{-3} \text{ G}, \end{aligned} \tag{4.2}$$

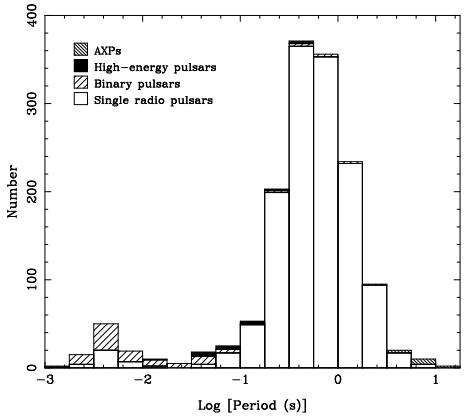

Figure 4.1: Summary of observed pulsar periods from the Australia Telescope National Facility Pulsar Catalogue (Manchester et al., 2005).

where $R = 10^6$ cm is a typical NS radius. Pulsars therefore possess large magnetic fields which, coupled to the rapid rotation, produce intense electric fields which are capable of accelerating particles to high energies, driving the pulsar wind and powering the observed nebulae.

If the spin-down rate of a pulsar is assumed to have the form (Manchester and Taylor, 1977)

$$\dot{\Omega} = -k\Omega^n, \tag{4.3}$$

where k is a constant, n is the braking index ($n = 3$ if the spin-down is only due to magnetic dipole radiation) and $\Omega = 2\pi/P$ is the pulsar's angular velocity, the age of a pulsar can be found from the solution to the differential equation (equation 4.3), which is given by the integration

$$\int_{\Omega_0}^{\Omega} \Omega^{-n}\, d\Omega = \int_0^{\tau} -k\, dt,$$

where a pulsar is "born" with an angular velocity $\Omega_0 = 2\pi/P_0$ at time $t = 0$ and spins-down to an angular velocity $\Omega = 2\pi/P$ at an age $t = \tau$. Therefore, the age of any pulsar is given by (e.g. Gaensler and Slane, 2006)

$$\tau = \frac{P}{(n-1)\dot{P}}\left[1 - \left(\frac{P_0}{P}\right)^{n-1}\right], \tag{4.4}$$

where the constraint $n \neq 1$ must be applied and the k term is eliminated by using equation (4.3). To determine the age, we need to know the initial period, P_0, which cannot be observed, and the value of the breaking index, n. The second derivative of the angular frequency is

$$\ddot{\Omega} = n\frac{\dot{\Omega}^2}{\Omega},$$

from which it is possible to determine the breaking index, n, if the second derivative can be

measured from long term light curves. This has only been done for a small number of pulsars and it has been found that the breaking index is $n < 3$ (e.g. Livingstone et al., 2005). Due to the uncertainties in the true age of a pulsar, the age is normally defined in terms of its characteristic age

$$\tau_{\rm char} = \frac{P}{2\dot{P}},$$

which is derived from equation (4.4) under the assumption that $P \gg P_0$ and that the spin-down is only due to magnetic dipole radiation ($n = 3$).

The spin-down power or luminosity of a pulsar (equation 4.1) is dependent on the spin period, P, which will decrease over time as the pulsar slows down. It can be shown from equation (4.3) that the spin period of the pulsar changes with time as (e.g. Gaensler and Slane, 2006)

$$P = P_0 \left(1 + \frac{t}{\tau_0}\right)^{\frac{1}{n-1}}, \tag{4.5}$$

where P_0 is the initial spin period,

$$\tau_0 = \frac{P_0}{(n-1)\dot{P}_0}, \tag{4.6}$$

and $\dot{P}_0$ is the initial spin-down rate. Substituting equation (4.5) into equation (4.1) shows that the spin-down luminosity at any time, t, is given by (e.g. Gaensler and Slane, 2006; Pacini and Salvati, 1973)

$$\dot{E} = \dot{E}_0 \left(1 + \frac{t}{\tau_0}\right)^{-\left(\frac{n+1}{n-1}\right)}, \tag{4.7}$$

where $\dot{E}_0$ is the initial spin-down power. The consequence of equation (4.7) is that for times $t \ll \tau_0$ the spin-down luminosity remains approximately constant.

4.2 Pulsar wind nebula

This section summarizes some of the important properties regarding pulsar winds and PWNe, following to some extent the discussion in reviews by Gaensler and Slane (2006) and Kirk et al. (2009); the reader is referred to these papers and references therein for a detailed review.

4.2.1 The pulsar wind

Goldreich and Julian (1969) showed that for a pulsar in a vacuum with a dipolar magnetic field aligned along the axis of rotation, the force on a particle due to the magnetic field would be

$$\left(\frac{F_E}{F_{\rm grav}}\right)_p = 5 \times 10^8 \cos^2\theta \, P^{-1} \left(\frac{B}{10^{12}\ {\rm G}}\right) \left(\frac{R}{10^6\ {\rm cm}}\right)^3 \left(\frac{M}{M_\odot}\right)^{-1},$$

and

$$\left(\frac{F_E}{F_{\rm grav}}\right)_e = 8\times10^{11}\cos^2\theta\,P^{-1}\left(\frac{B}{10^{12}\ {\rm G}}\right)\left(\frac{R}{10^6\ {\rm cm}}\right)^3\left(\frac{M}{M_\odot}\right)^{-1},$$

times greater than the gravitation force, for protons and electrons respectively, where θ is the polar angle. This effectively shows that a pulsar, despite its large gravitational field, cannot be surrounded by a vacuum and must be enveloped by a particle filled magnetosphere. An estimate of the particle density of the magnetosphere around PSR B1259-63 can be made by (Goldreich and Julian, 1969)

$$\begin{aligned} n &= 7\times10^{-2}\,\frac{B}{P}\ {\rm cm}^{-3} \\ &\sim 5\times10^{11}\left(\frac{B}{3.3\times10^{11}\ {\rm G}}\right)\left(\frac{P}{47.7625\ {\rm ms}}\right)^{-1}\ {\rm cm}^{-3}, \end{aligned}$$

where the magnetic field strength has been estimated from equation (4.2).

Goldreich and Julian (1969) proposed the situation depicted in Fig. 4.2: Within the radius of the light cylinder, $r_L = c/\Omega$, the pulsar is surrounded by a magnetosphere of particles which are attached to magnetic field lines and corotate with the pulsar. This region is also known as the near zone. Beyond the light cylinder particles cannot corotate as this would require them to have a velocity which exceeds the speed of light. Field lines beyond the light cylinder are open, and particles can travel along these lines forming the pulsar wind. This region is therefore known as the wind zone. The maximum energy of an escaping particle was calculated by Goldreich and Julian (1969) to be

$$\epsilon_{\rm max} = 3\times10^{12}\,\frac{Z}{P^2}\left(\frac{R}{10^6\ {\rm cm}}\right)^3\left(\frac{B}{10^{12}\ {\rm G}}\right)\ {\rm eV},$$

where Z is the electric charge of the particle.

If the magnetic field is assumed to be strongest at the equator there exists an open field line which has the same electric potential as the surrounding medium. This is known as the critical line. Below the critical line (towards the equator) protons or ions are accelerated out in the wind, while above the line (towards the poles) electrons are accelerated (Fig. 4.2). The acceleration of particles within the light cylinder can lead to the production of gamma-rays through curvature radiation, which can in turn create electron-positron pairs via photon-photon absorption (Sturrock, 1971).

It is now believed that primary particles initiate a pair-cascade which leads to electrons-positrons flowing away from the polar caps at a rate of (e.g. Kirk et al., 2009)

$$\begin{aligned} \frac{{\rm d}N}{{\rm d}t} &= \kappa\frac{\Omega^2 B_* R^3}{ec} \\ &= 2.7\times10^{30}\kappa\left(\frac{B_*}{10^{12}\ {\rm G}}\right)\left(\frac{R}{10^6\ {\rm cm}}\right)^3\left(\frac{P}{1\ {\rm s}}\right)^{-2}\ {\rm s}^{-1}, \end{aligned}$$

where κ is the number of pairs that are created by each primary particle and B_* is the magnetic

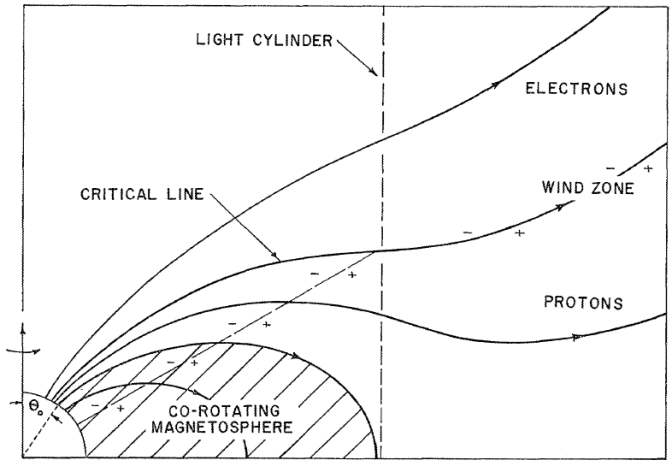

Figure 4.2: The region surrounding a pulsar as suggested by Goldreich and Julian (1969).

field strength at the polar caps. It is these leptons that constitute the particle component of the pulsar wind which will eventually radiate via synchrotron and IC cooling.

The spin-down luminosity is not only converted into particle energy. Rees and Gunn (1974) considered three components to the pulsar wind, namely the relativistic particles, electromagnetic waves and the non-varying component of the Poynting flux, all driven (or powered) by the spin-down luminosity. The ratio between the Poynting flux and the particle flux is defined by the ratio (e.g. Kirk et al., 2009)

$$\sigma = \frac{B^2}{4\pi n_{\rm e} \gamma m_{\rm e} c^2}, \tag{4.8}$$

where B is the magnetic field strength, $n_{\rm e}$ and γ are the number density and Lorentz factor of the leptons, and all terms are measured in the observer's frame. This effectively gives the ratio of the conversion of the spin-down luminosity into electromagnetic and kinetic energy.

The pulsar wind expands outwards away from the pulsar until it forms a shock front when it interacts with the surrounding medium. For isolated pulsars the surrounding medium is either the SNR or the interstellar medium (ISM) while for gamma-ray binaries the pulsar wind is confined by the stellar wind from the optical companion. The radiating post-shock region is known as the pulsar wind nebula (PWN). Models of the pulsar wind require that σ is small near the shock front (i.e. that most of the energy is in the leptons) to explain the observations of the Crab Nebula (e.g. Kennel and Coroniti, 1984a; Rees and Gunn, 1974).

4.2.2 The nebula

Fig. 4.3 shows the region around the pulsar and the PWN. The pulsar is surrounded by a corotating magnetosphere and outflowing wind of relativistic particles. Within the light cylinder (dashed circle) particles move along magnetic field lines and corotate with the pulsar. The pulsed

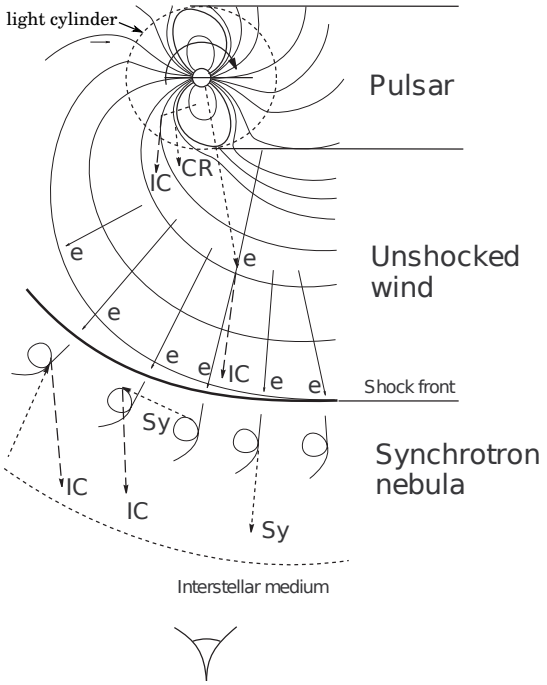

Figure 4.3: Pulsar, PWN and the corresponding emission regions; see text for details (adapted from Aharonian and Bogovalov, 2003).

radio, X-ray and gamma-ray emission from pulsars is believed to originate from within this light cylinder.

Beyond the light cylinder, the load produced by the relativistic particle wind on the magnetosphere results in the break-down of the corotation, causing the magnetosphere outside the light cylinder to trail the corotating magnetosphere within the light cylinder and the leptons to flow along the magnetic field lines. The weakening magnetic field in the wind zone results in synchrotron emission decreasing significantly since the energy loss time scales as (e.g. Lang, 1974, p. 31)

$$t_{1/2} \propto \frac{1}{B_{\perp}^2 E_{\mathrm{e}^{\pm}}}$$

where $B_{\perp}$ is the perpendicular component of the magnetic field and $E_{\mathrm{e}^{\pm}}$ is the energy of the particles. Similarly the gyroradius, r_g, becomes very large for particles moving near the speed of light (e.g. Lang, 1974, p. 28)

$$r_g \approx 2 \times 10^9 \frac{E_{\mathrm{e}^{\pm}}}{B} \text{ cm.}$$

The result is that the particles flow along the frozen in magnetic field lines and effectively do not radiate via synchrotron radiation. However, if there is a source of external photons, inverse Compton (IC) scattering can occur with the relativistic electrons (e.g. Aharonian and Bogovalov, 2003; Bogovalov and Aharonian, 2000).

A pulsar is surrounded by an expanding shell of material, released during the supernova event, and the pulsar wind and the resulting PWN are confined as they are forced into the supernova remnant (SNR) (e.g. Gaensler and Slane, 2006). A shock forms between the pulsar wind and the surrounding nebula at the point where the pressure of the pulsar wind and the pressure of the surrounding nebula are in equilibrium. The radial distance where this occurs is (e.g. Gaensler and Slane, 2006)

$$R_s = \left(\frac{\dot{E}}{4\pi \varrho c \mathbb{P}_{\rm Neb}} \right)^{1/2},$$

where $\dot{E}$ is the spin-down luminosity (equation 4.1), ϱ is the equivalent filling factor and $\mathbb{P}_{\rm Neb}$ is the pressure of the surrounding nebula. For a young pulsar wind expanding into the SNR the spin-down luminosity remains nearly constant for $t \ll \tau_0$ (equations 4.6 & 4.7) and the radius of the expanding PWN at time, t, is given by (e.g. Gaensler and Slane, 2006)

$$\begin{aligned} R_{\rm PWN} &\approx 1.5\, \dot{E}_0^{1/5} E_{\rm SN}^{3/10} M_{\rm ej}^{-1/2} t^{6/5} \\ &= 1.1 \text{ pc} \left(\frac{\dot{E}_0}{10^{38} \text{ erg s}^{-1}} \right)^{1/5} \left(\frac{E_{\rm SN}}{10^{51} \text{ erg}} \right)^{3/10} \left(\frac{M_{\rm ej}}{10 \text{ M}_\odot} \right)^{-1/2} \left(\frac{t}{10^3 \text{ yrs}} \right)^{6/5}. \end{aligned}$$

Here, $\dot{E}_0$ is the initial spin-down luminosity of the pulsar, $E_{\rm SN}$ is the kinetic energy of the supernova and $M_{\rm ej}$ is the mass of material released in the supernova. The underlying assumption here is that the expansion is completely spherically symmetric.

In the shock front, the leptons in the pulsar wind are thermalized and re-accelerated, producing a power-law distribution which can emit radiation via synchrotron and IC processes (e.g. Aharonian and Bogovalov, 2003; Gaensler and Slane, 2006). It was shown by Ginzburg and Syrovatskii (1965) that due to the synchrotron energy loss rate (e.g. Lang, 1974, p. 31)

$$t_{\rm sync} = \frac{9}{4} \frac{m_e^3 c^5}{e^4 \gamma} \frac{1}{B^2},$$

the synchrotron spectrum from this power-law distribution of emitting electrons will exhibit a sharp decrease in flux at frequencies above (e.g. Gaensler and Slane, 2006)

$$\begin{aligned} \nu > \nu_b &= \frac{3.1 \times 10^{23}}{H_\perp^3 t^2} \text{ Hz} \\ &\approx 10^{21} \left(\frac{B_{\rm PWN}}{10^{-6} \text{ G}} \right)^{-3} \left(\frac{t}{10^3 \text{ yrs}} \right)^{-2} \text{ Hz}, \end{aligned}$$

where $B_{\rm PWN}$ is the magnetic field of the PWN. Therefore, the synchrotron spectrum shows a "spectral break" at frequency ν_b, determined by the age of the emitting electrons. This has the effect that higher energy synchrotron radiation occurs closer to the pulsar.

It was shown by Bogovalov and Khangoulyan (2002b) that the conservation of energy flux in

the pulsar wind requires that the kinetic and electromagnetic energy of the pulsar wind has the form

$$\gamma + s = \gamma_0 + s_0, \tag{4.9}$$

where γ is the Lorentz factor, s is the electromagnetic energy flux in units of mc^2 and the subscript 0 indicates that the value is measured at the light cylinder. In other words, for the pulsar wind that moves out along streamlines, the sum of the kinetic and electromagnetic energy flux at the light cylinder must be equal to the sum just before the shock front. Due to the angular dependent relationship of the electric and magnetic fields, the Lorentz factor of the wind takes the angular dependent form

$$\gamma_1 = \gamma_0 + \gamma_m \sin^2\theta,$$

where γ_1 is the Lorentz factor of the pre-shocked wind just before the shock, γ_0 is the Lorentz factor at the light cylinder (≈ 200; Daugherty and Harding, 1982) and θ is the polar angle. This follows from equation (4.9) where it is assumed that the particle flux is isotropic, and that close to the shock we have $\gamma \gg s$. The term γ_m is the maximum Lorentz factor in the pre-shock wind and is determined by the electromagnetic energy flux, s_0. This maximum Lorentz factor is given by

$$\gamma_m = \left(\frac{\Omega R_{\rm NS}}{c}\right)^2 \frac{B_0^2}{4\pi n_0 mc^2} \approx 3 \times 10^6, \tag{4.10}$$

where $\Omega = 2\pi/P$, n_0 is the plasma density at the surface of the NS, and B_0 is the surface magnetic field strength. The decrease in the particle energy towards the poles by a factor $\sim 10^4$ leads to the formation of a torus shape shock-front and PWN around the pulsar (Fig. 4.4) while magnetic fields in the torus outflow can also result in the formation of a jet like structure and outflow around the poles of the pulsar (e.g. Bogovalov et al., 2005, Fig. 4.5). These torus and jet structures are observed in PWNe; for example X-ray observations of the Crab Nebula show a torus and jet structure (Fig. 4.6).

The supernova event that creates a pulsar is not completely symmetrical and the pulsar can obtain a velocity "kick" away from the centre of the SNR. As the pulsar moves through the SNR and eventually into the ISM, the PWN obtains a bow shock shape as the motion of the pulsar becomes supersonic with respect to the medium through which it moves (e.g. van der Swaluw et al., 2004). The ram pressure of the surrounding medium is then dependent on the speed at which the pulsar is moving through it and the shock will occur when (e.g. Gaensler and Slane, 2006)

$$\frac{\dot{E}}{4\pi\omega R_{w,0}^2 c} = \rho_0 v_{\rm psr}^2,$$

where ρ_0 is the density of the surrounding medium and $v_{\rm psr}$ is the speed of the pulsar. The distance $R_{w,0}$ is known as the stand-off distance and is the distance of the shock in the direction of the pulsar's motion. Due to the motion of the pulsar, the resulting shock will not be spherically symmetric around the pulsar and will form a bow shape shock (e.g. Fig. 4.7). Due to the motion of

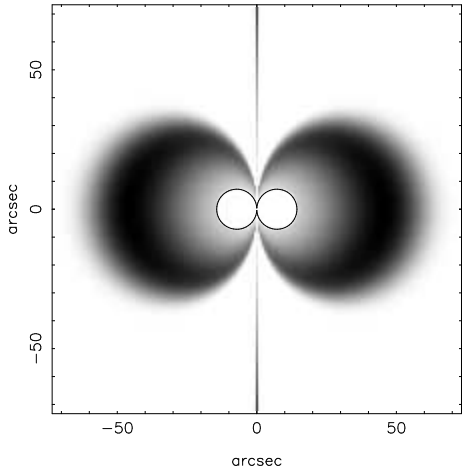

Figure 4.4: Simulation of synchrotron radiation from the PWN around PSR 0531 +21 due to the variation in the Lorentz factor of the pulsar wind given by equation (4.10) (Bogovalov and Khangoulyan, 2002a).

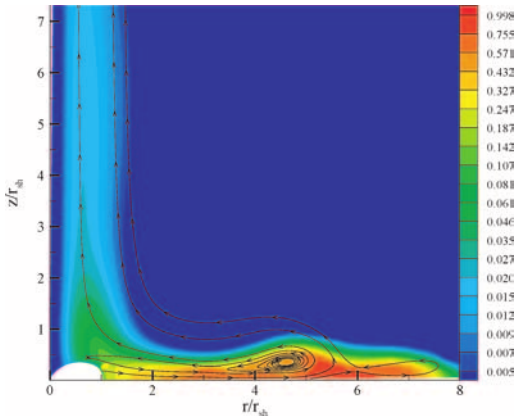

Figure 4.5: Simulation of synchrotron radiation from the PWN around a Crab–like pulsar due to the variation in the Lorentz factor of the pulsar wind and the magnetic collimation of the resulting outflow (Bogovalov et al., 2005).

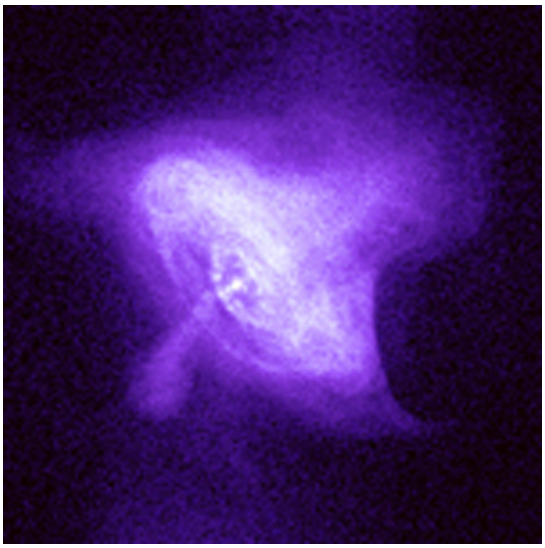

Figure 4.6: Chandra image of the Crab Nebula at 0.3-3 keV. The image shows the torus and jet features which are formed by the PWN (http://chandra.harvard.edu/photo/1999/0052/).

the pulsar around the optical companion, a similar bow shock is expected to occur in gamma-ray binary systems.

4.3 PWN in binary systems

In PSR B1259-63/LS 2883 it is believed that a stand-off shock forms between the 48 ms pulsar and the stellar wind, creating a PWN in the binary system. There is, however, some speculation about the nature of the other gamma-ray binary systems, in particular LS 5039, where the compact object is unknown. If the compact object in LS 5039 is a black hole, then the system could be an accretion driven microquasar. In this scenario the IC gamma-ray emission would be driven by the outflow of material in the relativistic jet. It was argued after the report of the detection of radio "jets" in LS 5039 (Paredes et al., 2000) and LSI+61 303 (Massi et al., 2004) (see section 3.4) that these two systems were microquasars which showed variable and precessing jets. However, Dubus (2006a) argued that:

1. The measured mass function of the systems did not conclusively show that the masses of the compact objects were $M > 3$ $M_\odot$, casting doubt on whether these compact objects were black holes. The mass functions were reconcilable with a neutron star mass of $M_{\rm NS} = 1.4$ $M_\odot$.

2. The radio and X-ray emission did not show any signatures of being accretion driven.

3. The observed radio "jets" could be explained by the complicated outflow expected from a PWN in a binary system.

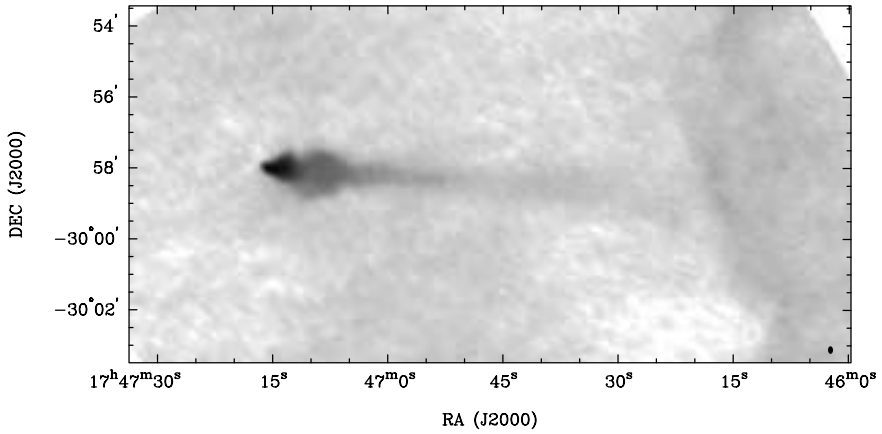

Figure 4.7: VLA image of G359.23-0.82 at 1.5 GHz showing the bow shock formation around the pulsar (adapted from Gaensler et al., 2004).

4. And lastly, while there had been no detection of pulsed emission from a pulsar in LS 5039 and LSI+61 303, the stellar wind could easily mask any pulsed radio emission through free-free absorption.

Dubus (2006a) argued in favour of PWNe driving all three of the then known gamma-ray binary systems (LS 5039, LSI+61 303 & PSR B1259-63), and presented a "scaling" model for the systems, based on an adaptation of the pulsar wind model by, among others, Kennel and Coroniti (1984a,b). Since this model encompasses concepts of PWNe and has a direct application to PSR B1259-63 and other gamma-ray binary systems, it is briefly summarized below. Following Dubus (2006a), this will be referred to as the binary plerion model.

4.3.1 Model parameters

The binary plerion model attempts to encapsulate a model that can be applied to all gamma-ray binary systems in terms of the shock radius or stand-off distance, R_s, the binary separation, d_s, and $\sigma\dot{E}$ which is the combination of the pulsar spin-down power, $\dot{E}$ (or luminosity, equation 4.1) and the ratio σ of the magnetic to the kinetic energy of the pulsar wind (equation 4.8).

The Kennel and Coroniti (1984a,b) model assumes that the spin-down luminosity is converted to kinetic energy in the particles (leptons) and electromagnetic waves. Therefore, the spin-down luminosity of the pulsar is related to the particle flux, F_p, and Poynting flux, $F_{E\times B}$, just before the shock at a radius, R_s, by

$$\begin{aligned} \frac{\dot{E}}{4\pi R_s^2} &= F_p + F_{E\times B} \\ &= \gamma n m_e c^3 + \frac{c}{4\pi} B^2, \end{aligned}$$

where it has been assumed that the particles are moving at velocities approaching the speed of

light. This can be re-written in terms of the ratio σ (equation 4.8) as (Kennel and Coroniti, 1984a,b)

$$\dot{E} = 4\pi n \gamma R_s^2 mc^3(1+\sigma), \tag{4.11}$$

which relates the spin-down luminosity to the particle and electromagnetic energy at the shock front. The parameters σ and $\dot{E}$ are then related by equations (4.8) & (4.11) which can then be written in the form given by Dubus (2006a) as

$$\frac{\dot{E}}{4\pi R_s^2 c} = \frac{B_1^2}{4\pi}\left(\frac{1+\sigma}{\sigma}\right) \tag{4.12}$$

$$\sigma = \frac{B_1^2}{4\pi n_1 \gamma_p^2 m_e c^2}, \tag{4.13}$$

where γ_p is the Lorentz factor of the pulsar wind before the shock, B_1 is the magnetic field in the observer's frame and n_1 is the density in the proper frame (or the frame co-moving with the shock).[i] The subscript 1 indicates that the parameters are measured before the stand-off shock while parameters with a subscript 2 are measured in the post-shock region. The stand-off distance is determined by the position where the pressure of the pulsar wind is balanced by the stellar wind,

$$\frac{\dot{E}}{4\pi R_s^2 c} = \rho_w(\mathbf{v}_w - \mathbf{v}_p)^2.$$

Here ρ_w and $\mathbf{v}_w$ are the mass density and velocity of the stellar wind at the shock, and $\mathbf{v}_p$ is the orbital velocity of the pulsar. The density of the stellar wind at the point of the stand-off shock can be determined from the stellar mass loss rate (Kudritzki and Puls, 2000)

$$\dot{M} = 4\pi r^2 \rho(r) v(r),$$

where $\rho(r)$ is the mass density and $v(r)$ is speed of the wind at the distance r from the star. If it is assumed that the orbital velocity is negligible in comparison with the wind velocity and that the stellar wind velocity approaches the terminal velocity ($\mathbf{v}_w \approx v_\infty$), it can be shown that

$$R_s \approx \frac{d_s}{1+(P_w/\dot{E})^{1/2}},$$

where d_s is the binary separation and $P_w = \dot{M} v_\infty c$ can be considered as the stellar wind power. The binary separation, d_s, is determined by the orbital parameters of the system. If $(P_w/\dot{E}) \gg 1$

[i] Note that by defining the lepton number density n_1 in the proper frame an additional γ_p factor appears in the denominator in equation (4.13) which is not present in equation (4.8) where all values are defined in the observer's frame.

the stand-off radius can be approximated by

$$R_s \approx 1.5 \times 10^{11} \left(\frac{d_s}{0.1 \text{ AU}}\right) \left(\frac{P_w}{10^{38} \text{ erg s}^{-1}}\right)^{-1/2} \left(\frac{\dot{E}}{10^{36} \text{ erg s}^{-1}}\right)^{1/2} \text{ cm.}$$

4.3.2 Lorentz factors

The plerion model assumes that the leptons in the pre-shock pulsar wind are mono-energetic (with Lorentz factor γ_p) and are re-accelerated at the shock front. Dubus (2006a) assumes that, after the shock, the lepton distribution has the form $n_\gamma \propto \gamma^{-2} \mathrm{d}\gamma$, between $\gamma_{\min}$ and $\gamma_{\max}$. It is therefore necessary first to determine the limits on the lepton energy. The minimum value is shown by Kennel and Coroniti (1984b) in the case $\sigma \ll 1$ to be given by

$$\gamma_{\min} \ln\left(\frac{\gamma_{\max}}{\gamma_{\min}}\right) \approx \frac{\gamma_p}{\sqrt{2}},$$

which Dubus (2006a) simplifies as

$$\gamma_{\min} \approx 0.1\gamma_p. \tag{4.14}$$

The maximum Lorentz factor is determined by the balance between the assumed acceleration time (estimated by the gyroradius) and the cooling time (assumed to be synchrotron cooling). In other words, a lepton can only accelerate to a certain maximum energy if the time taken to reach that energy is less than the time taken for the lepton to lose the energy through radiative cooling. This is determined by comparing the synchrotron and acceleration cooling times. The acceleration time is estimated by the gyroradius, and is given by

$$t_{\text{acc}} \approx \frac{\gamma m_e c}{eB}, \tag{4.15}$$

while the synchrotron cooling time is

$$t_{\text{sync}} = \frac{9}{4} \frac{m_e^3 c^5}{e^4 \gamma} \frac{1}{B^2}. \tag{4.16}$$

In the post-shock region the magnetic field strength, in the limit $\sigma \ll 1$, is given by (Kennel and Coroniti, 1984a)

$$\begin{aligned} B_2 &= 3(1-4\sigma)B_1 \\ &= 3(1-4\sigma)\left(\frac{\dot{E}}{cR_s^2}\frac{\sigma}{1+\sigma}\right)^{1/2}. \end{aligned} \tag{4.17}$$

Substituting the post-shock magnetic field (equation 4.17) into equations (4.15) & (4.16) it can be shown that the acceleration and synchrotron cooling times in the binary plerion model can

be approximated by

$$\begin{aligned} t_{\rm acc} &\approx 0.01 \left(\frac{\gamma}{10^6}\right) \left(\frac{\dot{E}}{10^{36}\ {\rm erg\ s^{-1}}}\right)^{-1/2} \left(\frac{\sigma}{10^{-3}}\right)^{1/2} \left(\frac{R_S}{10^{11}\ {\rm cm}}\right)\ {\rm sec}, \\ t_{\rm sync} &\approx 30 \left(\frac{\gamma}{10^6}\right)^{-1} \left(\frac{\dot{E}}{10^{36}\ {\rm erg\ s^{-1}}}\right)^{-1} \left(\frac{\sigma}{10^{-3}}\right)^{-1} \left(\frac{R_S}{10^{11}\ {\rm cm}}\right)^{2}\ {\rm sec}. \end{aligned}$$

Requiring that the acceleration time must always be less than the radiation time places a limit on the maximum lepton energy in the system which is found by $t_{\rm acc} \lesssim t_{\rm sync}$. It can then be shown that

$$\gamma_{max} \approx 5 \times 10^7 \left(\frac{\dot{E}}{10^{36}\ {\rm erg\ s^{-1}}}\right)^{-1/4} \left(\frac{\sigma}{10^{-3}}\right)^{-1/4} \left(\frac{R_S}{10^{11}\ {\rm cm}}\right)^{1/2}. \tag{4.18}$$

For lepton energy loss via IC scattering, the typical cooling time for a blackbody distribution of photons (scaled with distance) is given by (Blumenthal and Gould, 1970; Dubus, 2006a)

$$t_{KN} \approx 5.2 \left(\frac{\gamma}{10^6}\right) \left(\frac{3{\rm eV}}{kT_\star}\right)^2 \left(\frac{d_s}{R_\star}\right)^2 \left[\ln\left(\frac{4\gamma kT_\star}{m_e c^2}\right) - 1.98\right]^{-1}\ {\rm sec}. \tag{4.19}$$

When the synchrotron cooling time is less than the IC cooling time, i.e. $t_{\rm sync} < t_{\rm KN}$, synchrotron radiation will become the dominant cooling mechanism. From equations (4.16) & (4.19) it can be shown that this will occur for leptons with Lorentz factors

$$\gamma > \gamma_S \approx 1.2 \times 10^6 \frac{R_{11}}{d_{0.1}} \left(\frac{\dot{E}}{10^{36}\ {\rm erg\ s^{-1}}}\right)^{-1/2} \left(\frac{\sigma}{10^{-3}}\right)^{-1/2} \left(\frac{T_\star}{40\,000{\rm K}}\right) \left(\frac{R_\star}{10\ {\rm R_\odot}}\right), \tag{4.20}$$

where

$$\begin{aligned} R_{11} &= \left(\frac{R_S}{10^{11}\ {\rm cm}}\right), \\ d_{0.1} &= \frac{d_s}{0.1\ {\rm AU}}. \end{aligned}$$

The resulting shape of the synchrotron and IC spectra is determined by the minimum and maximum Lorentz factors, $\gamma_{\rm min}$ & $\gamma_{\rm max}$ (equations 4.14 & 4.18) and the energy above which synchrotron cooling begins to dominate over IC cooling, γ_S (equation 4.20). The peak emission for synchrotron radiation occurs at the energy (e.g. Lang, 1974, p. 29)

$$h\nu_c = \frac{3h}{4\pi} \frac{eH}{mc} \gamma^2 \sin\varphi,$$

while for IC scattering in the Klein-Nishina limit the scattered photon attains the energy $\epsilon = h\nu \approx \gamma m_e c^2$. The corresponding synchrotron and IC spectra are then described by the limiting

energies

$$\begin{aligned} h\nu_{sync,min} &\approx 1\left(\frac{\gamma_p}{10^6}\right)^2\left(\dot{E}_{36}\sigma_{-3}\right)^{1/2}\left(\frac{R_S}{10^{11}\text{ cm}}\right)^{-1}\text{ keV}, \\ h\nu_{sync,S} &\approx 150\left(\dot{E}_{36}\sigma_{-3}\right)^{-1/2}\left(\frac{T_\star}{40\,000\text{K}}\right)^2\left(\frac{R_\star}{10\text{ R}_\odot}\right)^2\left(\frac{R_{11}}{d_{0.1}^2}\right)\text{ keV}, \\ h\nu_{sync,max} &\approx 250\text{ MeV}, \end{aligned}$$

and

$$\begin{aligned} h\nu_{IC,min} &\approx 50\left(\frac{\gamma_p}{10^6}\right)\text{ GeV}, \\ h\nu_{IC,S} &\approx 0.6\left(\dot{E}_{36}\sigma_{-3}\right)^{-1/2}\left[\left(\frac{T_\star}{40\,000\text{K}}\right)\left(\frac{R_\star}{10\text{ R}_\odot}\right)\right]\left(\frac{R_{11}}{d_{0.1}^2}\right)\text{ TeV}, \\ h\nu_{IC,max} &\approx 25\left(\dot{E}_{36}\sigma_{-3}\right)^{-1/4}\left(\frac{R_S}{10^{11}\text{ cm}}\right)^{1/2}\text{ TeV}, \end{aligned}$$

respectively, where

$$\dot{E}_{36}\sigma_{-3} = \left(\frac{\dot{E}}{10^{36}\text{ erg s}^{-1}}\right)\left(\frac{\sigma}{10^{-3}}\right).$$

The estimates above illustrate that a PWN in a binary system is able to explain the multi-wavelength nature of these systems, covering more than 15 decades in energy (see e.g. Fig. 4.8).

4.3.3 Numerical model

Dubus (2006a) determined the post-shock binary plerion emission from the particle distribution along the plerion. If z is the normalized distance with respect to the stand-off distance along the length of the nebula, the particle distribution, $N(\gamma, z)$, was calculated by numerical integration of the differential equation (Dubus, 2006a)

$$\frac{\partial N}{\partial z} = \frac{\partial}{\partial \gamma}\left[\frac{\mathrm{d}\gamma}{\mathrm{d}z}N\right] + Q(\gamma)\delta(z-1),$$

where $\mathrm{d}\gamma/\mathrm{d}z$ is the change in particle energy along the plerion and $Q(\gamma)$ is the injected electron spectrum. The total change in the particle distribution is given by the energy loss from synchrotron, IC and adiabatic cooling

$$\frac{\mathrm{d}\gamma}{\mathrm{d}z} = \frac{R_s}{\nu}\left[\left(\frac{\mathrm{d}\gamma}{\mathrm{d}t}\right)_{\text{sync}} + \left(\frac{\mathrm{d}\gamma}{\mathrm{d}t}\right)_{\text{IC}} + \left(\frac{\mathrm{d}\gamma}{\mathrm{d}t}\right)_{\text{ad}}\right],$$

where the appropriate energy loss equations were applied.

Dubus (2006a) performed the numerical integration over the distance z by dividing z into multiple logarithmic divisions, within which the particle distribution was calculated. From the

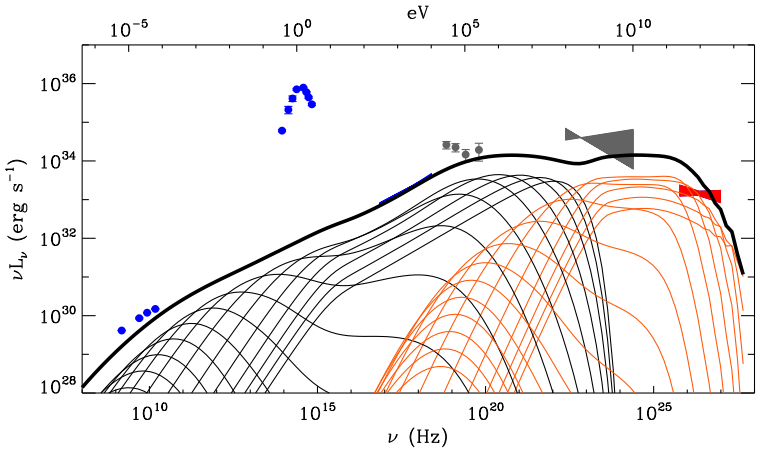

Figure 4.8: Calculated spectrum for LS 5039 using the binary plerion model. The thin grey and red lines correspond to the synchrotron and IC spectrum calculated in representative logarithmic values of z. The first line corresponds to $z = 0$, while the last line corresponds to $z \approx 1000$. The thick black line shows the total SED calculated from the sum over all z sections. The spectrum is calculated ignoring orbital motion. Radio, optical, X-ray, EGRET GeV upper-limits and TeV gamma-ray data points are also shown (Dubus, 2006a).

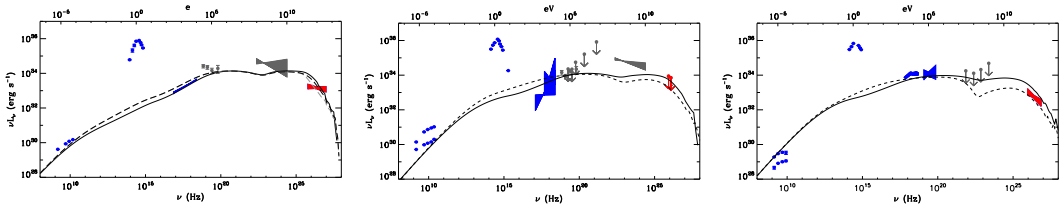

Figure 4.9: The calculated SED for LS 5039 (left), LSI+61 303 (middle) and PSR B1259-63 (right). Each figure shows the distribution at periastron (solid line) and apostron (dashed line) for each system. Additional effects of e.g. gamma-ray absorption are not shown. The parameters used to calculate the SED are given in Table 4.1 (adapted from Dubus, 2006a).

particle distribution and energy loss the resulting synchrotron and IC spectra can be determined. See Dubus (2006a), and reference therein, for a discussion of the numerical integration method and application.

The calculated non-thermal spectrum energy distribution (SED) for LS 5039 is shown in Fig. 4.8, along with radio, optical, X-ray, EGRET GeV upper-limits and TeV gamma-ray data points. The thin lines correspond to representative synchrotron (grey) and IC (red) spectra calculated in the z sections of the expanding plerion. The distribution does not consider the modification of the spectrum due to the change in the morphology of the plerion due to orbital motion, which Dubus (2006a) believes should not change dramatically in the case of LS 5039.

The SED for LS 5039, LSI+61 303, and PSR B1259-63 are shown in Fig. 4.9 at periastron (solid line) and apastron (dashed line) and the parameters used to calculate each spectrum are given in Table 4.1.

Table 4.1: Parameters for the SED calculations shown in Fig. 4.9 Dubus (2006a).

	$\dot{E}$ erg/s	γ_p	σ	R_s (periastron) cm	R_s (apostron) cm
LS 5039	10^{36}	10^5	0.01	2×10^{11}	4×10^{11}
LSI+61 303	10^{36}	10^5	0.02	8×10^{11}	4×10^{12}
PSR B1259-63	8×10^{35}	10^5	0.01	3×10^{12}	4×10^{13}

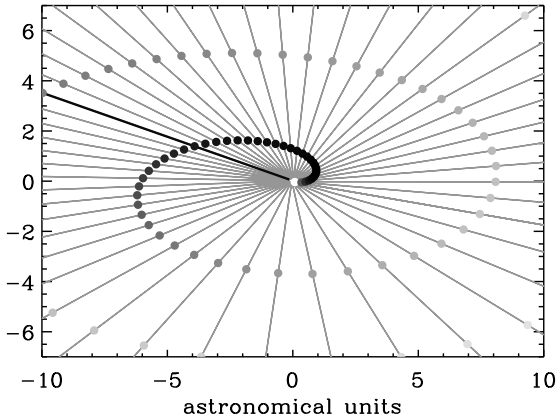

Figure 4.10: Flow of material in the plerion binary due to orbital motion. Material in the PWN will flow away from the optical companion, resulting in the formation of a "bending" morphology (Dubus, 2006a).

The orbital motion becomes important for the system morphology as material will "bend" due to the orbital motion, illustrated in Fig. 4.10. Material flows away from the direction of the optical companion and as the pulsar orbits the star, the outflow direction will change leading to the formation of a "bending" emission region. The computed radio maps at 5 GHz for LS 5039 are shown in Fig. 4.11.

The binary plerion model shows that the observed "jet" radio emission from LS 5039 and LSI+61 303 can be explained without appealing to a microquasar model. This model, combined with work by other authors and new radio images showing changing radio morphologies has put the plerion model on a firm footing for all gamma-ray binary systems, including the more recently detected sources.

The pulsar wind nebula model is able to explain the broad spectral energy distribution of LS 5039 and shows that this model is a viable model for all gamma-ray binary systems. Based on this assumption, this study has undertaken to investigate how the IC scattering of electrons originating in the pulsar wind can be influenced by the IR excess for the circumstellar disc of

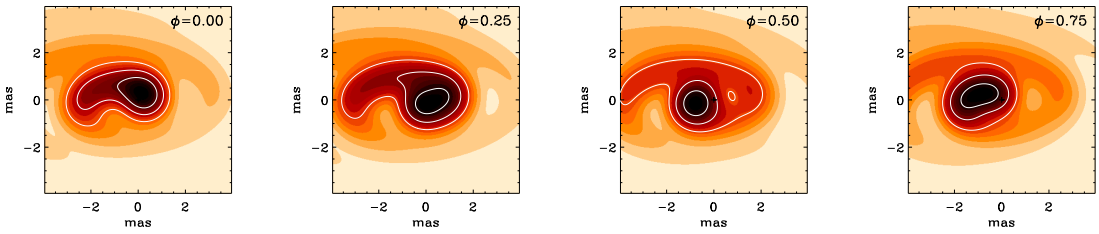

Figure 4.11: Simulation of the radio morphology for LS 5039 using the plerion model. Each map corresponds to the orbital morphology seen at different phases of the orbit. Guassian smoothing is applied to the simulations to match the expected radio emission at 5 GHz. The shading represents intensity with dark areas appearing brighter (Dubus, 2006a).

the Be star in PSR B1259-63.

Chapter 5

Compton and inverse Compton scattering

The Very High Energy (VHE) gamma-ray emission from PSR B1259-63/LS 2883 and other gamma-ray binaries is best explained through the up-scattering of soft photons (IR to optical) to high energies by relativistic electrons produced in the magnetosphere of the neutron star and flowing out in the pulsar wind. This process of electrons scattering photons to higher energies is known as inverse Compton (IC) scattering. In order to explain the gamma-ray emission it is necessary to understand the IC scattering process in relativistic scenarios. This chapter will present a summary of Compton and IC scattering as it pertains to the production of gamma-rays in gamma-ray binaries, and in PSR B1259-63 in particular.

The discussion considers isotropic and anisotropic scattering as the latter is important for gamma-ray binaries and will be important to explain gamma-ray variability, one of the signatures of the VHE emission from these systems. The discussion will also focus on IC scattering in the Thomson and Klein-Nishina limits since the cross-section in these two limits varies significantly and the larger cross-section in the Thomson limit is of fundamental importance to model the IC scattering of soft photons from the circumstellar disc.

Before beginning this chapter, in the interest of clarity, a few terms will first be defined. Compton scattering refers to the process of an electron and a photon scattering, and this generally refers to the case when the photon transfers energy to the electron, but the term can also be used more generally to refer to any scattering. Inverse Compton (IC) scattering is the "inverse" of classical Compton scattering and occurs when the energy of an electron is transferred to a photon. The up-scattering of soft-photons to VHE gamma-rays is a relativistic process and the discussion will consider the energy transfer in the frame co-moving with the relativistic electron, K', from which the transformation is made to the observer's rest frame, or laboratory frame, K. A quantity or variable that is primed (e.g. ϵ') refers to a measurement in the electron's rest frame, K', while unprimed variables refer to the observer's rest frame, K.

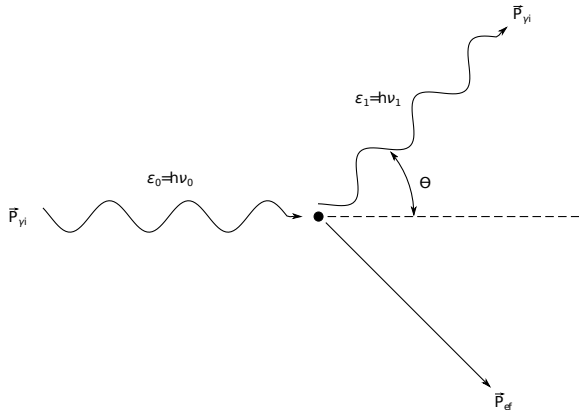

Figure 5.1: Compton scattering of a photon off a stationary electron.

5.1 Compton scattering equations

This section presents the derivation of the basic formulae for Compton and inverse Compton scattering, closely following the discussions of Blumenthal and Gould (1970) and Rybicki and Lightman (2004, pp. 195–223).

5.1.1 Compton scattering

The first and simplest problem that must be addressed is when a photon strikes a stationary electron (Fig. 5.1). The energy of the photon before scattering is ϵ_0 and the energy after scattering is ϵ_1. In order to determine the result of this collision the four-momentum before and after the collision must be considered. The initial ($\vec{P}_{\gamma i}$) and final ($\vec{P}_{\gamma f}$) four-momentum of the photon before and after scattering is:

$$\begin{aligned}
\vec{P}_{\gamma i} &= \left[P^0, P^j\right] \\
&= \left[\frac{h\nu_i}{c}, \frac{h\nu_i}{c}\bar{n}_i\right] \\
&= \frac{h\nu_i}{c}\left[1, \bar{n}_i\right] \\
&= \frac{\epsilon_0}{c}\left[1, \bar{n}_i\right],
\end{aligned}$$

and

$$\begin{aligned}
\vec{P}_{\gamma f} &= \left[P^0, P^j\right] \\
&= \frac{h\nu_f}{c}\left[1, \bar{n}_f\right] \\
&= \frac{\epsilon_1}{c}\left[1, \bar{n}_f\right],
\end{aligned}$$

where $\bar{n}_i$ and $\bar{n}_f$ are the unit vectors in the direction of motion. Similarly the initial ($\vec{P}_{ei}$) four-momentum of a stationary electron ($\gamma = 1$) with a rest mass, m_e, before scattering is:

$$\begin{aligned} \vec{P}_{ei} &= \left[P^0, P^j\right] \\ &= \left[m_e c, 0\right]. \end{aligned}$$

Here it is assumed that the motion of the electron after scattering is non-relativistic. From the conservation of momentum and energy

$$\bar{P}_{ei} + \bar{P}_{\gamma i} = \bar{P}_{ef} + \bar{P}_{\gamma f},$$

it follows that

$$\left(\bar{P}_{ei} + \bar{P}_{\gamma i} - \bar{P}_{\gamma f}\right)^2 = \bar{P}_{ef}^2,$$

where $\bar{P}_{ef}$ is the four-momentum of the electron after scattering. By making use of $\bar{P}_{ef}^2 = m_e^2 c^2$ it is then possible to show that the energy of the scattered photon is given by

$$\epsilon_1 = \frac{\epsilon_0}{1 + \frac{\epsilon_0}{m_e c^2}\left(1 - \cos\Theta\right)}, \tag{5.1}$$

where Θ is the angle of photon's deviation from it initial path (Fig. 5.1). The change in the wavelength due to Compton scattering is often expressed as

$$\Delta\lambda = \lambda_1 - \lambda_0 = \lambda_c\left(1 - \cos\Theta\right), \tag{5.2}$$

where λ_c is defined as

$$\lambda_c \equiv \frac{h}{m_e c},$$

and is known as the Compton wavelength ($\lambda_c = 2.426$ Å for an electron).

In this scenario energy is transferred from the photon to the electron which is initially at rest. If the wavelength of the photon is much larger than the Compton wavelength the change in wavelength is small (Equation 5.2) and the collision can be considered as approximately elastic.

5.1.2 Doppler shift formula

The previous section presented the energy transfer during the scattering between a photon and a stationary electron. In this case the electron gains energy from the photon and the photon loses energy, resulting in the observed change in wavelength. The next step is to calculate the energy transfer that occurs when a relativistic electron interacts with a low energy photon, i.e. the inverse Compton process. This can be done by converting the energy of the photon in the observer's frame, K, to the energy in the electron's rest frame, K', applying equation (5.1), and then converting the scattered photon's energy back to the observer's frame. The conversion

between rest frames can be made using the Doppler shift formulae and the transformations are quoted here.

If the angles between the direction of a photon and the direction of an electron are given by θ and θ' in K and K' respectively, the energy transformation equations are

$$\epsilon' = \epsilon\gamma(1 - \beta\cos\theta), \tag{5.3}$$

$$\epsilon = \epsilon'\gamma(1 + \beta\cos\theta'), \tag{5.4}$$

were γ is the Lorentz factor and $\beta = v/c$. The corresponding transformation of the angles between the respective references frames are

$$\cos\theta' = \frac{\cos\theta - \beta}{1 - \beta\cos\theta} \tag{5.5}$$

$$\cos\theta = \frac{\cos\theta' + \beta}{1 + \beta\cos\theta'}, \tag{5.6}$$

and

$$\sin\theta' = \frac{\sin\theta}{\gamma(1 - \beta\cos\theta)} \tag{5.7}$$

$$\sin\theta = \frac{\sin\theta'}{\gamma(1 + \beta\cos\theta)}. \tag{5.8}$$

Using equations (5.3)–(5.8) it is possible to convert the energies in the observer's frame, K, to the energies in the electron's rest frame, K', (and vice-versa). These equations are used to determine the energy transferred to photons in the observer's frame.

5.1.3 Inverse Compton scattering

Using the equations in sections 5.1.1 & 5.1.2 it is now possible to determine the observed energy change during IC scattering. In the observer's frame, K, a photon with an initial energy ϵ_0 will be up-scattered by a relativistic electron (with Lorentz factor γ) to an energy ϵ_1. In the electron's rest frame the corresponding initial and final energies are ϵ'_0 and ϵ'_1 respectively.

Fig. 5.2 shows the scattering in the observer's and electron's rest frame. If the electron is moving along the x-axis then the transformation of the photon energy is determined by the Doppler shift equations, which are

$$\epsilon'_0 = \epsilon_0\gamma\left(1 - \beta\cos\theta_0\right), \tag{5.9}$$

$$\epsilon_1 = \epsilon'_1\gamma\left(1 + \beta\cos\theta'_1\right). \tag{5.10}$$

In the electron's rest frame, equation (5.1) is now applicable to the scattering and the change in

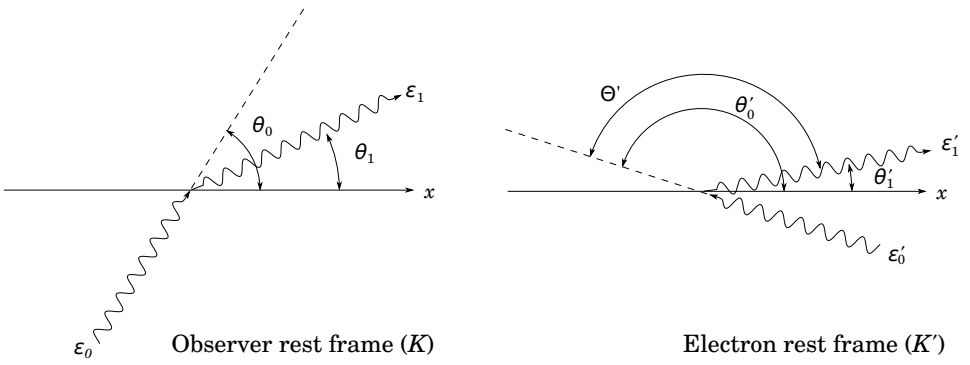

Figure 5.2: Inverse Compton scattering in the observer's (K) and electron's (K') rest frame. The azimuth angles of the incoming and scattered photons are not indicated (adapted from Rybicki and Lightman, 2004, p. 198).

energy is given by

$$\epsilon_1' = \epsilon_0' \left[1 + \frac{\epsilon_0'}{m_\mathrm{e}c^2}\left(1 - \cos\Theta'\right)\right]^{-1}, \tag{5.11}$$

where Θ' is the angle of deviation which is given by

$$\cos\Theta' = \cos\theta_1' \cos\theta_0' + \sin\theta_0' \sin\theta_1' \cos\left(\phi_0' - \phi_1'\right).$$

The angles θ_0' and θ_1' are defined in Fig. 5.2 and ϕ_0' and ϕ_1' are the corresponding azimuthal angles. While the Doppler shift transformation is only dependent on the angle relative to the direction of motion, the energy transfer during scattering in K' is dependent on the total angle of deviation which has additional degrees of freedom. For relativistic electrons, in K', the incoming photons will arrive in a small opening angle around the direction of the electrons motion due to relativistic beaming. This effectively means that for highly relativistic electrons $\theta_0' \approx \pi$.

The gain in energy as observed in the observer's frame then depends on the Doppler shift equations and is determined by the transformation of ϵ_1' to ϵ_1 using equation (5.10).

Kinematics

The initial energy of the photon in K' is given by equation (5.9) where the angle θ_0 is the angle between the incident photon and the electron in K and will be a minimum for a "head-tail" collision ($\theta_0 = 0$), and a maximum for a "head-head" collision ($\theta_0 = \pi$). The initial photon energy in K' then varies between

$$\begin{aligned} \epsilon_{0,\mathrm{min}}' &= \epsilon_0 \gamma \left(1 - \beta\right) \qquad (\text{for } \theta = 0) \\ \epsilon_{0,\mathrm{max}}' &= \epsilon_0 \gamma \left(1 + \beta\right) \qquad (\text{for } \theta = \pi), \end{aligned}$$

and the maximum scattered energy in K is

$$\epsilon_{1,\max} = \epsilon_1'\gamma(1+\beta) \qquad (\text{for } \theta_1' = 0)\,. \tag{5.12}$$

This can be further simplified by approximating $\beta \approx 1 - 1/2\gamma^2$ (as shown in Appendix A.1) and substituting this value into the equations for $\epsilon'_{0,\min}$ and $\epsilon'_{0,\max}$ gives

$$\begin{aligned} \epsilon'_{0,\min} &= \epsilon_0\gamma\,(1-\beta) \\ &\approx \epsilon_0\gamma\left(1-\left(1-\frac{1}{2\gamma^2}\right)\right) \\ &\approx \frac{\epsilon_0}{2\gamma}, \end{aligned} \tag{5.13}$$

and

$$\begin{aligned} \epsilon'_{0,\max} &= \epsilon_0\gamma\,(1+\beta) \\ &\approx \epsilon_0\gamma\left(1+\left(1-\frac{1}{2\gamma^2}\right)\right) \\ &\approx \epsilon_0\gamma\left(2-\frac{1}{2\gamma^2}\right) \\ &\approx 2\gamma\epsilon_0. \qquad (\text{for } \gamma \gg 1) \end{aligned} \tag{5.14}$$

Similarly, the maximum energy for the scattered photon in K can be approximated by

$$\epsilon_{1,\max} \approx 2\gamma\epsilon_1'. \tag{5.15}$$

By making use of the Taylor expansion, equation (5.11) can be shown to be approximated by (Appendix A.2)

$$\epsilon_1' \approx \epsilon_0'\left[1-\frac{\epsilon_0'}{m_\mathrm{e}c^2}\,(1-\cos\Theta')\right],$$

which in the Thomson limit, $\epsilon_0' \ll m_\mathrm{e}c^2$, reduces to an elastic scattering in the electron's rest frame, i.e. $\epsilon_1' \approx \epsilon_0'$. However, transformed to the observer's frame, the maximum energy transferred to the photon in the Thomson limit, using equations (5.14), (5.15) and $\epsilon_1' \approx \epsilon_0'$, is

$$\epsilon_{1,\max} \approx 4\gamma^2\epsilon_0. \tag{5.16}$$

This shows that in the Thomson limit the energy of a photon can be increased by a factor $\sim \gamma^2$ during IC scattering. However, in the Klein-Nishina limit, $\epsilon_0' \gg m_\mathrm{e}c^2$, the energy of the scattered photon is limited by the energy of the incoming electron. This implies that the maximum allowed energy is

$$\epsilon_{1,\max} \approx \gamma m_\mathrm{e}c^2.$$

The maximum energy in the Klein-Nishina regime is determined in the same way as in the Thomson limit with the exception that in the electron's rest frame the energy transfer cannot be approximated by $\epsilon_1' \approx \epsilon_0'$. As was shown above, the Doppler equations result in the maximum energies $\epsilon_0' = 2\gamma\epsilon_0$ and $\epsilon_1 = 2\gamma\epsilon_1'$ under the assumption that $\gamma \gg 1$, $\theta_0 = \pi$ and $\theta_1' = 0$. The choice $\theta_0 = \pi$ means that $\theta_0' = \pi$ and assuming $\phi_1' = \phi_0'$[i] this reduces $\cos\Theta'$ to

$$\cos\Theta' = \cos(\theta_1' - \theta_0') = -1,$$

and therefore equation (5.11) reduces to

$$\epsilon_1' = \frac{\epsilon_0'}{1 + (2\epsilon_0')/(m_\mathrm{e}c^2)}.$$

Substituting in the values of ϵ_0' and ϵ_1 shows that the maximum allowed energy in K is

$$\epsilon_{1,\max} = \frac{4\gamma^2\epsilon_0}{1 + (4\gamma\epsilon_0/m_\mathrm{e}c^2)}. \tag{5.17}$$

Comparing this to the maximum allowed energy derived in the Thomson limit (equations 5.16) shows that the denominator term now constraints the maximum value of ϵ_1 to less than $4\gamma^2\epsilon_0$. Equation (5.17) can be written in the form

$$\epsilon_{1,\max} = \gamma m_\mathrm{e}c^2 \left(\frac{1}{1 + \frac{1}{\gamma^2}\left(\frac{\gamma m_\mathrm{e}c^2}{4\epsilon_0}\right)} \right),$$

which, for $\gamma \gg 1$ reduces to $\epsilon_1 \approx \gamma m_\mathrm{e}c^2$, or the energy of the electron before scattering. This implies that $\epsilon_1 \approx \gamma m_\mathrm{e}c^2$ is the maximum energy that can be transferred to a photon during highly relativistic IC scattering, as it is the maximum energy that the electron possesses before scattering.

5.2 The IC scattering cross-section

The probability that a photon will scatter from an electron is determined by the scattering cross-section, which ranges between the Thomson (classical) and Klein-Nishina (quantum) limits. The two cross-section formulae, and the comparison between them, are presented below.

[i] This effectively says that the scattered photon moves in the direction of the electron's initial momentum (relativistic beaming).

5.2.1 Thomson cross-section

From non-relativistic electrodynamics it can be shown that the differential cross-section for an electron of charge, e, and mass, m_e, is given by (e.g Rybicki and Lightman, 2004, p. 91)

$$\frac{d\sigma}{d\Omega} = \frac{e^4}{m_\mathrm{e}^2 c^4} \sin^2\vartheta = r_0^2 \sin^2\vartheta, \tag{5.18}$$

where $d\sigma$ is the differential cross-section, $d\Omega = \sin\vartheta\, d\vartheta d\varphi$ is the solid angle in the direction of scattering, and

$$r_0 \equiv \frac{e^2}{m_\mathrm{e} c^2},$$

is the classical electron radius. Integrating equation (5.18) over the whole solid angle gives,

$$\begin{aligned} \sigma_\mathrm{T} &= \int \frac{d\sigma}{d\Omega}\, d\Omega \\ &= \int_0^{2\pi}\int_0^{\pi} r_0^2 \sin^2\vartheta\, \sin\vartheta\, d\vartheta\, d\phi \\ &= \frac{8\pi}{3} r_0^2, \end{aligned} \tag{5.19}$$

where σ_T is the total scattering cross-section and is know as the Thomson cross-section. The values of the classical electron radius and Thomson cross-section are $r_0 = 2.82 \times 10^{-13}$ cm and $\sigma_\mathrm{T} = 6.65 \times 10^{-25}$ cm^2 respectively.

Equations (5.18) & (5.19) apply for polarized radiation, but as shown in e.g. Rybicki and Lightman (2004, pp. 90-93), the general results can be found by treating unpolarized light as two linear polarized beams. The scattering then occurs as shown in Fig. 5.3, where $\hat{\mathbf{n}}$ is the direction of scattering, and $\hat{\epsilon}_1$ and $\hat{\epsilon}_2$ are the two linear polarized components of the unpolarized light. The orientation is chosen such that the angle between $\hat{\epsilon}_1$ and $\hat{\mathbf{n}}$ is ϑ and the angle between $\hat{\epsilon}_2$ and $\hat{\mathbf{n}}$ is $\pi/2$. Therefore the differential cross-section is given by (e.g. Rybicki and Lightman, 2004, p. 93)

$$\begin{aligned} \frac{d\sigma}{d\Omega} &= \frac{1}{2}\left[\left(\frac{d\sigma(\vartheta)}{d\Omega}\right) + \left(\frac{\sigma(\pi/2)}{d\Omega}\right)\right] \\ &= \frac{1}{2} r_0^2 \left(1 + \sin^2\vartheta\right) \\ &= \frac{1}{2} r_0^2 \left(1 + \cos^2\theta\right), \end{aligned} \tag{5.20}$$

where $\theta \equiv \pi/2 - \vartheta$. Integration over the solid angle in equation (5.20) shows that the total scattering cross-section remains

$$\sigma = \sigma_\mathrm{T} = \frac{8\pi}{3} r_0^2.$$

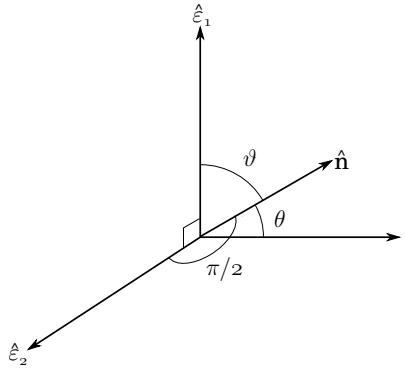

Figure 5.3: Scattering of un-polarized light in the classical regime; see text for details (adapted from Rybicki and Lightman, 2004, p. 92).

5.2.2 Klein-Nishina cross-section

The Klein-Nishina forumula gives the total differential scattering cross-section for unpolarized light, taking into account quantum electrodynamics. The differential cross-section is given by (Heitler, 1954)

$$\frac{d\sigma}{d\Omega} = \frac{r_0^2}{2}\frac{\epsilon_1^2}{\epsilon_0^2}\left(\frac{\epsilon_0}{\epsilon_1} + \frac{\epsilon_1}{\epsilon_0} - \sin^2\theta\right), \tag{5.21}$$

where ϵ_0 and ϵ_1 are the energies of the incoming and scattered photons respectively. The total cross-section is then given by (e.g. Rybicki and Lightman, 2004, p. 197)

$$\sigma_{\rm IC} = \sigma_{\rm T}\frac{3}{4}\left[\frac{1+x}{x^3}\left\{\frac{2x(1+x)}{1+2x} - \ln(1+2x)\right\}\frac{1}{2x}\ln(1+2x) - \frac{1-3x}{(1+2x)^2}\right], \tag{5.22}$$

where $x \equiv h\nu/m_{\rm e}c^2$.

The most important consequence of the Klein-Nishina formula is that it shows a reduction in the scattering cross-section at higher energies. Therefore in the Thomson limit, the cross-section will be larger than in the Klein-Nishina regime, which implies a greater probability of scattering and hence a higher scattering rate from softer photons. In the limiting cases of the Thomson limit ($x \ll 1$) and the extreme Klein-Nishina limit ($x \gg 1$), it can be shown that equation (5.22) can be approximated by (e.g. Rybicki and Lightman, 2004, p. 197)

$$\sigma \approx \sigma_{\rm T}\left(1 - 2x + \frac{26x^2}{5} + \cdots\right), \quad x \ll 1,$$

and

$$\sigma = \frac{3}{8}\sigma_{\rm T}x^{-1}\left(\ln 2x + \frac{1}{2}\right) \quad x \gg 1,$$

respectively. Fig. 5.4 plots the size of the scattering cross-section in units of the Thomson scattering cross-section and shows that for $h\nu \gtrsim m_{\rm e}c^2$ the cross-section rapidly decreases. Also shown in the figure are the Thomson and Klein-Nishina limit approximations, which deviate

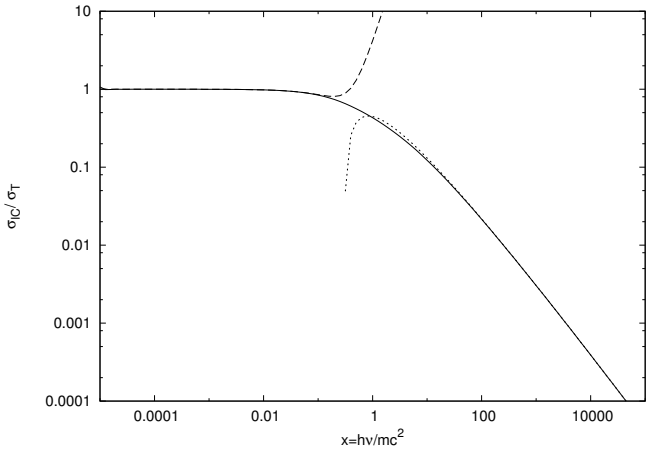

Figure 5.4: The full Klein-Nishina scattering cross-section, $\sigma_{\rm IC}$, plotted as a fraction of the Thomson scattering cross-section, $\sigma_{\rm T}$ (solid line). Also shown are the Thomson (dashed line) and Klein-Nishina limit (dotted line) approximations.

from the correct formula at $x = h\nu/m_{\rm e}c^2 \approx 1$.

5.3 A useful invariant

Before summarizing the derivation of the IC spectrum, it is helpful to consider the useful invariant (e.g. Blumenthal and Gould, 1970)

$$\frac{dn}{\epsilon} = \frac{dn'}{\epsilon'},$$

used in the derivation of the scattering equation. Following from e.g. Rybicki and Lightman (2004, p. 199), the differential photon density per energy level is related to the distribution function, $f(p)$, by

$$n\, d\epsilon = f(p) d^3p, \tag{5.23}$$

where d^3p is the associated momentum volume. The distribution function, $f(p)$ is an invariant quantity since

$$\begin{aligned} f(p) &= \frac{dN}{d\mathcal{V}} \\ &= \frac{dN}{d^3x\, d^3p} \\ &= \frac{dN'}{\frac{1}{\gamma} d^3x'\, \gamma d^3p'} \\ &= \frac{dN'}{d^3x'\, d^3p'} \\ &= f(p'), \end{aligned}$$

where $dN = dN'$ is the invariant differential particle number. It, therefore, follows that

$$\frac{f(p)d^3p}{\epsilon} = \frac{f(p')d^3p'}{\epsilon'},$$

since both energy and momentum transform as $\gamma(1 - \beta\cos\theta)$. Therefore, from the definition in equation (5.23),

$$\frac{n\,d\epsilon}{\epsilon} = \frac{n'\,d\epsilon'}{\epsilon'}$$

or

$$\frac{dn}{\epsilon} = \frac{dn'}{\epsilon'},$$

where $dn = n\,d\epsilon$, is the differential number density per energy.

5.4 Isotropic spectrum

Equations (5.9)-(5.11) model the energy transferred during a single scattering event but in order to predict the observed spectrum from IC scattering it is necessary to calculate the rate at which the scattering occurs. This section will summarize the results for isotropic scattering, averaging over all angles, while the process of anisotropic scattering will be discussed in section 5.5

5.4.1 Isotropic IC spectrum - Thomson limit

The spectrum for IC scattering is obtained by determining the scattering rate per unit energy. This scattering rate is most easily determined in the electron's rest frame and then converted to the observer's rest frame. The total scattering rate (not per energy) in the rest frame K' is simply

$$\frac{dN'}{dt'} = c\int \sigma dn',$$

where c is the speed of the photons, σ is the scattering cross-section and dn' is the number density in K'. In the Thomson limit this reduces to

$$\frac{dN'}{dt'} = c\sigma_{\mathrm{T}}n',$$

where σ_{T} is the Thomson cross-section. The scattering rate in the electron's rest frame, K', can be converted to the observer frame, K, by making use of the Lorentz transformation of time,

$dt = \gamma dt'$ combined with the invariant quantity dn/ϵ (Blumenthal and Gould, 1970),

$$\begin{aligned}\frac{dN}{dt} &= \frac{1}{\gamma}\frac{dN'}{dt'} \\ &= \frac{1}{\gamma}c\int \sigma\epsilon'\frac{dn'}{\epsilon'} \\ &= \frac{1}{\gamma}c\int \sigma\left[\gamma\epsilon(1-\beta\cos\theta_0)\right]\frac{dn}{\epsilon} \\ &= c\int \sigma(1-\beta\cos\theta_0)\,dn.\end{aligned}$$

If an isotropic photon distribution is considered then the average must be taken over the angular term and

$$\langle 1-\beta\cos\theta_0\rangle = 1-\beta\langle\cos\theta_0\rangle = 1,$$

and the scattering rate is $dN/dt = \sigma_{\rm T}cn$ in the Thomson limit.

The IC spectrum can be calculated from the electron scattering rate per unit energy ϵ_1, which is given by (e.g. Blumenthal and Gould, 1970)

$$\frac{dN'_{\gamma,\epsilon}}{dt'\,d\epsilon'\,d\Omega'_1\,d\epsilon'_1} = dn'(\epsilon';\epsilon)\,c\frac{d\sigma}{d\epsilon'_1\,d\Omega'_1}, \tag{5.24}$$

where $dn'(\epsilon';\epsilon)$ is defined to be the photon density in K' within the energy range $d\epsilon$ and $d\sigma/d\epsilon'_1\,d\Omega'_1$ is the differential scattering cross-section. The subscript γ,ϵ indicates that this is the scattering rate per electron energy (expressed in terms of the Lorentz factor, γ) and initial photon energy (ϵ_0), i.e.

$$dN_{\gamma,\epsilon} \equiv \frac{dN}{d\gamma\,d\epsilon_0}.$$

It can be shown that the photon density within the energy range $d\epsilon$ in K' can be written in terms of observer's frame photon density as (Blumenthal and Gould, 1970)

$$dn'(\epsilon';\epsilon) = n_{\rm ph}(\epsilon)\left(\frac{\epsilon'_0}{2\epsilon_0^2\gamma}\right)S\left(\epsilon'_0;\frac{\epsilon_0}{2\gamma},2\gamma\epsilon_0\right)d\epsilon. \tag{5.25}$$

Here a step function S has been introduced to restrict the energy of the photons in K' to the allowable energy range $\epsilon_0/2\gamma < \epsilon'_0 < 2\gamma\epsilon_0$, which is defined by the kinematics of IC scattering (equations 5.13 & 5.14). Therefore, the step function has the form

$$S\left(\epsilon'_0;\frac{\epsilon_0}{2\gamma},2\gamma\epsilon_0\right) = \begin{cases} 1 & \text{for } \frac{\epsilon_0}{2\gamma} < \epsilon'_0 < 2\gamma\epsilon_0 \\ 0 & \text{otherwise.}\end{cases}$$

The scattering rate per energy (ϵ_1) in the observer's frame is then found by transforming the scattering rate in K' to K and by integrating over the initial energy and solid angle in K'. This

is given by

$$\frac{dN_{\gamma,\epsilon}}{dt\, d\epsilon_1} = \int_{\epsilon'} \int_{\Omega'} \frac{dN_{\gamma,\epsilon}}{dt'\, d\epsilon'\, d\Omega'_1\ d\epsilon'_1} \left(\frac{dt'}{dt}\right) \left(\frac{d\epsilon'_1}{d\epsilon_1}\right) d\epsilon'\, d\Omega'_1, \tag{5.26}$$

where $dN_{\gamma,\epsilon}/dt'\, d\epsilon'\, d\Omega'_1\ d\epsilon'_1$ is given by equation (5.24). In the Thomson limit the differential scattering cross-section is given by (equation 5.20)

$$\frac{d\sigma}{d\epsilon'_1\, d\Omega'_1} = \frac{1}{2} r_0^2 \left(1 + \cos^2\Theta'\right) \delta\left(\epsilon'_1 - \epsilon'\right), \tag{5.27}$$

where the Dirac delta function,

$$\delta(x) = \begin{cases} 1 & x = 0 \\ 0 & \text{elsewhere} \end{cases},$$

has been introduced to indicate that only the energy $\epsilon' = \epsilon'_1$ is considered.

By substituting equations (5.24), (5.25) & (5.27) into equation (5.26) and making use of the transformations

$$\left(\frac{dt'}{dt}\right) \left(\frac{d\epsilon'_1}{d\epsilon_1}\right) = \frac{1}{\gamma^2(1 - \cos\theta'_1)},$$

it can readily be shown that the scattering rate per unit electron and photon energy is (e.g. Blumenthal and Gould, 1970)

$$\frac{dN_{\gamma,\epsilon}}{dt\, d\epsilon_1} = \frac{\pi r_0^2 c}{2\gamma^4} \frac{n_{\rm ph}(\epsilon_0)\, d\epsilon}{\epsilon_0^2} \left(2\epsilon_1 \ln \frac{\epsilon_1}{4\gamma^2\epsilon_0} + \epsilon_1 + 4\gamma^2\epsilon_0 - \frac{\epsilon_1^2}{2\gamma^2\epsilon_0}\right), \tag{5.28}$$

after integrating over $d\epsilon' d\Omega'_1$. This gives the number of photons scattered per second per energy level (ϵ_1) for a single electron (with a Lorentz factor γ) off photons with an initial energy ϵ_0, for an isotropic distribution of electrons and photons in the Thomson limit. Of particular importance to this study is the photon distribution $n_{\rm ph}(\epsilon_0)$ which is determined by whether the photon originates from the star or the circumstellar disc in the Be-binary system.

Minimum and maximum photon energy

The minimum and maximum values of ϵ_1 are defined by the kinematics of the inverse Compton scattering discussed in section 5.1.3 (p. 77). The minimum energy transfer corresponds to zero (i.e. no energy is transferred to the photon), while the maximum energy transfer will increase the photon energy by a factor $\sim \gamma^2$. The final scattered photon energy must then lie within the range,

$$\epsilon_0 \lesssim \epsilon_1 \lesssim 4\gamma^2\epsilon_0.$$

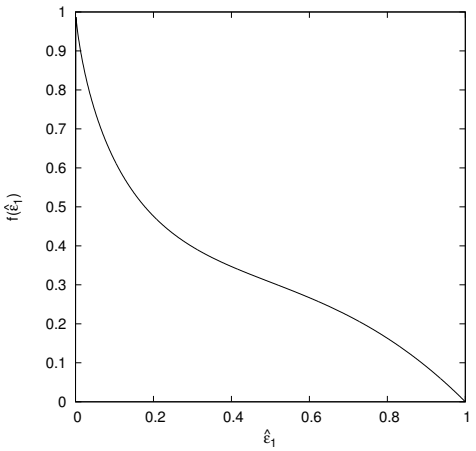

Figure 5.5: Plot of $f(\hat{\epsilon}_1)$ as shown in Blumenthal and Gould (1970).

Spectral shape

Expressing equation (5.28) in terms of the ratio of the final energy to the maximum energy, i.e.

$$\hat{\epsilon}_1 = \frac{\epsilon_1}{4\gamma^2\epsilon},$$

the shape of the isotropic Thomson limit IC spectrum can be shown to be given by (Blumenthal and Gould, 1970)

$$\frac{dN_{\gamma,\epsilon}}{dt\, d\hat{\epsilon}_1} = 8\pi r_0^2 c n_{\rm ph}(\epsilon) f(\hat{\epsilon}_1)\, d\epsilon,$$

where

$$f(\hat{\epsilon}_1) = 2\hat{\epsilon}_1 \ln \hat{\epsilon}_1 + \hat{\epsilon}_1 + 1 - 2\hat{\epsilon}_1^2.$$

Fig. 5.5 displays this function which show that the isotropic Thomson limit IC spectrum is a maximum at $\hat{\epsilon}_1 = 0$ and produces a broad decaying spectrum.

5.4.2 Isotropic IC spectrum - Klein-Nishina spectrum

In order to model TeV energy gamma-ray binaries it is necessary to calculate the IC scattering rate using the full Klein-Nishina differential scattering cross-section (equation 5.21):

$$\frac{d\sigma_{\rm exact}}{d\Omega_1'\, d\epsilon_1'} = \frac{1}{2} r_0^2 \left(\frac{\epsilon_1'}{\epsilon_0'}\right)^2 \left(\frac{\epsilon_0'}{\epsilon_1'} + \frac{\epsilon_1'}{\epsilon_0'} - \sin^2\Theta'\right) \delta\left(\epsilon_1' - \frac{\epsilon_0'}{1 + (\epsilon_0'/m_{\rm e}c^2)(1-\cos\Theta')}\right),$$

where the Dirac delta function has been introduced to limit the photon energies to only those that are allowed by IC scattering (equation 5.11). By expressing the energy of the scattered photon in units of the electron rest mass energy, i.e. $E_1 = \epsilon_1/\gamma m_e c^2$, the scattering rate per unit energy, for a single electron interacting with an isotropic photon density distribution $n_{\rm ph}(\epsilon)$ (i.e.

number density of photons per unit energy), is expressed as (Jones, 1968)

$$\frac{dN_{\gamma,\epsilon}}{dt\,dE_1} = \frac{2\pi r_0^2 mc^3}{\gamma}\frac{n_{\rm ph}(\epsilon_0)\,d\epsilon}{\epsilon_0}\left[2q\ln q + (1+2q)(1-q) + \frac{1}{2}\frac{(\Gamma_\epsilon q)^2}{1+\Gamma_\epsilon q}(1-q)\right], \tag{5.29}$$

where

$$\Gamma_\epsilon = \frac{4\epsilon_0\gamma}{m_{\rm e}c^2}$$

and

$$q = \frac{E_1}{\Gamma_\epsilon(1-E_1)},$$

following the presentation given in Blumenthal and Gould (1970). This is the exact expression for the scattering rate provided that $\gamma \gg 1$.

The limit between IC scattering in the Thomson and Klein-Nishina regime is determined by the parameter, Γ_ϵ. The Thomson limit applies when $\epsilon_0' \ll m_{\rm e}c^2$, and therefore, by using the transformation of energy, $\epsilon_0' = \epsilon_0\gamma(1-\beta\cos\theta_0)$ which has a maximum value of $\approx 2\epsilon_0\gamma$, it is clear the Thomson limit holds for $2\gamma\epsilon_0/m_{\rm e}c^2 \ll 1$. Similarly, if the simplifying ratio $\Gamma_\epsilon \ll 1$ the scattering formula (equation 5.29) reduces to Thomson approximation.

Minimum and maximum photon energy

The limits on E_1 are determined by the limits on ϵ_1. The minimum value will occur if there is no energy transfer, while the maximum allowed energy is given by equation (5.17), and the limits on ϵ_1 are therefore

$$\epsilon_0 \le \epsilon_1 \le \frac{4\gamma^2\epsilon_0}{1+(4\gamma\epsilon_0/m_{\rm e}c^2)},$$

or if written in terms of E_1,

$$\frac{\epsilon_0}{\gamma m_{\rm e}c^2} \le E_1 \le \frac{\Gamma_\epsilon}{1+\Gamma_\epsilon}.$$

Spectral shape

Following Blumenthal and Gould (1970) the shape of the IC spectrum can be illustrated by plotting the normalized function

$$F(\hat{E}_1,\Gamma_\epsilon) = A^{-1}f(\hat{E}_1,\Gamma_\epsilon),$$

where

$$A = \int_0^1 f(\hat{E}_1,\Gamma_\epsilon)\,d\hat{E}_1,$$

$\hat{E}_1$ is defined by

$$E_1 = \frac{\Gamma_\epsilon}{1+\Gamma_\epsilon}\hat{E}_1,$$

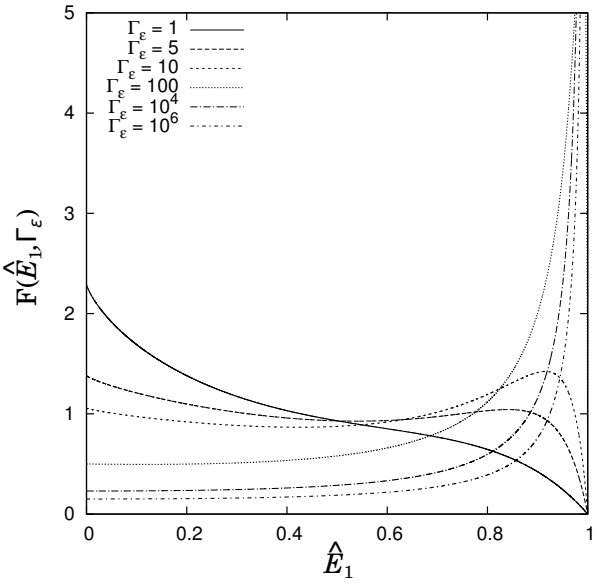

Figure 5.6: Shape of the normalized isotropic IC scattering distribution function (adapted from Blumenthal and Gould, 1970).

and the function $f(\hat{E}_1, \Gamma_\epsilon)$ is determined by the term within the square brackets in equation (5.29). A plot of $F(\hat{E}_1, \Gamma_\epsilon)$ (Fig. 5.6) shows that for a low value of Γ_ϵ, the shape of the function approaches that of the Thomson limit function (Fig. 5.5). At higher values of Γ_ϵ this approximation does not apply and the distribution of the scattered photons peaks at high energies. This peak occurs since at very large values of Γ_ϵ, the relativistic electron transfers all of its energy to the scattered photon, i.e. $\epsilon_1 \rightarrow \gamma m_e c^2$. Therefore, in the Klein-Nishina regime, the vast majority of scattered photons have an energy near the maximum allowed energy, resulting in a peak in the distribution function (Fig. 5.6).

5.4.3 Total scattering rate

Equation (5.29) gives the distribution of the scattering rate for a single electron scattering off a photon distribution within the energy range $d\epsilon$. If we are to extend this to gamma-ray production in binary systems it is necessary to consider the scattering from a distribution of electrons and photons. To extend the calculation to multiple electron scatterings, an electron distribution function needs to be introduced. This distribution is normally expressed as a power-law function e.g.

$$n_e(\gamma) = \begin{cases} K_e \gamma^{-p} & \gamma_{\min} < \gamma < \gamma_{\max}, \\ 0 & \text{elsewhere} \end{cases} , \tag{5.30}$$

where the distribution is confined to the energy region $\gamma_{\min}$ to $\gamma_{\max}$. The total scattering rate per unit energy for an electron distribution is then found by integrating over the initial electron

and photon energies, i.e.

$$\frac{dN_{\rm total}}{dtd\epsilon_1} = \int_{\epsilon_0}\int_{\gamma} n_{\rm e}(\gamma) \times \left(\frac{1}{\gamma m_{\rm e}c^2}\frac{dN_{\gamma,\epsilon}}{dt\,dE_1}\right) d\gamma\, d\epsilon, \tag{5.31}$$

where

$$\frac{1}{\gamma m_{\rm e}c^2}\frac{dN_{\gamma,\epsilon}}{dt\,dE_1} = \frac{dN_{\gamma,\epsilon}}{dt\,d\epsilon_1}.$$

This equation is applicable to an isotropic distribution of electrons and photons.

In equation (5.29), $n_{\rm ph}(\epsilon)\,d\epsilon$ is the differential photon number density and in the case of a blackbody distribution of photons is given by (e.g. Blumenthal and Gould, 1970)

$$n_{\rm ph}(\epsilon) = \frac{1}{\pi^2(\hbar c)^3}\frac{\epsilon^2}{{\rm e}^{\epsilon/kT}-1}.$$

For IC scattering in PSR B1259-63/LS 2883 the photon distribution cannot be considered as a simple blackbody distribution as the disc modifies the stellar spectrum via free-free and free-bound emission. The photon spectrum must, therefore, be calculated from the COG method discussed in Chapter 6.

5.5 Anisotropic inverse Compton scattering

Section 5.4 above is applicable to scattering between an isotropic distribution of electrons and photons. In gamma-ray binaries, however, the effects of anisotropic scattering may be very important to model the gamma-ray spectrum.

If we consider the energy transfer in the Thomson limit then $\epsilon_1' \approx \epsilon_0'$ and from equations (5.9) & (5.10) it can be shown that the energy of a scattered photon in the observer's frame is

$$\begin{aligned}\epsilon_1 &= \epsilon_0\gamma^2\left(1-\beta\cos\theta\right)\left(1+\beta\cos\theta_1'\right)\\ &= 2\epsilon_0\gamma^2\left(1-\cos\theta\right),\end{aligned}$$

assuming $\beta \to 1$ and that the photon is scattered in the direction of the electron's motion (i.e. $\theta_1' \to 0$). This shows that the final energy which is observed depends on the angle between the direction of the electron and the incoming photon.

Consider Fig. 5.7 which shows IC scattering in a circular binary system, with the observer located to the right of the sketch. Because of the high energy of the electrons, photons are up-scattered in the direction of the electrons' original momentum. Therefore, the observed gamma-rays are up-scattered by electrons that were originally moving towards the observer. Near point P_1, any observed photons deviated from their original trajectory far more than photons observed from position P_2. This means that photons observed from point P_1 will have a higher energy than photons observed from P_2, and this will result in an observed modulation of the gamma-ray emission. In contrast, an isotropic approximation of the gamma-ray emission would predict

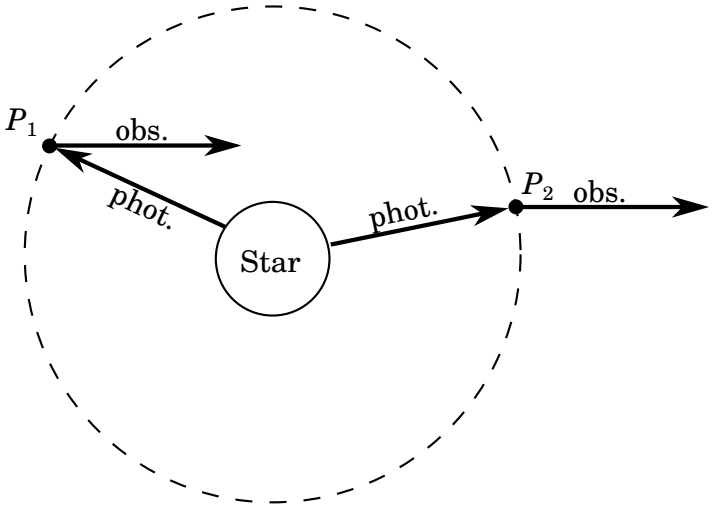

Figure 5.7: Sketch of IC scattering in a circular binary system. The observer, to the right of the figure, will observe higher energy photons from scattering at P_1 than at P_2 due to the anisotropic effects.

no variation in the gamma-ray spectrum, as it is calculated by averaging over all angles. It is therefore necessary to derive an anisotropic spectrum that will take into account the direction of scattering.

Anisotropic scattering has been considered in detail by Fargion et al. (1997) and has been adapted to the case of LS 5039 by Dubus et al. (2008) who showed that the combination of anisotropic scattering and gamma-ray absorption can explain certain features of the H.E.S.S. light curve, e.g. the model predicts the peak seen at around orbital phase 0.85 (Fig. 5.8).

The magnitude of the anisotropic effect is also dependent on the observed inclination[ii] of the binary system. For a systems with a high inclination, the change in the scattering angle is larger relative to the observer. Consider again the sketch in Fig. 5.7. For the the observer to the right of the figure, there is a large change in scattering angle (i.e. the angle between the original direction of the photon and the direction of the observer) between P_1 and P_2. However, if the system is observed face-on, the scattering angle would be $\sim 90\ ^\circ$ at positions P_1 and P_2 and there would be no anisotropic effects. Therefore, systems with a larger inclination exhibit larger anisotropic effects. The inclination of LS 5039 ($i \approx 60^\circ$ if the compact companion is a neutron star, Dubus et al., 2008) is higher than the value for PSR B1259-63, ($i \approx 33^\circ$, Negueruela et al., 2011) and the effects of anisotropic scattering from the star alone will be less for PSR B1259-63 in comparison to LS 5039. However, the presence of a large circumstellar disc around LS 2883, which can be rotated relative to the orbital plane, introduces anisotropic effects which may be extremely important.[iii]

[ii]The inclination of a binary system is defined to be the viewing angle of the binary system, measured relative to the normal to the binary plane. Therefore, a system with an inclination $i = 0^\circ$ is observed face-on, while a system with an inclination $i = 90^\circ$ is observed edge-on.

[iii]The higher eccentricity of PSR B1259-63 ($e \approx 0.87$) in comparison to LS 5039 ($e \approx 0.24$), also introduces

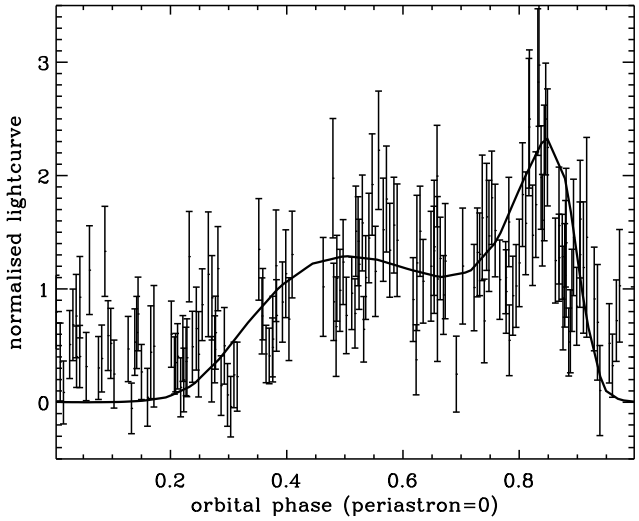

Figure 5.8: Normalized H.E.S.S. light curve of LS 5039 with the predicted flux using the combined effects of anisotropic IC scattering and gamma-ray absorption (adapted from Dubus et al., 2008).

Below we summarize the results for anisotropic inverse Compton (AIC) scattering, following the discussion in Fargion et al. (1997) and its application to LS 5039 discussed by Dubus et al. (2008). We present the full scattering formula correct over all allowed energies.

5.5.1 The AIC kernel

Following the convention in Dubus et al. (2008) this study will refer to the function which must be integrated over electron and photon energies to produce the total AIC spectrum as the kernel of the AIC code. The kernel contains the basic scattering rate per electron and is similar to equation (5.29) in the isotropic approximation, with the exception that equation (5.29) already contains a term for the photon density, $n_{\rm ph}(\epsilon)$, which is not included in the anisotropic kernel.

The scattering rate for a single electron is more easily calculated in the electron rest frame, which can then be converted to the observer's frame by

$$\frac{dN_{\gamma,\epsilon}}{dt\, d\epsilon_1\, d\Omega_1} = \frac{dN'_{\gamma,\epsilon}}{dt'\, d\epsilon'_1\, d\Omega'_1} \frac{dt'}{dt} \frac{d\epsilon'_1}{d\epsilon_1} \frac{d\Omega'_1}{d\Omega_1} \tag{5.32}$$

where

$$\frac{dN'_{\gamma,\epsilon}}{dt'\, d\epsilon'_1\, d\Omega'_1} = \iint c \frac{dn'}{d\epsilon'\, d\Omega'} \frac{d\sigma}{d\epsilon'_1\, d\Omega'_1}\, d\Omega' d\epsilon', \tag{5.33}$$

is the scattering rate in the rest frame of the electron. Here $d\sigma/d\epsilon'_1\, d\Omega'_1$ is the electron's differential scattering cross-section as discussed above and $dn'/d\epsilon'\, d\Omega'$ is the photon distribution in the electron rest frame. Following Fargion et al. (1997) and Dubus et al. (2008), the photon distri-

greater changes in the photon density during the orbital period, which results in a greater modulation in the gamma-ray emission. This is, however, independent of the anisotropic effect.

bution can be considered to be mono-energetic and mono-directional, which will provide an AIC kernel that calculates the scattering rate for only one photon energy and direction. Integrating the kernel over the appropriate initial photon energies and angles will then provided the final AIC spectrum.

If the photon distribution in the observer's frame is mono-energetic and mono-directional then

$$\frac{dn}{d\epsilon\, d\Omega} = \delta(\epsilon - \epsilon_0)\delta(\cos\theta - \cos\theta_0)\delta(\phi - \phi_0),$$

and this can be converted into the electron's rest frame by

$$\frac{dn'}{d\epsilon'\, d\Omega'} = \frac{dn}{d\epsilon\, d\Omega}\frac{d\Omega}{d\Omega'},$$

making use of the invariance of $dn/d\epsilon = dn'/d\epsilon'$ (Blumenthal and Gould, 1970). The photon distribution can be converted to K' by making use of the Doppler shift formulae, and it can be shown that the photon distribution in K' is related to the distribution in K by (see Appendix A.3),

$$\frac{dn'}{d\epsilon'\, d\Omega'} = \gamma(1 - \beta\cos\theta_0)\delta\left(\epsilon' - \epsilon_0\gamma[1 - \beta\cos\theta_0]\right)\delta\left(\cos\theta' - \frac{\cos\theta_0 - \beta}{1 - \beta\cos\theta_0}\right)\delta(\phi' - \phi'_0). \quad (5.34)$$

The scattering kernel is then obtained by integrating equation (5.32) over Ω_1, the solid angle into which the photons scatter. By combining equations (5.32) and (5.33) the final scattering kernel is

$$\frac{dN_{\gamma,\epsilon}}{dt\, d\epsilon_1} = \int_{\Omega'_1}\int_{\Omega'}\int_{\epsilon'} c\left(\frac{dn'}{d\epsilon'\, d\Omega'}\right)\left(\frac{d\sigma}{d\epsilon'_1\, d\Omega'_1}\right)\frac{dt'}{dt}\frac{d\Omega'_1}{d\Omega_1}\frac{\epsilon'_1}{\epsilon_1}\, d\epsilon'\, d\Omega'\, d\Omega'_1. \quad (5.35)$$

This gives the scattering rate per electron with Lorentz factor γ, scattering off photons with energy ϵ_0 for a specific angle of deviation. The final kernel is found by substituting in the photon distribution (equation 5.34) and the differential cross-section, and performing the integration. The result is shown below using the Thomson and the full Klein-Nishina cross-section.

The AIC kernel in the Thomson limit

In the Thomson limit, the differential cross-section is given by equation (5.27) and by making use of

$$\frac{dt'}{dt}\frac{d\Omega'_1}{d\Omega_1}\frac{\epsilon'_1}{\epsilon_1} = \frac{1}{\gamma^2(1 - \beta\cos\theta_1)},$$

the scattering kernel (equation 5.35) can be integrated. As shown in Cerutti (2010), in order to perform the integration, the Dirac delta property

$$\delta(f(x)) = \sum_i \frac{1}{|\frac{df}{dx}|_{x=x_i}}\delta(x - x_i),$$

such that $\forall i, f(x_i) = 0$, is introduced. The final solution for the anisotropic kernel in the Thomson limit is (Fargion et al., 1997)

$$\frac{dN_{\gamma,\epsilon}}{dt\, d\epsilon_1} = \frac{\pi r_e^2 c}{2\beta\gamma^2\epsilon_0}\left[3 - C_{\theta_0}^2 + \left(3C_{\theta_0}^2 - 1\right)\frac{1}{\beta^2}\left(\frac{\epsilon_1}{\gamma^2\epsilon_0(1-\beta\cos\theta_0)} - 1\right)^2\right], \tag{5.36}$$

where

$$C_{\theta_0} = \frac{\cos\theta_0 - \beta}{1 - \beta\cos\theta_0}.$$

From the transformation of photon energy from K to K' (equations 5.9 & 5.10) it can be shown that the energy of a scattered photon in the observer's frame is

$$\epsilon_1 = \epsilon_0\gamma^2\left(1 - \beta\cos\theta_0\right)\left(1 + \beta\cos\theta_1'\right) = \epsilon_0\left(1 - \beta\cos\theta_0\right)\frac{1 + \beta\cos\theta_1'}{1 - \beta^2},$$

in the Thomson limit ($\epsilon_1' \approx \epsilon_0'$) and therefore the minimum and maximum allowed values for ϵ_1 are (Fargion et al., 1997)

$$\epsilon_{1,\min} = \epsilon_0\frac{1 - \beta\cos\theta_0}{1 + \beta} \quad (\theta_1' = \pi),$$

and

$$\epsilon_{1,\max} = \epsilon_0\frac{1 - \beta\cos\theta_0}{1 - \beta} \quad (\theta_1' = 0).$$

These limits also apply to the isotropic scattering as discussed in section 5.4, but are written in a different form. Examples of the resulting shape of the spectrum (equation 5.36) are shown in Fig. 5.9, combining some examples shown in Fargion et al. (1997). As shown in Cerutti (2010), equation (5.36) reduces to the Jones (1968) isotropic formula when averaged over the solid angle.

The Klein-Nishina AIC kernel

Dubus et al. (2008) extended the Thomson limit approximation above to higher energies by calculating the integration in equation (5.35) using the full Klein–Nishina cross-section. The imposed condition is $\gamma \gg 1$ and therefore it is possible to simplify the scattering angle Θ' as shown below. Writing the scattering angle (in K') in terms of the angles in the observer's frame (K) gives

$$\begin{aligned}\cos\Theta' &= \cos\theta_1'\cos\theta_0' + \sin\theta_0'\sin\theta_1'\cos\left(\phi_0' - \phi_1'\right)\\ &= \frac{\cos\theta_1 - \beta}{1 - \beta\cos\theta_1}\frac{\cos\theta_0 - \beta}{1 - \beta\cos\theta_0} + \frac{\sin\theta_0}{\gamma(1 - \beta\cos\theta_0)}\frac{\sin\theta_1}{\gamma(1 - \beta\cos\theta_1)}\cos(\phi_0 - \phi_1),\end{aligned}$$

and if $\gamma \gg 1$, the second term in the equation scales as $1/\gamma^2 \to 0$, and therefore

$$\cos\Theta' \approx \cos\theta_1'\cos\theta_0'.$$

This approximation effectively means that all scattered photons move along the direction of the

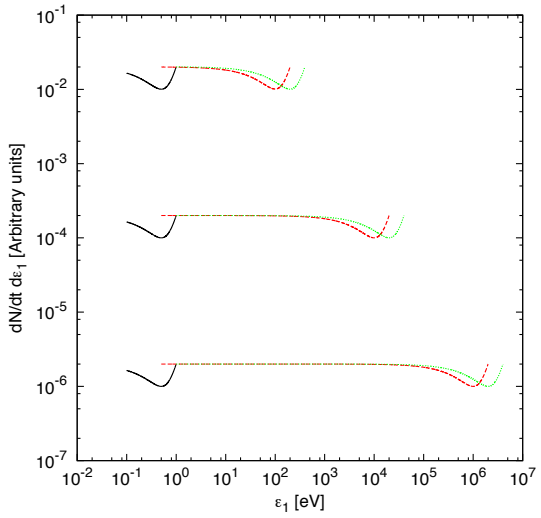

Figure 5.9: Examples of the spectrum from the AIC kernel in the Thomson limit (equation 5.36). The spectrum is plotted for $\theta_0 = 0$ (solid lines), $\theta_0 = \pi/2$ (dashed lines) and $\theta_0 = \pi$ (dotted lines), for $\gamma = 10$ (black), $\gamma = 100$ (red) & $\gamma = 1000$ (green) from top to bottom (adapted from Fargion et al., 1997).

electrons' initial momentum (relativistic beaming). The final solution for the Klein-Nishian, AIC kernel is given by

$$\frac{dN_{\gamma,\epsilon_0}}{dt\, d\epsilon_1} = K_0 \frac{\pi r_e^2 c(1-\beta\cos\theta_0)}{\gamma(1-\beta x_0)}\left[1+\mu_0^2+\left(\frac{\gamma\epsilon_1}{m_e c^2}\right)^2 \frac{(1-\beta x_0)^2(1-\mu_0)^2}{1-\frac{\gamma\epsilon_1}{m_e c^2}(1-\beta x_0)(1-\mu_0)}\right], \tag{5.37}$$

where

$$\mu_0 = \left(\frac{x_0-\beta}{1-\beta x_0}\right) C_{\theta_0},$$

$$x_0 = \frac{1-\frac{\epsilon_0}{\epsilon_1}(1-\beta\cos\theta_0)+\frac{\gamma\epsilon_0}{m_e c^2}(1-\beta\cos\theta_0)(1+\beta C_{\theta_0})}{\beta+\frac{\gamma\epsilon_0}{m_e c^2}(1-\beta\cos\theta_0)(\beta+C_{\theta_0})},$$

and

$$K_0 = \frac{\left(1-\frac{\gamma\epsilon_1}{m_e c^2}\left[1+\beta C_{\theta_0}-(\beta+C_{\theta_0})\, x_0\right]\right)^2}{\left|\beta\gamma\epsilon_1+\frac{\epsilon_1^2}{m_e c^2}C_{\theta_0}\right|}.$$

The energy limits on equation (5.37) are

$$\epsilon_{1,\min} = \frac{(1-\beta\mu_0)\epsilon_0}{1+\frac{\epsilon_0}{\gamma m_e c^2}+\left[\beta^2+2\beta\mu_0\left(\frac{\epsilon_0}{\gamma m_e c^2}\right)+\left(\frac{\epsilon_0}{\gamma m_e c^2}\right)^2\right]},$$

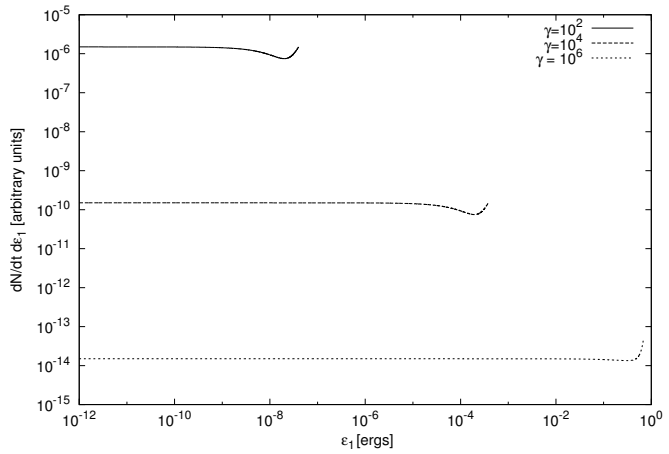

Figure 5.10: Spectrum from the full AIC kernel (equation 5.37), plotted for $\cos\theta_0 = -1$ and $\epsilon_0 = 10^{-12}$ erg (following Cerutti, 2010).

and

$$\epsilon_{1,\max} = \frac{(1-\beta\mu_0)\epsilon_0}{1+\frac{\epsilon_0}{\gamma m_e c^2} - \left[\beta^2 + 2\beta\mu_0\left(\frac{\epsilon_0}{\gamma m_e c^2}\right) + \left(\frac{\epsilon_0}{\gamma m_e c^2}\right)^2\right]}.$$

Equation (5.37) (Fig. 5.10) can now be used as the kernel to calculate the AIC spectrum from a gamma-ray binary system.

5.5.2 The AIC spectrum

The AIC kernels derived in section 5.5.1 can now be used to model the gamma-ray emission from a gamma-ray binary system. The derived kernels determine the scattering rate of an electron with a specific Lorentz factor, γ, off a photon with energy ϵ_0, at a specific angle θ_0. In the shock fronts around PWNe there is a distribution of electron and photon energies, and scattering can occur over a range of angles defined by the size of the photon source and the direction of the observer. The total scattering rate is then determined by

$$\frac{dN_{\rm tot}}{dt\,d\epsilon_1} = \int_{\epsilon_0}\int_{\Omega}\int_{\gamma} n_{\rm e}(\gamma) n_{\rm ph}(\epsilon_0) \frac{dN_{\gamma,\epsilon}}{dt\,d\epsilon_1}\, d\gamma\, d\epsilon_0\, d\Omega, \tag{5.38}$$

where $dN_{\gamma,\epsilon_0}/dt\,d\epsilon_1$ is given by equation (5.37), $n_{\rm e}(\gamma)$ is the electron distribution, assumed to be a power law given by equation (5.30), and $n_{\rm ph}(\epsilon_0)$ is the photon distribution.

The integration with respect to Ω must be carried out over the solid angle subtended by the photon source. For the case of a star the coordinate system can be orientated such that there is

a symmetry around the azimuthal angle, and the integral becomes

$$\begin{aligned}\int d\Omega &= \int_0^{2\pi}\int_0^{\alpha} \sin\theta \, d\theta d\phi \\ &= 2\pi \int_0^{\alpha} \sin\theta \, d\theta,\end{aligned}$$

where α is the maximum polar angle of the star define by (Dubus et al., 2008)

$$\sin\alpha = \frac{R_*}{d}.$$

The integration in equation (5.38) is performed numerically, and by calculating the value of α at different points in the orbit it is possible to model the varying AIC gamma-ray spectrum.

The integration over the circumstellar disc is not as simple and a different coordinate system must be chosen to calculate the solid angle the disc subtends with respect to the electron cloud. The details of this coordinate system and its application to AIC in PSR B1259-63 are discussed in Chapter 7.

5.6 Gamma-ray absorption

Gamma-ray absorption may have an important effect on the observed gamma-ray emission and this section will briefly summarize this process. If IC gamma-ray production occurs in a region with a high photon density, soft photons are up-scattered to gamma-ray energies, and the new gamma-rays can then interact with the photon field to produce an electron-positron pair through photon-photon interaction. This has the effect of decreasing the observed gamma-ray emission and produces a gamma-ray absorption mechanism.

It can be shown that the collision of two photons of energy ϵ_γ and ϵ_*[iv] moving in directions $\hat{\mathbf{e}}_\gamma$ and $\hat{\mathbf{e}}_*$ respectively can results in pair production if (Gould and Schréder, 1967)

$$\epsilon_\gamma \epsilon_* \geq \frac{2m_e^2c^4}{1-\hat{\mathbf{e}}_\gamma \cdot \hat{\mathbf{e}}_*}. \tag{5.39}$$

The effective total cross-section for this interaction is given by (Coppi and Blandford, 1990)

$$\sigma_{\gamma\gamma} = \frac{3}{16}\sigma_{\mathrm{T}}(1-\beta'^2)\left[(3-\beta'^4)\ln\left(\frac{1+\beta'}{1-\beta'}\right) - 2\beta'(2-\beta'^2)\right], \tag{5.40}$$

where β' is the speed (in units of c, i.e. $\beta' = v/c$) in the centre-of mass reference frame of the

[iv] Since this study considers IC gamma-ray production in gamma-ray binaries, photon-photon absorption will occur between a gamma-ray and a stellar photon. The symbols for the photons have been chosen to reflect this.

electron/positron pair. Defining the variable (Gould and Schréder, 1967)

$$s \equiv \frac{\epsilon_\gamma \epsilon_*}{2m_e^2 c^4} \left(1 - \hat{\mathbf{e}}_\gamma \cdot \hat{\mathbf{e}}_*\right),$$

and using equation (5.39) shows that the photon-photon pair production can only occur if $s > 1$. Furthermore it can it can be shown that

$$\beta' = \left(1 - \frac{1}{s}\right)^{1/2},$$

and therefore the total cross-section is dependent only on s.

Dubus (2006b) discussed the effects of gamma-ray absorption in high mass binary systems consisting of a compact object and a bright non-degenerate star. Here, a gamma-ray with energy ϵ_γ emitted from the compact object must pass through the dense photon field emitted from the non-degenerate star, and can interact with a photon from the star with energy ϵ_*. The directions of the gamma-ray and stellar photons are $\hat{\mathbf{e}}_\gamma$ and $\hat{\mathbf{e}}_*$ respectively. The differential absorption opacity for a gamma-ray of energy ϵ_γ is (Gould and Schréder, 1967)

$$d\tau_{\gamma\gamma} = (1 - \hat{\mathbf{e}}_\gamma \cdot \hat{\mathbf{e}}_*)\, n_{\rm ph} \sigma_{\gamma\gamma}\, d\epsilon\, d\Omega\, dl,$$

where $n_{\rm ph}$ is the photon number density, and the integration is over all stellar photon energies, $d\epsilon$, emitted from a surface within a solid angle $d\Omega$, along the length that the gamma-ray travels, dl. This is shown in Fig. 5.11 where a gamma-ray travels a distance l from point I to point P where it interacts with a stellar photon. From the chosen orientation of the system, the angle between the two photons is defined in terms of

$$1 - \hat{\mathbf{e}}_\gamma \cdot \hat{\mathbf{e}}_* = 1 + \cos\Psi \cos\theta + \sin\Psi \cos\phi \sin\theta,$$

where θ and Ψ are shown in the figure and ϕ is the azimuthal angle in the $x - y$ plane.

Figure 5.12 shows the results of the numerical calculations of the optical depth around a $T = 40\,000$ K, $R = 10$ R$_\odot$ star, parameters which are consistent with LS 5039 (Dubus, 2006b). The observed gamma-ray scattering rate is predicted to decrease by the amount $\exp(-\tau_{\gamma\gamma})$ across the orbit.

The process of pair production can result in the additional effect of pair cascade. A gamma-ray photon emitted from the compact object can produce an electron/positron pair, and if the electron and positron have sufficient energy, they can also up-scattered stellar photons to gamma-ray energies. This process can then repeat with photon-photon interaction resulting in pair-production, the created electron and positron resulting in gamma-ray production, and the new gamma-rays producing more electron/positron pairs. This is known as pair cascade and can result in the decrease of the gamma-ray absorption.

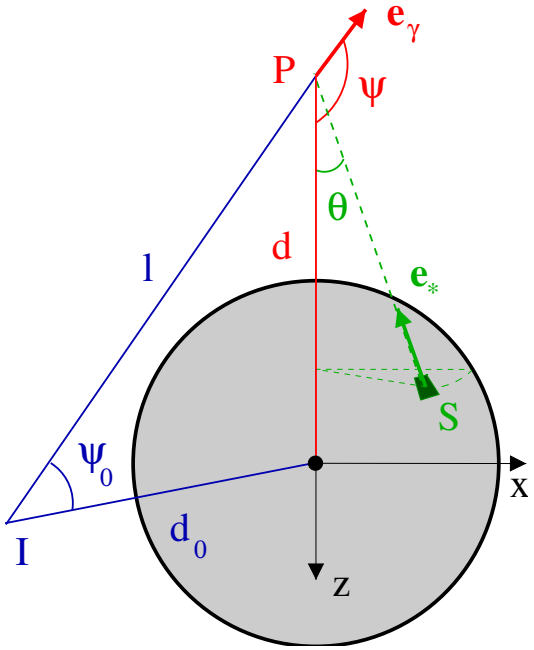

Figure 5.11: Diagram showing the interaction between a gamma-ray photon travelling in direction $\hat{\mathbf{e}}_\gamma$ and a stellar photon moving in direction $\hat{\mathbf{e}}_*$; the details are discussed in the text (Dubus, 2006b).

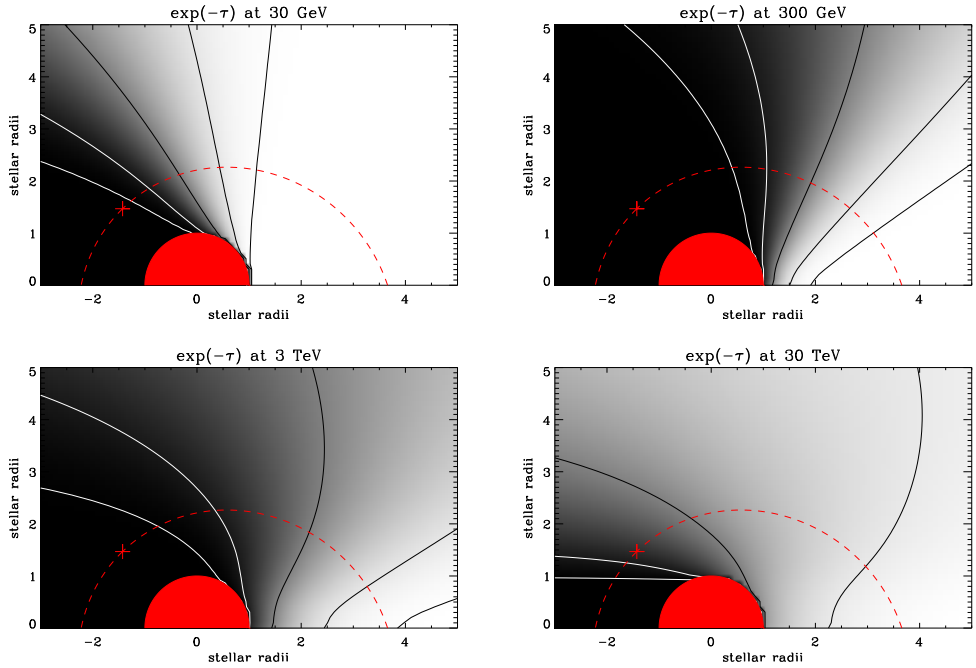

Figure 5.12: Gamma-ray absorption in a massive star with a temperature of 40 000K and a radius of 10 $R_\odot$, for four different gamma-ray energies with the observer located to the right of the star in the plane of the figure. The grey-scale indicates the gamma-ray absorption, $\exp(-\tau)$, and the darker the region the more absorption occurs. The contour lines show the position of 1%, 10%, 50%, 90% and 99% absorption. The dotted line represents the orbital path of LS 5039 (Dubus, 2006b).

Chapter 6

The curve of growth method

The spectra of Be stars show a distinct low frequency and infrared (IR) excess above the black-body component usually associated with a B-type star (e.g. Fig. 6.6). The excess is believed to be the result of thermal free-free and free-bound emission in the circumstellar disc. This excess radiation in the IR may be instrumental in the process of gamma-ray production via inverse Compton (IC) scattering which may result in these systems being strong gamma-ray emitters under certain conditions. In order to determine the IR excess associated with Be stars, the observed flux measurements are used to model the complete spectrum using the so called Curve of Growth (COG) method initially proposed by Waters (1986). This method is based on earlier work to model the IR emission from early type stars with enhanced spherical outflow by Lamers and Waters (1984); Panagia and Felli (1975) Wright and Barlow (1975). While this is an empirical model, and more advanced models for the outflow around Be stars have been proposed (see e.g. Okazaki et al., 2011, for an application to PSR B1259-63), the COG method provides a fit to the optical and IR flux from the Be star and circumstellar disc and serves as a good approximation for the IR excess from LS 2883.

The first part of this chapter focuses on the COG method presented by Waters (1986) and discusses certain aspects of this model, the second part derives a modification of this model to allow for a calculation of the IR flux from an arbitrarily orientated disc and the last section discusses how the COG method was used to constrain the IR excess from PSR B1259-63 using archive data and mid-IR observations that were obtained with VISIR/VLT[i] during January 2011.

6.1 Basic equations

An ionized plasma, such as is found in the circumstellar disc, consists of free electrons moving in a medium of charged ions and neutral atoms. When an electron moves near an ion, it is either accelerated around the ion (remains free) or is captured by (or bound) to the ion, resulting in the

[i]The VLT and VISIR are discussed in Chapter 2, section 2.8.4.

emission of a photon. These radiation processes are known as free-free emission (Bremsstrahlung) or free-bound (recombination) emission, respectively. The circumstellar disc around a B star is treated as an isothermal region in the Waters (1986) model, and it emits via thermal free-free and free-bound radiation. See e.g. Rybicki and Lightman (2004, pp. 155–166), Lang (1974, pp.42–52) and Irwin (2007, pp. 237–242) for a further discussion on free-free and free-bound emission and absorption.

The specific intensity originating from an emitting plasma is determined by the optical depth, τ_ν, through the material and the source function S_ν of the material which is defined as the ratio between the emission, j_ν and absorption, α_ν, coefficients (Rybicki and Lightman, 2004, p. 13),

$$S_\nu \equiv \frac{j_\nu}{\alpha_\nu}.$$

The general solution for the specific intensity observed from a source through an emitting region is (e.g. Rybicki and Lightman, 2004, pp. 12–15)

$$I_\nu(\tau_\nu) = I_\nu(0)\mathrm{e}^{-\tau_\nu} + \int_0^{\tau_\nu} \mathrm{e}^{-(\tau_\nu - \tau'_\nu)} S_\nu(\tau'_\nu)\, d\tau'_\nu, \tag{6.1}$$

$$= I_\nu(0)\mathrm{e}^{-\tau_\nu} + S_\nu(1 - \mathrm{e}^{-\tau_\nu}), \tag{6.2}$$

where it is assumed that the source function, S_ν, remains constant at all optical depths, that is

$$S_\nu(\tau) = \text{constant}.$$

The first term on the right hand sides of the equations 6.1 & 6.2 is the contribution to the specific intensity from the background source corrected for the extinction due to absorption. The second term is the internal emission and absorption of the emitting region. This situation is illustrated in Fig. 6.1 where the observed specific intensity is a combination of the specific intensity $I_\nu(0)$ originating from some object at $\tau_\nu = 0$ and the additional absorption and emission which occurs in the intermediate material. For the case of an emitting plasma with no background source, $I_\nu(0) = 0$ and the equation (6.2) reduces to

$$I_\nu = S_\nu(1 - \mathrm{e}^{-\tau_\nu}).$$

The contribution to the specific intensity from the plasma depends on the optical depth through the medium and (e.g. Irwin, 2007, p. 194)

$$I_\nu = \begin{cases} S_\nu & \tau_\nu \gg 1 \\ S_\nu \tau_\nu = j_\nu l & \tau_\nu \ll 1, \end{cases} \tag{6.3}$$

where l is the length of the line-of-sight through the plasma, and where the approximation $\mathrm{e}^{-\tau_\nu} \approx 1 - \tau_\nu$ has been made. For large optical depths the specific intensity approaches that of

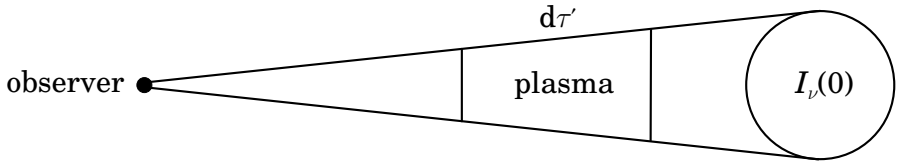

Figure 6.1: The observed specific intensity is the combination of the specific intensity originating from a plasma at $\tau = 0$ and additional absorption and emission from the intermediate material.

the source function, while for small optical depths, it is dependent only on the emission from the plasma.

For the emission from the circumstellar disc around Be stars, the source function and optical depth is determined by the properties of the material and free-free and free-bound emission. The simplifying assumption is made that the circumstellar disc is in a state of local thermodynamic equilibrium (LTE) and, therefore, the source function is given by Planck's function, i.e. $S_\nu = B_\nu$, where (e.g. Rybicki and Lightman, 2004, p. 22)

$$B_\nu(T) = \frac{2h\nu^3/c^2}{\mathrm{e}^{h\nu/kT} - 1}.$$

For the thermal free-free and free-bound emission from the circumstellar disc the specific intensity given by equation (6.1) reduces to (e.g. Wright and Barlow, 1975)

$$I_\nu(q) = \int B_\nu(T)\, \mathrm{e}^{-\tau_\nu}\, d\tau, \tag{6.4}$$

where the optical depth is determined by the free-free and free-bound absorption in the circumstellar disc.[ii] The total flux from the circumstellar disc is then determined by integrating over the optical depth and the total area of the disc. Since it is assumed that the source function for the material in the circumstellar disc is given by Planck's function, for regions with a high optical depth ($\tau_\nu \gg 1$) the circumstellar disc approaches a blackbody emitter, i.e. $I_\nu = B_\nu$.[iii]

Fig. 6.2 shows a schematic diagram of a Be star and circumstellar disc in the equatorial plane. As a first approximation the disc is assumed to be perpendicular to the line-of-sight and observed at infinity which simplifies the modelling. Below we shall follow the derivation of the COG method following the pattern laid out in Waters (1986). In the derivation of the COG method the author measures distances in units of the stellar radius, R_*. For example, the radial distance is measured as the dimensionless variable $x \equiv r/R_*$. Similarly the impact parameter, q, and the length along the line-of-sight, z, shown in Fig. 6.2 are dimensionless lengths. The dimensional length can then be found by multiplying the dimensionless quantity by the radius

[ii] This equation determines both the absorption and emission in the plasma, since the source function, $S_\nu = B_\nu$ includes both emission and absorption effects.

[iii] When a plasma is in thermal equilibrium, the source function, S_ν, is given by Planck's function. Such a region produces thermal radiation. However, radiation is only considered to be blackbody radiation when the specific intensity is described by Planck's function, i.e. $I_\nu = B_\nu$ (Rybicki and Lightman, 2004, p. 16).

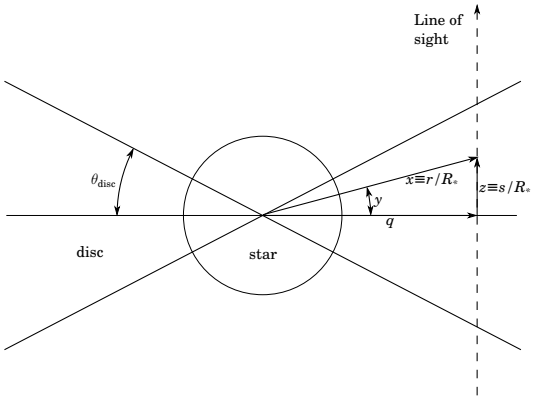

Figure 6.2: Schematic diagram used to calculate the COG method. Adapted from Waters (1986).

of the star, R_*.

Under the COG method it is assumed that the disc has a constant half-opening angle, $\theta_{\rm disc}$, extends to a finite radius, $R_{\rm disc}$, and has a density profile that decreases with radius from the star as $\rho \propto r^{-n}$, where n is determined by the fit to observational data. In order to determine the IR excess the first step is to calculate the optical depth through the disc, which is defined as

$$\tau_\nu = \int \kappa_\nu \, ds, \tag{6.5}$$

where κ_ν is the absorption coefficient and s is the length along the line-of-sight. The length s can be defined in terms of the dimensionless length as $s = R_* z$ as is shown in Fig. 6.2. The absorption coefficient for free-free and free-bound emission is given by (Brussaard and van de Hulst, 1962)

$$\kappa_\nu = 3.692 \times 10^8 \left\{1 - \mathrm{e}^{-h\nu/kT}\right\} \bar{z^2} \left\{g(\nu,T) + b(\nu,T)\right\} T^{-1/2} \nu^{-2} \varpi n_{\rm i}^2 \quad (\mathrm{cm}^{-1}), \tag{6.6}$$

where k and h are the Boltzmann and Planck constants, ν is the frequency, T is the temperature, $\bar{z}$ is the mean value of the squared atomic charge, ϖ is the electron to ion number ratio, $n_{\rm i}$ is the ion number density, and $g(\nu,T)$ and $b(\nu,T)$ are the Gaunt free-free and free-bound factors respectively.

In order to write the optical depth in the form given in Waters (1986) it is necessary to re-arrange the absorption coefficient, κ_ν into a wavelength dependent term and a variable which

is determined by the COG fit to the observational data. Therefore, from equation (6.6)

$$\begin{aligned}
\kappa_\nu &= 3.692\times10^8\left\{1-\mathrm{e}^{-h\nu/kT}\right\}\bar{z^2}\left\{g(\nu,T)+b(\nu,T)\right\}T^{-1/2}\nu^{-3}\varpi n_{\mathrm{i}}^2 \quad (\mathrm{cm}^{-1})\\
&= \left\{1-\mathrm{e}^{-h\nu/kT}\right\}\left\{g(\nu,T)+b(\nu,T)\right\}\nu^{-3}\left[3.692\times10^8\bar{z^2}T^{-1/2}\varpi n_{\mathrm{i}}^2\right]\\
&= \frac{\left(\frac{h\nu}{kT}\right)}{\left(\frac{h\nu}{kT}\right)}\times\left\{1-\mathrm{e}^{-h\nu/kT}\right\}\left\{g(\nu,T)+b(\nu,T)\right\}\nu^{-3}\left[3.692\times10^8\bar{z^2}T^{-1/2}\varpi n_{\mathrm{i}}^2\right]\\
&= \frac{1-\mathrm{e}^{-h\nu/kT}}{\left(\frac{h\nu}{kT}\right)}\left\{g(\nu,T)+b(\nu,T)\right\}\nu^{-3}\left(\frac{h\nu}{kT}\right)\left[3.692\times10^8\bar{z^2}T^{-1/2}\varpi n_{\mathrm{i}}^2\right]\\
&= \lambda^2\frac{1-\mathrm{e}^{-h\nu/kT}}{\left(\frac{h\nu}{kT}\right)}\left\{g(\nu,T)+b(\nu,T)\right\}\frac{1}{c^2}\frac{h}{kT}\left[3.692\times10^8\bar{z^2}T^{-1/2}\varpi n_{\mathrm{i}}^2\right]\\
&= X_\lambda\left(\frac{1}{c^2}\frac{h}{kT}\left[3.692\times10^8\bar{z^2}T^{-1/2}\varpi n_{\mathrm{i}}^2\right]\right), \qquad (6.7)
\end{aligned}$$

where

$$X_\lambda = \lambda^2\left\{\left(1-\mathrm{e}^{-h\nu/kT}\right)/\left(h\nu/kT\right)\right\}\left\{g(\nu,T)+b(\nu,T)\right\}, \qquad (6.8)$$

is the wavelength dependent part. It is assumed that the mass density profile of the disc is of the form

$$\rho = \rho_0\left(\frac{r}{R_*}\right)^{-n} = \rho_0 x^{-n}, \qquad (6.9)$$

where ρ_0 is the density at the base of the disc and $x \equiv (r/R_*)$ is the dimensionless radial distance. Therefore, the ion number density (cm^{-3}) can be re-written in terms of the mass density ($\mathrm{g/cm}^3$) as

$$\begin{aligned}
n_{\mathrm{i}} &= \frac{\rho}{\langle m_{\mathrm{i}}\rangle}\\
&= \frac{\rho_0 x^{-n}}{\mu m_{\mathrm{p}}},
\end{aligned}$$

where μ is the mean atomic weight in units of proton mass, and m_{p} is the mass of a proton. Substituting this into equation (6.7) gives

$$\begin{aligned}
\kappa_\nu &= X_\lambda\left(\frac{h}{c^2k}3.692\times10^8\bar{z^2}T^{-3/2}\varpi\left[\frac{\rho_0 x^{-n}}{\mu m_{\mathrm{p}}}\right]^2\right)\\
&= X_\lambda\left(3.692\times10^8\frac{h}{c^2k}m_{\mathrm{p}}^{-2}\bar{z^2}T^{-3/2}\mu^{-2}\varpi\rho_0^2x^{-2n}\right)\\
&= \left(\frac{R_*}{R_*}\right)\left(\frac{R_\odot}{R_\odot}\right)\times X_\lambda\left(3.692\times10^8\frac{h}{c^2k}m_{\mathrm{p}}^{-2}\bar{z^2}T^{-3/2}\mu^{-2}\varpi\rho_0^2\right)x^{-2n}\\
&= X_\lambda X_{*,d}\,R_*^{-1}x^{-2n},
\end{aligned}$$

where

$$\begin{aligned} X_{*,d} &= \left[3.692 \times 10^{8} \frac{h}{c^2 k} m_{\rm p}^{-2} R_{\odot}\right] \bar{z^2} T^{-3/2} \mu^{-2} \varpi \rho_0^2 \frac{R_*}{R_{\odot}} \\ &= 4.923 \times 10^{35} \bar{z^2} T^{-3/2} \mu^{-2} \varpi \rho_0^2 \frac{R_*}{R_{\odot}}, \end{aligned} \tag{6.10}$$

is a variable which is determined by the COG fit. Therefore, κ_ν can be written in terms of the wavelength dependent part X_λ, the variables X_* and R_*, and the geometry dependent part, x^{-2n} as

$$\begin{aligned} \kappa_\nu &= X_\lambda X_* R_*^{-1} x^{-2n} \\ &= E_{\nu,d} R_*^{-1} x^{-2n}, \end{aligned}$$

which is the form presented in Waters (1986).

In equation (6.5) the line-of-sight, s, lies along the dimensionless length z (Fig. 6.2) and therefore the total length is given by

$$s = R_* z,$$

where z can be written in terms of the dimensionless radial distance, x, and impact factor, q, as

$$z = \left(x^2 - q^2\right)^{1/2},$$

as shown in Fig. 6.2. Therefore,

$$\begin{aligned} ds &= R_*\, dz \\ &= R_*\, x \left(x^2 - q^2\right)^{-1/2} dx, \end{aligned}$$

where the derivative is only in terms of x since along any length z the impact factor q remains constant. The optical depth through the disc (equation 6.5) can then be written as

$$\begin{aligned} \tau_\nu &= \int \kappa_\nu\, ds \\ &= \int E_{\nu,d} R_*^{-1} x^{-2n} R_* x \left(x^2 - q^2\right)^{-1/2} dx \\ &= E_{\nu,d} \int x^{-2n+1} \left(x^2 - q^2\right)^{-1/2} dx. \end{aligned} \tag{6.11}$$

Equation (6.11) can be further simplified by making the change of variable $y = \cos^{-1}(q/x)$, where the angle y is defined in Fig. 6.2, which changes the equation to an integral over the

opening angle of the circumstellar disc. The substitution

$$\begin{aligned} x &= \frac{q}{\cos y}, \\ dx &= q \sec y \tan y \, dy, \end{aligned}$$

can then be made and equation (6.11) simplifies to

$$\begin{aligned} \tau_\nu(q) &= E_{\nu,d} \int \left(\frac{q}{\cos y} \right)^{-2n+1} \left(q^2 \sec^2 y - q^2 \right)^{-1/2} q \sec y \tan y \, dy \\ &= E_{\nu,d} q^{-2n+1} \int_y \cos^{2n-2} y \, dy. \end{aligned} \tag{6.12}$$

When the Be star is assumed to be viewed face on, and the disc has a half-opening angle $\theta_{\rm disc}$, the maximum optical depth, $\tau_{\rm max}(q)$, is calculated by integrating equation (6.12) from $-\theta_{\rm disc}$ to $\theta_{\rm disc}$.[iv] The total specific intensity along any line-of-sight is then (from equation 6.4 and e.g. Wright and Barlow, 1975)

$$\begin{aligned} I_\nu(q) &= \int_0^{\tau_{\rm max}(q)} B(\nu, T) \mathrm{e}^{-\tau_\nu} \, d\tau \\ &= B(\nu, T) \left(1 - \mathrm{e}^{-\tau_{\rm max}(q)} \right), \end{aligned} \tag{6.13}$$

where $B(\nu, T)$ is the Planck function. The equation above holds for lines-of-sight which do not intercept the star, i.e. for $q \geq 1$ in Fig. 6.2, while it is assumed that the photon spectrum from the star dominates for $q < 1$ and that the specific intensity is

$$I_\nu(q) = I_{\nu,*}, \tag{6.14}$$

where $I_{\nu,*}$ is the specific intensity which originates from the blackbody or Kurucz model atmosphere of the star.

The flux from a radiation field with a specific intensity I_ν is given by (e.g. Rybicki and Lightman, 2004)

$$F = \int I_\nu \cos\theta \, d\Omega,$$

where θ is the angle to the normal of the emitting surface and Ω is the solid angle subtending the emitting surface. The flux from a Be star and circumstellar disc at a distance D, where $D \gg qR_*$, can be written as an integration over q by making the substitution $\sin\theta \approx \theta \approx qR_*/D$

[iv] Since equation (6.12) is symmetrical it can be expressed as an integration between 0 and $\theta_{\rm disc}$ and the maximum optical depth, $\tau_{\rm max}$, is calculated as $2\tau_\nu(q)$. This is the form presented in Waters (1986).

and $\cos\theta \approx 1$, appropriate under the small angle approximation. Therefore

$$\begin{aligned} F &= \int I_\nu(q)\cos\theta\, d\Omega \\ &= \int_0^{2\pi}\int_\theta I_\nu(q)\cos\theta\sin\theta\, d\theta d\phi \\ &= 2\pi\int_q I_\nu(q)(1)\left(\frac{qR_*}{D}\right)\left(\frac{R_*}{D}\right) dq \\ &= \left(\frac{R_*}{D}\right)^2\int_0^{R_{\rm disc}/R_*} 2\pi q\, I_\nu(q)\, dq, \end{aligned} \tag{6.15}$$

where the integration is from the centre of the star to the edge of the disc. Using equations (6.12)–(6.15) it is possible to model the IR excess of a Be star by fitting the five parameters, $n, X_*, R_{\rm disc}, T_{\rm disc}$ and $\theta_{\rm disc}$.

6.1.1 The Gaunt factors

Gaunt factors[v] (for free-free emission and denoted by the symbol g) were introduced by John Arthur Gaunt (Gaunt, 1930), as the correction to the semi-classical formula of Kramers (1923), for calculating the continuous absorption in astrophysical plasmas. The choice of the symbol's letter g may be co-incidental, to quote from Jeffreys (1990),

> [h]owever I think from comparing equation (65) on p.861 of Kramers (1923) that Gaunt took the symbol for an undetermined factor from Kramers in the first place and it may have amused him that it was his own initial.

In order to find the COG fit to the Be star spectrum it is necessary to use or calculate the correct Gaunt factors in equation (6.6). Waters and Lamers (1984) published tables of free-free and free-bound Gaunt factors for stellar plasmas. The Gaunt factors were calculated by making use of a hydrogenic approximation. In section 6.3.1 (and in van Soelen and Meintjes, 2011) these tables are used to apply the COG method to LS 2883, the optical companion in PSR B1259-63, while values not included in the tables are interpolated by a linear fit between adjacent points. However, to model the anisotropic IC scattering the disc spectrum must be treated separately from the stellar spectrum and the IR excess must be calculated at frequencies beyond the limits of the published tables. I therefore calculated Gaunt factors at all frequencies considered for the COG fit and the anisotropic inverse Compton calculations. To ensure that my calculated Gaunt factors be consistent with those tabulated by Waters and Lamers (1984), I followed the same procedure as was presented by these authors. Note that the values obtained in this way are only approximate, but the errors in the values are not large (∼10%–20%) and the method used results in a good fit to the data using the COG method. I did not think it necessary therefore to consider more accurate methods to calculate the Gaunt factors as I do not believe that such

[v] The first recorded reference to this term as the "Gaunt factor" is attributed to Chandrasekhar (1939).

a calculation would provide an improvement in the over all COG fit and prediction of the broad optical and IR spectral distribution.

The procedure followed by Waters and Lamers (1984) to calculate the Gaunt free-free and free-bound factors for a reasonable stellar gas mixture is summarized below.

Free-free Gaunt factors

The average free-free Gaunt factor for high frequencies was calculated from the approximation in Gronenschild and Mewe (1978), which is a fit to the graphical solution in Karzas and Latter (1961), and is given by

$$\bar{g}_{\rm ff,GM}(\nu,T) = \left[\left(\frac{\sqrt{3}}{\pi}\mathrm{e}^{x}K_0(x)\right)^2 + (a - b\log_{10} u)^2\right]^{1/2},$$

where

$$\begin{aligned} u &= \frac{h\nu}{kT} \\ x &= \frac{u}{2}\left(1+\sqrt{10\gamma^2}\right) \\ \gamma^2 &= Z^2\left(\frac{I_{\rm H}}{kT}\right) = 1.578\times10^5\frac{Z^2}{T} \\ a &= 1.20\exp\left(-\left[\frac{\log_{10}\gamma^2-1}{3.7}\right]^2\right) \\ b &= 0.37\exp\left(-\left[\frac{\log_{10}\gamma^2+1}{2}\right]^2\right). \end{aligned}$$

Here K_0 is the modified Bessel function of the second kind, Z is the atomic charge and $I_{\rm H}$ is the ionization energy of hydrogen. At lower frequencies the approximation given by (Allen, 1973, p. 103),

$$\bar{g}_{\rm ff,A} = 10.6 + 1.90\log_{10}(T) - 1.26\log_{10}(\nu) - 1.26\log_{10}(Z),$$

is used for the average Gaunt factor.

In Fig. 6.3, $\bar{g}_{\rm ff}$ is shown for a temperature of $T = 20\,000$ K and a charge of $Z = 1$ using both approximations above. The curves show that there is a discontinuity between the two approximations. Waters and Lamers (1984) chose to join the two curves at the point of intersection, $\bar{g}_{\rm ff,GM} = \bar{g}_{\rm ff,A}$, introducing a discontinuity in the first derivative at this join. The final free-free Gaunt factor is calculated as the maximum value of the two approximations,

$$g_{\rm ff} = \max\left(\bar{g}_{\rm ff,GM}, \bar{g}_{\rm ff,A}\right),$$

which is shown as the thick solid line in Fig. 6.3.

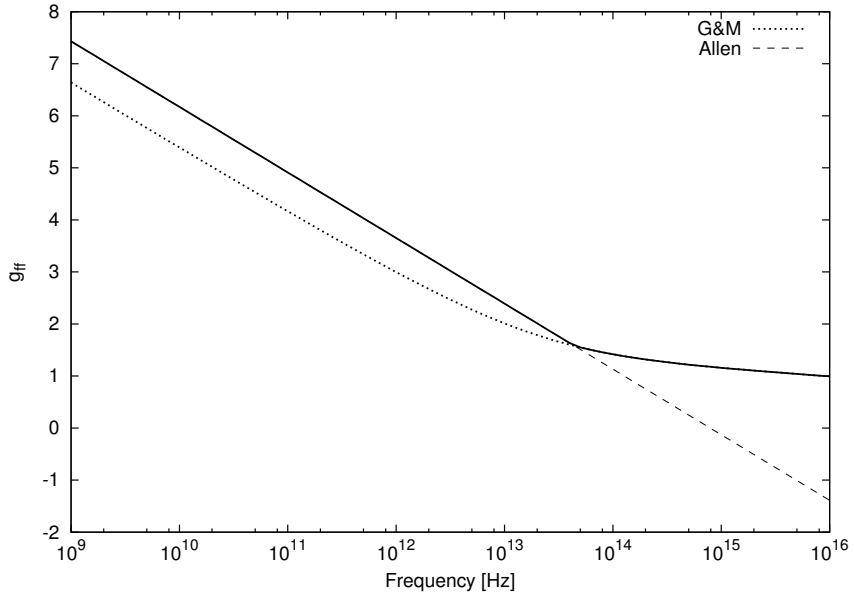

Figure 6.3: The free-free Gaunt factor calculated using the Gronenschild and Mewe (1978) (dotted line) and Allen (1973) (dashed line) approximations for $T = 20\,000$ K and $Z = 1$. The final value (solid line) is plotted using the maximum of the two approximations.

Free-bound Gaunt factors

The approximation of the averaged free-bound Gaunt factor, b, used in Waters and Lamers (1984) and in this study is taken from Brussaard and van de Hulst (1962):

$$b_z(\nu, T) = 2\theta \sum_{n=m_\nu}^{\infty} g_n \frac{\mathrm{e}^{\theta/n^2}}{n^3},$$

where

$$\theta = \frac{h\nu_0 Z^2}{kT}.$$

Here g_n is the free-free Gaunt factor, $\nu_0 = 3.28 \times 10^{15}$ Hz is the hydrogen ionization frequency and Z is the atomic charge. The value of m_ν is given by

$$m_\nu = Z \times \mathrm{int}\left(\sqrt{\nu_0/\nu}\right) + 1,$$

where the integer part of the square root must be taken. As shown in Brussaard and van de Hulst (1962), $g_n \approx 1$ in the frequency region of interest. We follow the approximation in Waters and Lamers (1984) by setting $g_n = 1$ for all frequencies. This introduces an error of approximately 10% – 20% by effectively removing the Gaunt correction term. However, at IR wavelengths and below ($\nu \ll kT/h$) the free-bound contribution is much lower than the free-free contribution and does not significantly affect the total free-free and free-bound contribution, $g(\nu, T) + b(\nu, T)$,

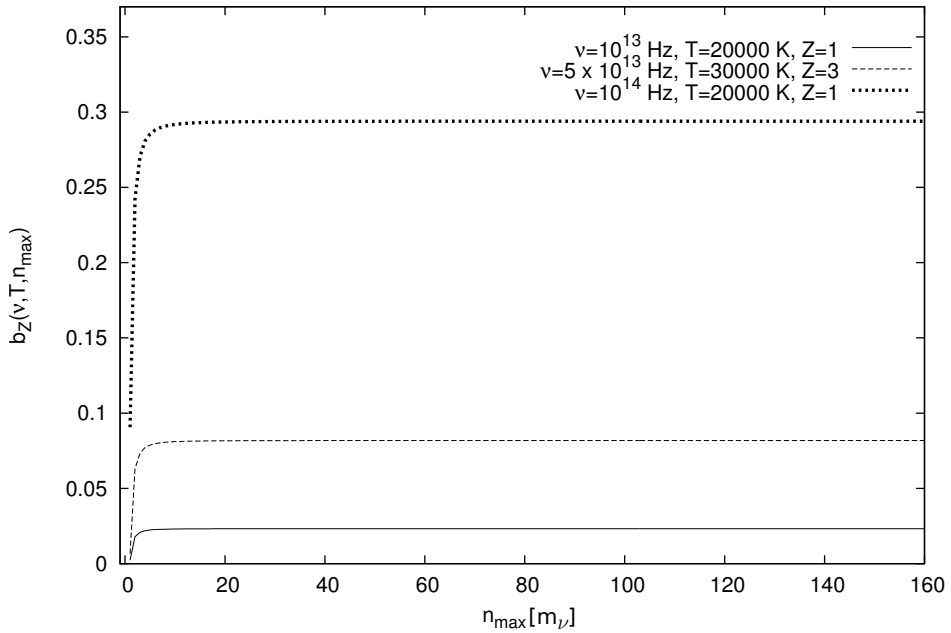

Figure 6.4: Three examples of the averaged free-bound Gaunt factor calculated from equation (6.16), plotted as a function of $n_{\max}$ (in units of m_ν).

while at higher frequencies ($\nu \gg kT/h$) free-bound emission dominates (e.g. Irwin, 2007, p. 252). The numerical estimate of the free-bound Gaunt factor, b, is then found from

$$b_z(\nu, T) = 2\theta \sum_{n=m_\nu}^{n_{\max}} \frac{\mathrm{e}^{\theta/n^2}}{n^3}, \tag{6.16}$$

where the sum is calculated to a maximum of $n_{\max} = (20 - 100) \times m_\nu$. To illustrate the validity of this approximation, Fig. 6.4 shows plots of three examples of b as a function of $n_{\max}$ (in units of m_ν). The plots shows that, in each case, the function converges to a constant value for $n_{\max} \approx 20\ m_\nu$.

Gas mixing

The final average Gaunt factor in Lamers and Waters (1984) is calculated for a gas mixture of H, He, and CNO, and the mixing equation is given by

$$\begin{aligned}(g+b)_{\mathrm{mixt}} \quad = \quad & \{R_{\mathrm{H}} f_{\mathrm{H+}}(g_1+b_1) + (R_{\mathrm{He}}/4)\,[f_{\mathrm{He+}}(g_1+b_1) + 4f_{\mathrm{He++}}(g_2+b_2)] \\ & + (R_{\mathrm{CNO}}/15)\,[f_{\mathrm{CNO+}}(g_1+b_1) + 4f_{\mathrm{CNO++}}(g_2+b_2) + 9f_{\mathrm{CNO+++}}(g_3+b_3)]\}\,/ \\ & \{R_{\mathrm{H}} f_{\mathrm{H+}} + (R_{\mathrm{He}}/4)\,[f_{\mathrm{He+}} + 2f_{\mathrm{He++}}] + \\ & (R_{\mathrm{CNO}}/15)\,[f_{\mathrm{CNO+}} + 2f_{\mathrm{CNO++}} + 4f_{\mathrm{CNO+++}}]\}\,, \end{aligned} \tag{6.17}$$

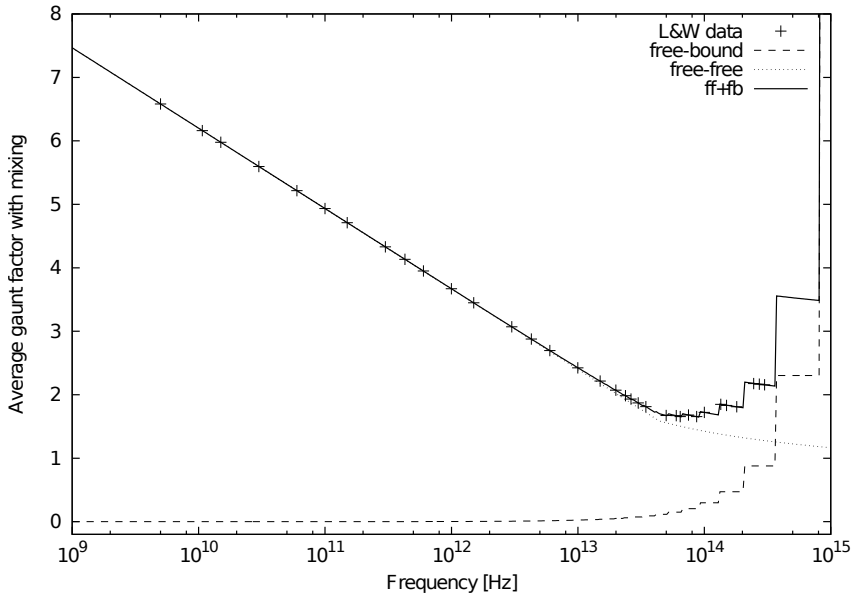

Figure 6.5: The calculated mixture Gaunt factor terms for $T = 20\,000$ K plotted together with the published data in Lamers and Waters (1984, Table IVd, p. 346). The solid line is the final calculated function, while the crosses represent the data points. Also shown is the result if only free-free (dotted line) or only free-bound (dashed line) Gaunt factors are used in the mixture calculation.

where $R_{\rm E}$ is the ratio of the element E in the gas mixture and $f_{{\rm E}i}$ is the fraction of the element that is in ionization state i. The results in the Lamers and Waters (1984) tables are given for a gas mixture of

$$\begin{aligned} R_H &= 0.70 \\ R_{He} &= 0.27 \\ R_{CNO} &= 0.03. \end{aligned}$$

I use these same ratios in this study. In Fig. 6.5 the calculated average mixture (for $f_{\rm H+} = 1$, $f_{\rm He+} = 1$ and $f_{\rm CNO++} = 1$ and all other $f_{{\rm E}i} = 0$) is plotted (solid line) with the published data in Lamers and Waters (1984, Table IVd, p. 346). Also shown in Fig. 6.5 is the calculated Gaunt factors of the mixture if only free-free or free-bound emission is considered. This shows that the free-bound contribution is negligible at frequencies below $\approx 10^{13}$ Hz, while it begins to dominate at higher frequencies.

6.1.2 Fitting stellar profiles

Before I discuss the modifications I have made to the COG method, I will first briefly discuss the fitting procedure that I used to fit the stellar profiles of LS 2883 to optical and IR data. If the ratio of the total measured flux to the expected flux from the star is defined as $Z_\nu = F_{\nu,{\rm total}}/F_{\nu,*}$,

and the excess flux is defined to be $Z_\nu - 1$. The flux from the star alone (excluding the flux from the disc) is given by (equations 6.12–6.15; Waters, 1986),

$$\begin{aligned} F_{\nu,*} &= \frac{R_*^2}{D^2} \int_0^1 2\pi q I_{\nu,*}\, dq \\ &= \frac{\pi R_*^2}{D^2} I_{\nu,*} \end{aligned}$$

where the range of integration is from the centre of the star ($q = 0$) to its surface ($q = 1$) where q is the impact parameter in units of stellar radii (Fig. 6.2). Similarly the flux from the disc will be found by integrating from $q = 1$ to $q = R_{\rm disc}/R_*$ and the excess flux ratio $Z_\nu - 1$ is given by

$$Z_\nu - 1 = \frac{F_{\nu,\rm disc}}{F_{\nu,*}} = \frac{B_\nu(T_{\rm disc})}{I_{\nu,*}} \int_1^{R_{\rm disc}/R_*} \left[1 - e^{-\tau_{\max}(q)}\right] 2q\, dq. \tag{6.18}$$

The Kurucz stellar atmosphere is fitted to optical data at frequencies $\nu > 3 \times 10^{14}$ Hz, to minimize the influence of the circumstellar disc. The flux is also scaled for the distance to the source by fitting the parameter $Y_{\rm shift} = \log(\pi R_*^2) - \log(D^2)$ (Telting et al., 1998) which is simply the decrease in flux due to distance, D. The IR excess from the circumstellar disc is then determined by the difference between the measured flux and the Kurucz predicted flux at IR wavelengths. This IR excess is then used to fit the COG model using the five parameters, $n, X_*, R_{\rm disc}, T_{\rm disc}$ and $\theta_{\rm disc}$. Following Telting et al. (1998), I fitted these five parameters can be fitted using the method of Levenberg–Marquardt (e.g. Press et al., 2007, pp. 801-806). However, following Telting et al. (1998) the temperature of the disc is assumed to be a fixed fraction of the temperature of the star, and the disc opening angle and disc radius is kept constant. The COG method is then only fitted to n and X_*. The resulting COG then models the flux from the circumstellar disc which, when added to the stellar contribution, predicts the observed IR excess. This broad band optical and IR spectrum from the star and disc is used in this study to model the anisotropic IC scattering in PSR B1259-63/LS 2883.

Fig. 6.6 shows an application of the COG method to X Persei undertaken by Telting et al. (1998). The authors combined new data with data already published in the literature in the period circa 1965 to 1995, and were able to show the evolution of the star from a disc to a "discless" state. The data showed two "discless" or low disc states between ∼1975–1977 and 1989–1992. As discussed in Chapter 3, the circumstellar discs of Be stars are variable and the infrared excess and the emission lines vary with the size of the disc. Telting et al. (1998) showed that during a discless state the data from X Persei could be fitted by a 31 000 K stellar atmosphere (lower line fitted to the solid dots in Fig. 6.6) while the COG method was fitted during a "disc" phase (upper line fitted to the open circles). The fitted COG parameters for X Persei are $n = 4.73$ and $\log_{10} X_* = 8.99$ while the remaining parameters were held at $R_{\rm disc} = 5.0 R_*$, $T_{\rm disc} = 0.8\ T_{\rm star} = 24\,800$ K and $\theta_{\rm disc} = 5°$.

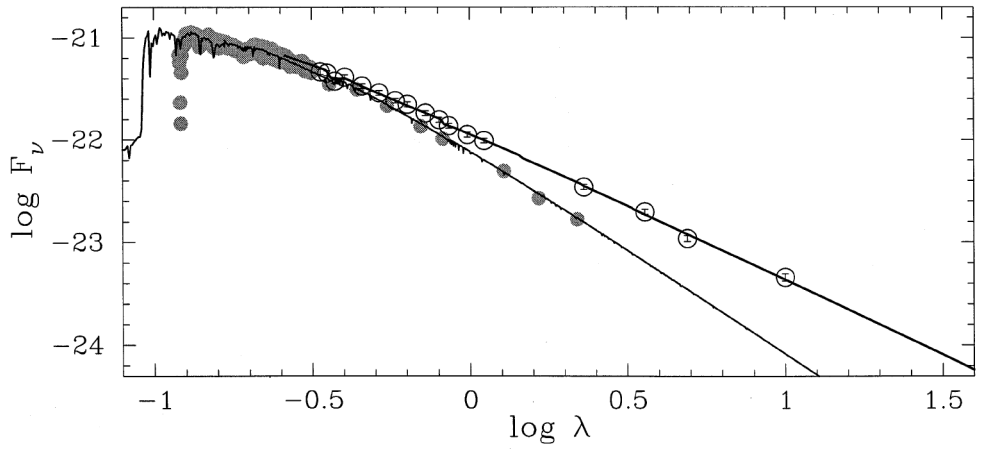

Figure 6.6: The IR excess from X Persei observed at times of high and low infrared excess. A Kurucz model with an effective temperature of $T_{\rm eff} = 31\,000$ K is fitted to the closed circles taken during a discless state, while a COG model is fitted to the open circles taken during a disc state; see text for details. Figure adapted from Telting et al. (1998).

6.2 Modification of the COG method

Waters (1986) showed that the observed flux from a moderately inclined disc will not deviate greatly from that of a disc observed face-on. However, from the point of view of the pulsar near periastron, the circumstellar disc will change dramatically in orientation, inclination and angular size. It is thus necessary to calculate the IR excess from a disc at any orientation. This requires a modification and extension of the COG model. The method I have used to make these modifications is discussed below. In the interest of readability, I have relegated some of the derivations to an appendix (Appendix B).

Fig. 6.7 shows the line-of-sight through the Be-star's circumstellar disc, which is not viewed face-on, i.e. the line-of-sight is not perpendicular to the disc mid-plane (compare to Fig. 6.2). From equation (6.5) the optical depth through the disc is

$$\begin{aligned} \tau_\nu &= \int \kappa_\nu \, dl \\ &= E_{\nu,\rm d} \int \tilde{r}^{-2n} \, dl, \end{aligned} \tag{6.19}$$

where $E_{\nu,\rm d} \equiv X_\lambda X_{*,d}$ is the disc parameter (equations 6.8 & 6.10), l is the length along the line-of-sight, and I assumed $\rho = \rho_0 (r/R_*)^{-n} \equiv \rho_0 \tilde{r}^{-n}$. Here the symbol $\tilde{r}$ denotes the dimensionless radial distance.[vi] Constructing a dimensionless impact parameter q such that $\tilde{r}^2 = q^2 + \tilde{l}^2$, where

[vi] I have chosen a different symbol for the dimensionless radial distance to distinguish it from the unmodified COG method.

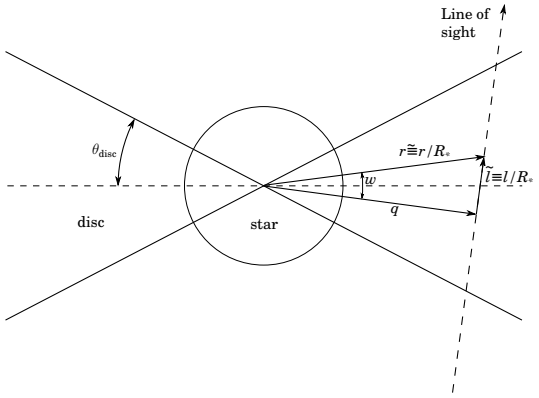

Figure 6.7: Schematic diagram used to calculate the modified COG method. The disc is not viewed face-on and, therefore, the line-of-sight is not perpendicular to the mid-plane of the disc (compare Fig. 6.2).

$\tilde{l} \equiv l/R_*$, equation (6.19) can be re-written in terms of $\tilde{r}$ as

$$\tau_\nu = E_{\nu,\mathrm{d}} \int \tilde{r}^{-2n+1} \left(\tilde{r}^2 - q^2\right)^{-1/2} \, d\tilde{r}.$$

Making the simplifying substitution $w = \cos^{-1}(q/\tilde{r})$ where w is the angle between q and $\tilde{r}$, results in

$$\tau_\nu = E_{\nu,\mathrm{d}} q^{-2n+1} \int_w \cos^{2n-2} w \, dw, \tag{6.20}$$

which is formally identical to equation (6.12). The difference is that, since the disc is not necessarily viewed face-on, the impact factor q is no longer defined to lie along the mid-plane of the disc and the maximum value of q is no longer determined by the size of the circumstellar disc. Further, the limits on the angle w are no longer defined by the half-opening angle of the disc and must be independently calculated for each line-of-sight considered. The specific intensity from any point of the disc is then calculated as (equation 6.13)

$$I_\nu(q) = B_\nu(T) \left(1 - \mathrm{e}^{-\tau_{\max}}\right), \tag{6.21}$$

where the loss of symmetry also means that $\tau_{\max}$ is not symmetrical around the azimuthal angle.

When calculating the isotropic inverse Compton spectrum (section 7.3 and van Soelen and Meintjes, 2011) the total integrated flux was used to calculate the photon spectrum, however, when calculating the anisotropic IC scattering from the circumstellar disc it is necessary to determine the scattering over the full solid angle of the disc and the intensity emitted from the disc at different angles. The specific intensity originating from the disc (equation 6.21) is determined from the optical depth (equation 6.20) which is dependent on the parameters, $E_{\nu,\mathrm{d}}$, q and w. The disc parameter $E_{\nu,\mathrm{d}} \equiv X_\lambda X_{*,d}$ is identical to the Waters and Lamers (1984) parameter (equations 6.8 & 6.10) and is given by the wavelength and the COG fit to $X_{*,d}$. The value of q and the limits on w are not the same as in the previous unmodified COG model and

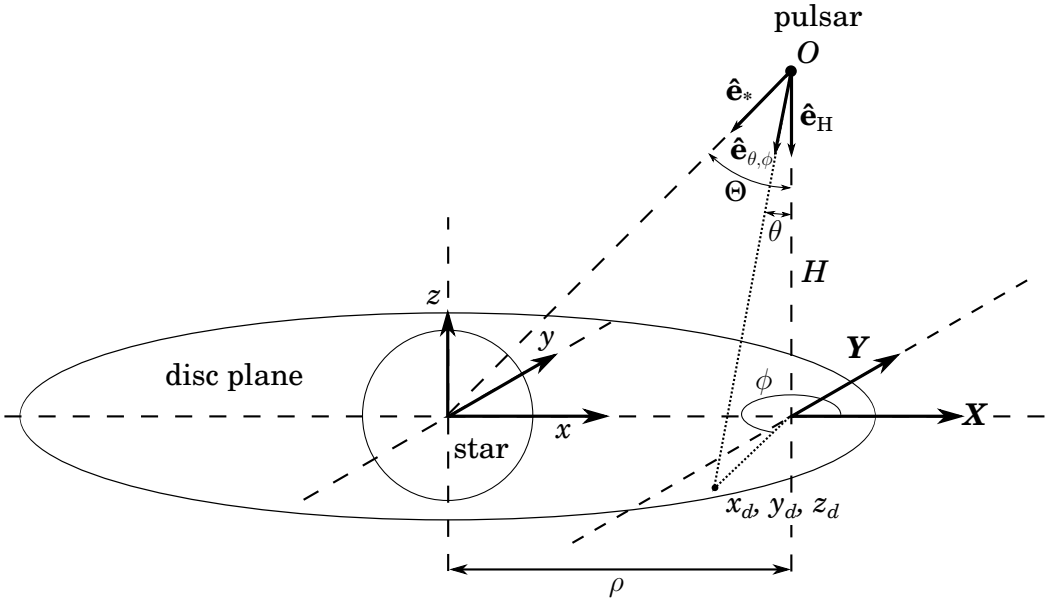

Figure 6.8: Coordinate system used to calculate the AIC scattering and IR excess. O is the centre of the pulsar-fed, relativistic electron cloud, which is a vertical height H above the disc and shifted a distance ρ horizontally from the centre of the star/disc. Directions expressed in the polar coordinate system can by translated to X, Y positions on the disc plane and to the star/disc Cartesian coordinate system (x, y, z) with the origin at the centre of the star and circumstellar disc.

therefore a solution for each of these terms must be determined.

Value of q

Consider the coordinate system shown in Fig. 6.8 (see e.g. Moskalenko and Strong, 2000; Pommé et al., 2003; Tryka, 1997). The pulsar lies at the centre of the coordinate system (point O), $\hat{\mathbf{e}}_*$ is the unit vector pointing towards the centre of the disc and star, and $\hat{\mathbf{e}}_H$ is pointing towards the disc along the normal to the disc. Any arbitrary line-of-sight from the pulsar to the disc along a unit vector $\hat{\mathbf{e}}_{\theta,\phi}$ will form an impact parameter q as is shown in Figs. 6.9 & 6.10, where ξ is the angle between $\hat{\mathbf{e}}_*$ and $\hat{\mathbf{e}}_{\theta,\phi}$. Defining the angle between $\hat{\mathbf{e}}_*$ and $\hat{\mathbf{e}}_H$ as Θ (Fig. 6.8) it can be shown that

$$\hat{\mathbf{e}}_* = \begin{pmatrix} \sin\Theta\cos\pi \\ \sin\Theta\sin\pi \\ \cos\Theta \end{pmatrix} = \begin{pmatrix} -\sin\Theta \\ 0 \\ \cos\Theta \end{pmatrix}$$

and

$$\hat{\mathbf{e}}_{\theta,\phi} = \begin{pmatrix} \sin\theta\cos\phi \\ \sin\theta\sin\phi \\ \cos\theta \end{pmatrix},$$

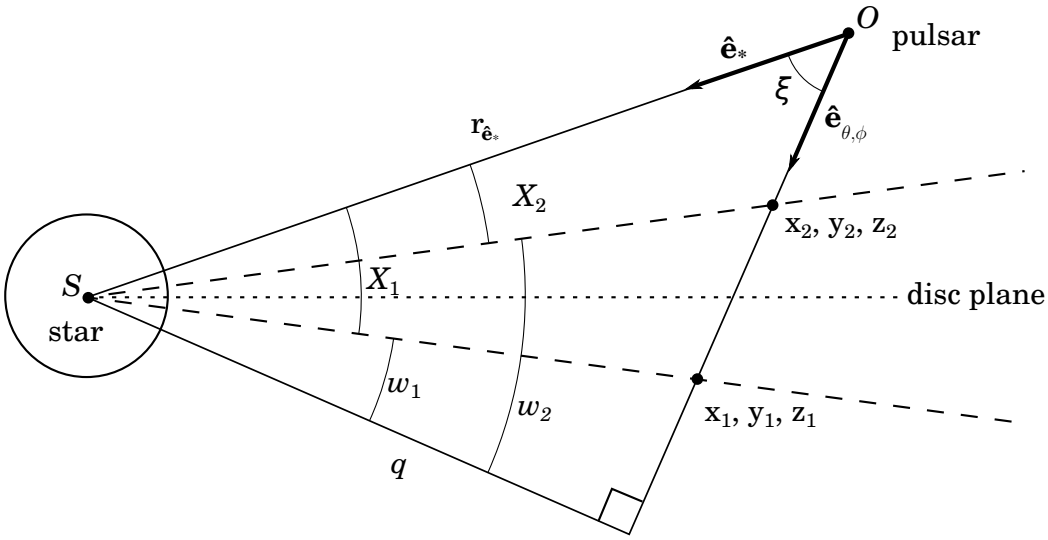

Figure 6.9: Sketch of the impact factor in the plane of $\hat{\mathbf{e}}_* \cdot \hat{\mathbf{e}}_{\theta,\phi}$ for $\xi < 0$.

where θ and ϕ specify an arbitrary direction. Therefore, the angle ξ can be determined from

$$\cos\xi = \hat{\mathbf{e}}_* \cdot \hat{\mathbf{e}}_{\theta,\phi} = \cos\Theta\cos\theta - \sin\Theta\sin\theta\cos\phi, \tag{6.22}$$

and the impact parameter is given by (Figs. 6.9 & 6.10)

$$q = r_{\hat{\mathbf{e}}_*}\sin\xi, \tag{6.23}$$

where $r_{\hat{\mathbf{e}}_*}$ is the distance from the pulsar to the star in units of R_*. For any arbitrary line-of-sight through the disc the impact factor, q, can then be determined by equations (6.22) and (6.23). It remains now to solve for the limits on w.[vii]

Limits on w if $\theta < 90°$

First the limit on w will be found for the case of a line-of-sight, $\hat{\mathbf{e}}_{\theta,\phi}$, when the polar angle $\theta < 90°$ (Fig. 6.8). Any line-of-sight in the direction $\hat{\mathbf{e}}_{\theta,\phi}$ cuts the plane of the disc at a position

$$\begin{aligned} X &= H\tan\theta\cos\phi \\ Y &= H\tan\theta\sin\phi, \end{aligned}$$

where H is the perpendicular height of the pulsar above the disc and the origin of X, Y is at the intercept of the line H with the disc plane (Fig. 6.8). The centre of the star/disc is a distance ρ

[vii]The symbols $r_{\hat{\mathbf{e}}_*}$ and w have been used instead of x and y, as were used in section 6.1, for two reasons: first to distinguish w from the angle y in Waters (1986) so that it is clear the limits are not simply $-\theta_{\rm disc}$ to $\theta_{\rm disc}$ and second to avoid confusion later when x and y will be used to refer to disc coordinates in Fig. 6.8.

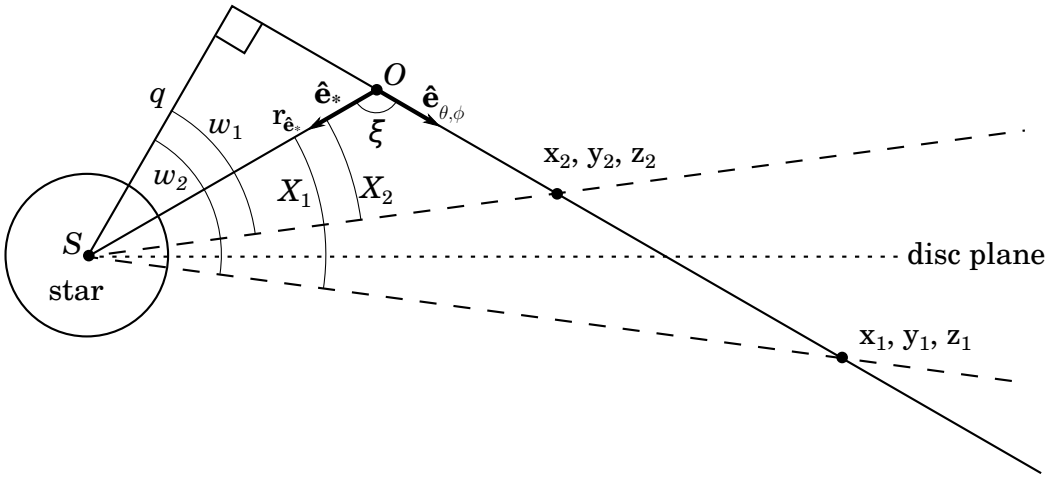

Figure 6.10: Sketch of the impact factor in the plane of $\hat{\mathbf{e}}_* \cdot \hat{\mathbf{e}}_{\theta,\phi}$ for $\xi > 0$.

away from the intercept of H with the disc plane and the X-axis is defined to lie along the line joining these points. Defining a new Cartesian reference system, x, y, z, such that the origin is at the centre of the star/disc, and that x and y are measured in the plane of the disc with $x \parallel X$ and $y \parallel Y$ (Fig. 6.8), the point of the plane intercept, (x_d, y_d, z_d), can be written in terms of X and Y as

$$\begin{aligned} x_d &= X + \rho \\ &= H \tan\theta \cos\phi + \rho \\ y_d &= Y \\ &= H \tan\theta \sin\phi, \\ z_d &= 0. \end{aligned}$$

In this coordinate system, the height of the disc, above the disc plane, at any point is

$$h_d = \sqrt{x^2 + y^2} \tan\theta_{\rm disc}, \tag{6.24}$$

where $\theta_{\rm disc}$ is the half-opening angle of the disc. For any line-of-sight ($\hat{\mathbf{e}}_{\theta,\phi}$), we can construct a distance h_l which is perpendicular to the disc plane and intercepts the line-of-sight. If h_l intercepts the disc plane at any distance Δx and Δy from the point of the disc plane intercept (x_d, y_d), then the length along h_l between the disc plane and the line-of-sight intercepts is

$$h_l = \sqrt{\Delta x^2 + \Delta y^2} \tan\theta_k, \tag{6.25}$$

where $\theta_k = \frac{\pi}{2} - \theta$. The point where the line-of-sight intercepts the disc above and below the disc plane can then be found by determining Δx and Δy by solving for $h_l = h_d$. This gives

$$\begin{aligned} h_l &= h_d \\ \sqrt{\Delta x^2 + \Delta y^2}\tan\theta_k, &= \sqrt{x^2+y^2}\tan\theta_{\rm disc} \\ &= \sqrt{(x_d+\Delta x)^2 + (y_d+\Delta y)^2}\tan\theta_{\rm disc}. \end{aligned} \tag{6.26}$$

Since in the plane of the disc,

$$\Delta y = \Delta x \tan\phi, \tag{6.27}$$

this equation can be substituted into equation (6.26) and the solution for Δx can be found. From the solution of Δx, the value of Δy can be determined from equation (6.27). Solving for Δx and Δy produces two solutions, which correspond to the top and bottom disc intercepts and the correct value must be chosen for each intercept as outlined in Appendix B.1. The coordinates of the disc intercepts are defined as (x_1, y_1, z_1) below the plane (or the lower disc intercept), and (x_2, y_2, z_2) above the plane, where

$$\begin{aligned} x_{1,2} &= x_d + \Delta x \\ y_{1,2} &= y_d + \Delta y, \end{aligned}$$

and the z coordinate is calculated as

$$\begin{aligned} z_1 &= -\left|\sqrt{x_1^2+y_1^2}\right|\tan\theta_{\rm disc} \\ z_2 &= +\left|\sqrt{x_2^2+y_2^2}\right|\tan\theta_{\rm disc}. \end{aligned}$$

The full derivation of the solution for Δx and Δy is given in Appendix B.1.

Using the coordinates (x_1, y_1, z_1) and (x_2, y_2, z_2) calculated above it is possible to construct a triangle as is shown in Figs. 6.9 and 6.10 in the plane of $\hat{\mathbf{e}}_* \cdot \hat{\mathbf{e}}_{\theta,\phi}$. These figures show detailed diagrams of the path of a line-of-sight through the circumstellar disc, and show all relevant angles and positions . Shown in the figures are the position of the star, the disc plane, the positions of the two disc intercepts (x_1, y_1, z_1) and (x_2, y_2, z_2), the impact parameter q, the centre of the electron cloud at $O = (x = \rho, y = 0, z = H)$ and the centre of the star at $S = (x = 0, y = 0, z = 0)$. The angles X_1 and X_2 are defined to be between the line joining the centre of the electron cloud and the centre of the star, SO, and the line joining the centre of the star and the two points of the

disc intersection respectively. The value of the angles are given by

$$X_1 = \cos^{-1}\left(\frac{\rho x_1 + H z_1}{(\rho^2 + H^2)^{1/2}\,(x_1^2 + y_1^2 + z_1^2)^{1/2}}\right)$$
$$X_2 = \cos^{-1}\left(\frac{\rho x_2 + H z_2}{(\rho^2 + H^2)^{1/2}\,(x_2^2 + y_2^2 + z_2^2)^{1/2}}\right).$$

From the sketches in Figs. 6.9 & 6.10 it can be seen that the limits on w are

$$w_1 = \frac{\pi}{2} - \xi - X_1$$
$$w_2 = \frac{\pi}{2} - \xi - X_2,$$

where the angle ξ was defined earlier (equation 6.22).

With the limits of w solved, the optical depth through the disc can now be calculated using equation (6.20). This allows the intensity of the radiation emitted from the circumstellar disc as seen from the pulsar's reference frame to be modelled.

Limits on w if $\theta \geq 90°$

The solutions for w in the case of a polar angle $\theta \geq 90°$ is very similar to that of $\theta < 90°$. A geometric solution is found for the two intercepts (x_1, y_1, z_1) and (x_2, y_2, z_2), from which it is then possible to determine the limits of w and find the optical depth using equation (6.20). The derivation for $\theta = 90°$ and $\theta > 90°$ is given in Appendixes B.2 and B.3 respectively.

6.3 Application to LS 2883

In this section the COG method is applied to optical and IR data from LS 2883. Section 6.3.1 presents the COG fit based on archived data and the Johnston et al. (1994) estimate of the colour excess, which was originally presented in van Soelen and Meintjes (2011). Section 6.3.2 presents a new COG fit which incorporates new IR data obtained with the VLT as part of a multi-wavelength campaign which was undertaken as part of this study (section 2.8). This new fit also uses the new colour excess proposed by Negueruela et al. (2011).

6.3.1 Constraining the IR excess from LS 2883 using archive data

The optical and infrared data used to model PSR B1259-63 in this section are taken from Westerlund and Garnier (1989), *2MASS* and *MSX* (Tables 6.1 & 6.2; data are available through the NASA/IPAC Infrared Science Archive.[viii] The IR and optical data were de-reddened with the DIPSO software package using the extinction measurement given in Westerlund and Garnier

[viii] http://irsa.ipac.caltech.edu/

Table 6.1: Optical magnitudes and colours for LS 2883 from Westerlund and Garnier (1989) (W&G89), Klare and Neckel (1977) (K&N77), Schild et al. (1983) (S83), Drilling (1991) (D91).

	W&G89	K&N77	S83	D91
V	10.01	10.04	10.05	10.07
B-V	0.754	0.74	0.72	0.73
U-B	-0.506	-0.44	-0.47	-0.47
$(U\text{-}B)_0$	-1.261			
A_ν	3.25			
$M_\nu(U\text{-}B)_0$	-4.6			

(1989) and following the assumptions of Johnston et al. (1994) which suggested a value for the extinction of E(B-V) = 1.05. A standard galactic extinction law was assumed.

The initial Kurucz atmosphere fits were done using the Kurucz (1992) model atmospheres obtained from the Space Telescope Science Institute[ix]. The tables only begin at a minimum frequency of $\sim 3.3 \times 10^{13}$ Hz and needed to be extended further into the IR regime. The last few data points lie within the Rayleigh-Jeans limit ($h\nu \ll kT$) for a stellar temperature of $\sim 20\,000$ K, and since in this limit $\log I_{\nu,*} \propto \log \nu$, the data points were extended to $\nu \approx 5.2 \times 10^9$ Hz (or $\lambda \sim 6$ cm) using a straight line fit.

The stellar temperature, T_*, and effective gravity, $\log g$, were determined by finding the best least squares fit of the Kurucz model atmospheres to the optical data above 3×10^{14} Hz (in order to limit the influence of the IR excess on the optical fit). The decrease in flux due to distance to the source from Earth (d) was also accounted for by scaling the intensity with the parameter $Y_{\rm shift} = \log(\pi R_*^2) - \log(d^2)$ (Telting et al., 1998). A best fit temperature and effective gravity of $T_* = 25\,000$ K and $\log\ g = 3.5$ respectively, were found, consistent with an early B type star.

The IR excess was then fitted to the IR data using the COG method. The disc temperature was chosen to be $T_{\rm disc} = 0.5\ T_* = 12\,500$ K and the disc radius $R_{\rm disc} = 50\ R_*$ as was inferred from the pulsar eclipse (section 2.1.2). Following the convention used by Telting et al. (1998) the half-opening angle was held at $\theta = 5°$. The remaining two parameters (n and X_*) were simultaneously fitted with the Levenberg-Marquardt method (e.g. Press et al., 2007, pp. 801-806) using the implementation in the ORACLE software package. This produced a best fit of $n = 2.37$ and $\log X_* = 7.87$ and the resulting fit is plotted in Fig. 6.11. Fits using a larger half-opening angle of $\theta \sim 18.5°$ as was suggested by Chernyakova et al. (2006) were also considered but produced no noticeable effect on the fitted optical/IR spectrum. The values of both fits are summarized in Table 6.3.

6.3.2 Further constraint using new VISIR/VLT data

As part of this study a multi-wavelength campaign was undertaken to observer PSR B1259-63/LS 2883 during the December 2010 periastron passage and infrared Service Mode observations

[ix] http://www.stsci.edu/science/starburst/Kurucz.html

Table 6.2: IR data for PSR B1259-63 from *2MASS* (J,H,Ks) and *MSX* (A,C). Data are available through the NASA/IPAC Infrared Science Archive.

Band	Wavelength μm	Magnitude	Flux Jy
J	1.235	8.026 ± 0.027	
H	1.662	7.699 ± 0.055	
Ks	2.159	7.248 ± 0.020	
A	8.28		0.2675 ± 0.0136
C	12.13		1.087 ± 0.5859

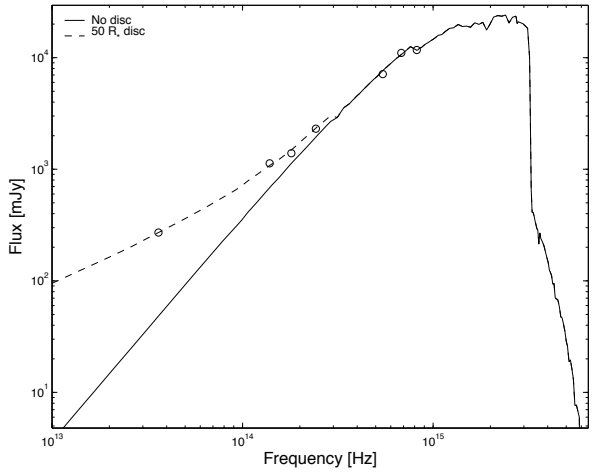

Figure 6.11: A Kurucz stellar atmosphere (solid line) and the modification introduced by the COG method (dashed line) fitted to data for PSR B1259-63/LS 2883 (Tables 6.1 & 6.2). The open circles are the optical and IR data points.

Table 6.3: Optical and IR fit to PSR B1259-63 using Tables 6.1 and 6.2

Optical fit		
$T_{\rm eff}$	25 000 K	
$\log g$	3.5	
$Y_{\rm shift}$	-19.14	
Curve of growth fit		
n	2.37	2.37
$\log X_*$	7.87	7.32
$R_{\rm disc}$	50 R_*	50 R_*
$T_{\rm disc}$	12 500 K	12 500 K
θ	5°	18.°5

were undertaken at the Very Large telescope (VLT) using the VLT Imager and Spectrometer for the mid Infrared (VISIR) at the European Southern Observatory (ESO). The operation of VISIR on the VLT is briefly summarized in section 2.8.4. This section discusses the results and reduction of the VISIR/VLT data and the application of the COG method to the combined archive and VISIR/VLT data.

VLT/VISIR observations

The mid-IR observations undertaken with VISIR on the VLT (observation run: 086.D-0136(B)) were obtained on the 5$^{\rm th}$ January 2011, approximately three weeks after the 14$^{\rm th}$ of December 2010 periastron passage of PSR B1259-63/LS 2883. The observations consisted of one pointing covering multiple bands in the broad N-band region (8 – 13 μm). The observations were executed using the standard `VISIR_img_obs_AutoChopNod` observing command with a perpendicular chop/nod direction, a chopping amplitude of 10″ and a random jitter of 3″. The total integration time was of the order of 60 seconds per filter and achieved signal-to-noise (S/N) ratios of $\lesssim 10$. The proposed integration times were determined based on the flux predictions made by the COG fit discussed in the previous section (Fig. 6.11) and were intended to achieve a S/N ratio of approximately 10. However, the observed flux was slightly lower than was predicted resulting in a slightly lower S/N ratio. The observations were calibrated with observations of the standard star HD92682, which was observed as part of the standard ESO procedure using the same experimental set-up as the science target observations. Observations of standard stars are taken within 3 hours of the observation of the science target and allow for an average calibration accuracy within $\sim 3\%$ (Smette and Vanzi, 2007).

The calibration star data were reduced with the `visir_img_phot` pipeline and the science target observations were reduced using the standard `visir_img_combine` pipeline to correct for the image nodding and chopping. Both reduction pipelines produce a single FITS (Wells et al., 1981) file with four measurements of the targets contained within each file. A flux conversion ratio was calculated by comparing the standard star measurements obtained during the observation

Table 6.4: VLT/VISIR data for LS 2883 observed on the 5th of January 2011.

Filter	central wavelength μm	half-band width μm	F mJy	error mJy
PAH1	8.59	0.42	261	40
ArIII	8.99	0.14	241	30
SIV	10.49	0.16	218	32
SIV_2	10.77	0.19	188	21
PAH2	11.25	0.59	208	31
SiC	11.85	2.34	198	18
PAH2_2	11.88	0.37	196	54
NeII	12.81	0.21	143	51

to the defined standard flux from this source for each filter. This flux conversion ratio was used to calibrate the measured flux from the science target.

The final error in the VLT observations of LS 2883 were calculated by combining the photometric error of each flux measurement and the standard deviation of the four measurements in each FITS file, for both the science target and standard star. This gives a photometry and standard deviation error for both the target and standard star, and the final error was calculated by combining these four errors using

$$\sigma_{\rm final} = \sqrt{\sigma^2_{\rm cal,phot} + \sigma^2_{\rm cal,std} + \sigma^2_{\rm sci,phot} + \sigma^2_{\rm sci,std}}.$$

Not included in the error calculation is the $\sim 3\%$ error associated with the calibration process and any error in the standard star's catalogue flux value. The calibrated flux at each filter from LS 2883 is summarized in Table 6.4.

Application of the COG model

The combined archive and observed data of LS 2883 (Tables 6.1, 6.2 & 6.4) were de-reddened with the DIPSO software package using the new colour excess, E(B-V) = 0.85, proposed by Negueruela et al. (2011) and the combined and de-reddened data are shown in Table. 6.5.

A fit for the Kurucz model was found by fitting the model atmosphere to the optical data points ($\nu > 3 \times 10^{14}$ Hz) to minimize the influence of the IR excess, using the same Kurucz tables as in section 6.3.1. A broad search between 25 000 – 35 000 K found a best fit atmosphere of $T = 27\,000$ K and $\log g = 5.0$, with $Y_{shift} = -19.5$. However, spectroscopic observations undertaken by Negueruela et al. (2011) suggested a stellar temperature of $T_* = 33\,500$ K and an effective gravity $\log g = 4.0$ for LS 2883 if the star was non-rotating. For this reason a stellar atmosphere with temperature $T_* = 33\,000$ K with $\log g = 4.0$ has been adopted, and a best fit was found to the optical data points. The calculated COG fit to the infrared excess was found using Gaunt factors which were calculated as was discussed in section 6.1.1, using the mixing parameters $f_{\rm H+} = 1$, $f_{\rm CNO+} = 1$ and all other $f_{{\rm E}i} = 0$ (as in Waters and Lamers, 1984, Table

Table 6.5: Combined data from LS 2883 de-reddened using E(B-V)=0.85.

Band	Wavelength μm	F_0 10^{-24} erg s^{-1} cm^{-2} Hz^{-1}	err 10^{-24} erg s^{-1} cm^{-2} Hz^{-1}
U	0.365	50.03	0.107
B	0.44	52.433	0.088
V	0.55	40.539	0.097
J	1.235	19.614	0.066
H	1.662	12.695	0.091
K	2.159	10.677	0.029
A	8.23	2.71	0.14
C	12.13	10.91	5.88
PAH1	8.59	2.64	0.41
ArIII	8.99	2.43	0.30
SIV	10.49	2.19	0.32
SIV_2	10.77	1.89	0.22
PAH2	11.25	2.09	0.31
SiC	11.85	1.99	0.18
PAH2_2	11.88	1.97	0.54
NeII	12.81	1.43	0.52

IVb, p. 344).

Recent observations of Be stars suggest that the circumstellar discs are very thin (e.g. Carciofi, 2011; Quirrenbach et al., 1997; Wood et al., 1997) and in the recent SPH modelling presented by Okazaki et al. (2011) the temperature of the disc is assumed to be $T_{\rm disc} = 0.6\,T_*$ and the height of the disc is $H(R_*)/R_* = 0.024$ ($\theta_{\rm disc} \approx 0.7°$). Adopting a thin disc fit would appear to be more consistent with current Be circumstellar disc theory and, therefore, a disc temperature of $T_{\rm disc} = 0.6T_*$, a disc half-opening angle of 1° and a disc size of $R_{\rm disc} = 50R_*$ was chosen for the new COG fit. As was discussed in the previous COG fit to LS 2883 (section 6.3.1), a larger disc opening angle slightly changes the fit of the COG parameters, but does not significantly change the overall shape for the predicted optical and IR flux. Since it is this optical/IR flux prediction which is ultimately of importance to this study, additional fits to different size opening angles were not considered.

Two COG fits were considered for both free-free+free-bound emission and for only free-free emission. The free parameters n and X_* where determined using the Levenberg–Marquardt method (e.g. Press et al., 2007, pp. 801-806). Fig. 6.12 shows the fitted stellar atmosphere (thin dotted line), the predicted IR flux from the disc for free-free (thin solid line) and free-free+free-bound (thin dashed line) emission, and the total expected flux fitted to the data points in Table 6.5. The flux from the MSX C-band (open square), which lies far above the predicted flux, was not included in the calculation of the COG fit as it appears to be an erroneous detection and an inspection of the MSX C-band map of the region does not appear to show a source (Fig. 6.13); the point is included for completeness. The parameters found for the COG method are given in Table 6.6.

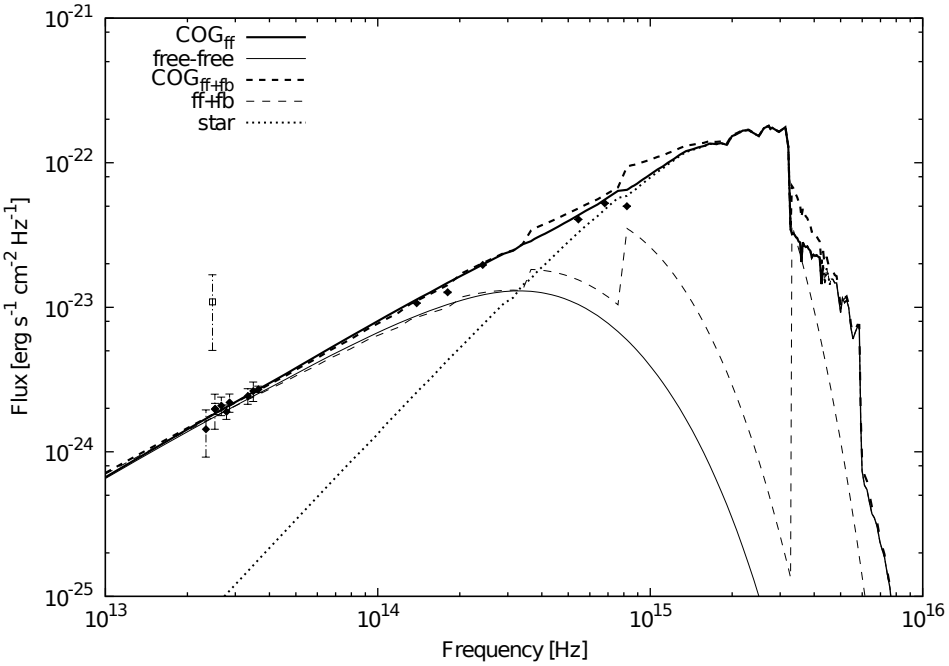

Figure 6.12: Kurucz atmosphere ($T_* = 33\,000$ K, $\log g = 4.0$) and COG method fitted to LS 2883 (Table 6.5). Shown in the figure is the fitted stellar atmosphere (thin dotted line), the predicted IR flux from the disc for free-free (thin solid line) and free-free+free-bound (thin dashed line) emission, and the total expected flux for star+free-free and star+free-free+free-bound (thick solid and thick dashed lines respectively) fitted to the data points in Table 6.5.

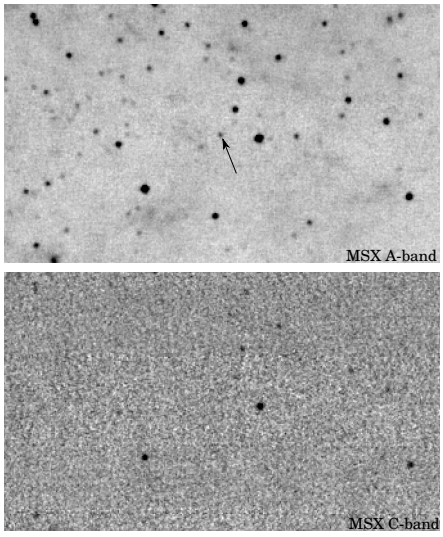

Figure 6.13: MSX map of the region of sky around PSR B1259-63. Top: A-band and the position of PSR B1259-63is indicated by the arrow. Bottom: C-band of the corresponding region.

Table 6.6: Fitting parameters of the COG method applied to Fig. 6.12, for free-free and free-free+free-bound (ff+fb) Gaunt factors, using the observational data in Table 6.5.

	free-free	ff+fb
n	3.0550	2.8389
$\log_{10} X_*$	10.245	9.9073
$R_{\rm disc}$	50 R_*	50 R_*
$T_{\rm disc}$	19 800 K	19 800 K
$\theta_{\rm disc}$	1°	1°

The calculated free-free+free-bound Gaunt factors create large discontinuities at frequencies $\gtrsim 2\times10^{14}$ Hz, while at frequencies below this the IR spectrum is dominated by free-free emission. These large fluctuations are not seen in COG fits to other Be stars discussed in Waters (1986) nor in the previous fit to LS 2883 (Fig. 6.11), as the COG model was calculated to a maximum frequency of $\approx 3\times10^{14}$ Hz, which is the limit of the tabulated Gaunt factors given in Waters and Lamers (1984). Below this frequency the influence of the free-bound emission is still minimal. A fit to the optical and IR data considering only free-free emission produces a smoother curve and this spectrum was adopted for the anisotropic modelling of the IC scattering from PSR B1259-63/LS 2883.

From the wavelength independent parameter $X_{*,d}$ given by equation (6.10) and fitted with the COG method, an estimate can be made of the density of the circumstellar disc. For the free-free fit (Fig. 6.12) it was assumed that H and CNO were ionized with one electron per ion resulting in a ratio of the number of electrons to the number of ions of $\varpi = 1$ and a mean atomic charge of $\bar{z} = 1$. From equation (6.10) and the fit $X_{*,d} = 10^{10.245}$ it can then be shown that

$$\begin{aligned}\frac{\rho_0}{\mu} &= \left[\frac{1}{4.923\times10^{35}} X_{*,d}\, T^{3/2} \left(\frac{R_*}{R_\odot}\right)^{-1}\right]^{1/2} \\ &= 1.039\times10^{-10}\ \text{g cm}^{-3},\end{aligned}$$

where ρ_0 is the density of the disc at the surface of the star and $\mu = \langle m_{\rm i}\rangle / m_{\rm p}$ is the mean mass of the ion in units of the proton mass. Assuming the mass of the ion is much larger than the mass of the electrons, the mass density can be approximated by $\rho_0 = n_{\rm i}\langle m_{\rm i}\rangle$ and therefore it follows that $\rho_0/\mu = n_{\rm i} m_{\rm p}$. Since the number of ions is equal to the number of electrons, i.e. $n_{\rm i} = n_{\rm e}$, the electron number density at the base of the disc ($r = R_*$) is $n_{\rm e} = (\rho_0/\mu)/m_{\rm p} \sim 6.22\times10^{13}$ cm^{-3}. As was discussed in Chapter 2 (section 2.1.2) this electron density results in the pulsed radio emission being completely obscured when the pulsar passes behind the circumstellar disc.

Chapter 7

Modelling the Compton spectrum

The main objective of this study is to investigate the influence the infrared (IR) excess, associated with the Be star, will have on the inverse Compton (IC) gamma-ray production in PSR B1259-63. It is believed that the pulsar wind nebula (PWN) surrounding the pulsar is the site of lepton acceleration (Chapter 4) and these particles interact with the photons from the combined star and disc system. The IC scattering of soft, infrared photons from the circumstellar disc can occur mainly in the Thomson limit, modifying the gamma-ray spectrum from the spectrum associated with a blackbody distribution of target photons. The effect of this IR excess has not been considered in previous studies of PSR B1259-63, nor for other gamma-ray binaries that contain Be stars, e.g. LSI+61 303. The first approach towards studying this effect utilized an isotropic approximation, the results of which have been published in van Soelen and Meintjes (2011). The study showed that the disc contribution increased the gamma-ray flux by a factor ~ 2 at GeV energies and based on this positive result a full anisotropic IC model has been developed. In this model the IC up-scattering of the anisotropic distribution of photons from the star and disc towards the observer has been considered around periastron. The model also incorporates the effects of the changing IC scattering angle and the solid angle subtended by the disc. A further complication is introduced by the geometry dependent optical depth through the circumstellar disc, which changes during the orbit, resulting in a varying IR excess.

The full, Klein-Nishina scattering kernels for isotropic (e.g. Blumenthal and Gould, 1970, equation 5.29) and anisotropic IC emission (Dubus et al., 2008; Fargion et al., 1997, equation 5.37) have been defined and discussed in Chapter 5. The total scattering rate is determined from the kernel by introducing the required photon and electron distributions, $n_{\rm ph}$ and $n_{\rm e}$ respectively, and integrating over the appropriate energy range and solid angle. For the isotropic approximation the integration is over a sphere while for the anisotropic modelling the exact solid angle subtending the star and disc from the position of the electron cloud must be determined.

This chapter begins with a discussion of the photon and electron distributions considered for the IC scattering (sections 7.1 & 7.2) before presenting the results related to the isotropic

(section 7.3) and anisotropic (section 7.4) modelling.

7.1 The photon density distribution

The photon distribution used for the IC scattering is determined by the intensity of the radiation from the star and the disc predicted by the COG model. For the isotropic modelling, only a single photon distribution was considered. This photon distribution was calculated from the flux predicted by the COG method (Fig. 6.11). For the anisotropic IC scattering, the photon distribution of the disc and the star must be treated separately as the photon number density depends on the direction of the incoming photons and varies over the solid angle. The parameters fitted by the COG method, utilizing the new colour excess and VLT data (Fig. 6.12) were used to predict the optical depth dependent IR emission associated with the disc. For the B-type star a blackbody photon distribution was considered.

The photon density can be determined from the modelled specific intensity, I_ν, as follows. The specific energy density per unit solid angle is given by (e.g. Rybicki and Lightman, 2004, pp. 1–8)

$$u_\nu(\Omega) = \frac{I_\nu}{c} \quad [\text{erg cm}^{-3}\ \text{Hz}^{-1}\ \text{ster}^{-1}]. \tag{7.1}$$

This is converted to the number of photons per unit volume per frequency per unit solid angle by dividing equation (7.1) by the photon energy ($\epsilon = h\nu$), giving

$$n_{\rm ph}(\nu) = \frac{u_\nu(\Omega)}{h\nu}.$$

This gives the number density per unit frequency, which is converted to the number density per unit energy as

$$\begin{aligned} n_{\rm ph}(\epsilon) &= \frac{\nu}{\epsilon} n_{\rm ph}(\nu) \\ &= \frac{n_{\rm ph}(\nu)}{h}. \end{aligned}$$

Therefore, by combining the above equations, the number of photons per unit energy per unit volume per unit solid angle is determined from the intensity by

$$n_{\rm ph}(\epsilon) = \frac{I_\nu}{h^2 \nu c} \ [\text{cm}^{-3}\ \text{erg}^{-1}\ \text{ster}^{-1}]. \tag{7.2}$$

Equation (7.2) is applicable to the anisotropic modelling, where the kernel must be integrated over the appropriate solid angle. For the isotropic scattering the photon distribution is considered to be uniformly distributed over a sphere and, therefore, the number of photons per unit energy

per unit volume can be found by

$$\begin{aligned} n_{\rm ph,iso}(\epsilon) &= \int n_{\rm ph}(\epsilon)\, d\Omega \\ &= n_{\rm ph}(\epsilon) \int_0^{2\pi} d\phi \int_0^{\pi} \sin\theta\, d\theta \\ &= \frac{4\pi I_\nu}{h^2 \nu c} \quad [{\rm cm}^{-3}\ {\rm erg}^{-1}]. \end{aligned} \tag{7.3}$$

If equation (7.3) is applied to an isotropic blackbody distribution, the intensity is determined by the Planck function and the photon number density is given by (e.g. Blumenthal and Gould, 1970)

$$n_{\rm ph,iso}(\epsilon) = \frac{1}{\pi^2(\hbar c)^3} \frac{\epsilon^2}{{\rm e}^{\epsilon/kT} - 1}.$$

The infrared excess from the circumstellar disc in PSR B1259-63/LS 2883 provides a large number of additional IR photons, which can enhance the expected IC spectrum. The specific intensity predicted by the COG model is (equations 6.13 & 6.14)

$$I_\nu(q) = \begin{cases} I_{\nu,*} & 0 \le q \le 1, \\ B_\nu(T_{\rm disc}) \left(1 - {\rm e}^{-\tau_{\rm max}(q)}\right) & 1 \le q \le R_{\rm disc}/R_*, \end{cases}$$

where q is the dimensionless impact parameter measured on the mid-plane of the disc (Fig. 6.2). The number of photons from the star and disc can be found from equation (7.2) by integrating over the appropriate solid angle. As is shown by equation (6.15), the integration over the solid angle can be written in terms of the impact parameter q and therefore

$$\begin{aligned} n_{\rm ph,tot} &= \frac{1}{h^2\nu c} \int I_\nu(q)\, d\Omega \\ &= \frac{1}{h^2\nu c} \left(\frac{R_*}{D}\right)^2 \int_0^{R_{\rm disc}/R_*} 2\pi I_\nu(q)\, dq \\ &= \left(\frac{F_{\nu,*}}{h^2\nu c}\right)_{\rm star} + \left(\frac{F_{\nu,{\rm disc}}}{h^2\nu c}\right)_{\rm disc}, \end{aligned}$$

which gives the number density scaled with the distance, D, to the source. To find the photon density at the source, it is necessary to correct for the scaling factor $(R_*/D)^2$. The total photon density is then given by the sum of the stellar and disc contributions, $n_{\rm ph,tot} = n_{\rm ph,star} + n_{\rm ph,disc}$. Fig. 7.1 plots the photon density of PSR B1259-63/LS 2883 (without scaling the flux with distance, i.e. $R_*/D = 1$) and shows the large increase in infrared photons that is introduced by the circumstellar disc. From Fig. 7.1 it can be seen that the combined Be star and disc system increases the IR photon density by more than an order of magnitude above that which is provided by the Be star alone. This presents interesting possibilities for gamma-ray production through IC scattering.

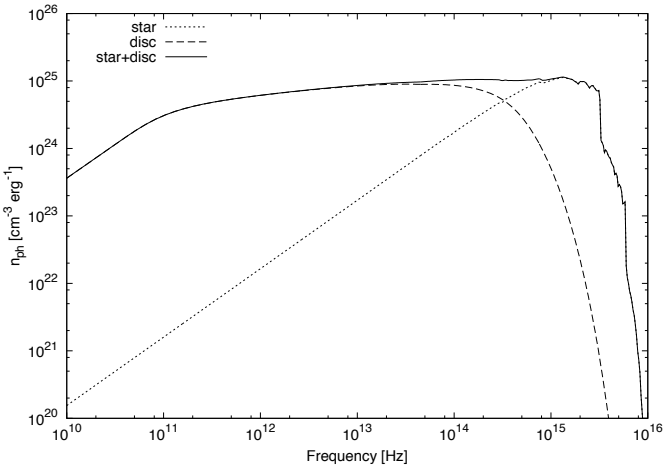

Figure 7.1: The photon number density (cm^{-3} erg^{-1}) for PSR B1259-63/LS 2883 (without scaling for distance), showing the stellar (dotted line), disc (dashed line) and total (solid line) contribution. The number density is derived from the observed and modelled flux for the system (Fig. 6.2).

7.2 The electron density distribution

A number of different electron distributions have been considered for the isotropic and anisotropic IC scattering, considering both pre-shock and post-shock electron distributions, which are applicable to PWNe. Each of these different distributions are discussed individually below.

7.2.1 Pre-shocked electrons

As discussed in section 4.2.2, the mono-energetic electrons in the pre-shock pulsar wind can radiate via IC scattering if there is an external source of photons. The IC scattering of the pre-shock pulsar wind was considered for PSR B1259-63 by Ball and Kirk (2000). The Lorentz factor of the pre-shock pulsar wind is typically of the order of $\gamma_p \sim 10^6$, based on modelling of the Crab Nebula, while the possibility of $\gamma_p \sim 10^4$ electrons has been suggested recently by Khangulyan et al. (2011a) to explain the post-periastron flare observed by *Fermi* after the December 2010 periastron passage (section 2.7). For the study of the isotropic approximation (van Soelen and Meintjes, 2011), published prior to the reported *Fermi* observations, only a pre-shocked wind of $\gamma = 10^6$ was considered while for the anisotropic approach both a $\gamma = 10^4$ and $\gamma = 10^6$ wind have been considered.

7.2.2 Post-shock electrons - adiabatic cooling

If the IC scattering occurs in the post-shock region, the injected electrons are assumed to initially have a power law distribution (equation 5.30),

$$n_{\rm e}(\gamma) = \begin{cases} K_{\rm e}\gamma^{-p} & \gamma_{\rm min} < \gamma < \gamma_{\rm max}, \\ 0 & \text{elsewhere}, \end{cases} \tag{7.4}$$

which results from re-acceleration in the shock front. In the post-shock region the electrons cool via radiative and adiabatic processes, which can modify the original shape of the spectrum. If only adiabatic cooling is considered, the shape of the electron spectrum does not change and keeps the original power law distribution. For the modelling that follows, in both the isotropic and anisotropic cases, a value of $K_{\rm e} = 1$ has been used. The constant $K_{\rm e}$ only gives weight to the electron spectrum and does not influence the spectral shape.

As discussed in Aharonian et al. (2005, see section 2.5, p. 14) the 2004 H.E.S.S. observations of PSR B1259-63 revealed a gamma-ray photon index of $\Gamma = 2.7$ which the authors suggest implies an electron index of $p \approx 2.2$. Using this electron index, two energy ranges were considered, $\gamma = 10^4 - 10^7$ and $\gamma = 10^6 - 10^7$, encompassing a broad and narrow electron distribution. This allows the effect of the IR excess from the circumstellar disc to be considered for a wide range of electron distributions.

A third example of a predominately adiabatically cooled electron distribution was adopted from Kirk, Ball, and Skjaeraasen (1999), where the authors considered both predominately adiabatic cooled electrons and radiative cooled electrons. The adiabatically cooled electrons are discussed here while the radiative cooled electrons are discussed in the following section (§ 7.2.3).[i] In the model presented by Kirk et al. (1999) the electrons are assumed to have an initial injection spectrum of the form given in equation (7.4). Following Kennel and Coroniti (1984a,b) the minimum Lorentz factor of the post-shock distribution is given by (Kirk et al., 1999)

$$\gamma_{\rm min} = \gamma_p \left(\frac{p-2}{p-1}\right)\left(\frac{1-\eta^{1-p}}{1-\eta^{2-p}}\right), \tag{7.5}$$

where γ_p is the Lorentz factor of the pre-shock electrons, p is the electron index and $\eta = \gamma_{\rm max}/\gamma_{\rm min}$ is the ratio between the maximum and minimum Lorentz factors. The variable η is adopted as a parameter of the model and it is assumed that $\eta = 100$ in all cases. Therefore, the maximum Lorentz factor is given by $\gamma_{\rm max} = \eta\gamma_{\rm min}$, and $\gamma_{\rm min}$ is determined from equation (7.5). The authors also introduce the parameter b, defined as the square root of the ratio between the synchrotron and IC power. Since $P_{\rm sync}/P_{\rm IC} = U_B/U_{\rm ph}$, where U_B and $U_{\rm ph}$ are the magnetic and photon energy density respectively (e.g. Rybicki and Lightman, 2004, pp. 199–202), the parameter b can

[i] It should be noted that the symbols used here are chosen to be consistent with this study. The symbols used in Kirk et al. (1999) are different to many of the symbols I have used here. I have used the same symbols to represent different quantities.

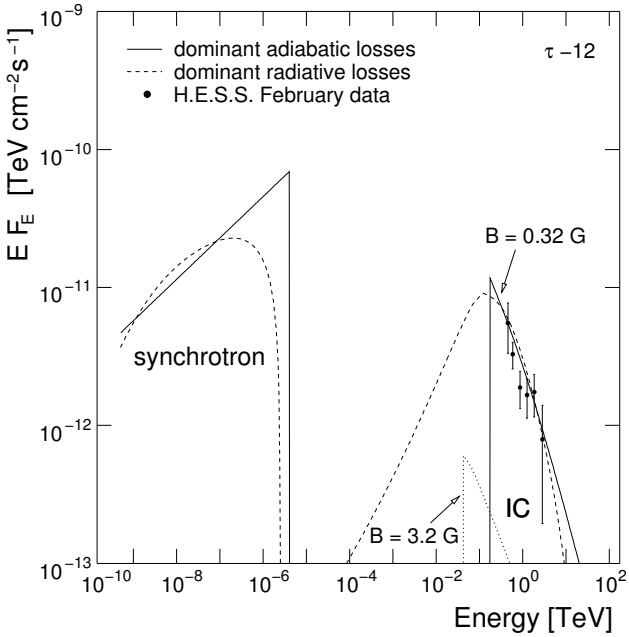

Figure 7.2: The 2004 H.E.S.S. observations of PSR B1259-63 compared to the different model predictions of the gamma-ray flux made by Kirk et al. (1999). Shown are the results for adiabatic and radiative cooled electrons, for two magnetic field strengths $B = 0.32$ and 3.2 G, which correspond to $b = 0.1$ and $b = 1$ respectively (Aharonian et al., 2005).

be defined as

$$b \equiv \sqrt{\frac{P_{\rm sync}}{P_{\rm IC}}} = \sqrt{\frac{B/8\pi}{\epsilon_0 n_{\rm ph}}}, \tag{7.6}$$

where Kirk et al. (1999) assumed that the target (stellar) photon distribution could be described by a mono-energetic distribution of energy ϵ_0. The authors considered two scenarios for the synchrotron and IC power; first for equal emission power, i.e. $P_{\rm sync} = P_{\rm IC}$ or $b = 1$, and second for the IC power dominating the synchrotron power, i.e. $P_{\rm sync} = 0.01 P_{\rm IC}$ or $b = 0.1$.

From X-ray observations of the source the authors constrained the injection (adiabatic) spectrum and the pre-shock Lorentz factor, assuming the X-ray emission is produced via synchrotron radiation (see Kirk et al., 1999, and references therein for a detailed discussion). Assuming the IC power dominates over the synchrotron power (i.e. $b = 0.1$), the electron spectrum was found to have an index of $p = 2.4$, and the pre-shock wind was found to have a Lorentz factor of $\gamma_p = 1.6 \times 10^6$. This implies a minimum and maximum post-shock Lorentz value of $\gamma_{\rm min} = 5.4 \times 10^5$ and $\gamma_{\rm max} = 5.4 \times 10^7$ (equation 7.5). This model spectrum for $b = 0.1$ was found to be comparable to the H.E.S.S. observations after the 2004 TeV detection (Fig. 7.2), and therefore the resulting electron distribution was adopted in this study.

All three of these distributions were considered for the isotropic modelling and, as shown in van Soelen and Meintjes (2011), produce a factor ~ 2 increase in the flux. Since the distribution

proposed by Kirk et al. (1999) is believed to be a more realistic approach to model the electron distribution in the PWN, only this adiabatically cooled electron distribution was considered for the anisotropic modelling.

7.2.3 Post-shock electrons - radiative cooling

When the electrons in the post-shocked region are predominately cooled by radiative processes, the electron distribution cannot be described by a simple power law. While the post-shocked electrons initially have a power law distribution, this is modified as the electrons lose energy via synchrotron and/or IC radiation. Following from Kirk et al. (1999), if the injection electron distribution is of the form given in equation (7.4), the radiatively cooled, modified electron distribution is given by

$$n_{\mathrm{e}}(\gamma) = \begin{cases} \dfrac{K_{\mathrm{e}}}{4\pi(p-1)} \dfrac{\gamma^{1-p} - \gamma_{\mathrm{max}}^{1-p}}{(\langle -\dot{\gamma}_{\mathrm{ic}} \rangle + \langle -\dot{\gamma}_{\mathrm{s}} \rangle)} & \text{for } \gamma_{\mathrm{min}} < \gamma < \gamma_{\mathrm{max}} \\ \\ \dfrac{K_{\mathrm{e}}}{4\pi(p-1)} \dfrac{\gamma_{\mathrm{min}}^{1-p} - \gamma_{\mathrm{max}}^{1-p}}{(\langle -\dot{\gamma}_{\mathrm{ic}} \rangle + \langle -\dot{\gamma}_{\mathrm{s}} \rangle)} & \text{for } \gamma < \gamma_{\mathrm{min}} \end{cases},$$

where $\langle \dot{\gamma}_{\mathrm{ic}} \rangle$ and $\langle \dot{\gamma}_{\mathrm{s}} \rangle$ represent the average rates of change of the Lorentz factor due to IC scattering and synchrotron radiation respectively. This modulation of the electron spectrum is based on Tavani and Arons (1997) and the values for the rates of change are presented in Appendix C.1.

In order to duplicate the electron distribution in Kirk et al. (1999), the effects of radiative cooling were calculated assuming the photon density is given by

$$n(R) = \frac{L_*}{4\pi R^2 c \epsilon_0},$$

where L_* is the stellar luminosity and ϵ_0 is the energy of the (assumed) mono-energetic target photon spectrum. For the analysis a luminosity of $L_* = 8.8 \times 10^3$ $\mathrm{L}_\odot$ and a target photon energy of $\epsilon_0 = 2.7 k T_{\mathrm{eff}}$ was assumed, with an effective temperature of $T_{\mathrm{eff}} = 22\,800$ K (following Kirk et al., 1999). If IC power dominates over the synchrotron power, i.e $b = 0.1$ as given by equation (7.6), the authors found an initial particle index of $p = 1.4$, and a pre-shock Lorentz factor of $\gamma_p = 5 \times 10^6$, which implies an energy range $\gamma = 4.3 \times 10^5 - 4.3 \times 10^7$ for $\eta = 100$ (see Kirk et al., 1999, for details). This spectrum also shows a qualitative fit to the H.E.S.S. observations.

This simplified modelling, which was applied to the isotropic case, cannot be readily extended to the more complicated star/disc scenario and the simplified mono-energetic photon cooling was considered to be a much less realistic approximation for the anisotropic case. Therefore, radiative cooling, and the additional modelling that it would require, was not considered for the anisotropic case. Based on the isotropic modelling, which shows that both the radiatively and adiabatically

cooled electron distributions increase the scattering rate by a factor ~ 2, it is believed that the radiatively cooled spectrum will increase the IC scattering by a similar factor as the adiabatically cooled spectrum.

It is not an unreasonable assumption that adiabatic cooling dominates near the stand-off shock, as the synchrotron radiative cooling time is (equation 4.16)

$$t_{\rm sync} \sim 770 \left(\frac{\gamma}{10^6}\right)^{-1} \left(\frac{B}{1\ {\rm G}}\right)^{-2}\ {\rm sec},$$

which, if the particles are travelling near the speed of light, implies the electrons traverse a distance

$$\begin{aligned} D_{\rm sync} &= c \times t_{\rm sync} \\ &\sim 2.3 \times 10^{13}\ {\rm cm}, \\ &\sim 36 R_*, \end{aligned}$$

before cooling. This is comparable with the assumed size of the circumstellar disc ($R_{\rm disc} \approx 50 R_*$), and therefore near the stand-off shock only adiabatic cooling is dominant.

7.3 Modelling the isotropic IC gamma-ray spectrum

The first attempt to investigate the influence of the IR excess was performed using an isotropic distribution. The results of this study have been presented in van Soelen and Meintjes (2011), which is included here.

Monthly Notices
of the
ROYAL ASTRONOMICAL SOCIETY

Mon. Not. R. Astron. Soc. **412,** 1721–1729 (2011) doi:10.1111/j.1365-2966.2010.18008.x

The effect of the infrared excess from the Be star on inverse Compton gamma-ray production in PSR B1259−63/SS 2883

B. van Soelen★ and P. J. Meintjes

Department of Physics, University of the Free State, Bloemfontein 9300, South Africa

Accepted 2010 November 9. Received 2010 November 1; in original form 2010 August 17

ABSTRACT

The binary system PSR B1259−63 consists of a 48-ms pulsar in a 3.4-yr orbit around a Be star, and unpulsed TeV gamma-ray emission has been detected near previous periastron passages. A likely source of the gamma-rays is the inverse Compton upscattering of target photons from the Be star by the ultrarelativistic electron/positron pulsar wind in the region of the plerion shock front. In this study, the effect of the infrared emission from the Be star's circumstellar disc on inverse Compton gamma-ray production in PSR B1259−63 is investigated by considering an isotropic photon/electron approximation. The modified photon density distribution is determined by using a curve of growth method fitted to previous optical and infrared observations. The inverse Compton scattering rate is calculated using the modified photon distribution and the exact scattering equation. It is shown that including the infrared emission increases the GeV gamma-ray flux by a factor of $\gtrsim$2.

Key words: radiation mechanisms: non-thermal – pulsars: individual: PSR B1259−63 – X-rays: binaries.

1 INTRODUCTION

Be stars – defined as B-type stars showing or having showed emission lines instead of absorption lines in the Balmer spectrum (Collins 1987) – are known to produce an infrared (IR) flux which is higher than predicted by Kurucz stellar atmosphere models (Kurucz 1979). It has long been speculated that Be stars possess an extended circumstellar envelope or disc (e.g. Struve 1931), and optical interferometry observations confirm the presence of an extended circumstellar envelope which is symmetrical around the rotation axis (see e.g. Quirrenbach et al. 1994). These circumstellar discs act as reverse accretion discs as they are regions (confined to a disc structure) of increased stellar outflow. The free–free and free–bound emission which occurs in the disc is presumably responsible for the observed IR excess. These discs also show great variability and grow and shrink over periods of hundreds to thousands of days. For a review of classical Be stars, see e.g. Porter & Rivinius (2003).

An important Be X-ray pulsar binary (Be-XPB) example is the TeV gamma-ray system PSR B1259−63 which consists of a 48-ms pulsar in orbit around a Be star, SS 2883, and was initially detected as part of a radio survey of the southern Galactic plane (Johnston et al. 1992, 1994). The orbit is eccentric ($e \approx 0.87$), and unpulsed TeV gamma-ray emission has been detected by High Energy Stereoscopic System (HESS)[1] close to the periastron passage (Aharonian et al. 2005, 2009). The circumstellar disc is misaligned to the orbital plane and the pulsar is believed to pass through it twice: before and after periastron. Previous observations have also detected unpulsed radio emission near periastron (e.g Johnston et al. 1999) and the system has been observed at X-ray frequencies across the whole orbit (see e.g. Cominsky, Roberts & Johnston 1994; Kaspi et al. 1995; Chernyakova et al. 2006, 2009). These observations show that the unpulsed emission is variable at all wavelengths with respect to the orbital period.

The system is powered by the spin-down luminosity of the pulsar, and the unpulsed radiation is believed to originate from a stand-off shock front between the pulsar and stellar wind; extensive modelling has been presented in Tavani & Arons (1997). In this model the X-rays are produced via synchrotron radiation of ultrarelativistic electrons (Lorentz factor $\gamma \sim 10^6$) and the gamma-ray emission through the inverse Compton (IC) scattering of target photons from the Be star. The ratio between the X-ray and gamma-ray flux is dependent on the radiative and adiabatic cooling times of the post-shocked wind, and IC cooling was predicted to increase near periastron. IC cooling of the pre-shocked wind was also suggested by Ball & Kirk (2000).

★E-mail: vansoelenb@ufs.ac.za

[1] Located near the Gamsberg Mountain in Namibia, consists of four Cherenkov imaging telescopes.

Table 1. Optical magnitudes and colours for SS 2883.

Catalogue	LSS	Spectral type	V	$B-V$	$U-B$	$(U-B)_0$	A_v	$M_v(U-B)_0$
Westerlund & Garnier (1989)	2883	OB+ce,1e,h	10.01	0.754	−0.506	−1.261	3.25	−4.6
Klare & Neckel (1977)	2883		10.04	0.74	−0.44			
Schild, Garrison & Hiltner (1983)	2883		10.05	0.72	−0.47			
Drilling (1991)	2883		10.07	0.73	−0.47			

A slower wind model has also been proposed (Chernyakova & Illarionov 1999, 2000) where the pulsar wind has a Lorentz factor of $\gamma \sim 10$–100 and upscatters the target photons from the Be star via IC processes to X-ray energies. The TeV gamma-rays are then explained via the interaction of the pulsar with the circumstellar disc and are the result of proton–proton collisions, IC scattering and bremsstrahlung emission (Kawachi et al. 2004; Chernyakova et al. 2006).

If the TeV gamma-rays are the result of IC scattering of target photons from the Be star, this implies that electron energies are of the order of TeV and the observed TeV gamma-rays are the result of scattering which occurred in the Klein–Nishina limit. While previous models have considered IC scattering in the general case, there are currently only TeV gamma-ray observations of PSR B1259−63 and the emphasis has been to model the TeV emission which will occur in the Klein–Nishina limit. Previous models have not considered how the scattering of the IR excess from the circumstellar disc, occurring in the Thomson limit, will influence the gamma-ray production.

It can be shown (e.g. Blumenthal & Gould 1970) that IC scattering between a relativistic electron with a Lorentz factor γ and a photon with a frequency ν will occur in the classical Thomson limit if

$$\nu \ll \frac{m_e c^2}{h\gamma}, \tag{1}$$

where h, m_e and c represent Planck constant, the electron mass and the speed of light, respectively. To explain the results of previous HESS observations of PSR B1259−63, Aharonian et al. (2005) proposed that electrons are accelerated in the shock between the pulsar ($\gamma \sim 10^6$–10^7) and stellar wind, resulting in the IC scattering of stellar photons. This scattering will occur in the Thomson limit for target photons with frequency $\nu \ll 10^{14}\ (\gamma/10^6)^{-1}$ Hz, i.e. radio to IR. The IR excess provides an additional reservoir of soft target photons for IC scattering and an attractive framework to explain gamma-ray production through IC scattering in the Thomson limit, where the cross-section is significantly higher than the Klein–Nishina limit. A more detailed discussion, especially focussing on the IC spectral properties, will be presented in Section 4.

Since the IR excess is tied to the growth and decay of the circumstellar disc, the size of the disc near periastron will influence gamma-ray production not only through the constraints on the plerion shock, but also through IC scattering in the Thomson limit.

This study will discuss the effect of the IR excess on IC gamma-ray production in Be-XPBs using PSR B1259−63 as a trial case. Results of modelling the full IC scattering spectrum (Thomson and Klein–Nishina limits) of an isotropic distribution of photons and electrons will be presented here as an initial argument towards the importance of the contribution of the IR excess. The additional effects of the different electron-cooling processes in the plerion shock front and the changing scattering angle, due to orbital motion, will not be discussed at this time as the goal of this paper is to validate the importance of the IR excess on IC gamma-ray production. In order to include the IR excess, the target photon distribution will be determined using the curve of growth method proposed by Lamers & Waters (1984; referred to hereafter as the COG method) fitted to previous optical and IR observations.

An outline of previous observations and studies of PSR B1259−63 will be presented (Section 2) before discussing the COG method (Section 3) and IC scattering (Section 4). Section 5 will outline the modelling undertaken in this study and Sections 6 and 7 will discuss the results and implications thereof.

2 PSR B1259−63/SS 2883

While this paper focuses only on one aspect of the multiwavelength emission from PSR B1259−63, a complete model needs to take into account all wavelengths to accurately explain the radiative processes in the system. Below, a brief summary is given of previous observations and modelling of the system which is relevant to the discussion presented in this paper.

There have been few photometric observations of SS 2883, the optical companion to PSR B1259−63, but some measurements are available in bright star catalogues (Table 1). For example, Westerlund & Garnier (1989) presented photometric and visual extinction measurements for SS 2883 as part of their catalogue of OB stars near the Southern Coalsack. Comparison of the catalogue's observations shows little change in the optical magnitude. From this and other observations, Johnston et al. (1994) confined the spectral range of SS 2883 to a O9-B2 type star and assumed a spectral type B2e, with $M_* \simeq 10\,\mathrm{M}_\odot$ and $R_* \simeq 6\,\mathrm{R}_\odot$. Johnston et al. (1994) also undertook spectroscopic observations of the system and observed double peak Hβ, Hγ, Hδ and He I 5876 emission lines. Analysis showed that the Hβ emission occurred at a radius of $8.5R_*$, assuming a Keplerian circumstellar disc, which infers a circumstellar disc radius $R_{\mathrm{disc}} > 8.5R_*$.

There are also few observations in the mid-to-near IR, but observations are available from the Two Micron All Sky Survey (2MASS; Skrutskie et al. 2006) and *Midcourse Space Experiment* (*MSX*)[2] (Price et al. 2001) missions. The IR data is shown in Table 2. Due to the large uncertainty in the C-band measurement, it was not considered when modelling this system.

In addition to the pulsed radio signal, an unpulsed radio signal has been detected from the system close to periastron (see e.g. Johnston et al. 2005). Observations of the system during consecutive periastron passages show an eclipse of the pulsar – and a decrease in the unpulsed synchrotron emission – roughly 20 d before and after periastron passage as it passes through and behind the circumstellar disc. For example, the pulsar eclipse lasted from 16 d before until 18 d after periastron during the 2000 passage (Connors et al. 2002) and

[2] Data from 2MASS and the *MSX* are available online through the NASA/IPAC Infrared Science Archive.

Table 2. IR data for PSR B1259−63 from 2MASS (J, H, K_s) and *MSX* (A, C).

Band	Wavelength (μm)	Magnitude	Flux (Jy)
J	1.235	8.026 ± 0.027	
H	1.662	7.699 ± 0.055	
K_s	2.159	7.248 ± 0.020	
A	8.28		0.2675 ± 0.0136
C	12.13		1.087 ± 0.5859

from 15.8 d before until 16.1 d after periastron during the 2004 passage (Johnston et al. 2005). At 16–20 d from periastron, the binary separation is ≈40–50R_*, assuming $M_{\rm pulsar} = 1.4\,{\rm M}_\odot$, which implies that the circumstellar disc must at least extend to these distances. While the synchrotron radio observations show many similarities, there are marked differences in the flux levels during consecutive periastron passages, attributed to variations in the circumstellar disc and material (see e.g. fig. 3 and discussion in Johnston et al. 2005).

As a result of the alignment of the unpulsed radio, X-ray, and the 2004 HESS light curves into two peaks around the same two orbital phases (before and after periastron passage), Chernyakova et al. (2006) suggested that the peaks in radio and X-ray, and the production of gamma-rays, was due to the pulsar passing through the disc. This implied a circumstellar disc with a half-opening angle 18°.5, inclined 70° to the orbital plane. This suggested disc geometry is, however, inconsistent with the radio eclipse (Khangulyan et al. 2007). In addition, the detection of TeV gamma-rays 47 d before the 2007 periastron passage, misaligned to the orbital phase position proposed above, suggests that IC scattering still plays a dominant role in gamma-ray production (Aharonian et al. 2009).

The exact position of the circumstellar disc and details behind the observed unpulsed radio, X-ray and gamma-ray emission (slow wind, $\gamma \sim 10^2$, or fast wind, $\gamma \sim 10^6$) remain unsolved and the observations of PSR B1259−63 by *Fermi* around the next periastron passage may help answer these questions. In this study, we assume that the electrons have a Lorentz factor $\gamma \sim 10^6$ and that the X-ray emission is the result of synchrotron radiation, while the gamma-rays are produced through IC scattering. Under this assumption, we present results of the full IC scattering of the Be star's photon spectrum taking into account the IR excess produced by the disc.

3 THE LAMERS AND WATERS CURVE OF GROWTH METHOD

In this paper, the COG method proposed by Lamers & Waters (1984) has been chosen to model the IR excess from the circumstellar disc. This method allows for some prediction of the variability of the IR excess that will occur because of the changing size of the disc. The method, as discussed in Lamers & Waters (1984), Waters (1986) and Telting et al. (1998), is summarized below.

Under the COG method it is assumed that the circumstellar disc has a half-opening angle θ, extends to a radius $R_{\rm disc}$ and has a power-law density profile that decreases with distance as

$$\rho(r) = \rho_0 \left(\frac{r}{R_*}\right)^{-n}.$$

For a Be star–disc system viewed face-on, the flux ratio between the disc and star is given by (Telting et al. 1998)[3]

$$\frac{F_{\nu,\rm disc}}{F_{\nu,*}} = \frac{B_\nu(T_{\rm disc})}{I_{\nu,*}} \int_1^{R_{\rm disc}/R_*} [1 - {\rm e}^{-2\tau_\nu(q)}]\, 2q\, {\rm d}q, \quad (2)$$

where $F_{\nu,*}$ is the flux from the star and $F_{\nu,\rm disc}$ is the flux from the disc, $B_\nu(T_{\rm disc})$ is the Planck blackbody function, $T_{\rm disc}$ is the temperature of the disc, $I_{\nu,*}$ is the intensity from the appropriate Kurucz model for the star and q is the impact parameter in units of the stellar radius. The optical depth, $\tau_\nu(q)$, is given by (Waters 1986)

$$\tau_\nu(q) = E_{\nu,\rm disc}\, q^{-2n+1} C(n, \theta),$$

where

$$C(n, \theta) = \int_0^\theta \cos^{2n-2} y\, {\rm d}y,$$

where θ, the half-opening angle, is in radians and $E_{\nu,\rm disc}$ is defined as the optical depth parameter for the disc. This parameter is given by

$$E_{\nu,\rm disc} = X_\lambda X_{*\rm d}$$

where

$$X_\lambda = \lambda^2 \{(1 - {\rm e}^{-h\nu/kT_{\rm disc}})/(h\nu/kT_{\rm disc})\} \times \{g(\nu, T_{\rm disc}) + b(\nu, T_{\rm disc})\}$$

and

$$X_{*\rm d} = 4.923 \times 10^{35} \overline{z^2} T_{\rm disc}^{-3/2} \mu^{-2} \xi \rho_0^2 \left(\frac{R_*}{{\rm R}_\odot}\right),$$

where λ is the wavelength, ν is the frequency, k is the Boltzmann constant, $g(\nu, T_{\rm disc}) + b(\nu, T_{\rm disc})$ is the sum of the free–free and free–bound gaunt factors,[4] $\overline{z^2}$ is the mean of the squared atomic charge, μ the mean atomic weight (units of proton mass) and ξ the ratio of the number of electrons to the number of ions.

The COG method can then be used to model a Be star's optical/IR flux by modifying a Kurucz model atmosphere at IR wavelengths with the flux ratio given by equation (2), which is calculated by fitting the five parameters n, X_*, $R_{\rm disc}$, $T_{\rm disc}$ and θ to IR data. The Kurucz model atmosphere is chosen by a least-squares fit to the optical data, which is assumed to be less affected by the IR excess. In practise, however, assumed values are taken for the disc temperature (taken to be a fraction of the stellar temperature) and half-opening angle. The temperature ratio, $T_{\rm disc} = 0.8T_*$, used in Lamers & Waters (1984), Waters (1986) and Telting et al. (1998) has been argued to be too high by Millar & Marlborough (1999) from their analysis of the energy gain/loss rate in four Be stars. For this reason, a lower temperature ratio of $T_{\rm disc} = 0.5T_*$ will be used in this study instead. From the pulsar eclipse, a last constraint can be placed on the disc radius and $R_{\rm disc} = 50R_*$ will be used in most instances. This corresponds to the separation between the pulsar and Be star at the start of the pulsar eclipse. In fact, from polarization and rotation measurements made around the 1994 periastron passage, Johnston

[3] In order to keep the notation consistent within this paper, $R_{\rm disc}$ is in units of centimetres and the integration in equation (2) is from 0 to ($R_{\rm disc}/R_*$). This is different to equation (6) in Telting et al. (1998), where the integration is from 0 to $R_{\rm disc}$, but $R_{\rm disc}$ is in units of stellar radii. In addition, the optical depth, $\tau(q)$, in Telting et al. (1998; their equations 2 and 6) is equivalent to $2\tau_\nu(q)$ as is given here, when the disc is viewed face-on.

[4] The free–free + free–bound gaunt factors published in tabular form in Waters & Lamers (1984) for wavelengths between 10^{-4} and 6 cm were used in this study.

et al. (1996) suggested that the pulsar begins to pass into the disc ∼100 d before and after periastron at a distance of $\sim 150 R_*$.

With this additional constraint on the disc radius, there are only two free parameters (n and X_*) which must be fitted to match the IR excess.

4 INVERSE COMPTON SCATTERING

A very brief discussion of IC scattering, presenting only the results relevant for this study, will now be given. For detailed reviews, see e.g. Blumenthal & Gould (1970) and Rybicki & Lightman (2004).

IC scattering involves the upscatter of photons to higher energies by relativistic electrons. It can be shown (e.g. Blumenthal & Gould 1970) that the interaction between relativistic electrons with velocity $\beta = v/c$ and photons with energy $h\nu$ results in the photons being upscattered to energies

$$\epsilon_\gamma \approx 4\gamma^2 h\nu$$

in the Thomson limit ($\gamma h\nu \ll m_e c^2$), and

$$\epsilon_\gamma \approx \gamma m_e c^2$$

in the extreme Klein–Nishina limit ($\gamma h\nu \gg m_e c^2$ and $\beta \rightarrow 1$). Although in the Thomson limit, the characteristic energy of the scattered photon is increased by a factor of $\sim\gamma^2$, it is still small compared to the energy of the relativistic electron. In the case of scattering in the ultrarelativistic limit, the scattered photon energies are limited by the electron energies.

In a single scattering event (a single electron scattering a single photon), the energy of the electron before scattering is given by $\gamma m_e c^2$ and the energy of the photon, before and after scattering, by ϵ and ϵ_1, respectively. By expressing the energy of the scattered photon in units of the electron rest-mass energy, i.e. $E_1 = \epsilon_1/\gamma m_e c^2$, the scattering rate per unit energy, for a single electron interacting with an isotropic photon density distribution $n(\epsilon)$ (i.e. number density of photons per unit energy), is expressed as (Blumenthal & Gould 1970)

$$\frac{\mathrm{d}N_{\gamma,\epsilon}}{\mathrm{d}t\,\mathrm{d}E_1} = \frac{2\pi r_0^2 m_e c^3}{\gamma}\frac{n(\epsilon)\,\mathrm{d}\epsilon}{\epsilon} \times \left[2q\ln q + (1+2q)(1-q) + \frac{1}{2}\frac{(\Gamma_\epsilon q)^2}{1+\Gamma_\epsilon q}(1-q)\right], \quad (3)$$

where

$$\Gamma_\epsilon = \frac{4\epsilon\gamma}{m_e c^2}, \qquad q = \frac{E_1}{\Gamma_\epsilon(1-E_1)}$$

and r_0 represents the classical electron radius. This is the exact expression for the scattering rate and is appropriate for all energies, provided that $\gamma \gg 1$, with E_1 within the range

$$\frac{\epsilon}{\gamma m_e c^2} \leq E_1 \leq \frac{\Gamma_\epsilon}{1+\Gamma_\epsilon}.$$

In equation (3), $n(\epsilon)\,\mathrm{d}\epsilon$ is the differential photon number density and in the case of a blackbody distribution of photons is (e.g. Blumenthal & Gould 1970)

$$n(\epsilon) = \frac{1}{\pi^2(\hbar c)^3}\frac{\epsilon^2}{\mathrm{e}^{\epsilon/kT}-1}.$$

To extend the calculations to multiple electron scatterings, an electron distribution function needs to be considered. This distribution is normally expressed as a power-law function e.g.

$$N_e(\gamma) = K_e\gamma^{-p}, \qquad \gamma_{\min} < \gamma < \gamma_{\max},$$
$$= 0, \qquad \text{elsewhere}, \quad (4)$$

where the distribution is confined to the energy region $\gamma_{\min}$ to $\gamma_{\max}$. The total scattering rate per energy for an electron distribution is then found by integrating over the initial electron and photon energies, i.e.

$$\frac{\mathrm{d}N_{\text{total}}}{\mathrm{d}t\,\mathrm{d}\epsilon_1} = \int_\epsilon\int_\gamma N_e(\gamma)\times\left(\frac{1}{\gamma m_e c^2}\frac{\mathrm{d}N_{\gamma,\epsilon}}{\mathrm{d}t\,\mathrm{d}E_1}\right)\mathrm{d}\gamma\,\mathrm{d}\epsilon. \quad (5)$$

5 MODELLING THE IC SCATTERING

5.1 Modelling the infrared excess

The optical and IR data used to model PSR B1259−63 in this paper is taken from Westerlund & Garnier (1989), 2MASS and *MSX* (Tables 1 and 2). The IR and optical data were dereddened with the DIPSO software package using the extinction measurement given in Westerlund & Garnier (1989) and following the assumptions of Johnston et al. (1994).

The initial Kurucz atmosphere fits were done using the Kurucz (1992) model atmospheres obtained from the Space Telescope Science Institute.[5] The tables only begin at a minimum frequency of $\sim 3.3 \times 10^{13}$ Hz and needed to be extended further into the IR regime. The last few data points lie within the Rayleigh–Jeans limit ($h\nu \ll kT$) for a stellar temperature of ∼20 000 K, and since in this limit $\log I_{\nu,*} \propto \log\nu$, the data points were extended to $\nu \approx 5.2 \times 10^9$ Hz (or $\lambda \sim 6$ cm) using a straight line fit.

The stellar temperature, T_*, and effective gravity, $\log g$, were determined by finding the best least-squares fit of the Kurucz model atmospheres to the optical data above 3×10^{14} Hz (in order to limit the influence of the IR excess on the optical fit). The decrease in flux due to distance to the source from Earth (d) was also accounted for by scaling the intensity with the parameter $Y_{\text{shift}} = \log(\pi R_*^2) - \log(d^2)$ (Telting et al. 1998). A best-fitting temperature and effective gravity of $T_* = 25\,000$ K and $\log g = 3.5$, respectively, were found, consistent with an early B-type star.

The IR excess was then fitted to the IR data using the COG method. The disc temperature was chosen to be $T_{\text{disc}} = 0.5T_* = 12\,500$ K and the disc radius $R_{\text{disc}} = 50R_*$ as was inferred from the pulsar eclipse. In this paper, the convention used by Telting et al. (1998) was followed and the half-opening angle was held at $\theta = 5^\circ$. The remaining two parameters (n and X_*) were simultaneously fitted with the Levenberg–Marquardt method using the implementation in the ORACLE software package. This produced a best fit of $n = 2.37$ and $\log X_* = 7.87$ and the resulting fit is plotted in Fig. 1. Fits using the larger half-opening angle ($\theta \sim 18.^\circ5$) suggested by Chernyakova et al. (2006) were also considered but produced no noticeable effect on the fitted optical/IR spectrum. The values are summarized in Table 3.

As a further check on these model simulations, COG fits were produced using the data and parameters given in Waters (1986) and Telting et al. (1998) for δ Cen and X Persei, respectively. These models were compared to the published results and were found to match extremely well.

5.2 Modelling the IC gamma-ray spectrum

The total number of IC scatterings is calculated from equation (5) and the photon distribution $n(\epsilon)$ is derived from the predicted flux as is given by the COG fit. This is different to previous models

[5] http://www.stsci.edu/science/starburst/Kurucz.html

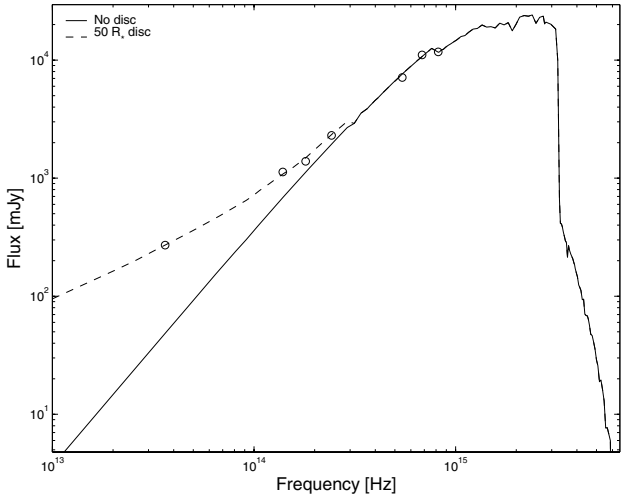

Figure 1. A Kurucz stellar atmosphere (solid line) and the modification created by the COG method (dashed line) fitted to data for PSR B1259−63/SS 2883. The open circles are the optical and IR data points.

Table 3. Optical and IR fit to PSR B1259−63.

Optical fit		
$T_{\rm eff}$	25 000 K	
$\log g$	3.5	
$Y_{\rm shift}$	−19.14	
COG fit		
n	2.37	2.37
$\log X_*$	7.87	7.32
$R_{\rm disc}$	$50R_*$	$50R_*$
$T_{\rm disc}$	12 500 K	12 500 K
θ	5°	18.°5

where either a blackbody or mono-energetic photon spectrum was assumed. The integration over ϵ was performed for the range $\epsilon = 3.45 \times 10^{-17}$ to 4.23×10^{-10} erg ($\sim 5.2 \times 10^{9}$–6.4×10^{16} Hz). At these limits, the ratio $n(\epsilon_{\rm limit})/\max(n(\epsilon))$ is 1.13×10^{-5} and 1.60×10^{-39}, respectively. The integration over γ was performed between the given $\gamma_{\rm min}$ and $\gamma_{\rm max}$ limits for each electron distribution case.

The electron distribution, $N_{\rm e}$, in the IC calculation depends on where the electrons are assumed to originate, and what additional cooling processes are applicable. The examples of pre-shocked, post-shocked adiabatic cooling and post-shocked radiative cooling are presented below. Since the aim of this study is to show the relative change in the flux of the gamma-ray spectrum, the models are not calibrated to fit the HESS data and two simplifying assumptions have been made in the analysis below; the value of $K_{\rm e} = 1$ was adopted for all cases and the photon density has not been scaled to the distance of the pulsar. Scaling the photon density simply decreases the overall gamma-ray flux by a constant value and does not change the relative shape.

5.2.1 *Pre-shocked electrons*

The possibility that IC scattering may occur in the pre-shocked region surrounding the pulsar has been discussed by Ball & Kirk (2000). In such a scenario, the pulsar wind would have an approximate mono-energetic distribution around $\gamma \sim 10^6$. Fig. 2 presents this scenario, which was calculated from equation (5) without integrating over γ. The scattering rate shows a significant increase when the IR excess is included.

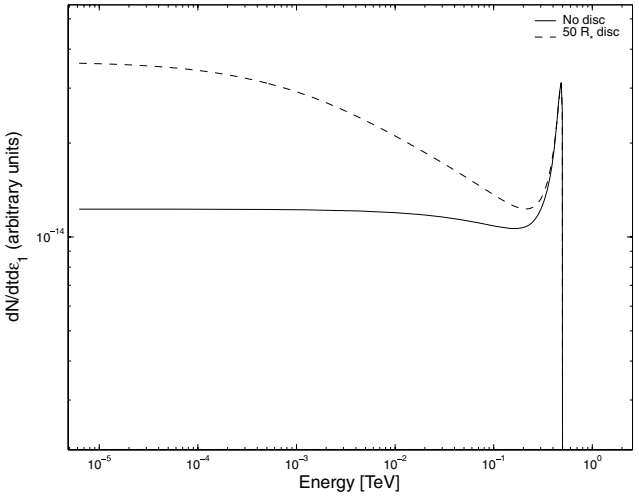

Figure 2. The predicted total scattering rate, $\mathrm{d}N_{\rm tot}/\mathrm{d}t\,\mathrm{d}\,\epsilon_1$, calculated for a mono-energetic electron $\gamma = 10^6$. The solid line is the expected gamma-ray flux without an IR excess and the dashed line shows the increased gamma-ray flux when the IR excess is included.

5.2.2 *Post-shock electrons – adiabatic cooling*

If cooling is dominated by adiabatic cooling in the post-shock region, the electron distribution is assumed to be a power law ($N_{\rm e} = \gamma^{-p}$). The HESS observations of PSR B1259−63 suggest that $p \approx 2.2$ (Aharonian et al. 2005) and this was adopted as a first approximation. Two energy ranges for γ were considered, $\gamma = 10^4$–10^7 and $\gamma = 10^6$–10^7, encompassing a broad and narrow electron distribution. The resulting scattering rates are shown in Figs 3 and 4, respectively. For the broad electron distribution, there is negligible influence on the gamma-ray flux when the IR excess is included. For the higher energy, narrow-band electron distribution, this is not the case and there is a significant increase in the scattering rate.

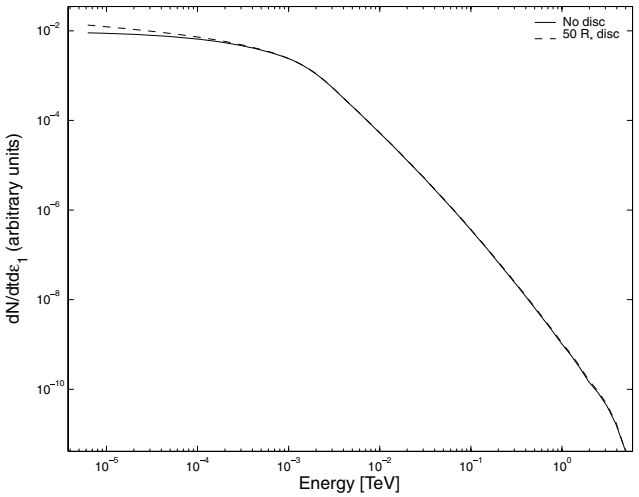

Figure 3. The predicted total scattering rate, $\mathrm{d}N_{\rm tot}/\mathrm{d}t\,\mathrm{d}\epsilon_1$, calculated using $p = 2.2$ for the range $\gamma = 10^4$–10^7. The electron distribution follows equation (4). The solid line is the expected gamma-ray flux without an IR excess and the dashed line shows the increased gamma-ray flux when the IR excess is included.

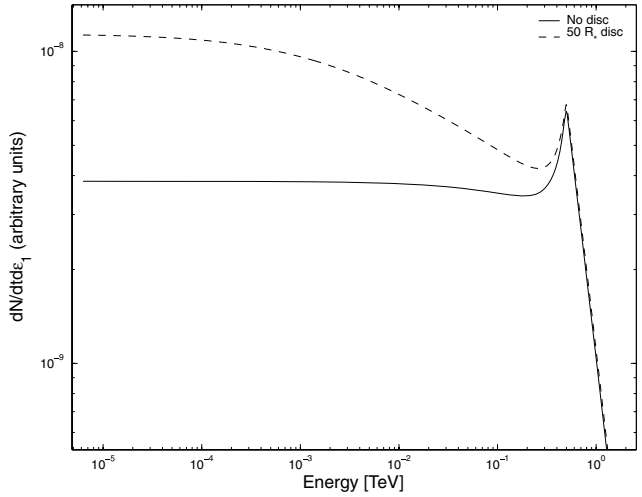

Figure 4. The predicted total scattering rate, $dN_{tot}/dt\,d\epsilon_1$, calculated using $p = 2.2$ for the range $\gamma = 10^6$–10^7. The electron distribution follows equation (4). The solid line is the expected gamma-ray flux without an IR excess and the dashed line shows the increased gamma-ray flux when the IR excess is included.

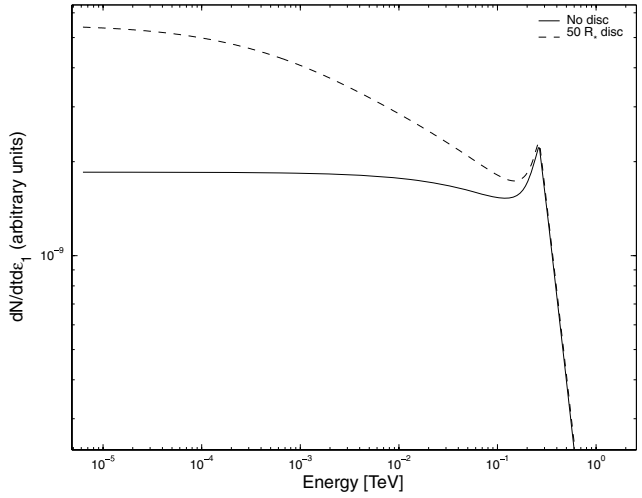

Figure 5. The predicted total scattering rate, $dN_{tot}/dt\,d\epsilon_1$, calculated using $p = 2.4$ for the range $\gamma = 5.4 \times 10^6$–5.4×10^7 (see Kirk et al. 1999). The electron distribution follows equation (4). The solid line is the expected gamma-ray flux without an IR excess and the dashed line shows the increased gamma-ray flux when the IR excess is included.

A third example of a predominantly adiabatic cooled electron distribution was taken from Kirk, Ball & Skjaeraasen (1999). Here the authors considered $p = 2.4$ and $\gamma = 5.4 \times 10^5$–5.4×10^7 and the spectrum is comparable to the HESS observations (see fig. 7 in Aharonian et al. 2005). The resulting scattering rate (assuming $K_e = 1$) is shown in Fig. 5. There is a significant increase in the scattering rate due to the IR excess, though slightly less than is presented in Fig. 4. The peak in the gamma-ray spectrum also occurs at a lower energy.

5.2.3 Post-shock electrons – radiative cooling

When the electrons in the post-shocked region also cool via synchrotron radiation, the electron distribution cannot be considered as a simple power law. While the post-shocked electrons initially have a power-law distribution, this is modified as the electrons lose energy via synchrotron radiation. An example of dominant radiation cooling, with a magnetic field strength of $B = 0.32$ G, was considered, also taken from Kirk et al. (1999). The initial electron spectrum was assumed to have an index of $p = 1.4$ and the energy range was $\gamma = 4.3 \times 10^5$–4.3×10^7. This modified electron distribution was used to model the scattering rate shown in Fig. 6. The details of the modification are beyond the scope of this paper and the reader is referred to Kirk et al. (1999). As with the previous models, a simplifying assumption of $K_e = 1$ has been made. The resulting plot is similar to Figs 4 and 5, and shows a significant increase in the scattering rate.

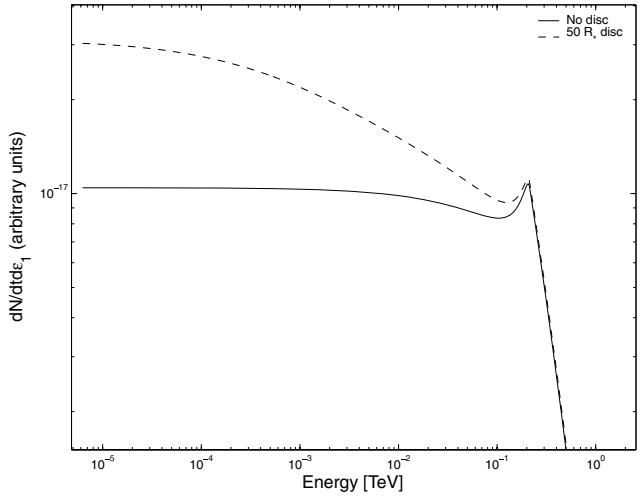

Figure 6. The predicted total scattering rate, $dN_{tot}/dt\,d\epsilon_1$, calculated using the electron spectrum from Kirk et al. (1999) for dominant radiative cooling; $B = 0.32$ G and $p = 1.4$ for the range $\gamma = 4.3 \times 10^5$–4.3×10^7. The solid line is the expected gamma-ray flux without an IR excess and the dashed line shows the increased gamma-ray flux when the IR excess is included.

The electron distributions used are summarized in Table 4.

6 DISCUSSION

6.1 The influence of the IR excess

The results above show that for the case when higher energy electrons dominate the IC scattering, the gamma-ray spectrum can be influenced by the IR excess. Fig. 7 shows the increase in the gamma-ray flux due to the inclusion of the IR excess as the ratio $F_{\nu,\mathrm{star+disc}}/F_{\nu,\mathrm{star}}$ versus energy for the different electron distributions considered.

The extent to which the gamma-ray spectrum is affected by the inclusion of the IR excess is dependent on which components of the Be star/disc spectrum are scattered in the Thomson limit. The peak in the stellar spectrum occurs at $\nu \sim (2$–$3) \times 10^{15}$ Hz (Fig. 1), and IC scattering will occur in the Thomson limit for electrons with Lorentz factors $\gamma \ll 10^5\,(\nu/10^{15}\,\mathrm{Hz})^{-1}$ (see equation 1). For the case of the broad electron energy distribution ($\gamma = 10^4$–10^7), the gamma-ray spectrum is dominated by electrons with Lorentz factors $\gamma = 10^4$ scattering photons from the peak of the stellar spectrum. This scattering will occur in the Thomson limit and produce gamma-rays with energies

$$\epsilon_1 \sim \gamma^2 h\nu \sim 10^9 \left(\frac{\gamma}{10^4}\right)^2 \left(\frac{\nu}{3 \times 10^{15}\,\mathrm{Hz}}\right)\ \mathrm{eV}.$$

Table 4. Summary of electron distributions considered.

Figure	Distribution	Origin	p	$\gamma_{\rm min}$	$\gamma_{\rm max}$
2	Mono-energetic	pre-shocked	–	10^6	10^6
3	Broad distribution	post-shock	2.2	10^4	10^7
4	Narrow distribution	post-shock	2.2	10^6	10^7
5	Adiabatic (Kirk et al. 1999)	post-shock	2.4	5.4×10^5	5.4×10^7
6	Radiative (Kirk et al. 1999)	post-shock	1.4	4.3×10^5	4.3×10^7

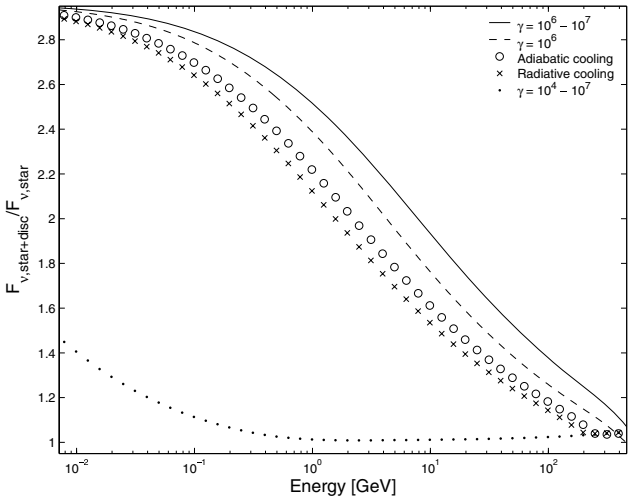

Figure 7. Fractional increase of the flux due to the inclusion for the IR excess for different electron distributions. The solid and dotted lines follow a power-law distribution with $p = 2.2$, the dashed line is for a mono-energetic pulsar wind, and the circle and crosses correspond to the electron distributions from Kirk et al. (1999) discussed in the text. A disc radius of $50R_*$ is assumed for all cases.

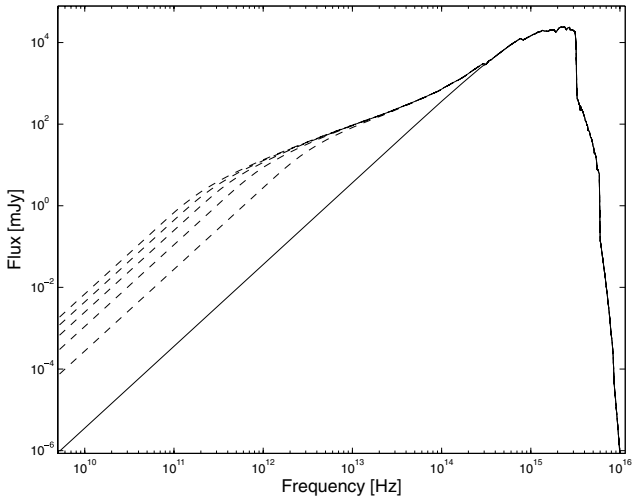

Figure 8. Broad energy distribution of SS 2883 predicted using the COG method. The solid line is the standard Kurucz model, while the dashed lines are the resulting IR excess for increasing disc sizes. The disc sizes are (from the bottom to the top) 10, 20, 30, 40 and $50R_*$. Only the disc radius is changed while the disc temperature and another parameters are the same as in Fig. 1.

As a result, the major contribution at GeV energies is from the Thomson scattering of the whole stellar spectrum and the resulting gamma-ray spectrum is negligibly affected by the IR excess, as is shown in Figs 3 and 7.

For electrons with Lorentz factors $\gamma = 10^5$, the scattering will occur in the Thomson limit only at frequencies $\nu \ll 10^{15}$ Hz. As a result, scattering of photons from the peak in the stellar spectrum will produce gamma-rays in the Klein–Nishina limit, while photons from the IR excess will scatter in the Thomson limit and increase the gamma-ray flux at GeV energies.

In Fig. 7 it is shown that, with the exception of the broad ($\gamma = 10^6$–10^7) electron distribution, the gamma-ray flux increases by a factor of $\gtrsim$2 at energies less than a few GeV. The results show that the inclusion of the IR excess in the target photon distribution can influence the production of gamma-rays in PSR B1259−63, particularly at GeV energies.

6.2 Variability of the gamma-ray emission

Since it is known that the circumstellar discs around Be stars are variable over periods of hundreds to thousands of days, the resulting change in the IR flux should also create variability in the GeV gamma-ray emission from PSR B1259−63.

A simple prediction can be made to show how the changing IR excess will modify the gamma-ray emission for PSR B1259−63. By changing the disc radius parameter in the COG method (while keeping the other parameters constant i.e., n, X_*, $T_{\rm disc}$ and θ), the magnitude of the IR excess can be simulated for different-sized circumstellar discs in PSR B1259−63. The resulting IR variability is shown in Fig. 8, where the lower solid line is a standard Kurucz model, and the dashed lines show the IR excess for increasing disc sizes. The consequential increase in the IC flux is shown in Fig. 9 as the ratio $F_{\nu,\rm star+disc}/F_{\nu,\rm star}$ versus energy. The same disc sizes are

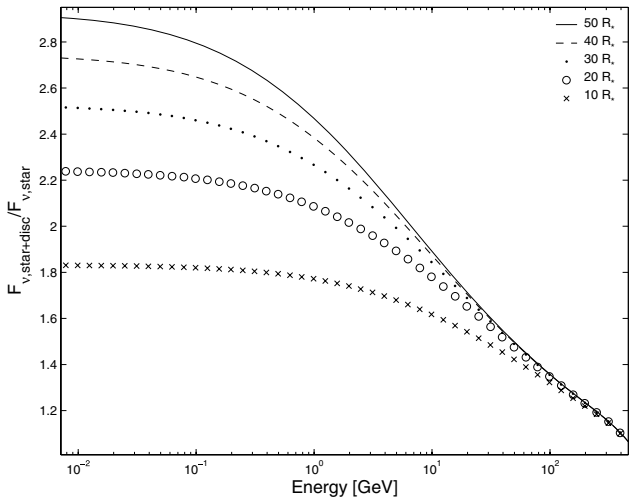

Figure 9. Predicted increase in the IC flux for different disc radii, shown as the ratio of the modified flux to the initial flux. The disc sizes are 10, 20, 30, 40 and $50R_*$ from the bottom to the top, and the photon number distribution is calculated as is shown in Fig. 8.

used as in Fig. 8 and the electron distribution follows the power law used in Fig. 4. Fig. 9 shows that by including the IR excess in the target photon distribution, the gamma-ray flux can increase by a factor of $\gtrsim$2 and show variability in the GeV energy range.

The modelling above assumes that the circumstellar disc only influences the photon distribution at IR wavelengths. However, it is known that the circumstellar disc also increases the magnitude of Be stars at optical wavelengths. This will greatly increase the total number of target photons and may result in an even greater possible variability of the gamma-ray flux during consecutive periastron passages. An increase in the Be star's flux at optical wavelengths could also lead to variability in the case of the broad electron distribution ($\gamma = 10^4$–10^7) as an increase in the flux near the peak of the stellar spectrum will lead to an increase in the total gamma-ray flux.

6.3 Detectability of the gamma-ray modulation

The increase in the gamma-ray flux due to the inclusion of the IR excess in an isotropic approximation will not be observable with current gamma-ray telescopes. If the modelled fluxes are compared to the HESS spectrum, the modified flux will fall below the *Fermi* detection threshold. A larger broad electron spectrum with more electrons around $\gamma \sim 10^4$ may produce a gamma-ray spectrum large enough to be detected by *Fermi*, but the variability due to the IR excess reported here would not be observable.

The analysis discussed here does however assume only isotropic scattering and the geometric size of the disc has not been considered. Anisotropic modelling of the system may show a more pronounced effect, especially close to periastron where the circumstellar disc not only provides an IR excess, but scattering will also occur over the larger solid angle of the disc.

7 CONCLUSION

PSR B1259−63 is a particularly important gamma-ray binary system since it contains an independently confirmed 48-ms pulsar compact object (as opposed to LS 5039 and LS I +61°303 where the nature of the compact object must be inferred) and the gamma-ray emission is most likely created through the IC scattering of target photons from the optical companion via the electrons/positrons emanating from the pulsar wind. Previous modelling of the IC gamma-ray emission has not taken into account the IR excess created by the circumstellar disc and how these additional target photons will influence the IC scattering.

In this paper, the Lamers & Waters (1984) COG method was fitted to SS 2883 using optical, near-IR and mid-IR data available in literature and archives, under the assumption that the circumstellar disc has a radius of $R_{\rm disc} = 50\ R_*$, and that the Be star is a main-sequence star with the parameters $T_* = 25\,000$ K, $\log g = 3.5$, $M_* \simeq 10\,{\rm M}_\odot$ and $R_* \simeq 6\,{\rm R}_\odot$ based on the least-squares fit performed in this paper and Johnston et al. (1994). The fit was used to calculate the target photon number density which was in turn used to calculate the IC spectrum for PSR B1259−63. For a first approximation, only isotropic scattering was considered in order to demonstrate the relevance of the IR excess.

The modelling shows that the IR excess has a non-trivial influence on the IC spectrum, particularly at GeV energy gamma-rays where the flux increases by a factor of $\gtrsim$2 for reasonable electron distributions. It has also been shown (since the circumstellar disc is variable) how changes in the IR excess will manifest as variability at gamma-ray energies. Consequently, observations of consecutive periastron passages may show differences in the GeV gamma-ray light curve as a result of a possibly changing IR excess.

The results presented above have implications for other Be-XPBs and gamma-ray binary systems. Previous modelling of the IC spectrum only considered a blackbody or mono-energy distribution for the target photons; however, the results above show that the IR excess from the circumstellar disc will have a non-trivial influence on the IC gamma-ray spectrum that must be accounted for when modelling PSR B1259−63.

ACKNOWLEDGMENTS

The authors are very grateful to O. de Jager for suggesting this study. This publication makes use of data products from the 2MASS, which is a joint project of the University of Massachusetts and the Infrared Processing and Analysis Center/California Institute of Technology, funded by the National Aeronautics and Space Administration and the National Science Foundation. This research made use of data products from the *MSX*. Processing of the data was funded by the Ballistic Missile Defense Organization with additional support from NASA Office of Space Science. This research has also made use of the NASA/ IPAC Infrared Science Archive, which is operated by the Jet Propulsion Laboratory, California Institute of Technology, under contract with the National Aeronautics and Space Administration. BvS is funded by the South African Square Kilometre Array Project. The authors would like to thank the anonymous reviewers for their comments which have improved this study.

REFERENCES

Aharonian F. et al., 2005, A&A, 442, 1
Aharonian F. et al., 2009, A&A, 507, 389
Ball L., Kirk J. G., 2000, Astroparticle Phys., 12, 335
Blumenthal G. R., Gould R. J., 1970, Rev. Modern Phys., 42, 237
Chernyakova M. A., Illarionov A. F., 1999, MNRAS, 304, 359
Chernyakova M. A., Illarionov A. F., 2000, Ap&SS, 274, 177
Chernyakova M., Neronov A., Lutovinov A., Rodriguez J., Johnston S., 2006, MNRAS, 367, 1201
Chernyakova M., Neronov A., Aharonian F., Uchiyama Y., Takahashi T., 2009, MNRAS, 397, 2123
Collins G. W., 1987, in Slettebak A., Snow T. P., eds, IAU Colloq. 92, Physics of Be Stars. Cambridge Univ. Press, Cambridge, p. 3
Cominsky L., Roberts M., Johnston S., 1994, ApJ. 427, 978
Connors T. W., Johnston S., Manchester R. N., McConnell D., 2002, MNRAS, 336, 1201
Drilling J. S., 1991, ApJS, 76, 1033
Johnston S., Manchester R. N., Lyne A. G., Bailes M., Kaspi V. M., Qiao G., D'Amico N., 1992, ApJ, 387, L37
Johnston S., Manchester R. N., Lyne A. G., Nicastro L., Spyromilio J., 1994, MNRAS, 268, 430
Johnston S., Manchester R. N., Lyne A. G., D'Amico N., Bailes M., Gaensler B. M., Nicastro L., 1996, MNRAS, 279, 1026
Johnston S., Manchester R. N., McConnell D., Campbell-Wilson D., 1999, MNRAS, 302, 277
Johnston S., Ball L., Wang N., Manchester R. N., 2005, MNRAS, 358, 1069
Kaspi V. M., Tavani M., Nagase F., Hirayama M., Hoshino M., Aoki T., Kawai N., Arons J., 1995, ApJ, 453, 424
Kawachi A. et al., 2004, ApJ, 607, 949
Khangulyan D., Hnatic S., Aharonian F., Bogovalov S., 2007, MNRAS, 380, 320
Kirk J. G., Ball L., Skjaeraasen O., 1999, Astroparticle Phys., 10, 31
Klare G., Neckel Th., 1977, A&AS, 27, 215
Kurucz R. L., 1979, ApJS, 40, 1

Kurucz R. L., 1992, inBarbuy B., Renzini A., eds, IAU Symp. 149, The Stellar Populations of Galaxies. Kluwer, Dordrecht, p. 225
Lamers H. J. G. L. M., Waters L. B. F. M., 1984, A&A, 136, 37
Millar C. E., Marlborough J. M., 1999, ApJ, 526, 400
Porter J. M., Rivinius T., 2003, PASP, 115, 1153
Price S. D., Egan M. P., Carey S. J., Mizuno D. R., Kuchar T. A., 2001, AJ, 121, 2819
Quirrenbach A., Buscher D. F., Mozurkewich D., Hummel C. A., Armstrong J. T., 1994, A&A, 283, L13
Rybicki G. B., Lightman A. P., 2004, Radiative Processes in Astrophysics. WILEY-VCH Verlag GmbH & Co. KGaA, Weinheim
Schild R. E., Garrison R. F., Hiltner W. A., 1983, ApJS, 51, 321
Skrutskie M. F. et al., 2006, AJ, 131, 1163
Struve O., 1931, ApJ, 73, 94
Tavani M., Arons J., 1997, ApJ, 477, 439
Telting J. H., Waters L. B. F. M., Roche P., Boogert A. C. A., Clark J. S., de Martino D., Persi P., 1998, MNRAS, 296, 785
Waters L. B. F. M., 1986, A&A, 162, 121
Waters L. B. F. M., Lamer H. J. G. L. M., 1984, A&AS, 57, 327
Westerlund B. E., Garnier R., 1989, A&AS, 78, 203

This paper has been typeset from a TEX/LATEX file prepared by the author.

7.4 Anisotropic inverse Compton (AIC) scattering

In van Soelen and Meintjes (2011) the influence of the IR excess on gamma-ray production was considered for an isotropic distribution and the calculations did not take into account the scaling of the photon distribution with distance, the change in the optical depth during the orbit, nor the change in solid angle during the orbit. It is clear, however, that the solid angle over the disc is much greater than the solid angle over the star alone. If we consider the binary system at periastron and disc aligned face-on with respect to the pulsar, the solid angle over the star or disc is given by

$$\Omega = 2\pi \left(1 - \cos\alpha\right),$$

where α is the polar angle shown in Fig. 7.3. At periastron the binary separation is $\sim 20R_*$ and, assuming a disc radius $\sim 50R_*$ with a negligible half-opening angle, $\theta_{\rm disc}$, it can be shown that $\alpha_* \sim 3^\circ$ for the star and $\alpha_{\rm disc} \sim 70^\circ$ for the disc. The total solid angle over the disc is then ~ 480 times greater than the solid angle subtended by the star and could present a significant additional source of photons over a large distance scale.

The H.E.S.S. detected TeV emission from PSR B1259-63 around periastron (Aharonian et al., 2005, 2009) implies that the Be star and disc provide favourable conditions for Very High Energy (VHE) gamma-ray production. The combined star and disc contribution provides an anisotropic target photon distribution and the IC scattering must be modelled utilizing the anisotropic, Klein-Nishina kernel (section 5.5.1). The total IC scattering rate is found by numerically performing the integration

$$\frac{dN_{\rm tot}}{dt\, d\epsilon_1} = \int_\Omega \int_{\epsilon_0} \int_\gamma n_{\rm e}(\gamma)\, n_{\rm ph}(\epsilon_0) \frac{dN_{\gamma,\epsilon}}{dt\, d\epsilon_1}\, d\gamma\, d\epsilon_0\, d\Omega,$$

where $n_{\rm e}(\gamma)$ and $n_{\rm ph}(\epsilon_0)$ are the electron and photon number density distribution respectively (sections 7.1 & 7.2), $dN_{\gamma,\epsilon}/dt\, d\epsilon_1$ is the anisotropic scattering kernel (equation 5.37), and the integration is performed over the full solid angle, Ω, subtended by the star and disc, from various vantage points around periastron. This numerical integration has been considered for LS 5039 (Dubus et al., 2008) where only the integration over the star is considered. The presence of an extended circumstellar disc in PSR B1259-63/LS 2883, however, introduces additional geometric constraints. To take into account the constraints imposed by the disc, it is helpful to choose a coordinate system which is best suited to calculate the scattering and relevant solid angles. For PSR B1259-63/LS 2883 it is therefore easier to treat the scattering from the star and disc separately using coordinate systems which are appropriate to each situation.

For the stellar contribution, a similar coordinate system as presented in e.g. Cerutti (2010) and Dubus et al. (2008), will be considered. The geometry of the circumstellar disc can be determined by adapting a geometry similar to that presented by Moskalenko and Strong (2000) where the IC scattering between cosmic rays and photons from the extended disc of the galactic plane was considered. This geometry also provides additional constraints on the solid angle of

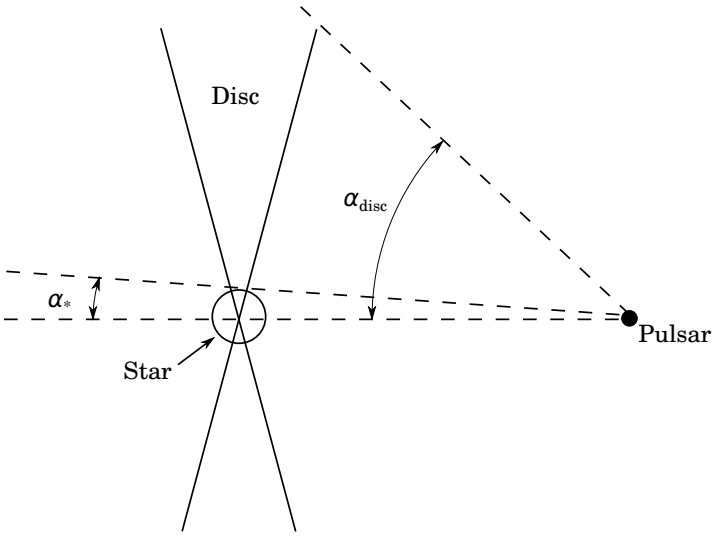

Figure 7.3: Sketch of the difference in the opening angle of the star and disc, assuming the disc is viewed face-on by the pulsar.

the disc as was presented by Moskalenko and Strong (2000) and by other authors (e.g. Pommé et al., 2003; Tryka, 1997).

The rest of this section will discuss the geometric effects that must be considered when modelling the AIC scattering. Sections 7.4.1 & 7.4.2 present the different coordinate systems considered and the calculation of the IC scattering angle in these systems, section 7.4.3 defines the solid angles in these systems, section 7.4.4 considers the effect of the angle to the normal of the disc surface, while additional geometric constraints are given in section 7.4.5. The constraints on the geometry is modified with respect to the modelling presented in Dubus et al. (2008), Cerutti (2010) and Moskalenko and Strong (2000).

7.4.1 Coordinate systems

The scattering from the star and the disc is most easily calculated if two different coordinate systems are chosen that best suit the scattering in each situation; the system for the star and disc will be known as $K^{\rm s}$ and $K^{\rm d}$ respectively. The angles in $K^{\rm s}$ and $K^{\rm d}$ are calculated from the angles in a third coordinate system K which is defined to lie in the same orientation as the binary system, and in which the relevant binary parameters are calculated. All coordinate systems remain centred on the pulsar/electron cloud and the unit vector $\hat{\mathbf{e}}_*$ points towards the centre of the star, the unit vector $\hat{\mathbf{e}}_{\rm obs}$ towards the observer and the unit vector $\hat{\mathbf{e}}_H$ point towards the normal of the disc. Variables with a superscript "s" are measured in $K^{\rm s}$, and those with a superscript "d" are measured in $K^{\rm d}$. The absence of a superscript indicates the variables are measured in K.

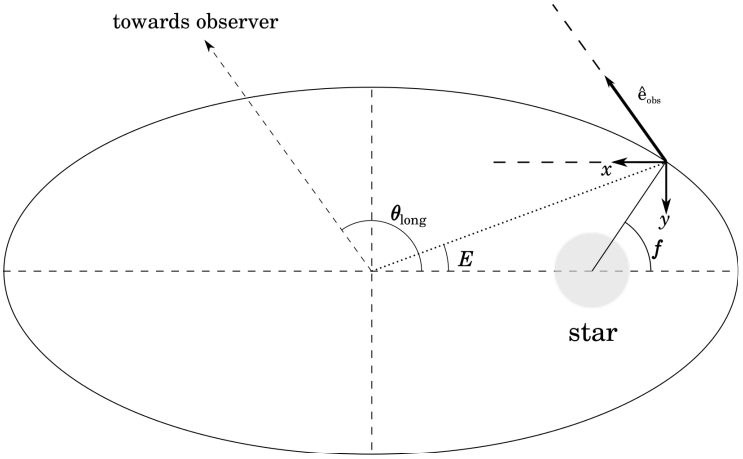

Figure 7.4: Binary system with the orbital plane observed face-on. The unit vector $\hat{\mathbf{e}}_{\rm obs}$ points towards the observer and the angles f and E are the true and eccentric anomaly respectively. Also shown is the longitude of periastron, $\theta_{\rm long}$. Figure adapted from Murray and Dermott (1999).

Orbital system: K

Consider the binary system in Fig. 7.4 which shows the orbital plane viewed face-on. The relevant system angles are calculated from the two-body problem and the notation presented in Murray and Dermott (1999, pp. 22–37) will be followed.

The relationship between the orbital period, T, and the semi-major axis, a, is given by the well known Keplerian relationship

$$T^2 = \frac{4\pi^2 a^3}{G(M+m)},$$

where G is the gravitational constant, and $M+m$ is the sum of the masses in the binary system. From the sum of the masses and the observed orbital period it is possible to determine the semi-major axis. The binary separation is calculated from

$$r = a(1 - e\cos E), \tag{7.7}$$

where e is the eccentricity of the system and E is the eccentric anomaly, i.e. the angle shown in Fig. 7.4. The value of E is calculated at any time t by solving for E where

$$E - e\sin E - n*(t-\tau) = 0, \tag{7.8}$$

where τ is the time of periastron and

$$n = \frac{2\pi}{T}.$$

Since equation (7.8) is dependent on E and the sine of E, the equation cannot be solved analytically and a numerical solution has been implemented in this study using the MATLAB/OCTAVE function `fzero`. Using the solution for E, the angle f (the true anomaly; Fig. 7.4) in the orbital

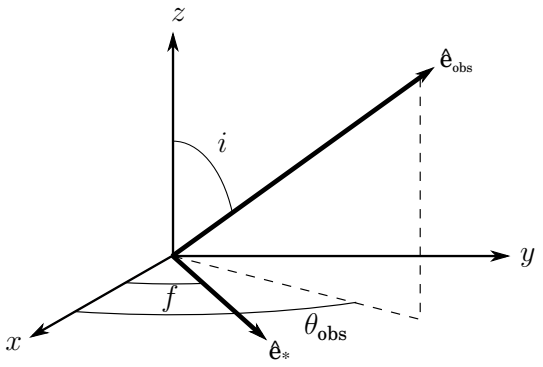

Figure 7.5: Coordinate system K relative to the orbital plane. The direction of the observer, $\hat{\mathbf{e}}_{\rm obs}$ is defined by the binary inclination, i, and the angle $\theta_{\rm obs}$ which is determined from the longitude of periastron. The direction of the star, $\hat{\mathbf{e}}_*$, which lies in the x-y plane, is defined by the true anomaly, f.

plane is found from

$$\tan\frac{f}{2} = \sqrt{\frac{1+e}{1-e}}\tan\frac{E}{2}. \tag{7.9}$$

A new Cartesian coordinate system, K, can be defined with the origin lying at the centre of the pulsar, the x-axis always parallel to the semi-major axis and directed away from periastron, the y-axis parallel to the semi-minor axis and the z-axis parallel to the normal of the orbital plane; this system is shown in Fig. 7.5.

In Fig. 7.5 the unit vector $\hat{\mathbf{e}}_*$ which points towards the centre of the star and disc, is defined by the true anomaly, f and lies in the $x-y$ plane. The unit vector $\hat{\mathbf{e}}_{\rm obs}$ points towards the observer and is defined by the polar angle i and the azimuthal angle $\theta_{\rm obs}$. The angle i is the inclination of the binary system ($i = 33°$; Negueruela et al., 2011) and $\theta_{\rm obs}$ is determined from the longitude of periastron, which is $\theta_{\rm long} \approx 139°$ for PSR B1259-63 (Johnston et al., 1994). The longitude of periastron is the angle between the direction of periastron and the direction of the observer (measured from the centre of the binary system; see Fig. 7.4) and since the x-axis of the K system is defined to point away from periastron, this implies that

$$\begin{aligned}\theta_{\rm obs} &= 180° + \theta_{\rm long} \\ &\approx 319°.\end{aligned}$$

The angles and binary separation of the system are calculated at any point in the orbit from the equations of the standard two body problem and are converted to the star ($K^{\rm s}$) and disc ($K^{\rm d}$) coordinate systems.

Star system: $K^{\rm s}$

The IC scattering of photons from the star is most easily calculated if we consider a coordinate system that is orientated such that the unit vector $\hat{\mathbf{e}}^{\rm s}_*$ is orientated along the z-axis and the unit

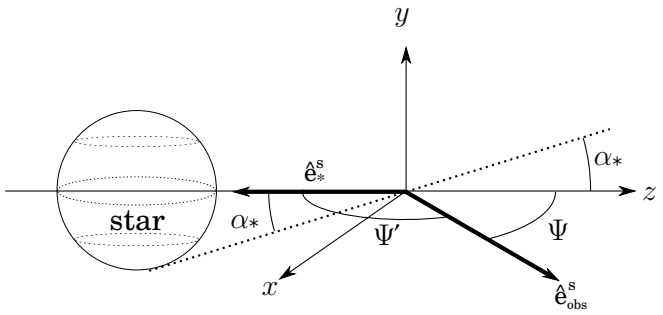

Figure 7.6: Coordinate system $K^{\rm s}$ which is used to determine the scattering angle for photons originating from the star (adapted from Cerutti, 2010).

vector $\hat{\mathbf{e}}^{\rm s}_{\rm obs}$ lies in the x-z plane, as is shown in Fig. 7.6. Here, the coordinate system is still centred on the electron cloud and pulsar. Therefore, in $K^{\rm s}$, the unit vector $\hat{\mathbf{e}}^{\rm s}_{\rm obs}$ can be defined only in terms of the angle Ψ, which simplifies the calculation of the scattering angle.

In K the unit vectors $\hat{\mathbf{e}}_*$ and $\hat{\mathbf{e}}_{\rm obs}$ can be defined as

$$\hat{\mathbf{e}}_* = \begin{pmatrix} \cos f \\ \sin f \\ 0 \end{pmatrix} \quad \text{and} \quad \hat{\mathbf{e}}_{\rm obs} = \begin{pmatrix} \sin i \cos\theta_{\rm obs} \\ \sin i \sin\theta_{\rm obs} \\ \cos i. \end{pmatrix}, \tag{7.10}$$

and therefore, in $K^{\rm s}$,

$$\Psi = \pi - \Psi', \tag{7.11}$$

where Ψ' is the angle between $\hat{\mathbf{e}}_*$ and $\hat{\mathbf{e}}_{\rm obs}$ defined by

$$\cos\Psi' = \hat{\mathbf{e}}_* \cdot \hat{\mathbf{e}}_{\rm obs} = \sin i \cos(f - \theta_{\rm obs}). \tag{7.12}$$

Note that in this case the solid angle subtended by the star relative to the electron cloud is determined by $\alpha_* = \sin^{-1}(R_*/r)$.

Disc system: $K^{\rm d}$

To determine the solid angle over the circular disc and the scattering angle of photons originating from the disc the system $K^{\rm d}$, illustrated in Fig. 7.7, is introduced.[ii] This coordinate system is adapted from Moskalenko and Strong (2000) and the origin is located at the centre of the pulsar/electron cloud (point O) which is a vertical height, H, above the disc plane and a horizontal displacement, ρ, from the centre of the disc. The z'-axis (polar axis) is orientated parallel to the normal of the disc and the x'-axis is along the length ρ as shown in Fig. 7.7. Since the origin of $K^{\rm d}$ is at the centre of the pulsar/electron cloud the distance r represents the binary separation. In order to convert from the K system to $K^{\rm d}$ system the vertical height above the disc, H, and

[ii] This is the same system which is used to determine the optical depth through the disc in the modified COG method discussed in Chapter 6.

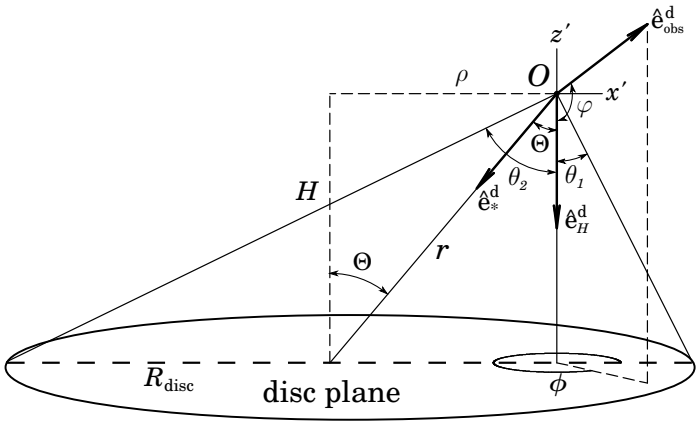

Figure 7.7: Coordinate system $K^{\rm d}$ which has been adapted from e.g. Moskalenko and Strong (2000). The origin is centred on the pulsar/electron cloud at position O, lies at a vertical height, H, above the disc plane and a horizontal displacement, ρ, from the centre of the disc.

the horizontal displacement, ρ, is determined by

$$\begin{aligned} \rho &= r\sin\Theta \\ H &= r\cos\Theta, \end{aligned}$$

where r is the binary separation and the angle Θ lies between the unit vectors $\hat{\mathbf{e}}^{\rm d}_{*}$ and $\hat{\mathbf{e}}^{\rm d}_{H}$ (Fig. 7.7). By defining the direction of $\hat{\mathbf{e}}_H$ in the orbital system (K) to be given by

$$\hat{\mathbf{e}}_H = \begin{pmatrix} \sin i_H \cos\theta_H \\ \sin i_H \sin\theta_H \\ \cos i_H \end{pmatrix},$$

it can be shown that the angle Θ can be calculated from

$$\hat{\mathbf{e}}_* \cdot \hat{\mathbf{e}}_H = \cos\Theta = \sin i_H \cos(f - \theta_H), \tag{7.13}$$

using the definition of $\hat{\mathbf{e}}_*$ given earlier. Here, the angles i_H and θ_H are determined from the assumed orientation of the circumstellar disc relative to the orbital plane and the position of the pulsar. During the binary orbit, the relative orientation of the pulsar to the circumstellar disc changes and, therefore, the disc parameters (r, Θ, H and ρ) also change. The binary separation, r, is determined from equation (7.7) while the derivations of the angles i_H, θ_H and Θ are given in Appendix C.2.

The next step is to define $\hat{\mathbf{e}}^{\rm d}_{\rm obs}$ in the $K^{\rm d}$ system, in terms of the polar angle φ and the

azimuthal angle ϕ, as shown in Fig. 7.7, such that

$$\hat{\mathbf{e}}^{\mathrm{d}}_{\mathrm{obs}} = \begin{pmatrix} \sin\varphi\cos\phi \\ \sin\varphi\sin\phi \\ \cos\varphi \end{pmatrix}.$$

By converting the direction of $\hat{\mathbf{e}}_{\mathrm{obs}}$ from the K to K^{d} system, it can be shown that the polar angle is given by

$$\varphi = \cos^{-1}\left[\sin i \sin i_H \cos\left(\theta_{\mathrm{obs}} - \theta_H\right) + \cos i \cos i_H\right], \tag{7.14}$$

and the azimuthal angle, ϕ, is given by

$$\phi = \cos^{-1}\left[\frac{\cos\Theta\cos\varphi - \cos\Psi'}{\sin\Theta\sin\varphi}\right], \tag{7.15}$$

where the angle Ψ' is given by equation (7.12). While the solution for ϕ is not unique, since $\phi \in [0, 2\pi]$ and $\cos\phi = \cos(2\pi \pm \phi)$, the two possible solutions are symmetric and will produce the same scattering rate. Therefore, using the solution for φ and ϕ the direction of $\hat{\mathbf{e}}^{\mathrm{d}}_{\mathrm{obs}}$ can be defined in K^{d}. The full derivation of the direction of $\hat{\mathbf{e}}^{\mathrm{d}}_{\mathrm{obs}}$ and equations (7.14) & (7.15) are given in Appendix C.3.

7.4.2 Scattering angle

In the anisotropic IC (AIC) scattering, it is assumed that the electrons are highly relativistic and that the photons scatter in the direction of the electrons' original momentum. This assumption was incorporated into the AIC scattering kernel and, as is shown by equation (5.37), the AIC scattering rate is dependent on the angle between the unperturbed path of the photon and the direction of the unscattered electron, in the observer's reference frame. This angle, defined here as the scattering angle, θ_{sc}, is given by the angle between the direction of the unperturbed photons path ($\hat{\mathbf{e}}_{\mathrm{ph}}$) and the direction of the observer ($\hat{\mathbf{e}}_{\mathrm{obs}}$), and is determined by

$$\hat{\mathbf{e}}_{\mathrm{ph}} \cdot \hat{\mathbf{e}}_{\mathrm{obs}} = \cos\theta_{\mathrm{sc}},$$

as is shown in Fig. 7.8. This scattering angle must be determined in both the stellar (K^{s}) and disc (K^{d}) coordinate systems.

Star system: K^{s}

From Fig. 7.6, if the direction a photon from the star would have travelled, without scattering, is defined by θ^*_{ph} and ϕ^*_{ph} then the scattering angle, θ_{sc}, for stellar photons is determined from

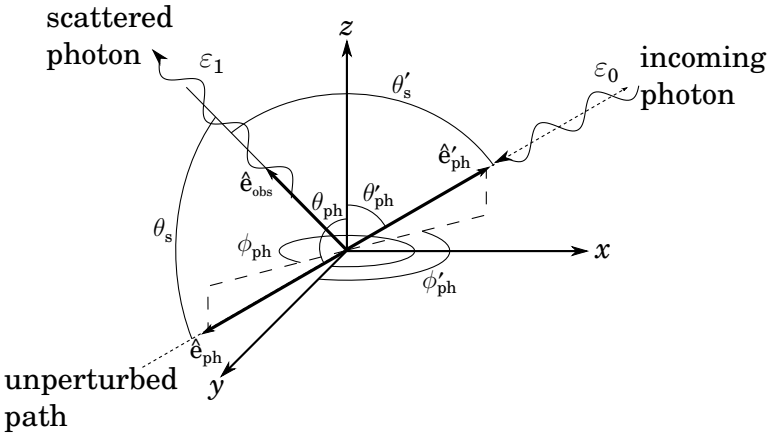

Figure 7.8: Scattering angle of an incoming photon, scattered in the direction of the observer.

(Dubus et al., 2008)

$$\hat{\mathbf{e}}^{\rm s}_{\rm ph} = \begin{pmatrix} \sin\theta^*_{\rm ph}\cos\phi^*_{\rm ph} \\ \sin\theta^*_{\rm ph}\sin\phi^*_{\rm ph} \\ \cos\theta^*_{\rm ph} \end{pmatrix} \quad \text{and} \quad \hat{\mathbf{e}}^{\rm s}_{\rm obs} = \begin{pmatrix} \sin\Psi \\ 0 \\ \cos\Psi \end{pmatrix},$$

and

$$\cos\theta_{\rm sc} = \hat{\mathbf{e}}^{\rm s}_{\rm ph}\cdot\hat{\mathbf{e}}^{\rm s}_{\rm obs} = \cos\Psi\cos\theta^*_{\rm ph} + \sin\Psi\sin\theta^*_{\rm ph}\cos\phi^*_{\rm ph}.$$

The limits on the angles are $\theta^*_{\rm ph} \in [0, \alpha_*]$ while symmetry implies that $\phi^*_{\rm ph} \in [0, 2\pi]$, where, $\alpha_* = \sin^{-1}(R_*/r)$ is the maximum polar angle. The constraint is determined by the size of the star.

Disc system: $K^{\rm d}$

For the scattering of photons from the circumstellar disc, a photon arriving from the disc at some angle $\theta_{\rm ph}$ and $\phi_{\rm ph}$ is defined by the unit vector $\hat{\mathbf{e}}^{\rm d'}_{\rm ph}$.[iii] As is shown in Fig. 7.8, the angle between $\hat{\mathbf{e}}^{\rm d'}_{\rm ph}$ and $\hat{\mathbf{e}}^{\rm d}_{\rm obs}$ is $\theta'_{\rm sc}$, while the scattering angle is given by $\theta_{\rm sc} = \pi - \theta'_{\rm sc}$. The angle $\theta'_{\rm sc}$ can be calculated from (Fig. 7.7)

$$\hat{\mathbf{e}}^{\rm d'}_{\rm ph} = \begin{pmatrix} \sin\theta_{\rm ph}\cos\phi_{\rm ph} \\ \sin\theta_{\rm ph}\sin\phi_{\rm ph} \\ \cos\theta_{\rm ph} \end{pmatrix} \quad \text{and} \quad \hat{\mathbf{e}}^{\rm d}_{\rm obs} = \begin{pmatrix} \sin\varphi\cos\phi \\ \sin\varphi\sin\phi \\ \cos\varphi \end{pmatrix},$$

and

$$\cos\theta'_{\rm sc} = \hat{\mathbf{e}}^{\rm d'}_{\rm ph}\cdot\hat{\mathbf{e}}^{\rm d}_{\rm ph} = \sin\theta_{\rm ph}\sin\varphi\cos(\phi_{\rm ph}-\phi) + \cos\theta_{\rm ph}\cos\varphi.$$

[iii] Note the subtle change in notation; here $\theta_{\rm ph}$ & $\phi_{\rm ph}$ define the direction of the incoming photon, $\hat{\mathbf{e}}'_{\rm ph}$, and not the direction the photon would have travelled in, $\hat{\mathbf{e}}_{\rm ph}$, as was defined by $\theta^*_{\rm ph}$ and $\phi^*_{\rm ph}$ in $K^{\rm s}$.

This allows the scattering angle to be determined for a photon from the disc, arriving from any direction.

The limit on the above calculations occurs if $\Theta = 0$, since the azimuthal angle of $\hat{\mathbf{e}}^{\mathrm{d}}_{\mathrm{obs}}$, cannot be found from equation (7.15). In this scenario it is required to determine the scattering angle and solid angle using the symmetric model that applies to the star.

7.4.3 Solid angle

The integration over the star and circumstellar disc, using the coordinate systems defined in section 7.4.1, must be limited to the appropriate solid angles. Therefore, the constraints on the polar and azimuthal angles must be found for each coordinate system.

Star system: K^{s}

The integration over the solid angle of the star is given by the integration over a sphere of radius R_*. Since the integration is symmetrical around the azimuthal angle the integration over the solid angle is given by

$$\Omega = \int_0^{2\pi} \int_0^{\alpha_*} \sin\theta \, d\theta d\phi,$$

where $\alpha_* = \sin^{-1}(R_*/r)$ is the maximum polar angle and r is the binary separation (Fig. 7.3). The solid angle is then only dependent on the binary separation during the orbital.

Disc system: K^{d}

The solid angle subtending the disc is determined using the coordinate system which is shown in Fig. 7.7. A simplified version of this coordinate system is shown in Fig. 7.9, presenting only the angles which are relevant to calculate the solid angle. Two scenarios are presented, namely $\rho < R_{\mathrm{disc}}$ and $\rho > R_{\mathrm{disc}}$. The derivation of the solid angle below is based on the general discussion presented in e.g. Pommé et al. (2003), and the more detailed presentation in e.g. Moskalenko and Strong (2000); Tryka (1997). In Fig. 7.9 the point O is at the centre of the electron cloud, which is a vertical height H above the disc plane and is shifted a horizontal distance ρ from the centre of the disc.

The solid angle over the disc is given by

$$\Omega = \int_\phi \int_\theta \sin\theta \, d\theta \, d\phi,$$

where appropriate limits must be imposed for the polar (θ) and azimuthal (ϕ) angles by the disc geometry. From Fig. 7.9 it is clear that the limits on the polar angles are determined by the

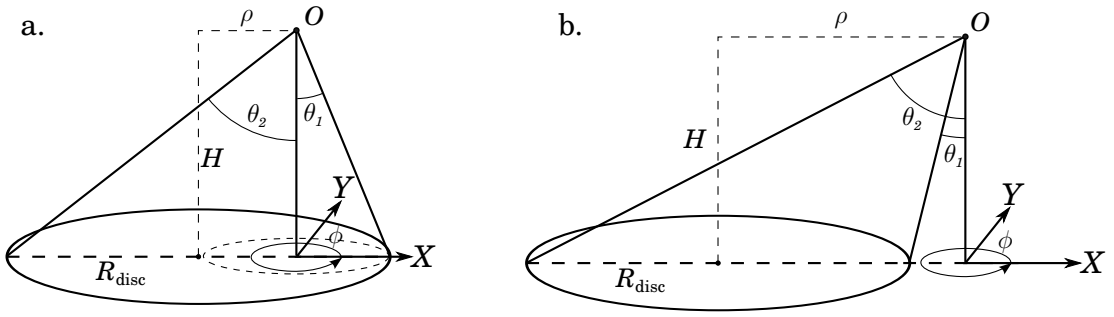

Figure 7.9: Coordinate system used to calculate the solid angle over a flat disc.

angles θ_1 and θ_2, which are given by

$$\begin{aligned} \theta_1 &= \tan^{-1}\left(\frac{|\rho - R_{\rm disc}|}{H}\right) \\ \theta_2 &= \tan^{-1}\left(\frac{R_{\rm disc} + \rho}{H}\right). \end{aligned}$$

When $\rho < R_{\rm disc}$ (Fig. 7.9a) the integration is for $\theta \in [0, \theta_2]$, while for $\rho > R_{\rm disc}$ (Fig. 7.9b) the polar angle is limited to $\theta \in [\theta_1, \theta_2]$.

For polar angles less than θ_1, there is no constraint on the azimuthal angle (i.e. $\phi \in [0, 2\pi]$), while for polar angles between θ_1 and θ_2 the azimuthal angle must be limited to angles in the disc plane. Any point (X, Y) on the disc plane is given by

$$\begin{aligned} X &= H \tan\theta \cos\phi, \\ Y &= H \tan\theta \sin\phi, \end{aligned}$$

and, since the disc is circular, the constraint $(X + \rho)^2 + Y^2 \leq R_{\rm disc}^2$ must apply. Therefore, substituting in the values for X and Y it can be shown that the azimuthal angle, ϕ, is limited to regions where

$$\cos\phi \leq \frac{R_{\rm disc}^2 - \rho^2 - H^2 \tan^2\theta}{2\rho H \tan\theta}. \tag{7.16}$$

The solid angle of the disc is calculated by dividing the integration into two regions, Ω_1 and Ω_2 such that

$$\begin{aligned} \Omega_1 &= \int_0^{2\pi}\int_0^{\theta_1} \sin\theta \, d\theta d\phi, \quad (\rho < R_{\rm disc}) \\ &= 0, \quad (\rho \geq R_{\rm disc}), \end{aligned} \tag{7.17}$$

and

$$\Omega_2 = \int_{\theta_1}^{\theta_2}\int_{\cos^{-1}(\tau_\phi)}^{2\pi - \cos^{-1}(\tau_\phi)} \sin\theta \, d\phi d\theta, \tag{7.18}$$

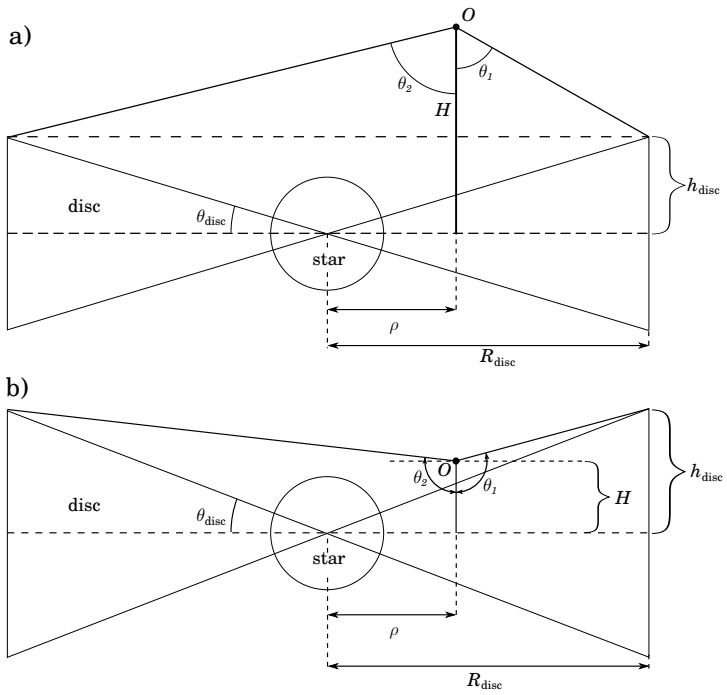

Figure 7.10: Be star and disc with half-opening angle $\theta_{\rm disc}$, for a): $H > h_{\rm disc}$ and b): $H < h_{\rm disc}$.

where τ_ϕ is the limit which must be applied to the azimuthal angle, given by (from equation 7.16)

$$\tau_\phi(\theta) = \frac{R_{\rm disc}^2 - \rho^2 - H^2 \tan^2\theta}{2\rho H \tan\theta}. \tag{7.19}$$

The total solid angle is then found from the sum $\Omega = \Omega_1 + \Omega_2$.

The above equations apply to the solid angle over a flat disc ($\theta_{\rm disc} = 0°$), but can easily be extended to a circumstellar disc with a finite half-opening angle $\theta_{\rm disc}$. This is shown in Fig. 7.10 for the two conditions $H > h_{\rm disc}$ and $H < h_{\rm disc}$, where H is the vertical height from the disc mid-plane and $h_{\rm disc} = R_{\rm disc} \tan\theta_{\rm disc}$. The derivation of the new limits are given in Appendix C.4, and the results are presented here.

For the condition $H > h_{\rm disc}$ (Fig. 7.10a), the solid angle is given by equations (7.17) & (7.18) where the new limits on the polar and azimuthal angles are (see Appendix C.4, pp. 241–242)

$$\begin{aligned}
\theta_1 &= \tan^{-1}\left(\left|\frac{\rho - R_{\rm disc}}{H - h_{\rm disc}}\right|\right) \\
\theta_2 &= \tan^{-1}\left(\frac{R_{\rm disc} + \rho}{|H - h_{\rm disc}|}\right) \\
\tau_\phi(\theta) &= \frac{R_{\rm disc}^2 - \rho^2 - (H - h_{\rm disc})^2 \tan^2\theta}{2\rho(|H - h_{\rm disc}|)\tan\theta}.
\end{aligned}$$

For the condition $H < h_{\rm disc}$ (Fig. 7.10b), the limits on the polar angle are given by (see

Appendix C.4, pp. 242–244)

$$\begin{aligned}\theta_1 &= \frac{\pi}{2} + \tan^{-1}\left(\frac{h_{\rm disc} - H}{R_{\rm disc} - \rho}\right)\\ \theta_2 &= \frac{\pi}{2} + \tan^{-1}\left(\frac{h_{\rm disc} - H}{R_{\rm disc} + \rho}\right),\end{aligned}$$

where $\theta_1 > \theta_2$ and the solid angle is then given by the sum of $\Omega_1 + \Omega_2$ where

$$\begin{aligned}\Omega_1 &= \int_0^{2\pi}\int_0^{\theta_2} \sin\theta\, d\theta d\phi,\\ \Omega_2 &= \int_{\theta_2}^{\theta_1}\int_{\phi} \sin\theta\, d\phi d\theta.\end{aligned}$$

At polar angles $\theta < \theta_2$, there is no geometric limit on the azimuthal angle (i.e. $\phi \in [0, 2\pi]$), but above θ_2 a new limit must be imposed on ϕ. The limits on ϕ' are given by

$$0 \le \phi \le \cos^{-1}(\tau_\phi) \quad \text{and} \quad 2\pi - \cos^{-1}(\tau_\phi) \le \phi \le 2\pi,$$

where τ_ϕ now has the form

$$\tau_\phi(\theta) = \frac{R_{disc}^2 - \rho^2 - (h_{\rm disc} - H)^2 \tan^2(\pi - \theta)}{2\rho(h_{\rm disc} - H)\tan(\pi - \theta)}.$$

There is one more limiting case for $\Theta = 0$, i.e. the disc is viewed face-on. In this case the solid angle simplifies to (see Appendix C.4, p. 244)

$$\Omega = 2\pi \int_0^{\alpha_{\rm disc}} \sin\theta\, d\theta,$$

where the integration over the azimuthal angle is for $\phi \in [0, 2\pi]$, while the limit on the polar angle is

$$\alpha_{\rm disc} = \tan^{-1}\left(\frac{R_{\rm disc}}{r - h_{\rm disc}}\right)$$

where r is the binary separation.

7.4.4 Angle to normal

The integration over the solid angle must correct for the projected surface area of the emitting source,

$$dA' = \cos\vartheta dA,$$

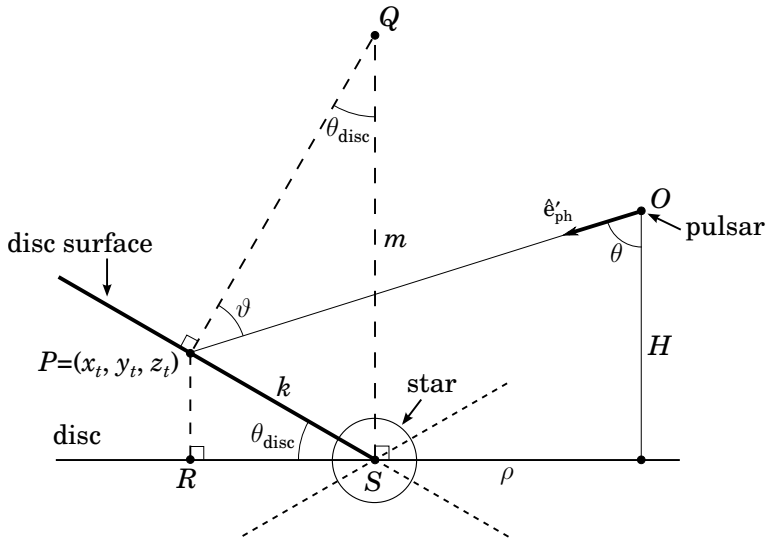

Figure 7.11: Angle to the normal of the surface of the disc. The pulsar/electron cloud is centred at O and the centre of the star/disc is at point S. The angle to the normal of the surface, ϑ is determined by angle $O\hat{P}Q$; see text for details.

where ϑ is angle to the normal of the surface element dA. The scattering rate equation then takes the form

$$\frac{dN_{\rm tot}}{dt\,d\epsilon_1} = \int_\theta \int_\phi \int_{\epsilon_0} \int_\gamma n_{\rm e}(\gamma)\, n_{\rm ph}(\epsilon_0) \frac{dN_{\gamma,\epsilon}}{dt\,d\epsilon_1} \cos\vartheta \sin\theta\, d\gamma\, d\epsilon_0\, d\theta\, d\phi,$$

where the additional $\cos\vartheta$ term relates to the project surface area.

For the integration over the disc, with a half-opening angle $\theta_{\rm disc}$, the angle to the normal of the surface depends on the half-opening angle and the direction of the incoming photon, as shown in Fig. 7.11. Point O is the centre of the electron cloud, ρ and H are the horizontal and vertical disc coordinates (Fig. 7.7), the bold solid line marks the top surface of the disc with a half-opening angle $\theta_{\rm disc}$, and the emitted photon originates from the point $P = (x_t, y_t, z_t)$ as measured from the centre of the star/disc (point S) as discussed in Chapter 6. The lines PQ and SQ, in Fig. 7.11, are constructed such that the line PQ is the normal to the disc surface at point P, the line SQ is normal to the disc mid-plane, and the lines intercept at Q. Also constructed is the line RP such that RP is normal to the disc mid-plane. From the figure it can be shown that the height of Q is given by

$$m = \frac{k}{\sin\theta_{\rm disc}},$$

where the length k is

$$k = \sqrt{x_t^2 + y_t^2 + z_t^2}.$$

In Fig. 7.11 the angle to the normal, ϑ is the angle $O\hat{P}Q$ and in a coordinate system centred

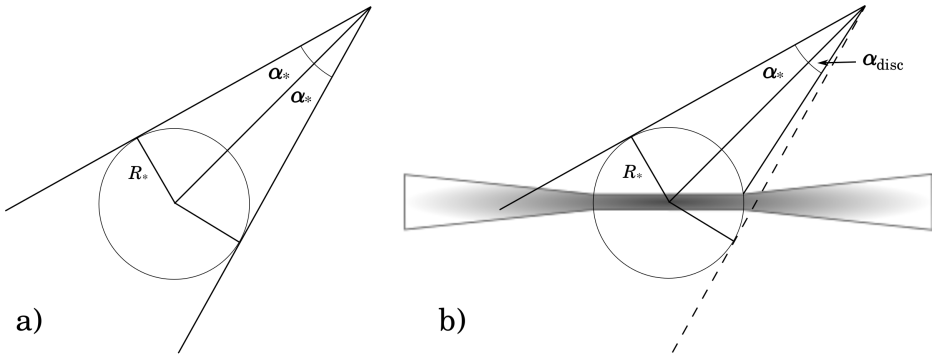

Figure 7.12: Additional constraints implied to the integration limits over the star/disc. On the left the full star is seen, while on the right, part of the star is hidden behind the disc, and part of the disc is hidden behind the star.

on P the points Q and O are defined by the vectors $\vec{Q} = (-x_t, -y_t, m - z_t)$ and $\vec{O} = (\rho - x_t, -y_t, H - z_t)$ respectively. The angle to the normal is then determined from

$$\begin{aligned} \cos\vartheta &= \frac{\vec{Q}\cdot\vec{O}}{||\vec{Q}||\,||\vec{O}||} \\ &= \frac{-x_t * (\rho - x_t) + y_t^2 + (m - z_t)(H - z_t)}{\sqrt{x_t^2 + y_t^2 + (m - z_t)^2} \times \sqrt{(\rho - x_t)^2 + y_t^2 + (H - z_t)^2}}. \end{aligned}$$

However, for discs with a small opening angle, the correction effect becomes negligible and does not result in a significant change in the photon density or the IC scattering rate. In these cases the angle to the normal can also be approximated as $\vartheta \approx \theta$, where θ is the polar angle.

7.4.5 Additional geometric constraints

The geometry considered so far has treated the star and disc independently. This must be modified by considering the scattering off a Be star, i.e. the scattering off the combined star-disc system. The effect of having the combined star-disc system is that part of the star is obscured by the disc and part of the disc is obscured by the star. It is necessary to determine whether, within the solid angle considered, the photon originates from the star or disc. This is shown in Fig. 7.12, where on the left hand side (a) the full star is seen, while on the right hand side (b), part of the star is hidden behind the disc, and part of the disc is hidden behind the star.

Since the star is completely opaque, photons which originate from the disc but which are obscured by the star will not influence the IC scattering. Therefore the AIC scattering from the disc is calculated by excluding lines-of-sight that are not visible. Similarly, photons which originate from the star but which are obscured by the disc will also not influence the IC scattering. Near the stellar surface the optical depth at optical wavelengths ~ 550 nm is greater than one. The disc may in fact be thicker near the star where material leaves the stellar surface. For this reason the stellar contribution towards the AIC scattering rate has been calculated by assuming,

first, that the star is not obscured by the disc (or the optical depth is negligible), and second, that the disc is completely opaque to the stellar photons. Practically this is implemented by determining during the numerical integration whether a direction first intercepts the star or the disc. The details of how this is accomplished are discussed in Appendix C.5.

7.5 The AIC gamma-ray spectrum

Using the constraints that have been determined above it is possible to calculate the AIC scattering rate at any point in the orbit from the equation

$$\frac{dN_{\rm tot}}{dt\,d\epsilon_1} = \int_{\epsilon_0}\int_{\Omega}\int_{\gamma} n_{\rm e}(\gamma)\, n_{\rm ph}(\epsilon_0)\frac{dN_{\gamma,\epsilon}}{dt\,d\epsilon_1}\cos\vartheta\, d\gamma\, d\epsilon_0\, d\Omega,$$

where $n_{\rm e}(\gamma)$ is the electron distribution, $n_{\rm ph}(\epsilon_0)$ is the target photon distribution, $dN_{\gamma,\epsilon}/dt\,d\epsilon_1$ is the AIC kernel and the $\cos\vartheta$ term is introduced to account for the change in the projected surface. This equation must be integrated numerically, and each term in the equation and the appropriate limits discussed above must be determined for each point in the orbit considered. The numerical integration was implemented using the FORTRAN programming language and the code was compiled with the Intel FORTRAN compiler, allowing for the implementation of multi-threading. This greatly reduced the length of time required to perform the numerical calculations. The program was executed on the University of the Free State's (UFS) High Performance Computer (HPC) where each instance of the program could be executed on a different node using up to a maximum of 48 CPUs.[iv] The calculation could be divided over different points in the orbit and executed simultaneously on different nodes.

The anisotropic scattering is presented here, showing both the preliminary results using the initial stellar parameters presented by Johnston et al. (1994)[v] and the results using the newer system parameters by Negueruela et al. (2011) and the corresponding COG fit. The photon distribution, $n_{\rm ph(\epsilon_0)}$, is determined for the star from a blackbody distribution and for the disc from the COG method as is outlined in section 7.1. The different electron distributions, $n_{\rm e}(\gamma)$, discussed in section 7.2, and applied to the AIC modelling are summarized in Table 7.1. Three orientations of the circumstellar disc were considered; one with the disc plane orientated at 90° to the orbital plane with the disc normal lying in the orbital plane parallel to the semi-minor axis (Fig. 7.13), a second with the disc plane orientated at 10° to the orbital plane, with the same rotation (Fig. 7.14) and the last using the orientation proposed by Chernyakova et al. (2006) and modelled by Okazaki et al. (2011), with the disc plane orientated at 45° to the orbital plane and the disc normal rotated 19° to the semi-minor axis (Fig. 7.15). Hereafter the orientations will be identified as the 90° disc, 10° disc and 45° disc respectively. For all cases the circumstellar disc is assumed to have a radius $R_{\rm disc} = 50R_*$.

[iv] Central Processing Units.

[v] The anisotropic scattering results using the Johnston et al. (1994) parameters have been presented in part in van Soelen and Meintjes (2012).

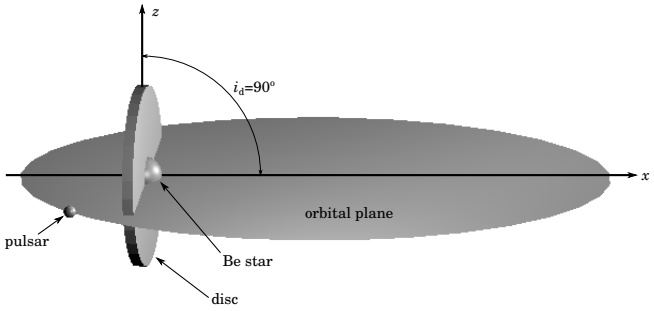

Figure 7.13: The 90° disc: The disc mid-plane is rotated by 90° to the orbital plane and the disc normal is parallel to the major axis.

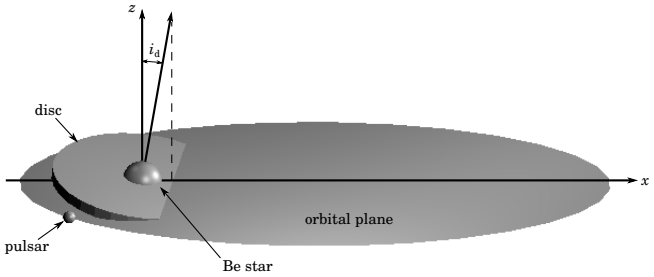

Figure 7.14: The 10° disc: The disc mid-plane is rotated by 10° to the orbital plane ($i_\mathrm{d} = 10°$) with the normal pointing away from periastron in the direction of the disc normal ($\theta_\mathrm{d} = 180°$).

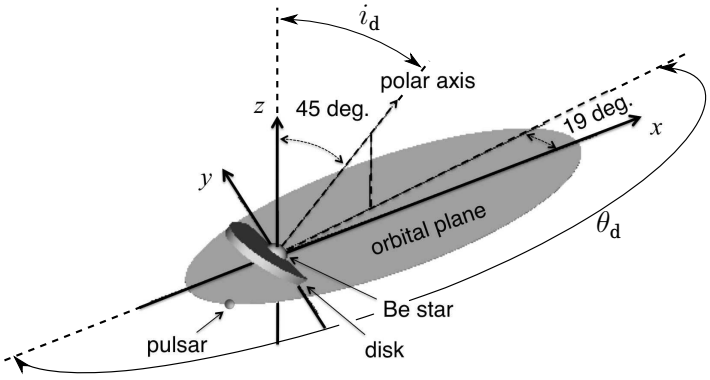

Figure 7.15: The 45° disc: the orientation of the circumstellar disc and orbital plane presented by Okazaki et al. (2011). The figure has been adapted to show the disc orientation angles i_d and θ_d considered in this study (figure adapted from Okazaki et al., 2011).

Table 7.1: Summary of the electron distributions, $n_e(\gamma)$, considered in this study.

Distribution	Origin	p	γ_{min}	γ_{max}
Mono-energetic (Khangulyan et al., 2011a)	pre-shock	-	10^4	10^4
Mono-energetic	pre-shock	-	10^6	10^6
Broad distribution	post-shock	2.2	10^4	10^7
Narrow distribution	post-shock	2.2	10^6	10^7
Adiabatic cooling (Kirk et al., 1999)	post-shock	2.4	5.4×10^5	5.4×10^7
Radiative cooling (Kirk et al., 1999)	post-shock	1.4	4.3×10^5	4.3×10^7

Table 7.2: Stellar and disc parameters for LS 2883 from Johnston et al. (1994) and van Soelen and Meintjes (2011, 2012).

Stellar parameters			
$M_{\rm star}$		10 $M_\odot$	
R_*		6 $R_\odot$	
$M_{\rm p}$		1.4 $M_\odot$	
T_*		25000 K	
i		36°	
Disc parameters			
$T_{\rm disc}$ (K)	12 500	15 000	15 000
n	2.3689	2.4753	2.4753
$R_{\rm disc}$		50 $R_{\rm star}$	
$\theta_{\rm disc}$	5°	0.7°	0.7°
Tilt to orbital plane	90°	45°	10°
Tilt to semi-major axis	0°	19°	0°

7.5.1 Johnston et al. (1994) system parameters

Johnston et al. (1994) found a mass and radius for the star $M_* = 10$ $M_\odot$ and $R_* = 6$ $R_\odot$ respectively, with a binary inclination $i = 36°$. These authors also adopted a colour excess of $E(B-V) = 1.05$ which corresponds to the IR-optical flux presented in Fig 6.11 (p. 122). The binary system parameters were determined for an assumed pulsar mass of $M_p = 1.4$ $M_\odot$. The appropriate integration limits were calculated following the procedure outlined in section 7.4.

Two different fits were considered for the disc photon spectrum. First, the fit considered in Fig. 6.11 was used for the 90° disc with a half-opening angle of 5°, while a second fit with a disc temperature of $T_{\rm disc} = 0.6T_*$ and a disc half-opening angle of 0.7°, corresponding to the parameters given by Okazaki et al. (2011), was used for the 45° and 10° discs. The IR excess was fitted using the COG method to the optical and IR data, and the disc parameters are summarized in Table 7.2. The resulting COG spectra for the 45° and 10° discs are almost identical to the spectrum shown in Fig. 6.11, and are therefore not shown. In all cases only free-free emission was considered for the disc emission while a blackbody distribution was used for the stellar spectrum.

Scattering spectrum

Fig. 7.16 shows the total scattering rate ($dN_{\rm tot}/dt\,d\epsilon_1$; equation 5.38) calculated for the Be star/disc system at periastron, using only the post-shock, adiabatically cooled electron distribution proposed by Kirk et al. (1999) and the disc parameters presented in Table 7.2. In order to better illustrate the ratio between the star and disc contributions, the scattering rate in Fig. 7.16 has been scaled (or normalized) to the maximum stellar scattering rate, i.e.

$$\frac{dN_{\rm norm}}{dt\,d\epsilon_1} = \frac{1}{A}\left(\frac{dN_{\rm tot}}{dt\,d\epsilon_1}\right), \tag{7.20}$$

where

$$A = \mathbf{max}\left(\frac{dN_{\rm tot,star}}{dt\,d\epsilon_1}\right). \tag{7.21}$$

The variable A is then a constant value determined by the maximum scattering rate predicted for the stellar contribution. The scattering rate from the disc was calculated assuming the angle to the normal could be approximated by a flat disc (i.e. $\vartheta \approx \theta$; see section 7.4.4). The solid lines show the scattering rate from the star (black), the 90° disc (blue), the 45° disc (green) and the 10° disc (red). The total flux (star+disc) is shown as the dashed lines, with the colours corresponding to the appropriate disc orientations. The stellar contribution is calculated without considering obstruction by the disc while the disc spectrum is calculated taking into account the obstruction by the star. This would be appropriate to a disc that is transparent to the stellar photons.

As is seen in Fig. 7.16, the scattering from the stellar (optical) photons occurs mainly in the Klein-Nishina regime, while the scattering of the soft (IR) photons, occurs mainly in the Thomson limit. As is shown in Fig. 5.6 (p. 88), when scattering occurs in the Klein-Nishina limit, the scattering rate peaks near the maximum allowed photon energy (i.e. near the initial energy of the electron), while in the Thomson limit the scattering rate is highest at the minimum allowed energy and is lowest at the maximum allowed energy. This results in the stellar contribution peaking at a few $\times\, 10^{11}$ eV, while the disc contribution is highest at lower energies. Below GeV energies, the total scattering rate (star+disc) is significantly higher than the stellar contribution alone. The disc contribution is greatest for the 90° disc, as it presents the largest solid angle, and is a factor ~ 2 larger than the scattering rate from the star alone.

Light curve

Fig. 7.17 shows the modelled integrated flux in the *Fermi* energy range ($\sim 0.1 - 100$ GeV) for PSR B1259-63/LS 2883. The light curve was calculated by summing over the flux in the *Fermi* energy range, where the flux is given by

$$F_\nu = h\epsilon_1 \times \frac{dN_{\rm tot}}{dt\,d\epsilon_1}, \tag{7.22}$$

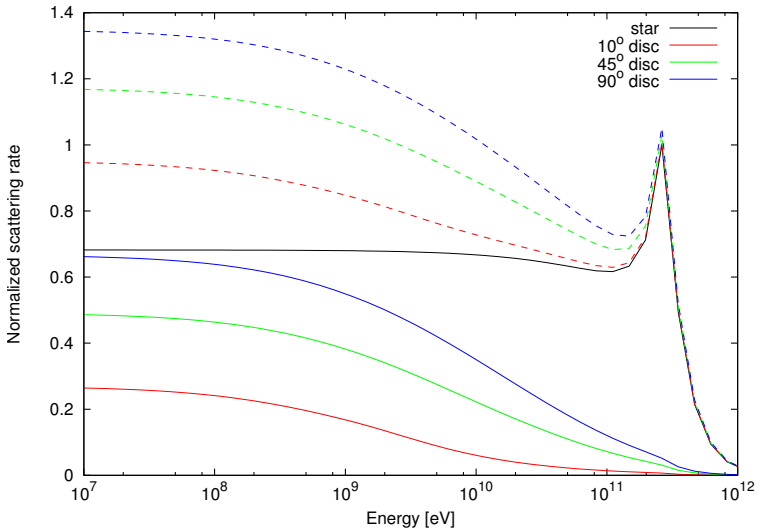

Figure 7.16: Modelled AIC scattering rate from the (unobscured) star and circumstellar disc in PSR B1259-63/LS 2883 at periastron, for post-shock electrons and the Johnston et al. (1994) parameters. The scattering has been normalized to the maximum scattering rate from the star (see text for details). The solid lines show the scattering rate from the star (black), the 90° disc (blue), the 45° disc (green) and the 10° disc (red). The total flux (star+disc) is shown as the dashed lines, with the colours corresponding to the appropriate disc.

where the scattering rate, $dN_{\rm tot}/dt\, d\epsilon_1$, is shown in Fig. 7.16. The light curve has also been scaled to the maximum stellar contribution in order to clearly show the relative differences between the stellar and disc contributed fluxes. In other words, the modelled *Fermi* light curve in Fig. 7.17 is plotted as the integrated flux at time t,

$$F_{\rm norm}(t) = B^{-1} \int F_\nu(t)\, d\nu, \tag{7.23}$$

where the integration is over the energy range $\sim 0.1 - 100$ GeV, and the normalization factor, B, is the maximum value of the integrated stellar flux at periastron, i.e.

$$B = \mathbf{max}\left(F_{\rm star}(t)\right). \tag{7.24}$$

While from Fig. 7.16, it can be seen that the disc contribution approaches the stellar contribution at $\epsilon_1 \lesssim 10^9$ eV, while at energies $\epsilon_1 > 10^{10}$ eV the disc contribution reduces to values below $0.4 \times dN_{\rm tot}/dt\, d\epsilon_1$. Since the energy range in Fig. 7.16 is plotted logarithmically, the integrated flux between $10^8 - 10^{11}$ eV (*Fermi* energy range: $\sim 0.1 - 100$ GeV), is dominated by the scattering at higher energies. As a result, the modelled *Fermi* light curve in Fig. 7.17 is still dominated by the stellar contribution.

Both the star and disc contributions peak near periastron, with the 90° disc peaking ~ 1 day before periastron due to the scattering angle and the 45° disc peak contribution occurring

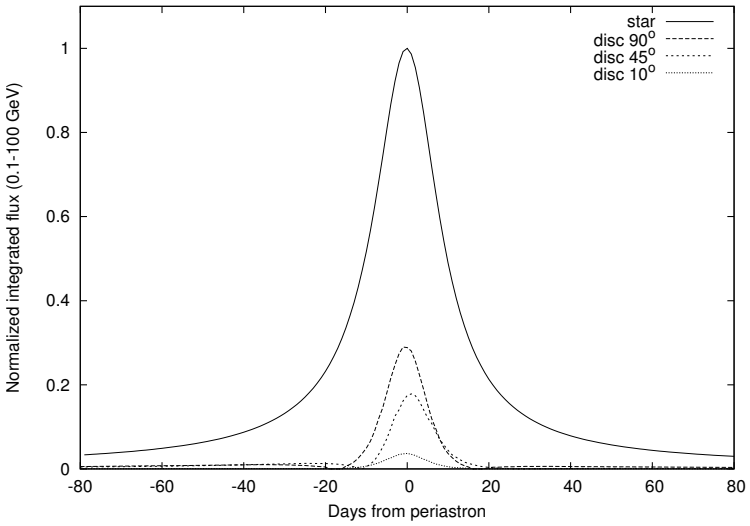

Figure 7.17: The modelled integrated flux in the *Fermi* energy range ($0.1 - 100$ GeV) from PSR B1259-63/LS 2883 using the system parameters in Table 7.2. The light curve is scaled to the peak stellar contribution at periastron, as is described in the text.

a few days after periastron due to the 19° rotation of the disc normal from the semi-major axis (Fig. 7.15). The 90° and 45° disc contributions are plotted separately in Fig. 7.18, which shows the slight off-set of the peak emission from periastron due to the rotation of the 45° disc from the semi-major axis. Both disc orientations show a slight rise in the flux as the pulsar approaches the disc at $\sim \tau - 20$ days (where τ is the epoch of periastron), which decreases just before the disc crossing, followed by a sharp increase in the flux after the disc crossing as head–to–head collisions readily occur in this region.

Since the disc scattering rate manifests predominately at lower energies, the AIC light curve in the H.E.S.S. energy range (> 100 GeV) is much less affected by the presence of the circumstellar disc, and is, therefore, not shown here.

7.5.2 Negueruela et al. (2011) system parameters

The observations by Negueruela et al. (2011) found a colour excess of $E(B-V) = 0.85$ for LS 2883, and these authors proposed a stellar mass of $M_* = 31$ $M_\odot$, a stellar radius of $R_* = 9.2$ $R_\odot$ and a binary inclination of $i = 33°$. The COG method was used to fit the new colour excess (Fig. 6.12, p. 126) and the best fit COG parameters were used to calculate the disc photon spectrum for the AIC calculation. As in section 7.5.1, only the free-free component was used to model the disc emission, while a blackbody distribution was used for the stellar component, with the same effective temperature as the fitted Kurucz model.

For the circumstellar disc, only a single half-opening angle of 1° was considered, consistent with a thin disc and for such a thin disc the angle to the normal can be approximated by $\vartheta \approx \theta$ (section 7.4.4). The adopted disc temperature was $T_{\rm disc} = 0.6T_*$ and the disc was considered

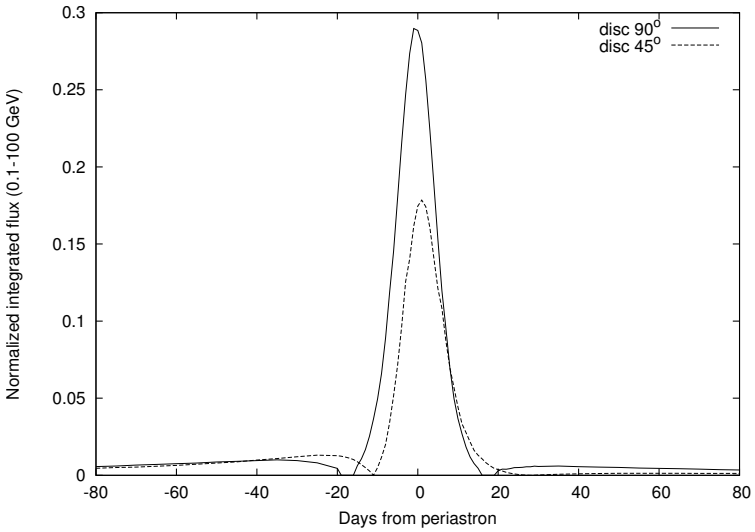

Figure 7.18: Comparison of the modelled integrated flux in *Fermi* energy range for the 90° and 45° disc orientations shown in Fig. 7.17. The 90° disc's peak contribution occurs approximately 1 day before periastron. Due to the orientation of the 45° disc (Fig. 7.15), the disc shows a slightly higher flux just before the disc crossing at $\tau - 15$ days, and the peak emission shifts to slightly after periastron.

to extend to a distance of $R_{\rm disc} = 50R_*$. The same disc orientations considered in section 7.5.1 were used and the star and disc parameters are summarized in Table 7.3

Three electron distributions were considered; a post-shock, adiabatically cooled electron spectrum with a power law ($p = 2.4$) distribution between $5.4\times10^5 < \gamma < 5.4\times10^7$ and two pre-shock electron distributions, which were assumed to be mono-energetic and centred at $\gamma = 10^4$ and $\gamma = 10^6$, respectively.

Scattering spectrum – post-shock electrons

The AIC scattering rate, ($dN_{\rm total}/dt\, d\epsilon_1$ equation 5.38), from the post-shocked, adiabatically cooled electron spectrum at periastron is shown in Fig. 7.19 using the Negueruela et al. (2011) stellar parameters and the corresponding fit to the COG method. As in section 7.5.1, the scattering rate has been scaled (normalized) to the peak (unobscured) stellar contribution, to better illustrate the ratio between the two contributions (see equations 7.20 & 7.21). The solid black line is the scattering rate from the (unobscured) star while the colour lines correspond to the disc scattering rate (solid lines) and the combined star+disc scattering rate (dashed lines). Similar to the previous results (section 7.5.1, Fig. 7.16) the disc contribution is highest at lower energies, since the scattering occurs in the Thomson limit, while the stellar contribution peaks at a few $\times\, 10^{11}$ eV, due to the scattering occurring mainly in the Klein-Nishina limit.

As is shown in Fig. 7.19, for the Negueruela et al. (2011) parameters the 45° and 90° disc contributions exceed the stellar contribution below ~ 1 and ~ 50 GeV respectively. This effectively means that the IC spectrum at GeV energies is dominated by scattering from the circumstellar

Table 7.3: Stellar and disc parameters for LS 2883 from Negueruela et al. (2011) and this study.

Stellar parameters			
$M_{\rm star}$		31 $M_\odot$	
R_*		9.3 $R_\odot$	
$M_{\rm p}$		1.4	
T_*		33 000 K	
i		33°	
Disc parameters			
$T_{\rm disc}$ (K)		19 800	
n		3.055	
$R_{\rm disc}$		50 $R_{\rm star}$	
$\theta_{\rm disc}$		1°	
Tilt to orbital plane	90°	45°	10°
Tilt to semi-major axis	0°	19°	0°

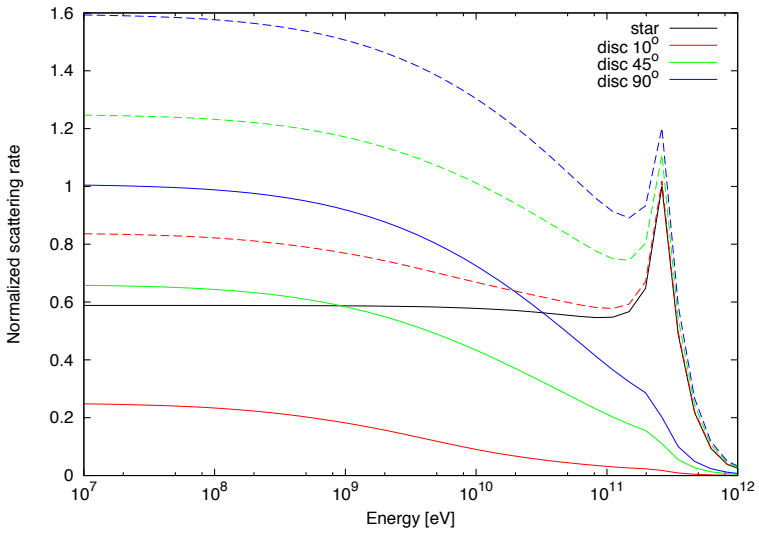

Figure 7.19: Modelled AIC scattering rate for the post-shock, adiabatically cooled electron distribution, from the star and circumstellar disc in PSR B1259-63/LS 2883 at periastron, using the system parameters proposed by Negueruela et al. (2011) and the COG method fitted to the modified spectrum. The scattering has been normalized to the maximum stellar scattering rate in the figure. The solid lines show the scattering rate from the star (black), 10° disc (red), 45° disc (green) and 90° disc (blue). The dashed lines show the total flux (star+disc) using the corresponding colours.

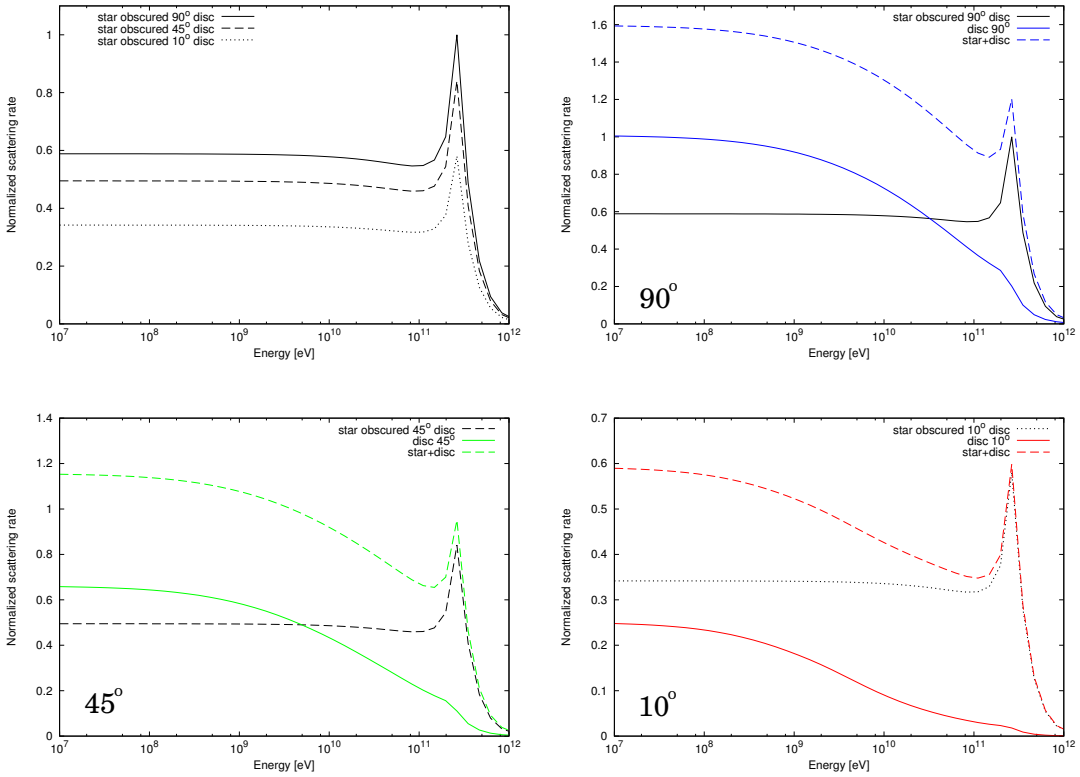

Figure 7.20: The modelled scattering spectrum from PSR B1259-63/LS 2883 at periastron (for the post-shock, adiabatically cooled electron distribution), showing the effect of the stellar spectrum being obscured by the circumstellar disc. All figures are scaled to the maximum unobscured stellar contribution as discussed in the text. Top left: The decrease in the stellar spectrum due to the stellar obscuration. Top right: The star and disc components including the obscuration of the stellar component for the 90° disc. Bottom left: the same for the 45° disc and bottom right: the same for the 10° disc.

disc for these two orientations. The modelled spectrum shows that the total scattering rate (star+disc contribution) is significantly greater than the stellar contribution alone.

The stellar contribution in Fig. 7.19 is calculated assuming the full solid angle of the star is observable by the pulsar/electron cloud (an unobstructed star, applicable to no circumstellar disc), but if the disc is thick enough to obscure part of the star (Fig. 7.12, section 7.4.5) it will result in a reduction of the stellar contribution. Fig. 7.20 shows the reduced stellar contribution (assuming that the disc is completely opaque to the stellar photons) and the associated disc scattering rate. In order to make a comparison between the obscured and unobscured stellar contribution, the scattering rates have been scaled with the same normalization parameter A (equation 7.21) in both Figs. 7.19 and 7.20. For the 90° disc, the star is not obscured at periastron, and is therefore identical to Fig. 7.19. However, for the 45° and 10° discs, the star is obscured at periastron and the associated stellar contribution decreases. This has the effect of increasing the contribution of the disc component relative to the stellar component.

Light curve – post-shock electrons

The integrated flux around periastron, using the parameters above, is shown in Figs. 7.21 & 7.22 for the *Fermi* and H.E.S.S. energy ranges respectively. The light curves show the modelled integrated flux around periastron, which has been scaled to the maximum (unobscured) stellar contribution as was outlined in section 7.5.1 (equations 7.22, 7.23 & 7.24). The scattering rates ($dN_{\rm tot}/dt\, d\epsilon_1$) shown in Figs. 7.19 & 7.20, were used to determine the integrated flux (equation 7.22) where the appropriate integration limit was applied. For the *Fermi* light curve the integrations energy range is $0.1 - 100$ GeV, while for the H.E.S.S. light curves the integration limit $0.380 - 2.321$ TeV was chosen. The H.E.S.S. integration limits were chosen to correspond to the results presented in Aharonian et al. (2005): the lower limit was chosen to correspond to their fig. 5, which presents the integrated flux above 380 GeV, while the upper limit, 2.321 TeV, is the highest reported energy in their fig. 4.[vi] Also shown in the figures are the stellar light curves if the disc obscures the star, which changes the shape and decreases the flux contribution from the star around periastron. The gaps in the modified stellar light curves correspond to periods when the pulsar is passing through the disc. The light curves show that the disc contribution is a minimum around the disc crossing epoch ($\tau \pm 20$ days) and a maximum around periastron.

Scattering spectrum – pre-shock electrons

The normalized AIC scattering spectrum for pre-shock electrons at periastron are shown in Fig 7.23 for a 90° disc. Two electron energies were considered, namely $\gamma = 10^4$ suggested by Khangulyan et al. (2011a) and $\gamma = 10^6$ considered by Kirk et al. (1999). The $\gamma = 10^4$ spectrum shows no indication of a peak in the scattering rate, usually associated with scattering in the Klein-Nishina regime. The highest scattering rate occurs at low energies for both the stellar and disc contributions, indicating that the scattering occurs in the Thomson limit. The scattering spectrum for the $\gamma = 10^6$ electrons shows that the stellar photons scatter in the Klein-Nishina regime (implied by the peak in the scattering rate at $\sim 5\times10^{11}$ eV), while the disc photons scatter in the Thomson regime. The scattering from the disc is higher than the stellar contribution for energies below $\sim 10^{10}$ eV and the inclusion of the disc contribution increases the total scattering rate by a ~ 2.

Lightcurve – pre-shock electrons

The predicted integrated flux at *Fermi* energies around periastron are shown for $\gamma = 10^4$ and $\gamma = 10^6$ pre-shock electrons in Fig. 7.23, scaled to the maximum stellar contribution. Only the 90° disc has been considered, using the same orientation as for the post-shock electrons. While the $\gamma = 10^4$ electrons do not significantly alter the light curve, the $\gamma = 10^6$ electrons produce a disc contribution which is significant across the period under consideration, resulting

[vi] The exact value of the upper limit is given in data released with the publication, available from the H.E.S.S. website: *www.mpi-hd.mpg.de/hfm/HESS/pages/publications/auxiliary/AA442_1.html*.

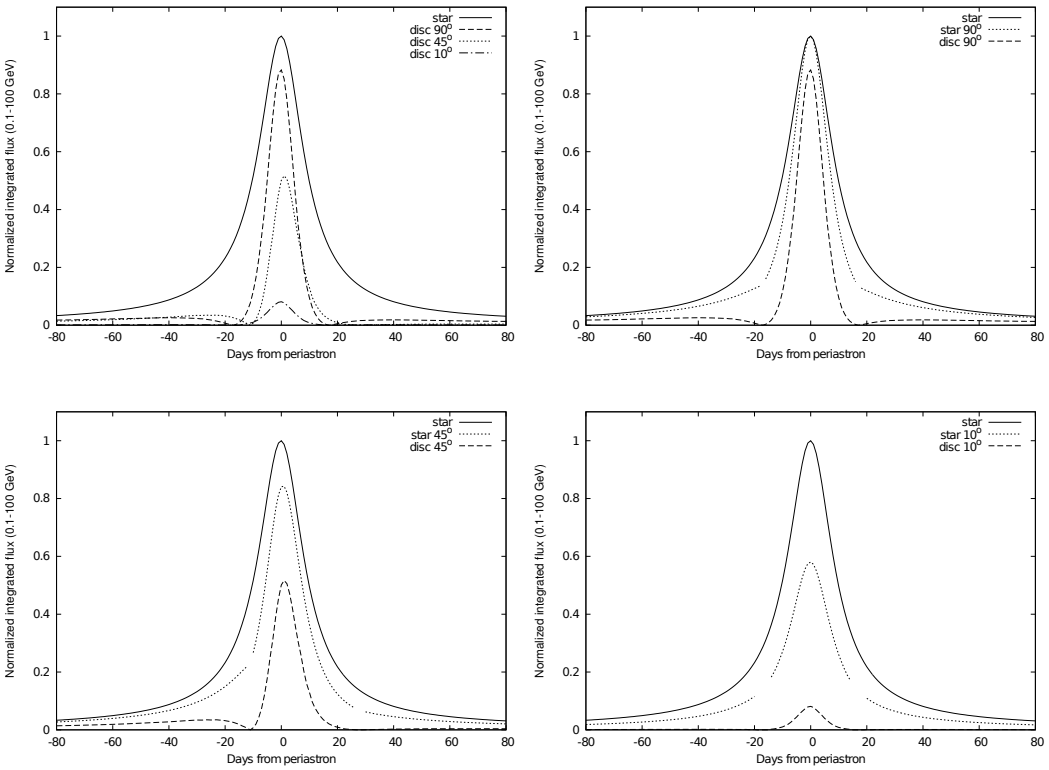

Figure 7.21: Corresponding integrated flux for the AIC scattering of the post-shock, adiabatically cooled electron distribution and the Negueruela et al. (2011) COG parameters at *Fermi* energies ($\sim 0.1 - 100$ GeV), normalized to the maximum stellar contribution. For each disc orientation, i.e. 90° (top right), 45° (bottom left) and 10° (bottom right), the disc contribution is compared with the unobscured and the obscured stellar contribution.

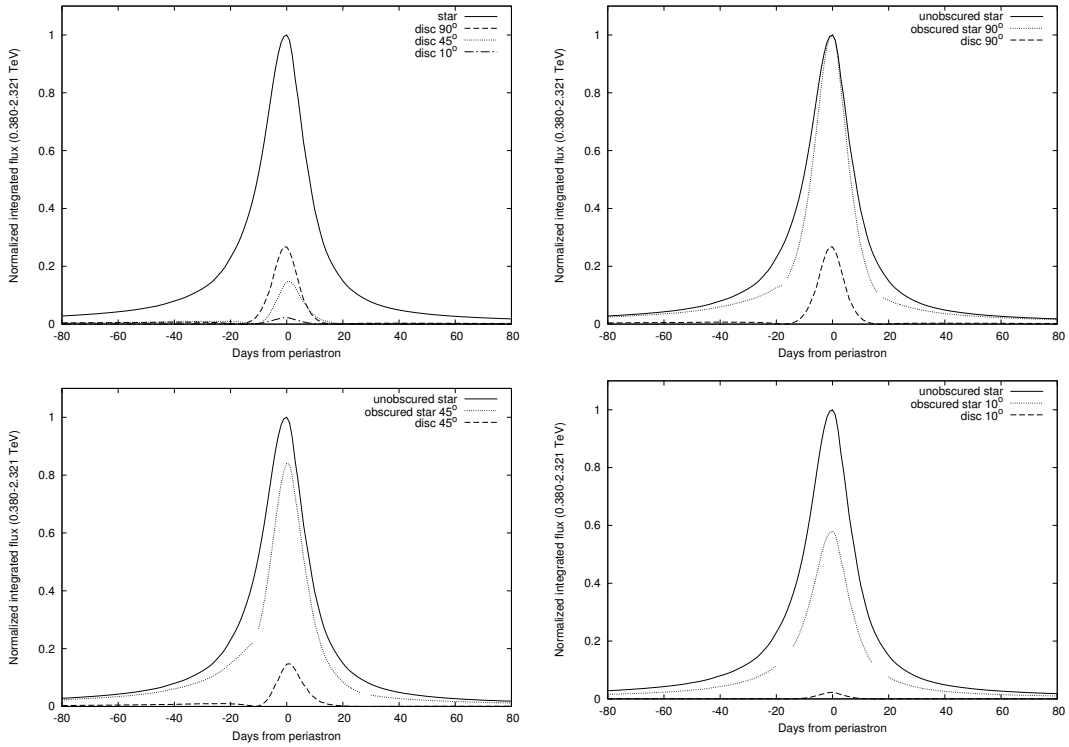

Figure 7.22: Same as Fig. 7.21, but at the H.E.S.S. energy range.

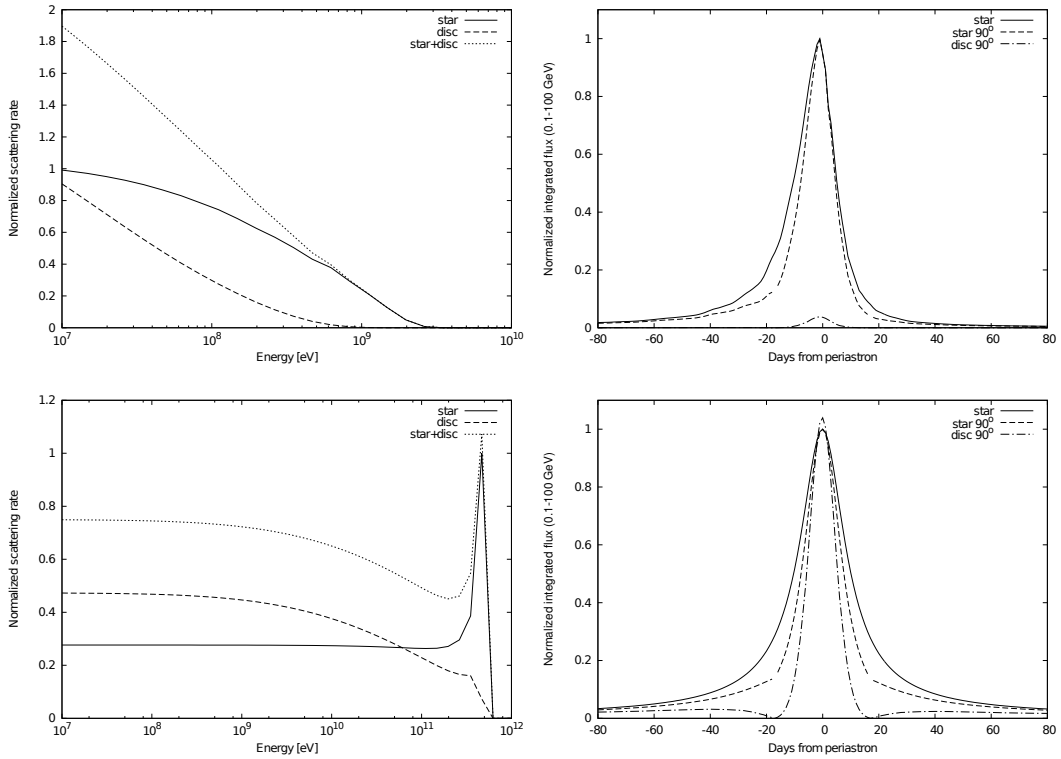

Figure 7.23: The normalized scattering spectrum (left) and integrated flux at *Fermi* energies (right) from the AIC scattering of pre-shocked electrons, using the Negueruela et al. (2011) COG parameters. The electron energies chosen were $\gamma = 10^4$ (top) and $\gamma = 10^6$ (bottom). The figures are normalized to the relevant maximum stellar contribution.

in a higher flux than the stellar contribution at periastron. The disc minimum occurs around the disc crossing epoch ($\sim \tau \pm 20$ days) while the maximum occurs around periastron.

7.5.3 Summary of the AIC scattering

As is shown in sections 7.5.1 and 7.5.2, for both the Johnston et al. (1994) and the Negueruela et al. (2011) parameters, the inclusion of the IR excess significantly increases the IC scattering rate. The increase is highest for the 90° circumstellar disc orientation since the pulsar observes/views the disc face-on at periastron, presenting the greatest solid angle at the position of closest approach. This disc orientation was specifically considered in-order to present the system with the greatest possibility of significantly increasing the scattering rate. The 45° orientation, proposed by Okazaki et al. (2011), also presents a significant increase in the scattering rate, though the effect is not as significant for the 10° orientation.

For the different electron distributions considered, the adiabatically cooled electron distribution adopted from Kirk et al. (1999) is believed to be the most realistic, and is known to produce a reasonable fit to the observed 2004 H.E.S.S. spectrum. For this distribution, the optical photons from the star scattered in the Klein-Nishina regime, while the (soft) IR photons from the circumstellar disc scattered in the Thomson limit. This results in the disc contribution dominating at GeV (*Fermi*) energies, while the stellar contribution dominates at TeV (H.E.S.S.) energies. However, the increase in the scattering rate is not able to account for the *Fermi* "flare" observed after the December 2010 periastron passage.

The mono-energetic $\gamma = 10^4$, pre-shock electron distribution proposed by Khangulyan et al. (2011a) to explain the *Fermi* flare, has also been considered in this study. As is shown in Fig. 7.23, both the stellar and disc photons scatter in the Thomson limit and, while the scattering rate does increase, the integrated flux over the *Fermi* energy range ($0.1 - 100$ GeV) shows no evidence for a flaring event as the photon density remains too low near the disc crossing epoch.

Chapter 8

Discussion

The results of the isotropic calculations have been discussed in van Soelen and Meintjes (2011) and, therefore, this chapter will focus on discussing the results from the anisotropic scattering presented in Chapter 7. This chapter begins by considering the effect of the different COG model parameters on the AIC scattering rate, before discussing the general AIC results presented in Chapter 7. The chapter concludes with a general discussion of the implications of these results and the prospect of future studies.

8.1 Comparison of the COG fits

The most striking difference between the predicted gamma-ray flux using the Johnston et al. (1994) and Negueruela et al. (2011) parameters (hereafter referred to as the J94 and N11 parameters respectively) is the increase in the gamma-ray flux due to the disc photon contribution for PSR B1259-63/LS 2883 (compare Figs. 7.16 & 7.19). Before discussing the implication of the predicted gamma-ray spectrum it is necessary to discuss the effect the J94 and N11 parameters have on the total multi-wavelength flux (radio to optical) from the Be star and disc. A brief comparison will also be made of the effects Kurucz distribution used in the isotropic modelling, and the blackbody distribution that was considered for the anisotropic modelling.

8.1.1 The relative IR excess

J94 proposed a colour excess of E(B-V) = 1.05 and a distance to the source of 1.5 kpc for LS 2883, while the more recent and extensive observations undertaken by N11 determined a colour excess of E(B-V) = 0.85, with a proposed distance of 2.3 kpc (section 2.2, p. 11) The newer distance measurement is more consistent with the distance suggested by the radio pulsar dispersion measurement (e.g. Table 2.1, p. 6) and the calculated distance to two nearby stars (Negueruela et al., 2011). Both colour excess terms have been applied to LS 2883 for comparison and the resulting COG fits are shown in Figs. 6.11 & 6.12. The decrease in the colour excess term

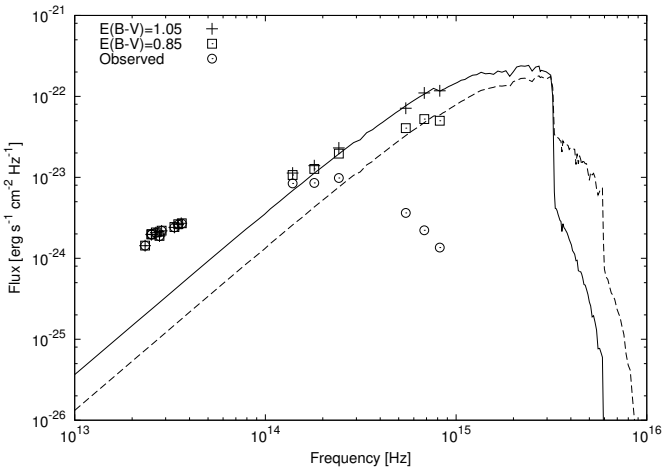

Figure 8.1: The observed, uncorrected optical and IR flux (open circles) and the de-reddened data using E(B-V) = 1.05 (crosses) and E(B-V) = 0.85 (open squares), shown without error bars. Shown for comparison is the best fit stellar flux for $T_* = 25\,000$ K at a distance of $D \sim 1.5$ kpc (solid line) and $T_* = 33\,000$ K at a distance of $D \sim 2.3$ kpc (dashed line). Note that the larger distance results in the hotter star having a fainter, corrected flux.

proposed by N11 effectively implies that LS 2883 is less affected by interstellar extinction than was implied by the J94 parameters. The observed optical and IR flux from LS 2883 is shown in Fig. 8.1, along with the de-reddened fluxes and the two best fit stellar fluxes for comparison. Since interstellar extinction influences optical photons more than IR photons the choice of the colour excess term has a significant effect on the optical data and a minimal to negligible effect on the near- and mid-IR data. The hotter star ($T_* = 33\,000$ K) appears fainter in Fig. 8.1 due to the increased observational distance ($D \sim 2.3$ kpc). The newer N11 colour excess shows that the deviation of the disc's IR excess flux from the standard stellar atmosphere is significantly higher than was predicted by the J94 parameters. The choice of the J94 or N11 parameters therefore influences the ratio of the optical to the IR flux, and the N11 parameters lead to an increase in the IR excess.

Fig. 8.2 compares both the stellar and the COG flux from LS 2883 without scaling for distance, from which it can be seen that utilizing the N11 parameters not only increases the brightness of the optical star but also increases the brightness of the circumstellar disc, particularly between 10^{13} to 10^{15} Hz. The N11 COG fit also deviates from the stellar contribution at a slightly higher frequency of $\sim 10^{15}$ Hz while the J94 COG fit deviates at $\sim$ few $\times\, 10^{14}$ Hz. This is clearly illustrated in Fig. 8.3 which displays the ratio of the total flux (star and disc) to the flux from the star alone (i.e. $F_{\rm star+disc}/F_{\rm star}$). The N11 parameters reveal a higher ratio, particularly between $\sim 10^{13} - 10^{15}$ Hz.

The improved N11 parameters therefore increase the circumstellar disc gamma-ray contribution in two ways. First, the IR excess is higher which increases the photon density from the disc and the associated number of IC scatterings that occur. Second, the large increase in

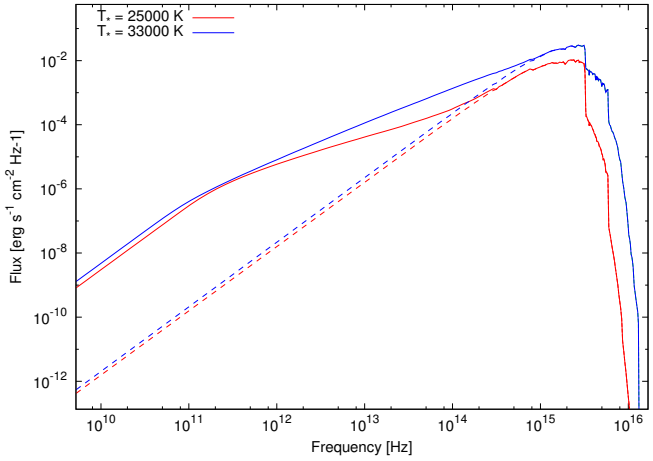

Figure 8.2: The predicted flux from LS 2883, without scaling for distance, for a $T_* = 25\,000$ K star using the J94 COG parameters (red line) and a $T_* = 33\,000$ K star using the N11 COG parameters (blue line). The dashed lines indicate the stellar contributions without the IR excess. The N11 parameters produces a noticeably higher IR excess between $10^{13} - 10^{15}$ Hz.

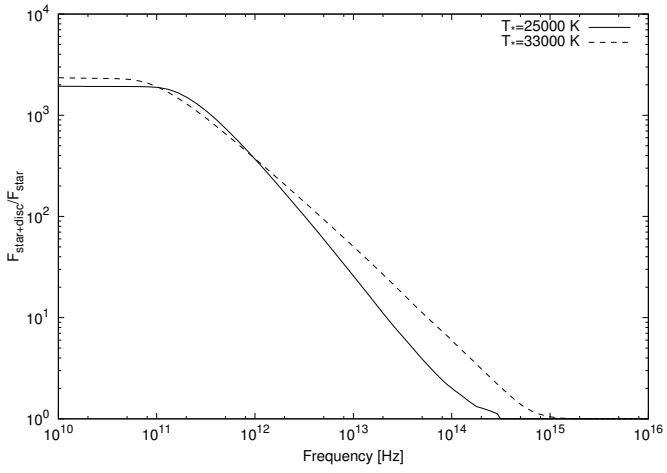

Figure 8.3: Ratio between the total flux (star and disc) to the flux from the star alone using the J94 (solid line) and N11 (dashed line) parameters.

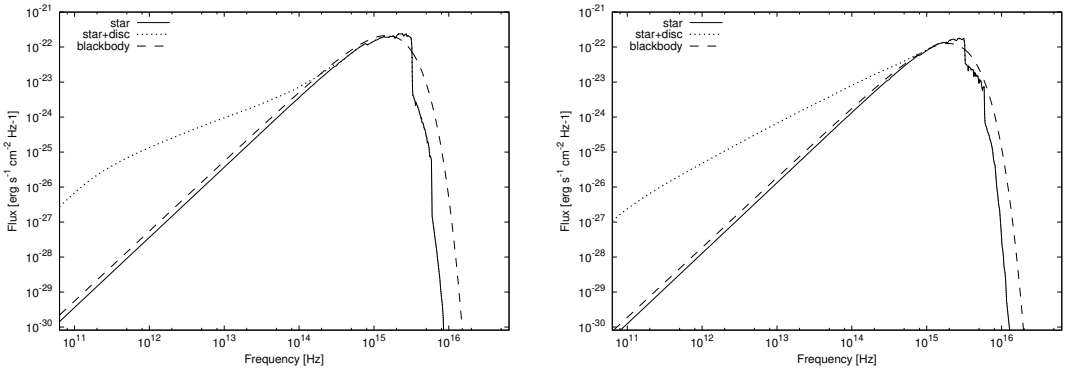

Figure 8.4: The Kurucz atmosphere (solid line), the blackbody stellar approximation (dashed line) and the COG fit (dotted line) using the J94 (left) and N11 (right) parameters.

the disc/stellar flux ratio between $\sim 10^{13} - 10^{15}$ Hz, leads to the production of High Energy (HE; $\sim 0.1 - 100$ GeV) gamma-rays in the Thomson and near Klein-Nishina limit. The frequency at which the Thomson approximation ceases to be valid and where we must change to the Klein-Nishina approximation is given by

$$\begin{aligned} \nu &\approx \frac{mc^2}{h\gamma} \\ &\approx 10^{14} \left(\frac{\gamma}{10^6}\right)^{-1} \text{ Hz}, \end{aligned}$$

and, therefore, the IC scattering produces HE gamma-ray production without a significant decrease in the scattering cross-section associated with the extreme Klein-Nishina limit (section 5.2).

8.1.2 Blackbody distribution and the Kurucz atmosphere

In the anisotropic calculation of the IC spectrum a blackbody distribution was used to determine the photon density from the star. In contrast, the full Kurucz atmosphere was used in the isotropic approximation. Since the blackbody spectrum is a smooth function it decreases the time and the number of integration steps required to calculate the AIC scattering rate. Fig. 8.4 compares the flux from the Kurucz stellar atmosphere, the blackbody approximation and the COG fit for the J94 and N11 parameters. For both cases the blackbody spectrum produces a good match to the stellar spectrum, but is slightly brighter at most wavelengths, with the exception of frequencies around the peak stellar emission. The choice of a blackbody approximation is therefore suitable, but it may slightly overestimate the stellar contribution at GeV energies, where the disc contribution is most important.

8.1.3 Effects due to rapid rotation

In all the modelling presented in this study, it has been assumed that the B-star (without the circumstellar disc) can be approximated by a perfect, isothermal sphere. It is, however, known from modelling and observations that rapidly rotating stars are not spherical and can show a temperature gradient between the pole and equator. Negueruela et al. (2011) estimated parameters for PSR B1259-63/LS 2883 (Table 2.4, p. 12) and found the temperature and radius varied by $\sim 20\%$ between the pole and equator. The effect of gravitational darkening has not been included in this study since it is believed that it will not result in a significant correction to the inverse Compton scattering.

8.2 Anisotropic scattering

The results of the isotropic IC scattering were discussed in van Soelen and Meintjes (2011), included in this thesis as pages 137 to 145. In this section, therefore, I will focus on results of the anisotropic scattering calculation.

8.2.1 Flux increase

To illustrate the difference between the AIC scattering rate near periastron for the J94 and N11 parameters, I compare the relative increase in gamma-ray flux using the J94 parameter to the increase using the N11 parameters. The resulting increase in the flux at periastron is shown in Fig. 8.5 for the J94 parameters and electron distribution discussed in Chapter 7. For these results the flux increased by less than a factor 2 around 1 GeV depending on the orientation of the circumstellar disc. This is slightly less than that predicted by the isotropic approximation in van Soelen and Meintjes (2011, pp. 137–145 in this thesis). The flux increase obtained by using the anisotropic approximation in Fig. 8.5 was determined using the same parameters that were used to calculate the isotropic approximation (fig. 7 in van Soelen and Meintjes, 2011, p. 143 in this thesis). The flux increase obtained by using the N11 parameters for different electron distributions (pre– and post–shock) is shown in Fig. 8.6, where the increase in the flux is of the same order as the isotropic approximation, i.e. greater than a factor ~ 2.

Since the anisotropic calculation is highly directional, photons that arrive over the wide solid angle of the disc do not all scatter with the same energy. Unlike the isotropic approximation where an average scattering angle was considered and the total photon distribution was assumed to be isotropically distributed, the anisotropic model is based on a photon distribution which is spread out over the solid angle spanning the disc. This effect results in a slight decrease in the influence of circumstellar disc in the J94 anisotropic calculation.

The increase in the N11 spectrum is of the same order as the isotropic approximation because, as was discussed in section 8.1.1, the change in the colour excess has the effect of increasing the IR excess (Figs. 8.2 & 8.4). The disc is therefore brighter because of a higher disc temperature

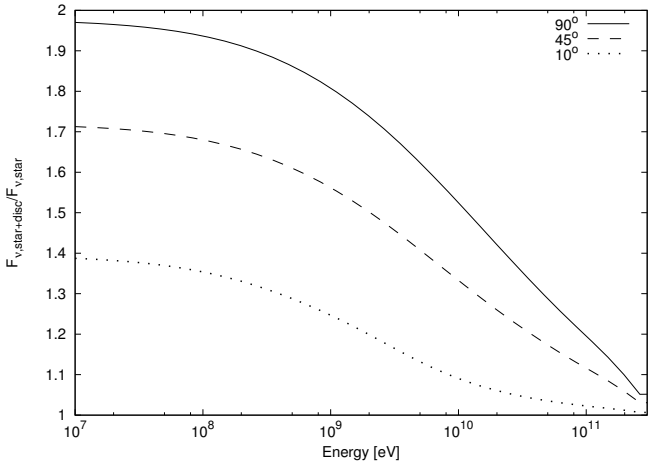

Figure 8.5: Ratio of the total flux (star+disc contribution) to the flux from the unobscured star contribution, calculated at periastron with the J94 parameters. The lines are determined for the 90° disc (solid line), 45° disc (dashed lines) and 10° disc (dotted line) orientations using the electron distribution and disc parameters discussed in Chapter 7.

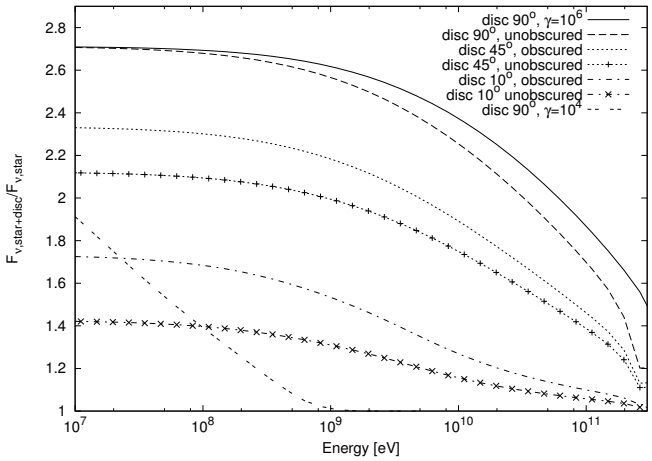

Figure 8.6: Ratio of the total flux (star+disc contribution) to the flux from the star contribution, calculated at periastron with the N11 parameters. Indicated on the graph are the adiabatic cooled spectra, calculated for the three disc orientations, with and without the star being obscured. Also shown are the results for the scattering of pre-shock mono-energetic electrons ($\gamma = 10^4$ and $\gamma = 10^6$).

and is brighter relative to the star. This relative increase in the photon spectrum increases the influence of the disc photon contribution.

The disc calculated with the N11 parameters is also brighter between $10^{13} - 10^{15}$ Hz (section 8.1.1). Since in the Thomson limit the energy of the scattered photon, $\epsilon_1 = h\nu_1$, relates to the energy of the incoming photon, $\epsilon_0 = h\nu_0$, as $\epsilon_1 \propto \gamma^2\epsilon_0$, the disc contribution remains more significant towards higher energies, e.g.

$$\epsilon_1 \lesssim 2 \left(\frac{\gamma}{10^6}\right)^2 \left(\frac{\nu_0}{10^{14}\text{ Hz}}\right) \text{ TeV}.$$

This can be verified by comparing Fig. 7.16 (p. 164) and Fig. 7.19 (p. 167). For the isotropic approximation the disc contribution is already decreasing significantly at ~ 1 GeV (fig. 7 in van Soelen and Meintjes, 2011) while for the N11 anisotropic approximation the contribution remains nearly constant till above ~ 5 GeV (Fig. 8.6). The disc contribution then remains higher over the HE ($\sim 0.1 - 100$ GeV) and VHE ($\gtrsim 100$ GeV) energy range and has a greater influence on the observed gamma-ray luminosity.

8.2.2 Light curves

The predicted AIC integrated flux around periastron (Figs. 7.17, 7.21, 7.22 & 7.23) shows that the disc contribution exhibits three properties: firstly, the contribution is a maximum around periastron; secondly, there is a slight increase just before the disc crossing epoch and a minimum at the disc crossing ($\sim \tau \pm 20$ days); and lastly, the rise after the disc crossing is much faster than the slow rise just before the disc crossing. This modelled disc contribution light curve is a combination of the photon distribution of the circumstellar disc and the IC scattering angle, as discussed below.

Fig. 8.7 shows the photon number density (at $\nu = 10^{12}$ Hz) from the disc, as observed by the pulsar, for $\tau - 60$ to 0 days from periastron for the 90° disc orientation. The figure has been calculated assuming the pulsar approaches the disc from the right (see Fig. 8.9). The photon number density was determined from the optical depth along lines-of-sight through the circumstellar disc using the COG method discussed in Chapter 6, and by considering the change in projected surface area (i.e. $dA = \cos\vartheta dA'$). It is important to note that a constant scaling was not used, but was adjusted to show the disc clearly in Fig. 8.7.

As shown in Fig. 8.7 and by the profile of the intensity from the disc (Fig. 8.8), the maximum intensity from the disc occurs at higher (optical) frequencies near the centre of the disc. Consequently, while the disc photon distribution occurs over a wide solid angle, near the disc crossing at a distance $\sim 50R_*$ the intensity from the disc is very low, and the bright central region only extends over a small solid angle. Near periastron the pulsar is closer to the star and the bright region of the disc provides a larger solid angle for IC scattering. This results in a much larger disc contribution at periastron as opposed to at the disc crossing epoch.

The scattering after the disc crossing epoch rapidly increases due to more favourable scattering

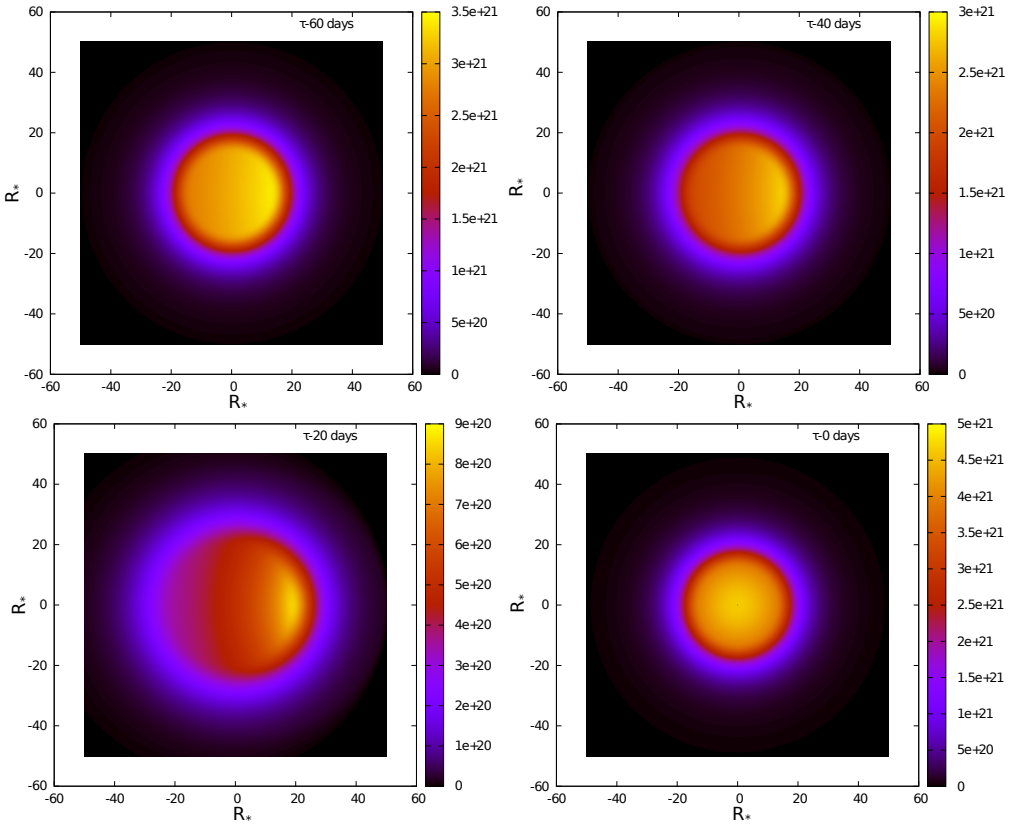

Figure 8.7: Photon number density from the disc (at $\nu = 10^{12}$ Hz) for $\tau - 60$ to $\tau - 0$ days from periastron for a disc orientated 90° to the disc plane, with the disc face-on at periastron. The photon number density, which is calculated by integrating over a line-of-sight through the disc, is plotted versus the point in the mid-plane of the disc where the line-of-sight will cross. This indicates how the photon density, as observed by the pulsar, varies during the orbit. The density was calculated assuming the pulsar approaches the disc from the right of the image.

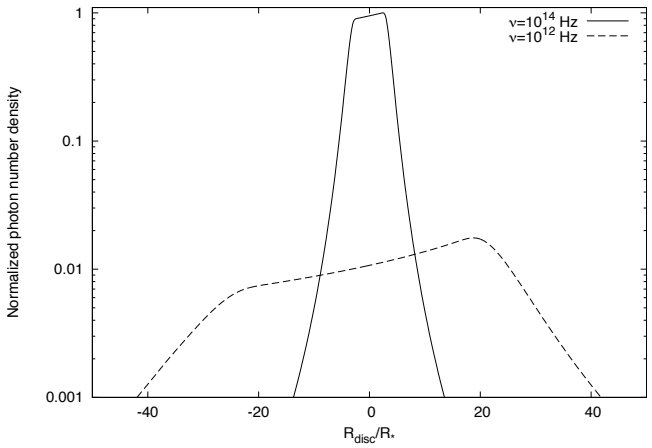

Figure 8.8: Profile of the photon number density (at $\nu = 10^{12}$ and $\nu = 10^{14}$ Hz) along a horizontal cross-section of the circumstellar disc in Fig. 8.7, at $\tau - 20$ days. The highest intensity from the disc occurs at higher (optical) frequencies near the centre of the disc/star. Note that the y-axis is scaled logarithmically and that the photon number density has been scaled to the maximum value in the figure.

angles. Consider position A and B shown in Fig. 8.9. At position A, all scattering can occur in predominantly head-head collisions while at position B predominantly head-tail collisions occur. On the other hand, the AIC scattering of the stellar photons follows a smooth transition which results in a smooth light curve and not the sharp increase and decrease seen for the disc contribution.

The combined effects of the photon density and the IC scattering angle are responsible for the predicted AIC light curves. Additional effects such as the heating of the circumstellar disc due to the pulsar crossing or the break-up of the disc as predicted by smooth particle hydrodynamic (SPH) models (e.g. Okazaki et al., 2011) have not been considered.

It should also be noted that the intensity of the circumstellar disc may be underestimated. The observed Doppler shifting of Hβ emission lines suggests that they occur at $\sim 8R_*$ (Johnston et al., 1994), beyond the distance where the COG model predicts the continuum radiation should occur. Intense regions of emission further out in the circumstellar disc, near to the disc crossing region, may increase the scattering rate. However, more complicated modelling of a Keplerian circumstellar disc, also predicts that the majority of the flux should lie close to the star (see Fig. 3.12, p. 40). It, therefore, seems unlikely that it will increase the flux to the levels required to explain the observed *Fermi* flare.

It may also be possible that shock-heating of the circumstellar disc could locally increase the disc intensity, providing additional photons for IC scattering, and significantly influence the gamma-ray light curve. Khangulyan et al. (2011a) have suggested that the observed *Fermi* flare is due to the shock-heating of the disc and the IC scattering of the pre-shocked pulsar wind with a Lorentz factor of $\gamma \sim 10^4$. There are, however, a few problems with the model presented by these authors. Firstly, the authors assumed that the shock-heating of the circumstellar disc

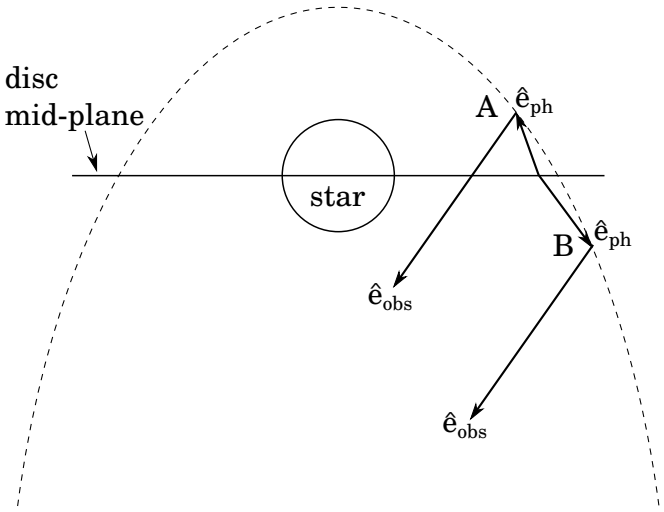

Figure 8.9: Illustration of the scattering angles near the disc crossing. The dashed line indicates the orbit of the pulsar.

would be sufficient to provide additional photons but do not present evidence that such a process would be effective enough to heat the disc considerably. Secondly, the authors do not explicitly state in the paper how the photon spectrum is calculated and have presumably used a blackbody approximation for the assumed disc temperatures. Thirdly, observations of the post-periastron disc appear to show that the IR flux from the disc has remained fairly stable (sections 8.3). And lastly, the model proposed a large opening angle for the circumstellar disc and requires the pulsar to leave the disc at $\sim \tau + 30$ days near the observed *Fermi* flare. This contradicts the radio observations which begin to detect the pulsed radio emission $\tau + 15$ days after periastron (Abdo et al., 2011).

8.2.3 Angle to the disc normal

The anisotropic IC scattering presented in the previous chapter considered scattering of photons from a disc with a small opening angle and it was assumed the angle to the normal of the disc could be approximated by the polar angle (i.e. $\vartheta = \theta$ in section 7.4.4). This is equivalent to assuming a flat disc. Fig. 8.10 compares the calculated values for the 90° and 45° disc using the flat disc approximation and the correctly calculated angle for a disc with a 1° half-opening angle. The figure shows that for the small opening angle considered the flat disc approximation holds. As such it is not necessary to consider a more complicated geometry for the disc.

Since recent observations of Be stars suggest that the circumstellar discs are very thin (e.g. Carciofi, 2011; Quirrenbach et al., 1997; Wood et al., 1997) a thin disc fit would appear to be more consistent with new Be circumstellar disc theory. Therefore, for the N11 parameters, only a thin disc was considered.

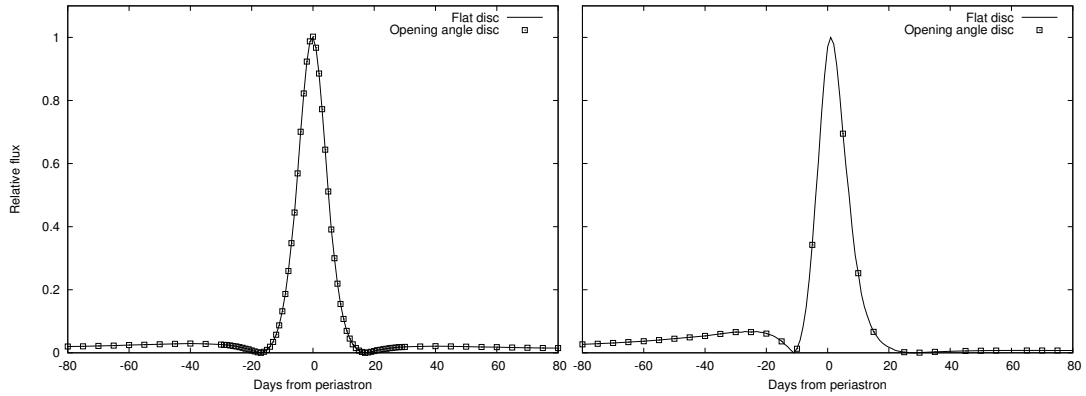

Figure 8.10: Comparison between the AIC light curves (at *Fermi* energies) calculated using the flat disc assumption (solid line) and calculating the angle to the disc normal for a 1° half-opening angle (open squares) for the 90° disc (left) and the 45° disc (right).

8.3 State of the disc post-periastron

SPH simulations of PSR B1259-63/LS 2883 around periastron have suggested that the disc would be disrupted by the passage of the pulsar during the periastron passage. This could result in changes in the observed optical and IR emission from the disc. However, observations near periastron on the 5$^{\text{th}}$ of January 2011 with VISIR/VLT found a flux that was of the same order as earlier observations with *Midcourse Space Experiment* (MSX) (Table 6.5 & Fig. 6.12).

Similarly, spectroscopic observations undertaken by A. Odendaal (Fig. 8.11) of LS 2883 with the SAAO 1.9 m telescope, utilizing the grating spectrograph (1200 lines mm^{-1} grating and $\sim$ 1 Å resolution), shows a very prominent Hα emission line and no indication of stellar Hα absorption, indicating that the circumstellar disc completely dominates the stellar absorption at the same frequency. These observations, which took place approximately four months after periastron, indicate that the Be star is still surrounded by a substantial circumstellar disc. The observed equivalent width for the Hα line is EW ≈ -50 Å, similar to the measurement reported by N11 (EW $= -54 \pm 2$ Å). This may be an indication that the disc remains prominent despite the pulsar passage or, alternatively, may indicate a very rapid recovery which would reflect a high disc viscosity.

8.4 Absorption effects

As was discussed in section 5.6 (p. 96) Dubus (2006b) investigated the effect of photon-photon absorption in LS 5039, while recently Khangulyan et al. (2011b) have considered absorption in PSR B1259-63/LS 2883 due to the star alone (and not the circumstellar disc). The question can be asked whether the IR excess from the circumstellar disc will significantly influence photon-photon absorption? If the circumstellar disc leads to a substantial absorption of the GeV energy gamma-rays, the *Fermi* flare might be explainable in terms of the pulsar leaving a region of high

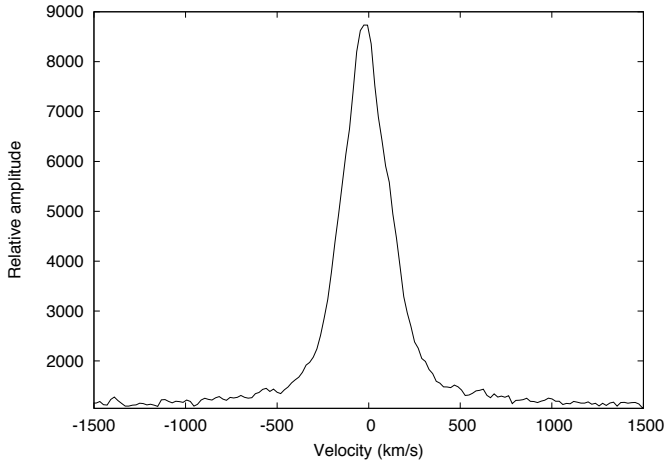

Figure 8.11: Hα emission line of PSR B1259-63/LS 2883 taken during April 2011 with the SAAO 1.9m telescope (Odendaal, 2011).

photon absorption which obscured the gamma-ray emission. Based on the results in this study we argue below that the disc will not significantly influence photon-photon absorption.

The IR excess from the circumstellar disc influences the IC gamma-ray production for two reasons: firstly the large size of the circumstellar disc increases the solid angle over which target photons arrive and secondly, the IC scattering cross-section increases with decreasing photon energy (section 5.2, p. 79). Therefore, IC scattering can readily occur with photons from the circumstellar disc. This is not true for photon-photon absorption which is limited to cases where the photons possess sufficient energy for electron-positron pair production. In other words the condition (equation 5.39)

$$\epsilon_\gamma \epsilon_* \geq \frac{2m_e^2c^4}{1-\hat{\mathbf{e}}_\gamma \cdot \hat{\mathbf{e}}_*},$$

must be satisfied, where ϵ_γ is the gamma-ray photon energy and ϵ_* is the energy of a photon from the star or disc. If the photons emitted from the circumstellar disc do not have sufficient energy, pair production cannot occur and the circumstellar disc will not influence photon absorption.

The minimum energy required for electron-positron pair production can be approximated by considering the average scattering angle between the photons, given by

$$\begin{aligned} \langle 1-\hat{\mathbf{e}}_\gamma \cdot \hat{\mathbf{e}}_* \rangle &= 1-\langle \cos\vartheta \rangle \\ &= 1. \end{aligned} \tag{8.1}$$

The minimum photon energy $\epsilon_{*,\mathrm{min}}$ required for photon-photon absorption with a gamma-ray of energy ϵ_γ is then

$$\epsilon_{*,\mathrm{min}} = \frac{2m_e^2c^4}{\epsilon_\gamma}.$$

For a TeV energy photon, the minimum required frequency for the stellar photon is determined by

$$\nu_{*,\min} = 1.26 \times 10^{14} \left(\frac{\epsilon_\gamma}{1 \text{ TeV}}\right)^{-1} \text{ Hz}.$$

The COG fit shown in Fig. 6.12 (p. 126) shows that at $\nu \sim 10^{14}$ Hz the flux from the circumstellar disc is still higher than the stellar flux. However, most of the flux emitted from the circumstellar disc originates close to the surface of the star (Fig. 8.8). Therefore, as with the IC scattering, the influence of the IR excess on photon-photon absorption should peak around periastron.

While the TeV gamma-rays will be slightly affected by photons from the disc, the GeV energy gamma-rays detected by *Fermi* should not be affected. The $\epsilon_\gamma \sim 10^9$ eV gamma-rays reported by *Fermi* (section 2.7, p. 20) would require X-ray photons with an minimum frequency of $\nu \sim 10^{17}$ Hz for absorption, which is much greater than the frequency contribution for the disc (or the star). The photon energy of the disc is too low to influence the GeV energy gamma-rays.

While photon-photon absorption due to stellar photons should be important for TeV gamma-rays, the effect should not be significant for GeV photons. Photon-photon absorption of GeV gamma-rays will require interaction with X-ray photons. If the X-ray emission occurs outside the GeV gamma-ray production site, photon-photon absorption may be an important mechanism to explain the modulations of the detected *Fermi* emission. An extended X-ray emission region has been detected around PSR B1259-63/LS 2883 (Pavlov et al., 2011) and this might be an indication that X-ray/GeV gamma-ray photon-photon absorption is important in the system. TeV energy gamma-rays would not be affected by X-ray energy photons since the photon-photon cross-section goes to zero, i.e. $\sigma_{\gamma,\gamma} \to 0$, as can be shown by equation (5.40).

8.5 Consequences of the model

Both the isotropic approximation and the more detailed anisotropic approximation have shown that by considering only the IR excess from the circumstellar disc and by not considering any of the other factors (such as, changes in the particle density, changes of size with orbital motion of the PWN, and radiative cooling effects), the total gamma-ray flux at GeV energies increases by a factor ~ 2. It was thought, the extended size of the disc may completely dominate at the disc crossing epoch. However, as has been shown by the modified COG method, the IR intensity at the disc crossing is faint, and most of the emission occurs close to periastron.

Fig. 8.12 shows the calculated gamma-ray energy spectrum at periastron (for the adiabatically cooled electron spectrum and a 90° disc) plotted, for comparison, together with the 2004 H.E.S.S. and 2010 *Fermi* observations. The figure shows the pre–periastron and the post–periastron (flare) spectra detected *Fermi* around the 2010 periastron passage (Abdo et al., 2011), and the combined H.E.S.S. spectrum, including all data around the 2004 periastron passage (fig. 3 in Aharonian

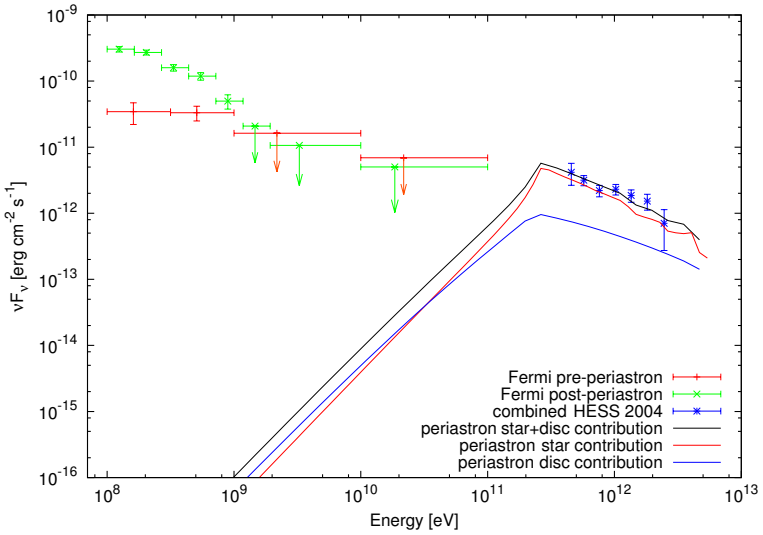

Figure 8.12: Comparison between of the predicted spectrum at periastron (for the adiabatically cooled electron spectrum and a 90° disc) to the pre– and post–periastron *Fermi* (2010) and combined 2004 H.E.S.S. observations. The vertical arrows indicate upper limits on the *Fermi* detections. The model prediction has been linearly scaled to find the best fit to the observational data. See text for details.

et al., 2005). The curve predicted by the model was calculated from

$$\begin{aligned} \nu F_\nu &= C\left(\frac{\epsilon_1}{h}\right)\left(h\epsilon_1 \frac{dN_{\rm tot}}{dt\, d\epsilon_1}\right) \\ &= C\left(\epsilon_1^2 \frac{dN_{\rm tot}}{dt\, d\epsilon_1}\right), \end{aligned}$$

where C is a scaling constant. The scattering rate is shown in Fig. 7.19 (p. 167). The constant C is introduced to account for the distance to the source (2.3 kpc), the normalization of the electron spectrum ($K_{\rm e} = 1$ was assumed for all electron distributions), the size of the emitting region, the fraction of the total number of electrons in the PWN that are directed towards the observer, and pair-cascade effects. No assumptions have been made about these effects in this study. They have been considered by other authors (e.g. Dubus, 2006a,b; Kirk et al., 1999; Tavani and Arons, 1997). This study has only considered the relative change in the scattering rate due to the inclusion of the IR excess. To illustrate the difference between the additional flux predicted in this study, and the unexpected *Fermi* detection around periastron, which is not explained by any model, I have made the simplifying assumption that the flux can be linearly scaled by the constant C to the observed data. The modelled spectrum produces a good fit to the H.E.S.S. data. This is expected since, firstly, a best fit value is determined for C, and secondly, the electron distribution used,

$$n_{\rm e} \propto \gamma^{-2.4} \quad \text{for } 5.4 \times 10^5 \leq \gamma \leq 5.4 \times 10^7,$$

which was taken from Kirk et al. (1999), was in good agreement with the 2004 H.E.S.S. observations (Aharonian et al., 2005). No additional assumptions are therefore necessary regarding the magnitude of the electron number density or the size of the emission region surrounding the pulsar.

As illustrated in Fig. 8.12, the curve showing the predicted change in the gamma-ray flux lies a few orders of magnitudes below that showing the *Fermi* detection limit and is therefore undetectable. This prediction is in agreement with the prediction for the system before the *Fermi* detection after the 2010 periastron passage. Modelling by, e.g. Chernyakova et al. (2009) (see Fig 2.13, p. 20), also considered the predicted emission at GeV energies, but did not predict gamma-ray emission at the energies detected by *Fermi* where the luminosity was $\approx 100\%$ of the spin-down power of the pulsar. Chernyakova et al. (2009) considered a much broader electron distribution than was considered in the anisotropic modelling of this study, which provides a higher flux at GeV energies. The isotropic model (van Soelen and Meintjes, 2011) showed that, for a broad electron distribution, the IC scattering is dominated by stellar photons, which scatter predominantly in the Thomson limit, and that the spectrum is less affected by the photons originating from the disc. For this reason a broad electron distribution was not considered in the anisotropic model. The prediction of the model of Chernyakova et al. (2009) also lies orders of magnitude below the *Fermi* detection. Applying the factor 2 increase in the GeV flux shown by Fig 2.13 (p. 20) would not increase the spectrum to the energy level required to explain the *Fermi* flare. This flare is a special event. To model an emission of this kind requires a novel mechanism and processes that appear not to have been considered to date. The construction of a model is further complicated by the fact that observations at other wavelengths showed no unusual or flaring behaviour.

Fig. 8.13 shows two possibilities discussed by Abdo et al. (2011) to explain the *Fermi* flare. The first (Fig. 8.13a) assumes an increase in the bremsstrahlung emission by requiring that the local density in the star wind/environment increases by an order of magnitude. The second (Fig. 8.13b) requires anisotropic synchrotron emission from $E_{\rm e} = 10^{15}$ eV electrons ($\gamma \approx 2 \times 10^8$), which is modelled assuming an injection electron spectrum with a bulk Lorentz factor of $\gamma_p \sim 10^9$ (Chernyakova et al., 2011).

Additional effects such as the Doppler boosting of the gamma-ray emission may also increase the emission (e.g. Dubus et al., 2010). Khangulyan et al. (2011a) have suggested that photons from the shock-heated disc IC scatter off electrons with $\gamma \sim 10^4$. The shock-heating of the disc may have a very significant effect on the IC spectrum. However, the extent to which the heating will affect the circumstellar disc is unclear, and it is unknown whether this will provide a sufficient number of photons.

PWNe are known to produce X-ray jet-like structures as is seen in systems such as the Crab Nebula (Fig. 4.6, p. 63). If material is ejected in a jet-like structure in PSR B1259-63 this could account for the sudden rise and the subsequent slower decay of the gamma-ray emission seen by *Fermi*. Such a flare might accelerate electrons to the required energy ($\gamma_p \sim 10^9$), producing

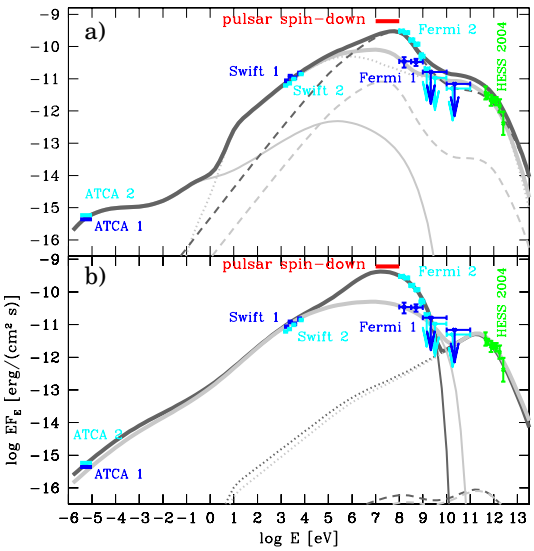

Figure 8.13: Two scenarios presented in Abdo et al. (2011) to attempt to explain the observed *Fermi* emission near periastron. Both figures show the synchrotron (thin solid line), the inverse Compton (dotted line) and bremsstrahlung (dashed line) that could occur from the system before periastron (light grey) and during the *Fermi* flare event (dark grey). **Top:** The flare explained as an increase in the bremsstrahlung emission due to an order of magnitude increase in the density of the circumstellar material. **Bottom:** The flare explained due to an increase in the anisotropic synchrotron emission from $E_e = 10^{15}$ eV electrons ($\gamma \approx 2 \times 10^8$).

emission by synchrotron radiation without changing the emission at other wavelengths.

The 2010 periastron was the first observed with *Fermi*. It is thus not known whether this flare was an isolated event or whether it will be a regular feature of future periastron passages. Before the *Fermi* observations, it was not known of what strength the GeV flux would be, nor whether the system could be detected. I expect that the effects predicted by this study will be observable, in particular the factor ~ 2 increase in the flux. The predictions of my model fall short of the *Fermi* detection threshold, and might even be dwarfed by the observed flare.

The model presented in this study also predicts variability at Very High Energies. The predicted flux will be high enough for detection, but the predicted variability is smaller than the error in the measurement and therefore would not be detected currently at significant levels. However, Be stars are known to display variability at optical magnitudes. While the COG model predicts a change at optical frequencies for LS 2883 (Fig 6.12, p. 126) the increase in the flux may be greater than predicted here. As was shown for SXP11.5 (Fig. 3.14, p. 44), the I magnitude changes from approximately 14.5 mag to 15.8 mag, which corresponds to a change by a factor ~ 3 in the flux during periods of high disc activity. The corresponding predicted change shown for LS 2883 at the I filter frequency is a factor ~ 1.7. The change in the optical magnitude may therefore be larger than that which was predicted here using the sparse archive optical measurements.

8.6 Future work

A number of crucial questions must still be answered for PSR B1259-63/LS 2883 and other Be gamma-ray binary systems. In particular, the effect of the pulsar passage on the Be star's circumstellar disc must be considered. SPH modelling undertaken by Okazaki et al. (2011) has suggested that the circumstellar disc will be significantly disrupted while Khangulyan et al. (2011a) have suggested that shock heating will provide sufficient additional photons to produce the *Fermi* flare observed after the December 2010 periastron passage. Both questions have significant implications for other Be binary/gamma-ray binary systems. We may be able to resolve these issues by an observation campaign designed to determine the degree to which the circumstellar disc is heated and/or disrupted. This would require high resolution spectroscopy and photometry with good time resolution during the next periastron passage which will occur in 2014. Theoretical models of wind collisions will also indicate the variation of the circumstellar disc. In the case of PSR B1259-63 and LSI+61 303, we may need to consider also that the circumstellar disc may be precessing. Such an effect, particularly in closer binary systems could have a large influence on the position of the disc crossing and could affect the multi-wavelength modulation.

Chapter 9

Conclusion

The binary star system PSR B1259-63/LS 2883 has remained a fascinating source since the detection of the pulsar approximately two decades ago. The interaction between the Be star and the millisecond pulsar produces multi-wavelength emission from radio up to TeV gamma-rays, covering 19 decades in energy. With the exception of the thermal spectrum associated with the Be star, there is no other evidence for thermal emission, and the remaining part of the multi-wavelength spectrum is believed to be the result of the interaction between the pulsar and the stellar wind, creating a pulsar wind nebula within the binary system. Recently it has been shown that both the radio and X-ray emission are extended, with the radio emission originating from outside the binary system during periastron (Moldón et al., 2011a; Pavlov et al., 2011).

TeV gamma-ray emission from PSR B1259-63 was detected by H.E.S.S. during the 2004 periastron passage (Aharonian et al., 2005), and while hadronic collisions have been suggested, the production of gamma-rays through the inverse Compton scattering of optical and IR photons by highly relativistic leptons in the pulsar wind remains a likely production mechanism, particularly for TeV energies. The optical companion in the system is a Be type star, known to possess a circumstellar disc which produces an IR flux. This flux is observed as an IR excess which is higher than predicted by blackbody and stellar atmosphere models. Since the gamma-rays in the system are produced by the up-scattering of photons, the presence of an extended and additional photon source could potentially have a significant effect on the gamma-ray production in PSR B1259-63/LS 2883. The question I have addressed in this thesis is, to what degree does the circumstellar disc influence gamma-ray production. I have focussed, in particular, on the IR emission.

To model the gamma-ray emission, it is necessary to model the anisotropic scattering, the IR excess, and how this excess changes during the orbital cycle. In this study, I have used a modified version of the curve of growth (COG) method, first proposed for Be stars by Waters (1986), to predict the flux and the variation in the flux during the periastron passage. I used optical and IR data obtained from literature and VLT observations to constrain the multi-wavelength emission

from the Be star and its circumstellar disc. To estimate the IR excess by means of the COG method, I used first the original stellar parameters proposed by Johnston et al. (1994), and then also the more recent parameters suggested by Negueruela et al. (2011) for the spectral type and colour excess. I modified the original COG method to allow the calculation of the optical depth through the circumstellar disc as observed from the pulsar at any point in the orbit and for any given orientation of the disc. From this, I determined the photon density for each time considered, and then applied it to the problem of Anisotropic Inverse Compton (AIC) scattering.

In this study, I considered both isotropic and anisotropic scattering for PSR B1259-63. The isotropic scattering was calculated using the IC formulae derived in Blumenthal and Gould (1970), while the anisotropic scattering was determined from the kernels derived by Fargion et al. (1997) and Dubus et al. (2008). In both cases the full Klein-Nishina scattering cross-section was considered. The isotropic modelling, presented in van Soelen and Meintjes (2011), did not take into account the change in the Be star/disc photon spectrum nor the change in the photon distribution during the orbit, but only considered the target photon spectrum determined utilizing the COG method and the Johnston et al. (1994) parameters. This method also did not consider the effects of the variation in the solid angle of the disc nor the direction of IC scattering. The anisotropic scattering (partially presented in van Soelen and Meintjes, 2012, see Appendix E) considered these additional effects, and determined the variation in the gamma-ray spectrum around periastron for different disc orientations.

In this study the leptons in the pulsar wind are assumed to be mono-energetic before the stand-off shock and are accelerated to a power-law energy distribution in the post-shock region. Both a pre– and post–shock distribution have been considered for the isotropic and anisotropic scattering. For PSR B1259-63, it can be shown that adiabatic cooling dominates near the stand-off shock, and for this reason only adiabatic cooling was considered for the AIC modelling. Radiative cooling was, however, considered for the isotropic modelling presented in van Soelen and Meintjes (2011). Additional effects on the electron distribution due to the changing density around the Be star were not considered.

The IC modelling showed that the inclusion of the IR excess associated with the circumstellar disc increased the GeV gamma-rays by a factor $\gtrsim 2$. This relative increase in the flux is partly dependent on the choice of the electron distribution. For a wide distribution (e.g. $10^4 \leq \gamma \leq 10^7$), as was shown for the isotropic modelling (fig. 3 in van Soelen and Meintjes, 2011, p. 141 in this thesis), or an electron distribution centred around $\gamma \sim 10^4$ (Fig. 8.6, p. 180), the IC scattering is dominated by the scattering of stellar photons in the Thomson limit. However, this study has shown that for the electron distribution proposed by Kirk et al. (1999), which has been shown to provide a reasonable fit to the 2004 H.E.S.S. observations, the IR excess from the circumstellar disc increases the gamma-ray flux by a factor ≥ 2 at GeV energies.

Figs. 7.17, 7.21, 7.22 & 7.23 illustrate the predicted light curves of the integrated flux for different electron distributions, disc orientations and COG fits. The integrated flux is determined for the reported *Fermi* and H.E.S.S. energy ranges. The light curves show that the circumstellar

disc is most influential close to periastron and, generally, after the disc crossing. This is a result of the disc being brightest near the stellar surface and with the associated favourable scattering angles after the disc crossing. While it was thought the flux may be highest near the disc crossing epoch ($\sim \tau \pm 20$ days), the low intensity of the disc at ~ 50 stellar radii from the star's surface does not provide a sufficient number of photons to increase significantly the gamma-ray flux in this region. This study has only considered a steady state disc and has not considered what effects the pulsar passage may have introduced on the circumstellar disc. Shock heating of the disc or clumping of material may result in regions of higher intensity which could result in more localised flux increases.

The additional effects such as changes in the electron cooling have not been considered, as these have been addressed by other authors. This study has focussed on the effect of the IR excess from the circumstellar disc in order to determine its influence on the production of GeV energy gamma-rays. The study finds that the gamma-ray flux could be increased by a factor greater than two at GeV energies, which is a significant increase. However, the predicted gamma-ray flux lies far below that detected by *Fermi* at the previous periastron passage. Neither this model, nor any other, has been able to give a definitive explanation of the flare that was observed by *Fermi* approximately one month after periastron.

The presence of a circumstellar disc has been shown to be significant for the modelling of PSR B1259-63/LS 2883 and since four of the six known gamma-ray binaries have a Be star optical companion, it is extremely important to incorporate the circumstellar disc into gamma-ray binary models. The effect of the circumstellar disc still presents many challenges which will need to be considered in any model for a Be binary system.

Acknowledgements

There are a number of people who must be thanked, because if it had not been for them this thesis would never have been possible.

- The South African SKA bursary program and the National Research Council (NRC) for funding my project.
- The numerical integrations were performed on the University of the Free State's High Performance Computing division. In particular I must thank Albert van Eck.
- My supervisor, Prof. Pieter Meintjes.
- Prof. Okkie de Jager, who originally suggested this study.
- My colleagues at the Department of Physics, in particular Pat van Heerden who assisted me at the Boyden observatory and Daniël Wium and Alida Odendaal, who went to Sutherland with me to help with observations.
- I am also very grateful for the help, collaboration and discussions with
  - Malcolm Coe,
  - Phil Charles,
  - Lee Townsend,
  - Liz Bartlette, and
  - Andri Rajoelimanana.
- My parents.
- Liza, for checking some of the grammar at the end.
- And, as always, Angie.

List of Acronyms

2MASS	Two Micron All Sky Survey
AGILE	Astrorivelatore Gamma a Immagini LEggero
AIC	Anisotropic Inverse Compton (scattering)
ASCA	Advanced Satellite for Cosmology and Astrophysics
ASM	All Sky Monitor
ATCA	Australia Telescope Compact Array
CCD	Charge-coupled device
COG	Curve of growth
ESO	European Southern Observatory
HE	High Energy (0.1 - 100 GeV)
H.E.S.S.	High Energy Stereoscopic System
IC	Inverse Compton (scattering)
IPAC	Infrared Processing and Analysis Center
IR	Infrared
IRSF	InfraRed Survey Facility
LAT	Large Area Telescope
LBA	[Australian] Long Baseline Array
LTE	Local Thermodynamic Equilibrium
mas	milli-arcseconds
MHD	Magnetohydrodynamics
MJD	Modified Julian Date
MSX	Midcourse Space Experiment
NASA	National Aeronautics and Space Administration
NS	Neutron Star
PWN	Pulsar Wind Nebula
ROSAT	**Rö**ntgen**sa**tellit
SED	Spectral Energy Distributions
SPH	Smoothed Particle Hydrodynamics
SNR	Supernova Remnant
UVES	Ultraviolet and Visual Echelle Spectrograph
VHE	Very High Energies (> 100 GeV)
VISIR	VLT imager and spectrometer for the mid infrared
VLA	Very Large Array
VLT	Very Large Telescope
XRB	X-ray Binary

List of Filters

The central wavelength and band-width of the filters discussed in this thesis are listed below.

Filter	central wavelength μm	band width μm
U	0.365	0.066
B	0.44	0.094
V	0.55	0.088
R	0.658	0.138
I	0.806	0.149
J	1.235	0.162
H	1.662	0.251
Ks	2.159	0.262
A	8.28	3.36
C	12.13	1.72
PAH1	8.59	0.84
ArIII	8.99	0.28
SIV	10.49	0.32
SIV_2	10.77	0.38
PAH2	11.25	1.18
SiC	11.85	4.68
PAH2_2	11.88	0.74
NeII	12.81	0.42

Bibliography

A. A. Abdo, M. Ackermann, M. Ajello, and *et. al*. Fermi LAT Observations of LS I +61°303: First Detection of an Orbital Modulation in GeV Gamma Rays. *ApJ Letters*, 701:L123–L128, 2009.

A. A. Abdo, M. Ackermann, M. Ajello, and *et. al*. Discovery of High-energy Gamma-ray Emission from the Binary System PSR B1259-63/LS 2883 around Periastron with Fermi. *ApJ Letters*, 736:L11+, 2011.

F. Aharonian, A. G. Akhperjanian, K.-M. Aye, and *et al.* Discovery of the binary pulsar PSR B1259-63 in very-high-energy gamma rays around periastron with HESS. *A&A*, 442:1–10, 2005.

F. Aharonian, A. G. Akhperjanian, A. R. Bazer-Bachi, M. Beilicke, and *et al.* 3.9 day orbital modulation in the TeV γ-ray flux and spectrum from the X-ray binary LS 5039. *A&A*, 460: 743–749, 2006.

F. Aharonian, A. G. Akhperjanian, B. Bazer-Bachi, Behera, and *et al.* Discovery of a point-like very-high-energy γ-ray source in Monoceros. *A&A*, 469:L1–L4, 2007.

F. Aharonian, A. G. Akhperjanian, G. Anton, and *et al.* Very high energy γ-ray observations of the binary PSR B1259-63/SS2883 around the 2007 Periastron. *A&A*, 507:389–396, 2009.

F. A. Aharonian and S. V. Bogovalov. Exploring physics of rotation powered pulsars with sub-10 GeV imaging atmospheric Cherenkov telescopes. *New Astronomy*, 8:85–103, 2003.

J. Albert, E. Aliu, H. Anderhub, and *et al.* Variable Very-High-Energy Gamma-Ray Emission from the Microquasar LS I +61 303. *Science*, 312:1771–1773, 2006.

J. Albert, E. Aliu, H. Anderhub, and *et. al.* Multiwavelength (Radio, X-Ray, and γ-Ray) Observations of the γ-Ray Binary LS I +61 303. *ApJ*, 684:1351–1358, 2008.

J. Albert, E. Aliu, H. Anderhub, and *et. al.* Periodic Very High Energy γ-Ray Emission from LS I +61°303 Observed with the MAGIC Telescope. *ApJ*, 693:303–310, 2009.

C. W. Allen. *Astrophysical quantities*. London: University of London, Athlone Press, 3rd ed., 1973.

C. Aragona, M. V. McSwain, E. D. Grundstrom, A. N. Marsh, R. M. Roettenbacher, K. M. Hessler, T. S. Boyajian, and P. S. Ray. The Orbits of the γ-Ray Binaries LS I +61 303 and LS 5039. *ApJ*, 698:514–518, 2009.

W. B. Atwood, A. A. Abdo, M. Ackermann, and *et al.* The Large Area Telescope on the Fermi Gamma-Ray Space Telescope Mission. *ApJ*, 697:1071–1102, 2009.

D. Baade, T. Rivinius, S. Štefl, and C. Martayan. Active OB Stars - an introduction. In C. Neiner, G. Wade, G. Meynet, & G. Peters, editor, *IAU Symposium*, volume 272 of *IAU Symposium*, pages 1–13, 2011.

L. Ball and J. G. Kirk. Probing pulsar winds using inverse compton scattering. *Astroparticle Physics*, 12:335–349, 2000.

S. D. Barthelmy, W. Baumgartner, J. Cummings, and *et al.* Swift-BAT/-XRT refined analysis on trigger 324362 (LS I +61 303). *GRB Coordinates Network*, 8215:1, 2008.

W. Becker and J. Truemper. The X-ray luminosity of rotation-powered neutron stars. *A&A*, 326:682–691, 1997.

D. Bhattacharya and E. P. J. van den Heuvel. Formation and evolution of binary and millisecond radio pulsars. *Physics Reports*, 203:1–124, 1991.

G. F. Bignami, P. A. Caraveo, R. C. Lamb, T. H. Markert, and J. A. Paul. Einstein X-ray identification of the variable radio star LSI +61°303. *ApJ Letters*, 247:L85–L88, 1981.

J. E. Bjorkman and J. P. Cassinelli. Equatorial disk formation around rotating stars due to Ram pressure confinement by the stellar wind. *ApJ*, 409:429–449, 1993.

G. R. Blumenthal and R. J. Gould. Bremsstrahlung, Synchrotron Radiation, and Compton Scattering of High-Energy Electrons Traversing Dilute Gases. *Reviews of Modern Physics*, 42: 237–271, 1970.

S. V. Bogovalov and F. A. Aharonian. Very-high-energy gamma radiation associated with the unshocked wind of the Crab pulsar. *MNRAS*, 313:504–514, 2000.

S. V. Bogovalov and D. V. Khangoulyan. The Crab Nebula: Interpretation of Chandra Observations. *Astronomy Letters*, 28:373–385, 2002a.

S. V. Bogovalov and D. V. Khangoulyan. On the origin of the torus and jet-like structures in the centre of the Crab Nebula. *MNRAS*, 336:L35–L55, 2002b.

S. V. Bogovalov, V. M. Chechetkin, A. V. Koldoba, and G. V. Ustyugova. Interaction of pulsar winds with interstellar medium: numerical simulation. *MNRAS*, 358:705–715, 2005.

S. D. Bongiorno, A. D. Falcone, M. Stroh, J. Holder, J. L. Skilton, J. A. Hinton, N. Gehrels, and J. Grube. A New TeV Binary: The Discovery of an Orbital Period in HESS J0632+057. *ApJ Letters*, 737:L11, 2011.

V. Bosch-Ramon, J. M. Paredes, M. Ribó, J. M. Miller, P. Reig, and J. Martí. Orbital X-Ray Variability of the Microquasar LS 5039. *ApJ*, 628:388–394, 2005.

P. J. Brussaard and H. C. van de Hulst. Approximation Formulas for Nonrelativistic Bremsstrahlung and Average Gaunt Factors for a Maxwellian Electron Gas. *Reviews of Modern Physics*, 34:507–520, 1962.

A. C. Carciofi. The circumstellar discs of Be stars. In C. Neiner, G. Wade, G. Meynet, & G. Peters, editor, *IAU Symposium*, volume 272 of *IAU Symposium*, pages 325–336, 2011.

A. C. Carciofi and J. E. Bjorkman. Non-LTE Monte Carlo radiative transfer. II . Nonisothermal solutions for viscous Keplerian disks. *ApJ*, 684:1374–1383, 2008.

A. C. Carciofi, A. T. Okazaki, J.-B. Le Bouquin, S. Štefl, T. Rivinius, D. Baade, , and C. A. Hummel. Cyclic variability of the circumstellar disk of the Be star ζ Tauri. II. Testing the 2D global disk oscillation model. *A&A*, 504:915–927, 2009.

J. Casares, M. Ribó, I. Ribas, J. M. Paredes, J. Martí, and A. Herrero. A possible black hole in the gamma-ray microquasar LS 5039. *MNRAS*, 364:899–908, 2005.

J. Casares, M. Ribo, I. Ribas, J. M. Paredes, F. Vilardell, and I. Negueruela. On the binary nature of the gamma-ray sources AGL J2241+4454 (=MWC 656) and HESS J0632+057 (=MWC 148). *ArXiv e-prints*, 2012.

J. P. Cassinelli, J. C. Brown, M. Maheswaran, N. A. Miller, and D. C. Telfer. A Magnetically Torqued Disk Model for Be Stars. *ApJ*, 578:951–966, 2002.

B. Cerutti. *High-Energy gamma-ray emission in compact binaries*. PhD thesis, Université de Grenoble, 2010.

S. Chandrasekhar. The Maximum Mass of Ideal White Dwarfs. *ApJ*, 74:81–82, 1931.

S. Chandrasekhar. *An introduction to the study of stellar structure*. Chicago, Ill., The University of Chicago press, 1939.

M. Chernyakova, A. Neronov, A Lutovinov, J. Rodriguez, and S Johnston. XMMNewton observations of PSR B125963 near the 2004 periastron passage. *MNRAS*, 367:1201–1208, 2006.

M. Chernyakova, A. Neronov, F. Aharonian, Y. Uchiyama, and T. Takahashi. X-ray observations of PSR B125963 near the 2007 periastron passage. *MNRAS*, 397:2123–2132, 2009.

M. Chernyakova, A. Neronov, A. Abdo, D. Parent, S. Johnston, and Y. Uchiyama. Multi-wavelength observations of psr b1259-63 during its 2010 periastron passage. private communications, 2011.

J. S. Clark, P. Reig, S. P. Goodwin, V. M. Larionov, P. Blay, M. J. Coe, J. Fabregat, I. Negueruela, I. Papadakis, and I. A. Steele. On the radio emitting high mass X-ray binary LS 5039. *A&A*, 376:476–483, 2001.

J. S. Clark, A. E. Tarasov, A. T. Okazaki, P. Roche, and V. M. Lyuty. Phase changes of the Be/X-ray binary X Persei. *A&A*, 380:615–629, 2001.

J. S. Clark, A. E. Tarasov, and E. A. Panko. Long term disc variability in the Be star *o* Andromedae. *A&A*, 403:239–246, 2003.

M. J. Coe. Be stars in X-ray binary systems. In M. A. Smith, H. F. Henrichs, and J. Fabregat, editors, *IAU Colloq. 175: The Be Phenomenon in Early-Type Stars*, volume 214 of *Astronomical Society of the Pacific Conference Series*, pages 656–667, 2000.

G. W. Collins, II. The use of terms and definitions in the study of Be stars. In A. Slettebak & T. P. Snow, editor, *IAU Colloq. 92: Physics of Be Stars*, pages 3–19, 1987.

L. Cominsky, M. Roberts, and Johnston S. Detection of X-ray emission from the PSR 1259-63/SS 2883 Binary System. *ApJ*, 427:978–983, 1994.

T. W. Connors, S. Johnston, R. N. Manchester, and D. McConnell. The 2000 periastron passage of PSR B1259-63. *MNRAS*, 336:1201–1208, 2002.

P. S. Coppi and R. D. Blandford. Reaction rates and energy distributions for elementary processes in relativistic pair plasmas. *MNRAS*, 245:453–469, 1990.

R. H. D. Corbet. Be/neutron star binaries - A relationship between orbital period and neutron star spin period. *A&A*, 141:91–93, 1984.

R. H. D. Corbet, C. C. Cheung, M. Kerr, and *et al.* 1FGL J1018.6-5856: a New Gamma-ray Binary. *The Astronomer's Telegram*, 3221:1, 2011.

S. R. Cranmer. A Pulsational Mechanism for Producing Keplerian Disks Around Be Stars. *ApJ*, 701:396–413, 2009.

J. K. Daugherty and A. K. Harding. Electromagnetic cascades in pulsars. *ApJ*, 252:337–347, 1982.

E. de Ona Wilhelmi, R. Terrier, R. Chaves, and *et al.* Observations of the supernova remnant SNR G284.3-1.8 from X-rays to VHE gamma-rays with XMM-Newton, Fermi and H.E.S.S. In *38th COSPAR Scientific Assembly*, volume 38, page 2803, 2010.

M. de Pasquale, S. D. Barthelmy, W. H. Baumgartner, and *et al.* Swift trigger 324362 (LS I +61 303 ?). *GRB Coordinates Network*, 8209:1, 2008.

P. B. Demorest, T. Pennucci, S. M. Ransom, M. S. E. Roberts, and J. W. T. Hessels. A two-solar-mass neutron star measured using Shapiro delay. *Nature*, 467:1081–1083, 2010.

V. Dhawan, A. Mioduszewski, and M. Rupen. LS I +61 303 is a Be-Pulsar binary, not a Microquasar. In T. Belloni, editor, *VI Microquasar Workshop: Microquasars and Beyond*, page 52, 2006.

L. M. Dray. On the metallicity dependence of high-mass X-ray binaries. *MNRAS*, 370:2079–2090, August 2006.

J. S. Drilling. UBV photometry of OB+ stars in the southern Milky Way. *ApJS*, 76:1033–1041, 1991.

G. Dubus. Gamma-ray binaries: pulsars in disguise? *A&A*, 456:801–817, 2006a.

G. Dubus. Gamma-ray absorption in massive X-ray binaries. *A&A*, 451:9–18, 2006b.

G. Dubus and B. Giebels. Swift BAT detection of a SGR-like burst from LS I+ 61 303. *The Astronomer's Telegram*, 1715:1, 2008.

G. Dubus, B. Cerutti, and G. Henri. The modulation of the gamma-ray emission from the binary LS 5039. *A&A*, 477:691–700, 2008.

G. Dubus, B. Cerutti, and G. Henri. Relativistic Doppler-boosted emission in gamma-ray binaries. *A&A*, 516:A18, 2010.

P. A. Evans, J. P. Osborne, O. Godet, J. A. Kennea, A. Falcone, and S. Campana. Swift trigger 324362 (LS I +61 303 ?): XRT. *GRB Coordinates Network*, 8211:1, 2008.

D. Fargion, R V. Konoplich, and A Salis. Inverse compton scattering on laser beam and monochromatic isotropic radiation. *Z. Phys. C.*, 74:571–576, 1997.

J. Frank, A. King, and D. J. Raine. *Accretion Power in Astrophysics: Third Edition.* Cambridge University Press, 2002.

B. M. Gaensler and P. O. Slane. The Evolution and Structure of Pulsar Wind Nebulae. *ARA&A*, 44:17–47, 2006.

B. M. Gaensler, E. van der Swaluw, F. Camilo, V. M. Kaspi, F. K. Baganoff, F. Yusef-Zadeh, and R. N. Manchester. The Mouse that Soared: High-Resolution X-Ray Imaging of the Pulsar-powered Bow Shock G359.23-0.82. *ApJ*, 616:383–402, 2004.

J. A. Gaunt. Continuous Absorption. *Royal Society of London Philosophical Transactions Series A*, 229:163–204, 1930.

V. L. Ginzburg and S. I. Syrovatskii. Cosmic Magnetobremsstrahlung (synchrotron Radiation). *ARA&A*, 3:297–350, 1965.

T. Gold. Rotating Neutron Stars as the Origin of the Pulsating Radio Sources. *Nature*, 218: 731–732, 1968.

P. Goldoni and S. Mereghetti. X-ray observations of the peculiar Be star LSI +61 303. *A&A*, 299:751–754, 1995.

Peter Goldreich and William II Julian. Pulsar Electrodynamics. *ApJ*, 157:869–880, 1969.

R. J. Gould and G. P Schréder. Pair Production in Photon-Photon Collisions. *Physics Review*, 155:1404–1407, 1967.

P. C. Gregory. Bayesian Analysis of Radio Observations of the Be X-Ray Binary LS I +61°303. *ApJ*, 575:427–434, 2002.

P. C. Gregory and A. R. Taylor. New highly variable radio source, possible counterpart of gamma-ray source CG135+1. *Nature*, 272:704–706, 1978.

E. H. B. M. Gronenschild and R. Mewe. Calculated X-radiation from optically thin plasmas - III. Abundance effects on continuum emission. *A&AS*, 32:283–305, 1978.

D. Hadasch. LS I +61 303 and LS5039 behavior in the high energy regime during two years of Fermi monitoring. In *25th Texas Symposium on Relativistic Astrophysics*, 2010.

R. W. Hanuschik. On the structure of Be star disks. *A&A*, 308:170–179, 1996.

J. Hardop, K. Rohlfs, A. Slettebak, and J. Stock. *Luminous Stars in the Northern Milky Way*, volume I. Hamburg-Bergedorf, Hamburger Sternwarte-Warner and Swasey Obs., 1959.

W. Heitler. *Quantum theory of radiation, International Series of Monographs on Physics*. Oxford: Clarendon, 3rd edition, 1954.

A. Hewish, S. J. Bell, J. D. Pilkington, P. F. Scott, and R. A. Collins. Observation of a Rapidly Pulsating Radio Source. *Nature*, 217:709–713, 1968.

J. A. Hinton, J. L. Skilton, S. Funk, and *et al.* HESS J0632+057: A New Gamma-Ray Binary? *ApJ Letters*, 690:L101–L104, 2009.

M. Hirayama, L. R. Cominsky, V. M. Kaspi, F. Nagase, M. Tavani, N. Kawai, and J. E. Grove. X-Ray/Gamma-Ray Observations of the PSR B1259-63-SS 2883 System near Apastron. *ApJ*, 521:718–722, 1999.

L. Howells. *The design of an automated data-analysis system for robotic telescopes and its application to Be stars*. PhD thesis, Liverpool John Moores University, 2002.

J. A. Irwin. *Astrophysics: Decoding the Cosmos, Published by Wiley-VCH Verlag, Wenheim, Germany,*. Wiley-VCH Verlag, 2007.

B. S. Jeffreys. John Arthur Gaunt (1904-1944). *Notes and Records of the Royal Society of London*, 44:73 – 79, 1990.

H. L. Johnson. Infrared Emission from Circumstellar Shells. *ApJ Letters*, 150:L39–L43, 1967.

H. L. Johnson, R. I. Mitchell, B. Iriarte, and W. Z. Wisniewski. UBVRIJKL Photometry of the Bright Stars. *Communications of the Lunar and Planetary Laboratory*, 4:99–110, 1966.

S. Johnston, A. G. Lyne, R. N. Manchester, D. A. Kniffen, N. D'Amico, J. Lim, and M. Ashworth. A high-frequency survey of the southern Galactic plane for pulsars. *MNRAS*, 255:401–411, 1992a.

S. Johnston, A. G. Lyne, R. N. Manchester, A. G. Lyne, M. Bailes, V. M. Kaspi, Q. Guojun, and N. D'Amico. PSR B1259-63: A binary radio pulsar with a Be star companion. *ApJ*, 387: L37–L41, 1992b.

S. Johnston, R. N. Manchester, A. G. Lyne, L. Nicastro, and J. Spyromilio. Radio and Optical Observations of the PSR:B1259-63 / SS:2883 Be-Star Binary System. *MNRAS*, 268:430–436, 1994.

S. Johnston, R. N. Manchester, A. G. Lyne, N. D'Amico, M. Bailes, B. M. Gaensler, and L. Nicastro. Radio observations of PSR B1259-63 around periastron. *MNRAS*, 279:1026–1036, 1996.

S. Johnston, R. N. Manchester, D. McConnell, and D. Campbell-Wilson. Transient radio emission from the PSR B1259-63 system near periastron. *MNRAS*, 302:277–287, 1999.

S. Johnston, N. Wex, L. Nicastro, R. N. Manchester, and A. G. Lyne. The 1997 periastron passage of the binary pulsar PSR B1259-63. *MNRAS*, 326:643–648, 2001.

S. Johnston, L. Ball, N. Wang, and R. N. Manchester. Radio observations of PSR B1259-63 through the 2004 periastron passage. *MNRAS*, 358:1069–1075, 2005.

F. C. Jones. Inverse Compton Scattering of Cosmic-Ray Electrons. *Physical Review*, 137:1306–1311, 1965.

F. C. Jones. Calculated Spectrum of Inverse-Compton-Scattered Photons. *Phys. Rev.*, 167: 1159–1169, 1968.

W. Karzas and R. Latter. Electron radiative transitions in a coulomb field. *ApJS*, 6:167–212, 1961.

V. M. Kaspi, M. Tavani, F. Nagase, M. Hirayma, M. Hoshino, T. Aoki, N. Kawai, and J. Arons. X-ray detection of PSR B1259-63 at periastron. *ApJ*, 453:424–432, 1995.

S. Kato. Low-frequency, one-armed oscillations of Keplerian gaseous disks. *PASJ*, 35:249–261, 1983.

A. Kawachi, T. Naito, J. R. Patterson, and *et al.* A Search for TeV Gamma-Ray Emission from the PSR B1259-63/SS 2883 Binary System with the CANGAROO-II 10 Meter Telescope. *ApJ*, 607:949–958, 2004.

C. F. Kennel and F. V. Coroniti. Confinement of the Crab pulsar's wind by its supernova remnant. *ApJ*, 283:694–709, 1984a.

C. F. Kennel and F. V. Coroniti. Magnetohydrodynamic model of Crab nebula radiation. *ApJ*, 283:710–730, 1984b.

D. Khangulyan, S. Hnatic, F. Aharonian, and S. Bogovalov. TeV light curve of PSR B1259-63/SS2883. *MNRAS*, 380:320–330, 2007.

D. Khangulyan, F. A. Aharonian, S. V. Bogovalov, and M. Ribo. Post-Periastron Gamma Ray Flare from PSR B1259-63/LS 2883 as a Result of Comptonization of the Cold Pulsar Wind. *ArXiv e-prints, arXiv:1107.4833*, 2011a.

D. Khangulyan, F. A. Aharonian, S. V. Bogovalov, and M. Ribó. Gamma-Ray Signal from the Pulsar Wind in the Binary Pulsar System PSR B1259-63/LS 2883. *ApJ*, 742:98, 2011b.

J. G. Kirk, L. Ball, and O. Skjaeraasen. Inverse Compton emission of TeV gamma rays from PSR B1259-63. *Astroparticle Physics*, 10:31–45, 1999.

J. G. Kirk, Y. Lyubarsky, and J. Petri. The Theory of Pulsar Winds and Nebulae. In W. Becker, editor, *Astrophysics and Space Science Library*, volume 357 of *Astrophysics and Space Science Library*, pages 421–450, 2009.

G. Klare and T. Neckel. UBV, Hbeta and polarization measurements of 1660 southern OB stars. *A&As*, 27:215–247, 1977.

D. A. Kniffen, W. C. K. Alberts, D. L. Bertsch, and *et al.* EGRET Observations of the Gamma-Ray Source 2CG 135+01. *ApJ*, 486:126–131, 1997.

H. A. Kramers. On the theory of X-ray absorption and on the continuous X-ray spectrum. *Phil. Mag.*, 46:836–871, 1923.

R.-P. Kudritzki and J. Puls. Winds from Hot Stars. *ARA&A*, 38:613–666, 2000.

R. L. Kurucz. Model Atmospheres for G, F, A, B and O stars. *ApJS*, 40:1–340, 1979.

R. L. Kurucz. Model Atmospheres for Population Synthesis. In B. Barbuy & A. Renzini, editor, *The Stellar Populations of Galaxies*, volume 149 of *IAU Symposium*, pages 225–232, 1992.

P. O. Lagage, J. W. Pel, M. Authier, and *et al.* Successful Commissioning of VISIR: The Mid-Infrared VLT Instrument. *The Messenger*, 117:12–16, September 2004.

H. J. G. L. M. Lamers and L. B. F. M. Waters. The infrared and radio spectrum of early-type stars with mass loss: I The curve of growth method. *A&A*, 136:37–52, 1984.

K. R. Lang. *Astrophysical formulae: A compendium for the physicist and astrophysicist.* New York, Springer-Verlag New York, Inc., 1974. 760 p., 1974.

U. Lee, H. Saio, and Y Osaki. Viscous excretion discs around Be stars. *MNRAS*, 250:432–437, 1991.

V. M. Lipunov. *The astrophysics of neutron stars.* Izdatel'stvo Nauka, Moscow, 1987.

M. A. Livingstone, V. M. Kaspi, and F. P. Gavriil. Long-Term Phase-coherent X-Ray Timing of PSR B0540-69. *ApJ*, 633:1095–1100, 2005.

F. Lucarelli, F. Verrecchia, E. Striani, and *et al.* AGILE detection of the new unidentified gamma-ray source AGL J2241+4454. *The Astronomer's Telegram*, 2761:1, 2010.

R. N. Manchester and J. H. Taylor. *Pulsars.* San Francisco CA (USA): W. H. Freeman, 1977.

R. N. Manchester, G. B. Hobbs, A. Teoh, and M. Hobbs. The Australia Telescope National Facility Pulsar Catalogue. *AJ*, 129:1993–2006, 2005.

J. Martí, J.M. Paredes, and M. Ribó. The system LS 5039: a new massive radio emitting X-ray binary. *A&A*, 338:L71–L74, 1998.

M. Massi, M. Ribó, J. M. Paredes, S. T. Garrington, M. Peracaula, and J. Martí. Hints for a fast precessing relativistic radio jet in LS I +61303. *A&A*, 414:L1–L4, 2004.

M. V. McSwain, D. R. Gies, R. L. Riddle, Z. Wang, and D. W. Wingert. The Orbit of the Massive X-Ray Binary LS 5039. *ApJ*, 558:L43–L46, 2001.

M. V. McSwain, D. R. Gies, W. Huang, P. J. Wiita, D. W. Wingert, and L. Kaper. The N Enrichment and Supernova Ejection of the Runaway Microquasar LS 5039. *ApJ*, 600:927–938, 2004.

A. Meilland, P. Stee, M. Vannier, and *et al.* First direct detection of a Keplerian rotating disk around the Be star α Arae using AMBER/VLTI. *A&A*, 464:59–71, 2007.

J. Moldón, S. Johnston, M. Ribó, J. M. Paredes, and A. T. Deller. Discovery of Extended and Variable Radio Structure from the Gamma-ray Binary System PSR B1259-63/LS 2883. *ApJ Letters*, 732:L10, 2011a.

J. Moldón, M. Ribó, and J. M. Paredes. Revealing the extended radio emission from the gamma-ray binary HESS J0632+057. *A&A*, 533:L7, 2011b.

I. V. Moskalenko and A. W. Strong. Anisotropic Inverse Compton Scattering in the Galaxy. *ApJ*, 528:357–367, 2000.

C. Motch, F. Haber, K. Denner, M. Pakull, and E. Janot-Pacheco. New massive X-ray binary candidates from the ROSAT Galactic Plane Survey. *A&A Supplement Series*, 323:853–875, 1997.

C.D. Murray and S.F. Dermott. *Solar System Dynamics*. Cambridge University Press, 1999.

T. Nagata, T. Tanabé, and I. S. Glass. *IRSF Observing Manual*, 2003.

I. Negueruela, M. Ribó, A. Herrero, J. Lorenzo, D. Khangulyan, and F. A. Aharonian. Astrophysical Parameters of LS 2883 and Implications for the PSR B1259-63 Gamma-ray Binary. *ApJ Letters*, 732:L11, 2011.

C. Neiner, G. Wade, G. Meynet, and G. Peters, editors. *Active OB Stars: Structure, Evolution, Mass Loss, and Critical Limits*, volume 272 of *IAU Symposium*, 2011.

A. Odendaal. Hα observations of PSR B1259-63/LS 2883, 2011. private communications.

A. T. Okazaki. Long-term V/R variations of Be stars due to global one-armed oscillations of equatorial disks. *PASJ*, 43:75–94, 1991.

A. T. Okazaki. On the confinement of one-armed oscillations in discs of Be stars. *ApJ*, 318: 548–560, 1997.

A. T. Okazaki, M. R. Bate, G. I. Ogilvie, and J. E. Pringle. Viscous effects on the interaction between the coplanar decretion disc and the neutron star in Be/X-ray binaries. *MNRAS*, 337: 967–980, 2002.

A. T. Okazaki, S. Nagataki, T. Naito, A. Kawachi, K. Hayasaki, S. P. Owocki, and J. Takata. Hydrodynamic Interaction between the Be Star and the Pulsar in the TeV Binary PSR B1259-63/LS 2883. *PASJ*, 63:893–901, 2011.

S. Owocki. Dynamical Processes in the Formation of Hot-Star Disks. In R. Ignace & K. G. Gayley, editor, *The Nature and Evolution of Disks Around Hot Stars*, volume 337 of *Astronomical Society of the Pacific Conference Series*, page 101, 2005.

S. Owocki and A. Ud-Doula. Magnetic Spin-Up of Line-Driven Stellar Winds. In L. A. Balona, H. F. Henrichs, & R. Medupe, editor, *Astronomical Society of the Pacific Conference Series*, volume 305 of *Astronomical Society of the Pacific Conference Series*, pages 350–357, 2003.

S. P. Owocki, S. R. Cranmer, and J. M. Blondin. Two-dimensional hydrodynamical simulations of wind-compressed disks around rapidly rotating B stars. *ApJ*, 424:887–904, 1994.

S. P. Owocki, S. R. Cranmer, and K. G. Gayley. Inhibition FO Wind Compressed Disk Formation by Nonradial Line-Forces in Rotating Hot-Star Winds. *ApJ Letters*, 472:L115, 1996.

F. Pacini and M. Salvati. On the Evolution of Supernova Remnants. Evolution of the Magnetic Field, Particles, Content, and Luminosity. *ApJ*, 186:249–266, 1973.

N. Panagia and M. Felli. The spectrum of the free-free radiation from extended envelopes. *A&A*, 39:1–5, 1975.

J. M. Paredes, J. Marti, M. Peracaula, and M. Ribo. Evidence of X-ray periodicity in LSI+61 303. *A&A*, 320:L25–L28, 1997.

J. M. Paredes, J. Martí, M. Ribó, and M. Massi. Discovery of a High-Energy Gamma-Ray-Emitting Persistent Microquasar. *Science*, 288:2340–2342, 2000.

J.M. Paredes, M. Ribó, E. Ros, J. Martí, and M. Massi. Conrmation of persistent radio jets in the microquasar LS 5039. *A&A*, 393:L99–L102, 2002.

G. G. Pavlov, C. Chang, and O. Kargaltsev. Extended Emission from the PSR B1259-63/SS 2883 Binary Detected with Chandra. *ApJ*, 730:2, 2011.

S. Pommé, L. Johansson, G. Sibbens, and B. Denecke. An algorithm for the solid angle calculation applied in alpha-particle counting. *Nuclear Instruments and Methods in Physics Research A*, 505:286–289, 2003.

J. M. Porter and T. Rivinius. Classical Be Stars. *PASP*, 115:1153–1170, 2003.

W. H. Press, S. A. Teukolsky, W. T. Vetterling, and B. P. Flannery. *Numerical Recipes: The Art of Scientific Computing*. Cambridge University Press, Cambridge, 3rd edition, 2007.

S. D. Price, M. P. Egan, S. J. Carey, D. R. Mizuno, and T. A. Kuchar. Midcourse Space Experiment Survey of the Galactic Plane. *AJ*, 121:2819–2842, 2001.

A. Quirrenbach, D. F. Buscher, D. Mozurkewich, C. A. Hummel, and J. T. Armstrong. Maximum-entropy maps of the Be shell star ζ Tauri from optical long-baseline. *A&A*, 283: L13–L16, 1994.

A. Quirrenbach, K. S. Bjorkman, J. E. Bjorkman, and *et al.* Constraints on the Geometry of Circumstellar Envelopes: Optical Interferometric and Spectropolarimetric Observations of Seven Be Stars. *ApJ*, 479:477–496, 1997.

A. F. Rajoelimanana, P. A. Charles, and A. Udalski. Very long-term optical variability of high-mass X-ray binaries in the Small Magellanic Cloud. *MNRAS*, 413:1600–1622, 2011.

N. Rea and D. F. Torres. Is the SGR-like burst from LS I +61 303? *The Astronomer's Telegram*, 1731:1, 2008.

M. J. Rees and J.E. Gunn. The Origin of the Magnetic Field and Relatiistic Particles in the Crab Nebula. *MNRAS*, 167:1–12, 1974.

P. Reig, J. Fabregat, and M. J. Coe. A new correlation for Be/X-ray binaries: the orbital period-Hα equivalent width diagram. *A&A*, 322:193–196, 1997.

M. Ribó, P. Reig, J. Martí, and J. M. Paredes. X-ray and radio observations of RX J1826.2-1450/LS 5039. *A&A*, 347:518–523, 1999.

M. Ribó, J. M. Paredes, J. Moldón, J. Martí, and M. Massi. The changing milliarcsecond radio morphology of the gamma-ray binary LS 5039. *A&A*, 481:17–20, 2008.

T. Rivinius. Links between Photospheric Activity and Formation of Circumstellar Structures of Be Stars. In A. T. Okazaki, S. P. Owocki, & S. Stefl, editor, *Active OB-Stars: Laboratories for Stellare and Circumstellar Physics*, volume 361 of *Astronomical Society of the Pacific Conference Series*, pages 219–229, 2007.

T. Rivinius, D. Baade, S. Stefl, O. Stahl, B. Wolf, and A. Kaufer. Stellar and circumstellar activity of the Be star MU Centauri. I. Line emission outbursts. *A&A*, 333:125–140, 1998.

G. B. Rybicki and A. P. Lightman. *Radiative Processes in Astrophysics*. Radiative Processes in Astrophysics, by George B. Rybicki, Alan P. Lightman,. Wiley-VCH, 2004.

G. E. Sarty, T. Szalai, L. L. Kiss, and *et al.* The γ-ray binary LS 5039: mass and orbit constraints from MOST observations. *MNRAS*, 411:1293–1300, 2011.

R. E. Schild, R. F. Garrison, and W. A. Hiltner. UBV photometry for southern OB stars. *ApJS*, 51:321–336, 1983.

A. Secchi. Schreiben des Herrn Prof. Secchi, Directors der Sternwarte des Collegio Romano, an den Herausgeber. *Astronomische Nachrichten*, 68:63, 1866.

A. Sierpowska-Bartosik and W. Bednarek. γ-rays from binary system with energetic pulsar and Be star with aspherical wind: PSR B1259-63/SS2883. *MNRAS*, 385:2279–2288, 2008.

J. L. Skilton, M. Pandey-Pommier, J. A. Hinton, and *et al.* The radio counterpart of the likely TeV binary HESSJ0632+057. *MNRAS*, 399:317–322, 2009.

M. F. Skrutskie, R. M. Cutri, R. Stiening, and *et al.* The Two Micron All Sky Survey (2MASS). *AJ*, 131:1163–1183, 2006.

A. Smette and L. Vanzi. *Very Large Telescope Paranal Science Operations VISIR User Manual*. European Southern Observatory, 81 edition, 2007.

P. Stee. Observations of circumstellar disks. In C. Neiner, G. Wade, G. Meynet, & G. Peters, editor, *IAU Symposium*, volume 272 of *IAU Symposium*, pages 313–324, 2011.

C. B. Stephenson and N. Sanduleak. New H-alpha emission stars in the Milky Way. *ApJS*, 33: 459–469, 1977.

C.B. Stephenson and N. Sanduleak. *Luminous Stars in the Southern Milky Way*, volume I of *1*. Warner and Swasey Obs., Hamburger Sternwarte-Warner and Swasey Obs., 1971.

O. Struve. On the origin of bright lines in spectra of stars of class B. *ApJ*, 73:94–103, 1931.

P. A. Sturrock. A Model of Pulsars. *ApJ*, 164:529–556, 1971.

T. Takahashi, T. Kishishita, Y. Uchiyama, and *et al.* Study of the Spectral and Temporal Characteristics of X-Ray Emission of the Gamma-Ray Binary LS 5039 with Suzaku. *ApJ*, 697: 592–600, 2009.

P. H. T. Tam, R. H. H. Huang, J. Takata, C. Y. Hui, A. K. H. Kong, and K. S. Cheng. Discovery of GeV γ-ray Emission from PSR B1259-63/LS 2883. *ApJ Letters*, 736:L10, 2011.

M. Tavani and J. Arons. Theory of High-Energy Emission from the Pulsar/Be Star System PSR 1259-63. I. Radiation Mechanisms and Interaction Geometry. *ApJ*, 477:439–464, 1997.

J. H. Telting, M. H. M. Heemskerk, H. F. Henrichs, and G. J. Savonije. Observational evidence for a prograde one-armed density structure in the equatorial disc of a Be star. *A&A*, 288: 558–560, 1994.

J. H. Telting, L. B. F. M. Waters, P. Roche, A. C. A. Boogert, J. S. Clark, D. de Martino, and P. Persi. The quatorial disc of the Be star X Persei. *MNRAS*, 296:785, 1998.

S. E. Thorsett and D. Chakrabarty. Neutron star mass measurements. I Radio pulsars. *Astro. Phys.*, 512:288–299, 1999.

D. F. Torres, N. Rea, P. Esposito, J. Li, Y. Chen, and S. Zhang. A magnetar-like event from LS I +61 303 and its nature as a gamma-ray binary. *ApJ in press , arXiv:1109.5008v1*, 744:106, 2012.

L. J. Townsend, M. J. Coe, R. H. D. Corbet, and *et al.* The orbital solution and spectral classification of the high-mass X-ray binary IGR J01054-7253 in the Small Magellanic Cloud. *MNRAS*, 410:1813–1824, 2011.

R. H. D. Townsend, S. P. Owocki, and I. D. Howarth. Be-star rotation: how close to critical? *MNRAS*, 350:189–195, 2004.

S. Tryka. Angular distribution of the solid angle at a point subtended by a circular disk. *Optics Communications*, 137:317–333, 1997.

E. van der Swaluw, T. P. Downes, and R. Keegan. An evolutionary model for pulsar-driven supernova remnants. A hydrodynamical model. *A&A*, 420:937–944, 2004.

B. van Soelen. An investigation into the nature of the relativistic compact object in the micro-quasar system ls 5039: A multi-wavelength study. Master's thesis, University of the Free State, 2007.

B. van Soelen and P. J. Meintjes. The effect of the infrared excess from the Be star on inverse Compton gamma-ray production in PSR B1259-63/SS 2883. *MNRAS*, 412:1721–1729, 2011.

B. van Soelen and P. J. Meintjes. Anisotropic scattering from the circumstellar disc in PSR B1259-63. to appear in: *International Journal of Modern Physics: Conference Series/ArXiv e-prints, arXiv:1201.1722*, 2012.

J. S. Vink, A. de Koter, and H. J. G. L. M. Lamers. Mass-loss predictions for O and B stars as a function of metallicity. *A&A*, 369:574–588, 2001.

N. Wang, S. Johnston, and R. N. Manchester. 13 years of timing of PSR B125963. *MNRAS*, 351:599–606, 2004.

L. B. F. M. Waters. The density structure of discs around Be stars derived from IRAS observations. *A&A*, 162:121–139, 1986.

L. B. F. M. Waters and H. J. G. L. M. Lamers. The infrared and radio spectrum of early type stars with mass loss. *A&A*, 57:327–352, 1984.

D. C. Wells, E. W. Greisen, and R. H. Harten. FITS - a Flexible Image Transport System. *A&AS*, 44:363–370, 1981.

B. E. Westerlund and R. Garnier. UBV-beta photometry of luminous early-type stars and emission-line stars in the Southern Coalsack region. *A&AS*, 78:203–215, 1989.

S. J. Williams, D. R. Gies, R. A. Matson, Y. Touhami, E. D. Grundstrom, W. Huang, and M. V. McSwain. The Be Star HD 215227: A Candidate Gamma-ray Binary. *ApJ* Letters, 723:L93–L97, 2010.

K. Wood, K. S. Bjorkman, and J. E. Bjorkman. Deriving the Geometry of Be Star Circumstellar Envelopes from Continuum Spectropolarimetry. I. The Case of zeta Tauri. *ApJ*, 477:926–939, 1997.

N. J. Woolf, Stein W.A., and P. A. Strittmatter. Infrared Emission from Be Stars. *A&A*, 9: 252–258, 1970.

A. E. Wright and M. J. Barlow. The radio and infrared spectrum of Early-type stars undergoing mass loss. *MNRAS*, 170:41–51, 1975.

V. Zabalza, J. M. Paredes, and V. Bosch-Ramon. On the origin of correlated X-ray/VHE emission from LS I +61 303. *A&A*, 527:A9, 2011.

Appendix A

Derivation of additional terms for the Compton scattering formulae

This appendix derives certain aspects of the Compton and inverse Compton scattering which, to improve readability have not been included in the body of the text.

A.1 Taylor expansion of β

The Taylor series expansion is given by

$$f(x) = f(a) + \frac{f'(a)}{1!}(x-a) + \frac{f''(a)}{2!}(x-a)^2 + \frac{f^{(3)}(a)}{3!}(x-a)^3 + ...$$

and the equation $\beta = (1-\gamma^{-2})^{1/2}$ can be written in the form

$$f(x) = (1-x^2)^{1/2},$$

where $x = 1/\gamma$. Therefore

$$\begin{aligned} f'(x) &= -x\left(1-x^2\right)^{-1/2} \\ f''(x) &= -\left(1-x^2\right)^{-1/2} - x^2\left(1-x^2\right)^{-3/2}, \end{aligned}$$

and using $a = 0$,

$$\begin{aligned} f(x) &= f(a) + \frac{f'(a)}{1!}(x-a) + \frac{f''(a)}{2!}(x-a)^2 + (\text{higher order terms}) \\ &\approx f(0) + \frac{f'(0)}{1!}(x) + \frac{f''(0)}{2!}(x)^2 \\ &= 1 + 0 + \frac{-1}{2}x^2 \\ &= 1 - \frac{1}{2\gamma^2}. \end{aligned}$$

Therefore, from the Taylor expansion it can be shown that

$$\beta = (1-\gamma^{-2})^{1/2} \approx 1 - \frac{1}{2\gamma^2}.$$

A.2 Taylor expansion of scattering equation

The Taylor expansion is given by

$$f(x) = f(a) + \frac{f'(a)}{1!}(x-a) + \frac{f''(a)}{2!}(x-a)^2 + \frac{f^{(3)}(a)}{3!}(x-a)^3 + ...$$

and the Compton scattering energy transfer equation is given by

$$\epsilon_1' = \epsilon_0' \left[1 + \frac{\epsilon_0'}{m_e c^2} (1 - \cos\Theta') \right]^{-1}$$

which can be written in the form

$$f(x) = x(1 - Ax)^{-1},$$

where $x = \epsilon_0'$ and $A = (1 - \cos\Theta')/m_e c^2$. Therefore,

$$\begin{aligned} f'(x) &= (1 + Ax)^{-1} - Ax(1 + Ax)^{-2} \\ f''(x) &= -A(1 + Ax)^{-2} - A(1 + Ax)^{-2} + 2A^2 x(1 + Ax)^{-3}. \end{aligned}$$

Applying the Taylor expansion for $a = 0$,

$$\begin{aligned} f(x) &= f(a) + \frac{f'(a)}{1!}(x-a) + \frac{f''(a)}{2!}(x-a)^2 + (\text{higher order terms}) \\ &\approx f(0) + \frac{f'(0)}{1!}(x) + \frac{f''(0)}{2!}(x)^2 \\ &= 0 + \frac{1}{1}x + \frac{-2A}{2}x^2 \\ &= x - Ax^2 \\ &= x(1-Ax) \\ &= \epsilon_0' \left[1 - \frac{\epsilon_0'}{m_e c^2}(1-\cos\Theta')\right]. \end{aligned}$$

Therefore,

$$\begin{aligned} \epsilon_1' &= \epsilon_0' \left[1 + \frac{\epsilon_0'}{m_e c^2}(1-\cos\Theta')\right]^{-1} \\ &\approx \epsilon_0' \left[1 - \frac{\epsilon_0'}{m_e c^2}(1-\cos\Theta')\right]. \end{aligned}$$

A.3 Translation of the mono-energetic beam from K to K'

A mono-energetic and mono-directional photon beam has the form

$$\frac{dn}{d\epsilon\, d\Omega} = \delta(\epsilon - \epsilon_0)\delta(\cos\theta - \cos\theta_0)\delta(\phi - \phi_0), \tag{A.1}$$

in the observer's system. This is converted to the rest frame of the electron by

$$\frac{dn'}{d\epsilon'\, d\Omega'} = \frac{dn}{d\epsilon\, d\Omega}\frac{d\Omega}{d\Omega'}, \tag{A.2}$$

since $dn/d\epsilon = dn'/d\epsilon'$ is invariant. The translation between the K and K' coordinate systems is given, for the photon energy, ϵ, by

$$\epsilon = \epsilon'\gamma(1 + \beta\cos\theta'),$$

and for the angle transformation by

$$\sin\theta = \frac{\sin\theta'}{\gamma(1+\beta\cos\theta)},$$

$$\cos\theta = \frac{\cos\theta' + \beta}{1 + \beta\cos\theta'}$$

and

$$\phi' = \phi.$$

There is no change in the azimuthal angle (ϕ) since the electron's motion is defined to be along the polar axis, and therefore only polar angles are transformed. Therefore, it is possible to write

$$\begin{aligned}\frac{d\Omega}{d\Omega'} &= \frac{\sin\theta}{\sin\theta'}\frac{d\theta}{d\theta'}\frac{d\phi}{d\phi'} \\ &= \left(\frac{1}{\gamma(1+\beta\cos\theta')}\right)\left(\frac{1}{\gamma(1+\beta\cos\theta')}\right)\left(\frac{1}{1}\right) \\ &= \frac{1}{\gamma^2(1+\beta\cos\theta')^2},\end{aligned}$$

where the small angle approximation, $d\theta \approx \sin\theta$, has been used. Substituting, $d\Omega/d\Omega'$ and equation (A.1) into equation (A.2) gives

$$\frac{dn'}{d\epsilon'\,d\Omega'} = \delta\left(\epsilon'\gamma(1+\beta\cos\theta') - \epsilon_0\right)\delta\left(\frac{\cos\theta'+\beta}{1+\beta\cos\theta'} - \cos\theta_0\right)\delta\left(\phi' - \phi'_0\right)\left(\frac{1}{\gamma^2(1+\beta\cos\theta')^2}\right). \tag{A.3}$$

As shown by Cerutti (2010), the Dirac functions in equation (A.3) can be re-written using the property

$$\delta(f(x)) = \sum_i \frac{1}{\left|\frac{df}{dx}\right|_{x=x_i}}\delta(x-x_i),$$

such that $\forall i, f(x_i) = 0$. Therefore, if this is applied to $\delta\left(\epsilon'\gamma(1+\beta\cos\theta') - \epsilon_0\right)$, the function $f(x)$ has the form

$$f(x) = x\gamma(1+\beta\cos\theta') - \epsilon_0,$$

where $x \equiv \epsilon'$ and the derivative of $f(x)$ has the form

$$\begin{aligned}\frac{df}{dx} \equiv \frac{df}{d\epsilon'} &= \frac{d}{d\epsilon'}\left(\epsilon'\gamma[1+\beta\cos\theta'] - \epsilon_0\right) \\ &= \gamma(1+\beta\cos\theta').\end{aligned}$$

The condition $\forall i, f(x_i) = 0$ is satisfied for $x = \epsilon'_0$, which implies $\cos\theta' = \cos\theta'_0$ and therefore

$$\left|\frac{df}{dx}\right|_{x=x_i} = \gamma(1+\beta\cos\theta'_0).$$

Therefore

$$\begin{aligned}\delta\left(\epsilon'\gamma(1+\beta\cos\theta') - \epsilon_0\right) &= \frac{1}{\gamma(1+\beta\cos\theta'_0)}\delta(\epsilon'-\epsilon'_0) \\ &= \frac{1}{\gamma(1+\beta\cos\theta'_0)}\delta\left(\epsilon' - \epsilon_0\gamma[1-\beta\cos\theta_0]\right).\end{aligned} \tag{A.4}$$

Similarly it can be shown that

$$\delta\left(\frac{\cos\theta'+\beta}{1+\beta\cos\theta'} - \cos\theta_0\right) = \delta\left(\cos\theta' - \frac{\cos\theta_0-\beta}{1-\beta\cos\theta_0}\right). \tag{A.5}$$

Substituting the Dirac delta functions (equations A.4 & A.5) into equation (A.3) gives

$$\frac{dn'}{d\epsilon'\, d\Omega'} = \gamma(1-\beta\cos\theta_0)\delta\left(\epsilon' - \epsilon_0\gamma[1-\beta\cos\theta_0]\right)\delta\left(\cos\theta' - \frac{\cos\theta_0-\beta}{1-\beta\cos\theta_0}\right)\delta(\phi'-\phi'_0).$$

Appendix B

Derivation of the disc intercepts for the COG method

B.1 Limiting case: $\theta < 90^\circ$

To find the position where a line-of-sight ($\hat{\mathbf{e}}_{\theta,\phi}$) with a direction defined by θ and ϕ, intercepts the disc above and below the disc plane, the values of Δx and Δy can be calculated by solving for $h_l = h_d$, given by equations (6.24) & (6.25):

$$\begin{aligned} h_l &= h_d \\ \sqrt{\Delta x^2 + \Delta y^2}\tan\theta_k, &= \sqrt{x^2 + y^2}\tan\theta_{\text{disc}} \\ &= \sqrt{(x_d + \Delta x)^2 + (y_d + \Delta y)^2}\tan\theta_{\text{disc}}, \end{aligned} \tag{B.1}$$

where

$$\theta_k = \frac{\pi}{2} - \theta, \tag{B.2}$$

and θ is the polar angle of the line-of-sight ($\hat{\mathbf{e}}_{\theta,\phi}$). Making the substitution $\Delta y = \Delta x \tan\phi$,

$$\begin{aligned} \left[\Delta x^2 + (\Delta x\tan\phi)^2\right]^{1/2}\tan\theta_k &= \left[(x_d + \Delta x)^2 + (y_d + \Delta x\tan\phi)^2\right]^{1/2}\tan\theta_{\text{disc}} \\ \therefore \left[\Delta x^2 + (\Delta x\tan\phi)^2\right]\tan^2\theta_k &= \left[(x_d + \Delta x)^2 + (y_d + \Delta x\tan\phi)^2\right]\tan^2\theta_{\text{disc}}. \end{aligned} \tag{B.3}$$

The term within square brackets on the LHS of equation (B.3) reduces to

$$\begin{aligned} \Delta x^2 + (\Delta x\tan\phi)^2 &= \Delta x^2\left(1 + \tan^2\phi\right) \\ &= \Delta x^2\sec^2\phi, \end{aligned}$$

and the term within square brackets on the RHS expands to

$$\begin{aligned}(x_d + \Delta x)^2 + (y_d + \Delta x \tan\phi)^2 &= x_d^2 + \Delta x^2 + 2x_d\Delta x + y_d^2 + \Delta x^2 \tan^2\phi + 2y_d \tan\phi \Delta x \\ &= \Delta x^2 \left(1 + \tan^2\phi\right) + \Delta x \left(2x_d + 2y_d \tan\phi\right) + x_d^2 + y_d^2 \\ &= \Delta x^2 \sec^2\phi + \Delta x \left(2x_d + 2y_d \tan\phi\right) + \left(x_d^2 + y_d^2\right).\end{aligned}$$

Substituting these terms back into equation (B.3) gives

$$\begin{aligned}\Delta x^2 \sec^2\phi \tan^2\theta_k &= \left[\Delta x^2 \sec^2\phi + \Delta x \left(2x_d + 2y_d \tan\phi\right) + \left(x_d^2 + y_d^2\right)\right] \tan^2\theta_{\text{disc}} \\ \therefore \Delta x^2 \sec^2\phi \frac{\tan^2\theta_k}{\tan^2\theta_{\text{disc}}} &= \left[\Delta x^2 \sec^2\phi + \Delta x \left(2x_d + 2y_d \tan\phi\right) + \left(x_d^2 + y_d^2\right)\right].\end{aligned}$$

This equation can be arranged into the form $a\Delta x^2 + b\Delta x + c$ and therefore

$$\left[\sec^2\phi \left(1 - \frac{\tan^2\theta_k}{\tan^2\theta_{\text{disc}}}\right)\right] \Delta x^2 + \left[2x_d + 2y_d \tan\phi\right] \Delta x + \left[x_d^2 + y_d^2\right] = 0 \tag{B.4}$$

and

$$\Delta x = \frac{-b \pm \sqrt{b^2 - 4ac}}{2a},$$

where

$$\begin{aligned}a &= \sec^2\phi \left(1 - \frac{\tan^2\theta_k}{\tan^2\theta_{\text{disc}}}\right) \\ b &= 2x_d + 2y_d \tan\phi \\ c &= x_d^2 + y_d^2.\end{aligned}$$

This produces two solutions for Δx, one larger than zero and the other less than zero, which are defined as $\Delta x_{>0}$ and $\Delta x_{<0}$ respectively. If the X coordinate of the disc mid-plane intercept, where X is defined in Fig. 6.8 (p. 116), is less than zero, i.e.

$$X = x - \rho < 0,$$

then $\Delta x_{>0}$ lies above the disc plane and $\Delta x_{<0}$ lies below it, while if

$$X = x - \rho > 0,$$

then $\Delta x_{>0}$ lies below the disc plane and $\Delta x_{<0}$ lies above it. The change in y is then determined by

$$\Delta y = \Delta x \tan\phi.$$

The solution above applies if $\Delta x \neq 0$, but in the case of $\phi = 0$ or $\phi = \pi$ there will be no

change in the x coordinate. In this case equation (B.1) simplifies to

$$\left(\Delta y^2\right)^{1/2} \tan\theta_k = \left[x_d^2 + (y_d + \Delta y)^2\right]^{1/2} \tan\theta_{\rm disc},$$

which can be solved for Δy similar to the solution of Δx above, and

$$\Delta y = \frac{-b \pm \sqrt{b^2 - 4ac}}{2a}, \tag{B.5}$$

where

$$\begin{aligned} a &= 1 - \frac{\tan^2\theta_k}{\tan^2\theta_{\rm disc}} \\ b &= 2y_d \\ c &= x_d^2 + y_d^2. \end{aligned}$$

This also produces two solutions for Δy, one larger than zero and the other less than zero, which are defined as $\Delta y_{>0}$ and $\Delta y_{<0}$ respectively. If the Y disc intercept (Fig. 6.8) is greater than zero, i.e.

$$Y = y > 0,$$

then $\Delta y_{<0}$ is above the plane, and $\Delta y_{>0}$ is below the plane, while if

$$Y = y < 0$$

then $\Delta y_{<0}$ is below the plane, and $\Delta y_{>0}$ is above it. For both cases $\Delta x = 0$.

From the solutions of Δx and Δy above, the x-y coordinates of the disc intercept can be determined from the appropriate values for Δx, Δy, and

$$\begin{aligned} x &= x_d + \Delta x \\ y &= y_d + \Delta y, \end{aligned}$$

where x_d, y_d is the intercept of the line-of-sight with the disc mid-plane (Fig. 6.8). The position (x_1, y_1) is defined to be below the plane, and the position (x_2, y_2) is defined to be above the plane. The z coordinate of the disc intercepts are defined by the height above the disc mid-plane, and therefore (equation 6.24)

$$\begin{aligned} z_1 &= -\left|\sqrt{x_1^2 + y_1^2}\right| \tan\theta_{\rm disc} \\ z_2 &= \left|\sqrt{x_2^2 + y_2^2}\right| \tan\theta_{\rm disc}. \end{aligned}$$

The derivation above assumes that the line-of-sight passes through the disc and does not

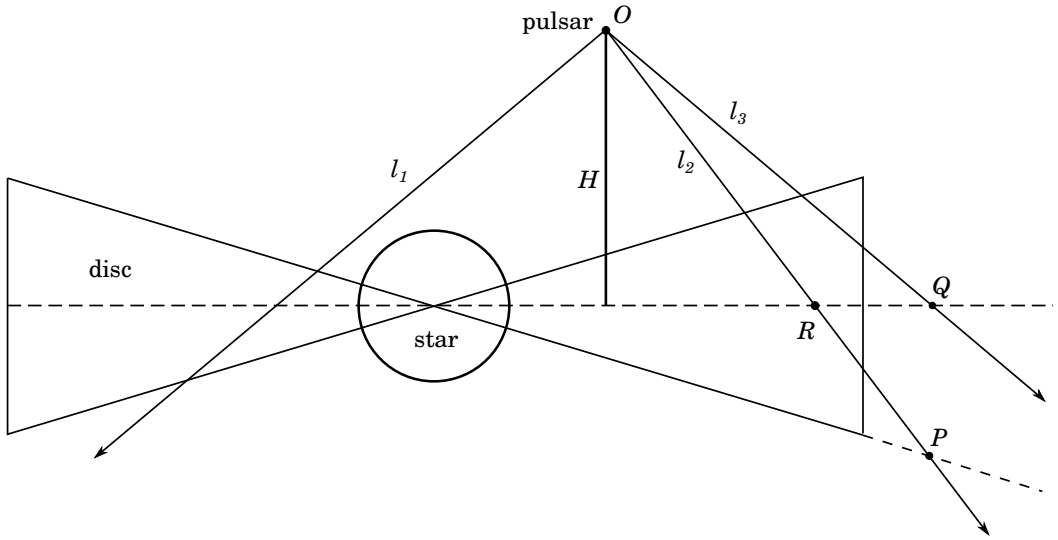

Figure B.1: Possible lines-of-sight through the disc.

reach the end of the disc. In the COG model it is assumed that the disc has a finite radius $R_{\rm disc}$ and abruptly ends at this radius. Compare lines l_1 and l_2 in Fig. B.1. Line l_1 passes straight through the disc and the derivation of the disc intercepts above holds. However, line l_2 reaches the edge of the disc without reaching the point P that the equations above would give as the end point.

For values where the bottom and mid-plane disc intercepts are beyond the radius of the disc, i.e. $\sqrt{x_1^2 + y_1^2} > R_{\rm disc}$ or $\sqrt{x_d^2 + y_d^2} > R_{\rm disc}$ respectively, the new limits for x_1 and y_1 are found by using the constraint on the size of the disc. The limit on the size of the disc is (Fig. 6.8)

$$(X + \rho)^2 + Y^2 \leq R_{\rm disc}^2,$$

and by making the substitution $Y = X \tan\phi$, the value of X can be found by solving for (Moskalenko and Strong, 2000)

$$(X + \rho)^2 + Y^2 - R_{\rm disc}^2 = 0 \tag{B.6}$$

$$(X + \rho)^2 + (X \tan\phi)^2 - R_{\rm disc}^2 = 0$$

$$\Rightarrow \quad \left(1 - \tan^2\phi\right) X^2 + 2\rho X + \rho^2 - R_{\rm disc}^2 = 0, \tag{B.7}$$

and therefore

$$X = \frac{-2\rho \pm \sqrt{(2\rho)^2 - 4\sec^2\phi\,(\rho^2 - R_{\rm disc}^2)}}{2\sec^2\phi} \tag{B.8}$$

and

$$Y = X \tan\phi. \tag{B.9}$$

If $\phi = \pi/2$ or $3\pi/2$ then $X = 0$ and equation (B.6) reduces to

$$\rho^2 + Y^2 - R_{\rm disc}^2 = 0,$$

and the value of Y is found from

$$Y = \sqrt{R_{\rm disc}^2 - \rho^2} \tag{B.10}$$

where Y has two possible answers. The correct solution for X and Y is chosen by determining from ϕ in which quadrant the correct solution must lie. If for example $0 \leq \phi \leq \pi/2$, then it is required that

$$\begin{aligned} X &> 0 \\ Y &> 0, \end{aligned}$$

while if $2\pi/3 \leq \phi \leq 2\pi$ it is required that

$$\begin{aligned} X &> 0 \\ Y &< 0. \end{aligned}$$

From the value of ϕ it is possible to determine what sign the correct solution must have and chose the appropriate values for X and Y. Using the correct solution, the new value for the bottom disc intersection point is found from

$$\begin{aligned} x_1 &= X + \rho \\ y_1 &= Y. \end{aligned} \tag{B.11}$$

If the disc plane intercept point is also beyond the disc limit (i.e. $x_d^2 + y_d^2 > R_{\rm d}^2$; point Q in Fig. B.1) then the z_1 coordinate lies above the disc plane, while if it is within the disc limit (point R in Fig. B.1) the z_1 coordinate is below the plane (compare the bottom intercepts for l_2 and l_3 in Fig. B.1). The solution to z_1 is then

$$z_1 = H - \frac{\left[(x_1 - \rho)^2 + y_1^2\right]^{1/2}}{\tan\theta} \qquad (\text{for } x_d^2 + y_d^2 > R_{\rm d}^2) \tag{B.12}$$

$$z_1 = \frac{\left[(x_1 - \rho)^2 + y_1^2\right]^{1/2}}{\tan\theta} - H \qquad (\text{for } x_d^2 + y_d^2 < R_{\rm d}^2), \tag{B.13}$$

where H is the height of point O above the disc mid-plane.

This approximation of an abrupt end is reasonable for two reasons: first if this approximation is not implied, at positions close to the disc, a line-of-sight with a large polar angle would result in the integration over s (the length of the line-of-sight in equation 6.5) for values much larger than the size of the disc, and second since the density decreases as r^{-n}, at the edge of the disc

the density is already very low and a sharp cut off should not result in a significant change to the flux in comparison to a more gradual disc edge.

B.1.1 Additional constraint: $\theta_k = \theta_{\rm disc}$

The solutions above hold for $\theta_k > \theta_{\rm disc}$ (equation B.2) but in the case that $\theta_k = \theta_{\rm disc}$ the intercept below the disc plane will be defined by the edge of the disc. The top intercept can be solved by using equation (B.3) which reduces, for $\theta_k = \theta_{\rm disc}$, to

$$\begin{aligned} & \left[\Delta x^2 + (\Delta x \tan\phi)^2\right] = \left[(x_d + \Delta x)^2 + (y_d + \Delta x \tan\phi)^2\right] \\ \Rightarrow \qquad & \Delta x = -\left(\frac{x_d^2 + y_d^2}{2x_d + 2y_d \tan\phi}\right), \end{aligned}$$

and $\Delta y = \Delta x \tan\phi$. Similarly to the previous solution, if $\Delta x = 0$ then the top intercept is defined by

$$\Delta y = -\frac{x_d^2 + y_d^2}{2y_d}.$$

Therefore

$$\begin{aligned} x_2 &= x_d + \Delta x \\ y_2 &= y_d + \Delta y \\ z_2 &= \left|\sqrt{x_2^2 + y_2^2}\right| \tan\theta_{\rm disc}. \end{aligned}$$

The value of the bottom disc intercept, which is defined by the edge of the disc, is found as is outlined by equations (B.6)–(B.13).

B.1.2 Additional constraint: $\theta_k < \theta_{\rm disc}$

When $\theta_k < \theta_{\rm disc}$, equation (B.4) produces two solutions for Δx which have the same sign. The intercept below the disc plane must be defined by the edge of the disc, while the solution of the top intercept is the value of Δx which has the smaller absolute value, i.e. if the two solutions for Δx are Δx_1 and Δx_2 then

$$\Delta x_{\rm top} = \pm \min(\|\Delta x_1\|, \|\Delta x_2\|), \tag{B.14}$$

where the sign of equation (B.14) must be the same as the sign of Δx_1 and Δx_2. The validity of this argument is illustrated in Fig. B.2: since Δx is measured relative to the disc plane intercept ($x_{\rm inter}$), the correct value of Δx is that which produces the smallest change in the x coordinate. Similarly if $\Delta x = 0$ the change in x is zero, and a solution can be found for Δy using

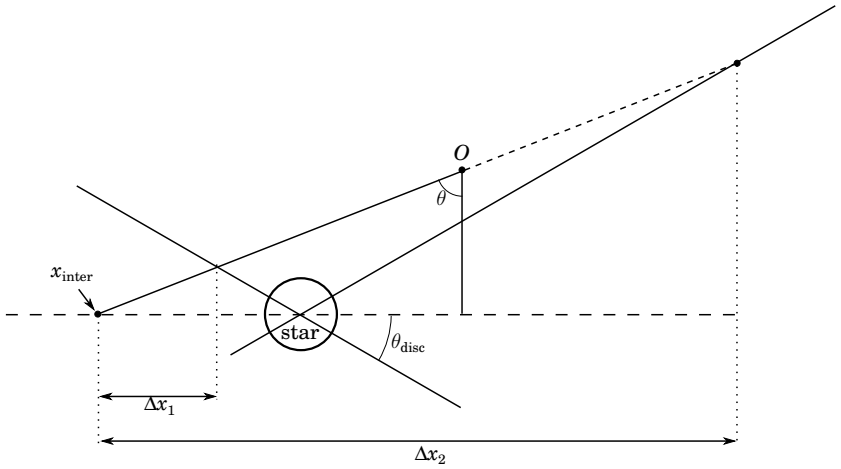

Figure B.2: Calculation of the disc intercept when $\theta_k < \theta_{\rm disc}$.

equation (B.5). Therefore

$$\begin{aligned} x_2 &= x_d + \Delta x_{\rm top} \\ y_2 &= y_d + \Delta y_{\rm top} \\ z_2 &= \left|\sqrt{x_2^2 + y_2^2}\right| \tan\theta_{\rm disc}, \end{aligned}$$

where

$$\Delta y_{\rm top} = \Delta x_{\rm top} \tan\phi.$$

The value of the bottom disc intercept, which is defined by the edge of the disc, is found as is outlined by equations (B.6)–(B.13).

B.2 Limiting case: $\theta = 90°$

When the polar angle $\theta = \frac{\pi}{2}$ (or $\theta = 90°$) the line-of-sight follows the situation shown in Fig. B.3. Tracing along the line, intercept P_1 occurs where the height of the disc equals the height H and P_2 occurs at the disc edge.

B.2.1 Solving for P_1

At any distance $r = \sqrt{x^2 + y^2}$ from the centre of the star, the height of the disc is given by (equation 6.24)

$$\begin{aligned} h_d &= \sqrt{x^2 + y^2} \tan\theta_{\rm disc} \\ &= r \tan\theta_{\rm disc}. \end{aligned}$$

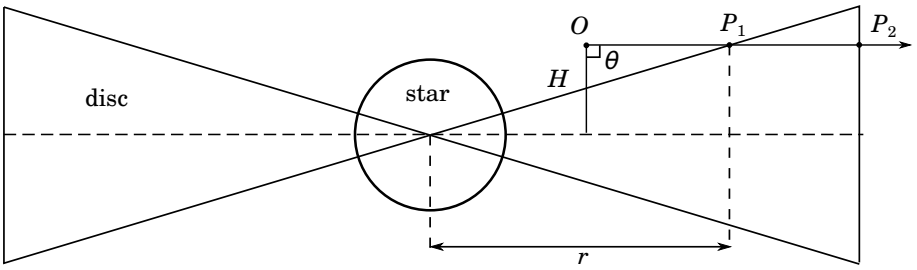

Figure B.3: Disc intercept for $\theta = 90°$.

Therefore the P_1 can be determined by requiring that $h_d = H$ or $H = r\tan\theta_{\rm disc}$. From this it follows that

$$\begin{aligned}
& r = \frac{H}{\tan\theta_{\rm disc}} \\
\Rightarrow \quad & r^2 = \frac{H^2}{\tan^2\theta_{\rm disc}} \\
\Rightarrow \quad & x^2 + y^2 = \frac{H^2}{\tan^2\theta_{\rm disc}} \\
\Rightarrow \quad & (X+\rho)^2 + Y^2 = \frac{H^2}{\tan^2\theta_{\rm disc}} \\
\Rightarrow \quad & (X+\rho)^2 + (X\tan\phi)^2 = \frac{H^2}{\tan^2\theta_{\rm disc}} \\
\Rightarrow \quad & \left(1+\tan^2\phi\right)X^2 + 2\rho X + \left(\rho^2 - \frac{H^2}{\tan^2\theta_{\rm disc}}\right) = 0.
\end{aligned} \tag{B.15}$$

Therefore, the value of X and Y can be found from

$$X = \frac{-2\rho \pm \sqrt{(2\rho)^2 - 4(\sec^2\phi)\left(\rho^2 - \frac{H^2}{\tan^2\theta_{\rm disc}}\right)}}{2\sec^2\phi},$$

and

$$Y = X\tan\phi.$$

If $\phi = \frac{\pi}{2}$ or $\frac{3\pi}{2}$ then $X = 0$ and if follows from equation (B.15) that

$$Y = \left(\frac{H^2}{\tan^2\theta_{\rm disc}} - \rho^2\right)^{1/2}.$$

Again this produces two solutions for X and Y where the correct value must be chosen by determining, from ϕ, in which quadrant the correct solution must lie. The disc intercept in the

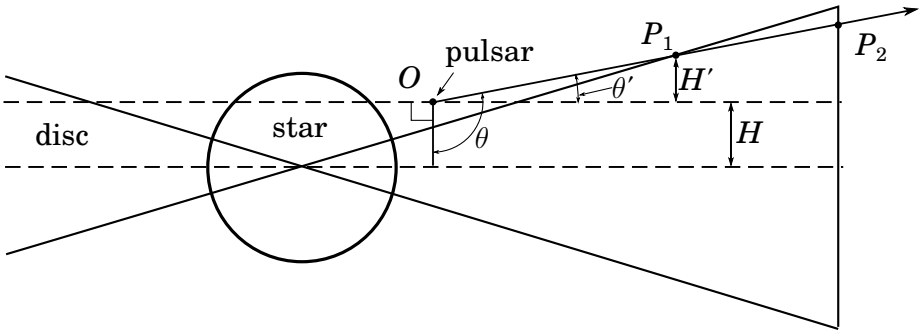

Figure B.4: Disc intercept for $\theta > 90°$.

x, y, z coordinate system is then found from

$$\begin{aligned} x_1 &= X + \rho \\ y_1 &= Y \\ z_1 &= H. \end{aligned}$$

B.2.2 Solving for P_2

The position of P_2 occurs at the edge of the disc, therefore it can be found by solving for the disc limits $x^2 + y^2 = R^2_{\rm disc}$ and the solution for x and y is identical to equations (B.7)–(B.11). Since the height of line-of-sight is always H, the z coordinate is simply $z_2 = H$.

B.3 Limiting case: $\theta > 90°$

When the polar angle $\theta > \frac{\pi}{2}$ (i.e. $\theta > 90°$) the line-of-sight follows the situation shown in Fig. B.4. Similar to section B.2, P_1 occurs when the height of the line-of-sight matches the height of the disc above the plane, and P_2 is constrained by the edge of the disc.

B.3.1 Solving for P_1

The height of a line-of-sight (h_l) above the disc mid-plane for $\theta > \pi/2$ is given by

$$h_l = H' + H,$$

where

$$H' = \sqrt{X^2 + Y^2}\tan\theta'$$

and

$$\theta' = \theta - \frac{\pi}{2},$$

has is shown in Fig. B.4. The coordinates X & Y are the disc coordinates defined in Fig. 6.8. The height of the disc at any point is (equation 6.24)

$$h_d = \sqrt{x^2 + y^2}\tan\theta_{\text{disc}},$$

and, therefore, the position of P_1 can be solved by requiring that $h_l = h_d$. Equating $h_l = h_d$ and using $Y = X\tan\phi$, gives

$$\begin{aligned} & \left(X^2+Y^2\right)^{1/2}\tan\theta' + H = \left(x^2+y^2\right)^{1/2}\tan\theta_{\text{disc}} \qquad \text{(B.16)} \\ \Rightarrow \quad & \left(X^2+Y^2\right)^{1/2}\tan\theta' + H = \left(\left[X+\rho\right]^2+Y^2\right)^{1/2}\tan\theta_{\text{disc}} \\ \Rightarrow \quad & \left[X^2+\left(X\tan\phi\right)^2\right]^{1/2}\tan\theta' + H - \left[\left(X+\rho\right)^2+\left(X\tan\phi\right)^2\right]^{1/2}\tan\theta_{\text{disc}} = 0. \end{aligned}$$

A solution for X must be found numerically by, for example, making use of the Bisection method, and requiring that the value of X lies in the correct quadrant as is determined from ϕ. The final x, y, z disc intercept coordinates for P_1 are then

$$\begin{aligned} x_1 &= X + \rho \\ y_1 &= Y = X\tan\phi \\ z_1 &= \left(X^2+Y^2\right)^{1/2}\tan\theta' + H. \end{aligned}$$

In the cases where $\phi = \frac{\pi}{2}$ or $\frac{3\pi}{2}$ then $X = 0$ and the equation (B.16) reduces to

$$\begin{aligned} & \left(Y^2\right)^{1/2}\tan\theta' + H = \left(\rho^2+Y^2\right)^{1/2}\tan\theta_{disc} \\ \Rightarrow \quad & \left(\tan^2\theta' - \tan^2\theta_{\text{disc}}\right)Y^2 + \left(2H\tan\theta'\right)Y + \left(H^2 - \rho^2\tan^2\theta_{\text{disc}}\right) = 0, \end{aligned}$$

and

$$Y = \frac{-b \pm \sqrt{b^2-4ac}}{2a},$$

where

$$\begin{aligned} a &= \tan^2\theta' - \tan^2\theta_{\text{disc}} \\ b &= 2H\tan\theta' \\ c &= (H^2 - \rho^2\tan^2\theta_{\text{disc}}). \end{aligned}$$

Based on ϕ the correct solution for Y must be chosen by requiring that the solution lies in the correct quadrant. The final x, y, z disc intercept coordinates are

$$\begin{aligned} x_1 &= \rho \\ y_1 &= Y \\ z_1 &= Y \tan\theta' + H. \end{aligned}$$

B.3.2 Solving for P_2

The solution of the x_2, y_2 coordinates is identical to the case of $\theta = 90°$ (equations B.7–B.11), while the value of z_2 is given by

$$\begin{aligned} z_2 &= H' + H \\ &= \left(X^2 + Y^2\right)^{1/2} \tan\theta' + H. \end{aligned}$$

Appendix C

Additional constraints on the AIC modelling

C.1 Averaged Lorentz rates of change due to radiative cooling

The rates of change of the Lorentz factors in section 7.2.3 are quoted here, and the reader is referred to Kirk et al. (1999) for a more detailed discussion. The change of the electron Lorentz factor due to IC scattering, averaged over scattering angles for an isotropic distribution of photons if given by (Jones, 1965)

$$\langle \dot{\gamma}_{\rm ic} \rangle = -\frac{4}{3} c N(R) \sigma_{\rm T} \gamma^2 \epsilon_0 G(\gamma, \epsilon_0),$$

where $\sigma_{\rm T}$ is the Thomson cross-section, $\epsilon_0 = 2.7 k T_{\rm eff}$ is the assumed representative energy, $N(R)$ is the photon density given, in terms of the stellar luminosity L_*, by

$$N(R) = \frac{L_*}{4\pi R^2 c h \nu_0},$$

and

$$G(\gamma, \epsilon) = \frac{9}{64 \gamma^4 \epsilon^3 \beta} \left\{ \gamma \left[f_1(\epsilon\bar{\gamma}) - f_1(\epsilon/\bar{\gamma}) \right] - \epsilon \left[f_2(\epsilon\bar{\gamma}) - f_2(\epsilon/\bar{\gamma}) \right] \right\},$$

where

$$\begin{aligned}
\bar{\gamma} &= \gamma + \left(\gamma^2 - 1\right)^{1/2} \\
f_1(z) &= (z + 6 + 3/z)\ln(1+2z) - (22z^3/3 + 24z^2 + 18z + 4)(1+2z)^{-2} \\
&\quad -2 + 2\mathrm{Li}_2(-2z) \\
f_2(z) &= (z + 31/6 + 5/z_3/2z^2)\ln(1+2z) - \\
&\quad (22z^3/3 + 28z^2 + 103z/3 + 17 + 3/z)(1+2z)^{-2} - 2 + 2\mathrm{Li}_2(-2z).
\end{aligned}$$

Here Li_2 is the Eulerian dilogarithm, defined as

$$\mathrm{Li}_2(x) = \int_x^0 \frac{\ln(1-t)}{t}\, dt.$$

The total power that is radiated by a synchrotron emitting electron is (e.g. Lang, 1974, p. 29)

$$P_{\mathrm{sync}} = \frac{2}{3}\frac{e^4}{m^2c^3}\beta^2\gamma^2 H^2 \sin^2\psi,$$

where e is the charge of an electron, and $\beta = v/c$. Assuming the electron is moving near the speed of light ($\beta \approx 1$) and averaging over the pitch angle ($\langle \sin^2\psi \rangle = 2/3$) the average power lost per electron is

$$\left\langle \frac{dE}{dt} \right\rangle = -\frac{4}{3} c\sigma_{\mathrm{T}} \frac{B^2}{8\pi},$$

or, since $E = \gamma mc^2$, the rate of change in the Lorentz factor is

$$\langle \dot{\gamma} \rangle = -\frac{4}{3}\frac{\sigma_{\mathrm{T}}}{mc}\frac{B^2}{8\pi}.$$

Kirk et al. (1999) defines the parameters b as the square root of the ratio between the synchrotron and IC power. Since $P_{\mathrm{sync}}/P_{\mathrm{IC}} = U_B/U_{\mathrm{ph}}$, where U_B and U_{ph} are the magnetic and photon energy density respectively (e.g. Rybicki and Lightman, 2004, pp. 199–202), the parameter b can be defined as

$$b \equiv \sqrt{\frac{B/8\pi}{h\nu_0 n_{\mathrm{ph}}}},$$

where ν_0 is the frequency of the photon and it is assumed that the photon distribution can be described by a mono-energetic energy ϵ_0. Therefore the average rate of change of the Lorentz factor due to synchrotron radiation can be written in the form (Kirk et al., 1999)

$$\langle \dot{\gamma}_S \rangle = -\frac{4}{3} c n_{\mathrm{ph}} \sigma_{\mathrm{T}} \gamma^2 \frac{\epsilon}{mc^2} b^2. \tag{C.1}$$

It should be noted that equation (C.1) has a slightly different form in Kirk et al. (1999) due to the different definitions of the variables.

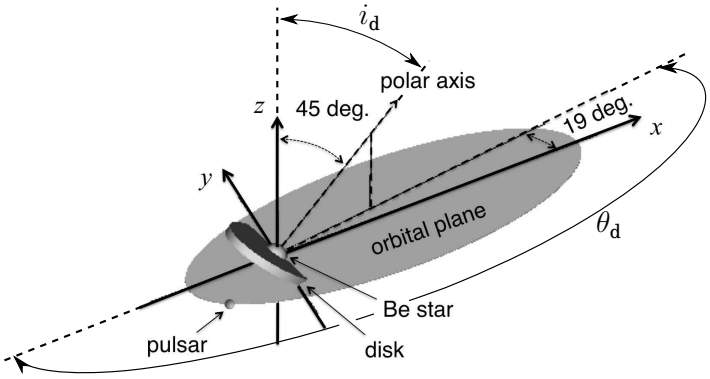

Figure C.1: The orientation of the circumstellar disc and orbital plane presented by Okazaki et al. (2011). The figure has been adapted to show the disc orientation angles $i_{\rm d}$ and $\theta_{\rm d}$ considered in this study (figure adapted from Okazaki et al., 2011).

C.2 The disc system $K^{\rm d}$: determining the value of Θ

All the coordinates in the disc system, $K^{\rm d}$, depend on the value of binary separation, r, and the angle Θ (Fig. 7.7). The binary separation is determined by the solution to the two body problem (equation 7.7), while the value of Θ must be found. Since the angle Θ lies between the unit vectors $\hat{\mathbf{e}}_H$ and $\hat{\mathbf{e}}_*$, if the unit vector $\hat{\mathbf{e}}_H$ can be defined in the orbital system, K, discussed in section 7.4.1, the angle can be determined from,

$$\hat{\mathbf{e}}_* \cdot \hat{\mathbf{e}}_H = \cos\Theta,$$

where $\hat{\mathbf{e}}_*$ is defined by equation (7.10). The unit vector $\hat{\mathbf{e}}_H$ is defined in K by the polar angle, i_H and the azimuthal angle θ_H.

In order to determine $\hat{\mathbf{e}}_H$ the position of the disc relative to the orbital plane is defined by the angles $i_{\rm d}$ and $\theta_{\rm d}$. The angle $i_{\rm d}$ is defined to be the angle between the normal to the disc and the normal to the orbital plane. In other words, if $i_{\rm d} = 0°$, the disc lies in the orbital plane, while if $i_{\rm d} = 90°$ the disc mid-plane is at 90° to the orbital plane. The angle $\theta_{\rm d}$ defines the azimuthal direction of the normal to the disc, relative to the semi-major axis of the orbital plane. The direction $\theta_{\rm d} = 0°$ is defined to be towards periastron. This disc orientation, and the corresponding angles, are chosen based on the observed or presumed disc orientation, and the values of $i_{\rm d}$ and $\theta_{\rm d}$ remain constant. In order to better illustrate these angles, Fig. C.1 shows the disc orientation consider in Okazaki et al. (2011) along with the appropriate angles. For this orientation, $i_{\rm d} = 45°$ and $\theta_{\rm d} = (180 + 19)° = 199°$.

As the pulsar orbits around the Be star/disc, the relative orientation of the disc changes, and therefore the values of i_H and θ_H (which define the unit vector $\hat{\mathbf{e}}_H$) must be calculated depending on the orientation. Fig. C.2 shows two situations, A and B, where the pulsar is "above" and "below" the disc respectively which changes the value of i_H. Fig. C.3 illustrates the relevant

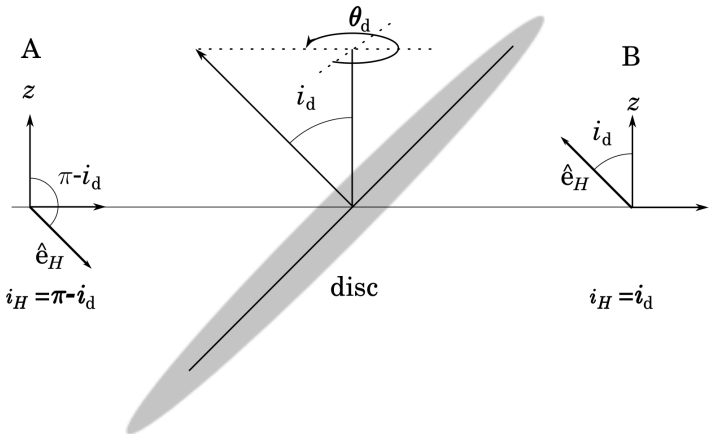

Figure C.2: Sketch of the possible pulsar/disc orientations indicating situation A where the pulsar is above the disc ($i_H = \pi - i_d$), and situation B where the pulsar is below the disc ($i_H = i_d$).

azimuthal angles for the disc position, for various disc and pulsar positions. Therefore, depending on the orientation of the disc (i_d & θ_d) and position of the pulsar (defined by the true anomaly, f) and values of i_H and θ_H can be determined. The true anomaly, f, found from equation 7.9, lies between $-\pi$ and π, but it is easier to determine whether the pulsar is above or below the disc in terms of the variable F such that $0 \leq F \leq 2\pi$; i.e. if $f \geq 0$, $F = f$, but if $f < 0$, $F = 2\pi + f$.

As can be seen from Figs. C.2 & C.3, if the pulsar and disc are orientated such that

$$\pi/2 < |F - \theta_\mathrm{d}| < 3\pi/2$$

the pulsar is below the disc (case B in Fig. C.2) and

$$\begin{aligned} i_H &= i_\mathrm{d} \\ \theta_H &= \begin{cases} \theta_\mathrm{d} + \pi & \text{for } \theta_\mathrm{d} < \pi \\ \theta_\mathrm{d} - \pi & \text{for } \theta_\mathrm{d} > \pi, \end{cases} \end{aligned}$$

otherwise the pulsar is above the disc (case A) and

$$\begin{aligned} i_H &= \pi - i_\mathrm{d} \\ \theta_H &= \theta_\mathrm{d}. \end{aligned}$$

Therefore, defining the unit vectors in K as (Fig. C.4)

$$\hat{\mathbf{e}}_* = \begin{pmatrix} \cos f \\ \sin f \\ 0 \end{pmatrix} \quad \text{and} \quad \hat{\mathbf{e}}_H = \begin{pmatrix} \sin i_H \cos \theta_H \\ \sin i_H \sin \theta_H \\ \cos i_H \end{pmatrix}, \tag{C.2}$$

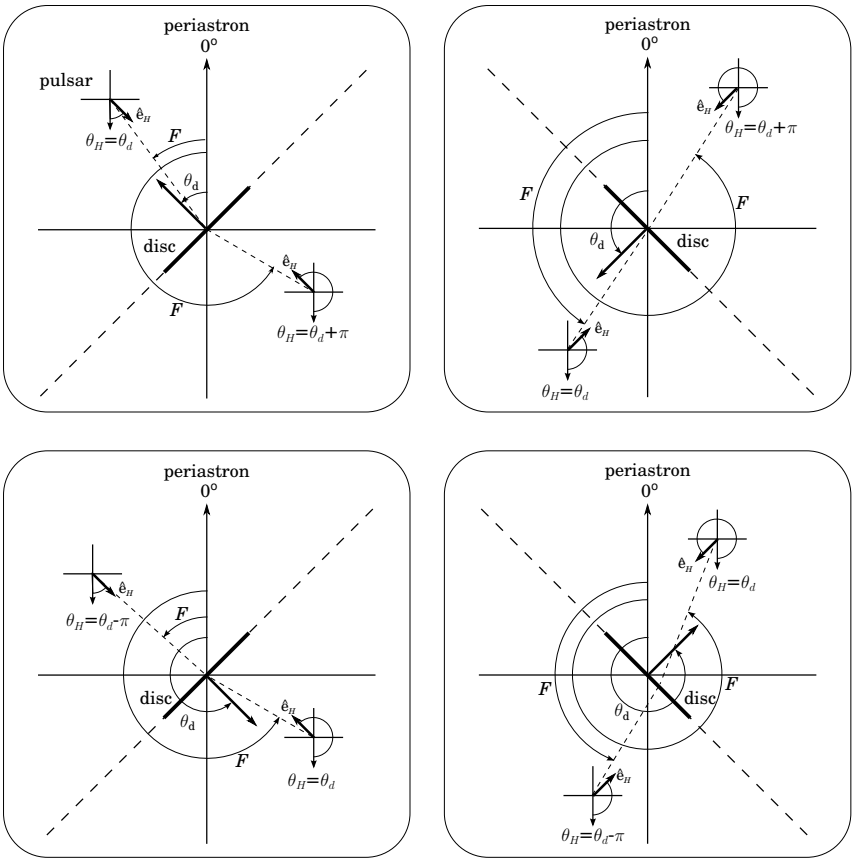

Figure C.3: Relative directions of $\theta_{\rm d}$ and θ_H shown in the orbital plane for different disc orientations and pulsar positions. Also shown in the figure is the relative direction of θ_H from the pulsar's position in the K coordinate system, centred on the pulsar position and the angle F. Only the azimuthal angles are shown.

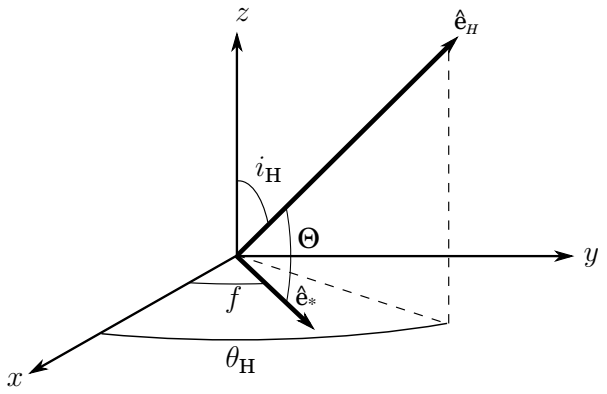

Figure C.4: Relative unit vectors for the disc coordinate system (K^{d}) shown in the orbital coordinate system (K).

the angle Θ can be calculated from

$$\hat{\mathbf{e}}_* \cdot \hat{\mathbf{e}}_H = \cos\Theta = \sin i_H \cos(f - \theta_H).$$

Since $\sin(\pi - i_{\mathrm{d}}) = \sin(i_{\mathrm{d}})$, $\sin i_H = \sin i_{\mathrm{d}}$ for all disc orientations and the solution to the angle Θ is given by

$$\Theta = \cos^{-1}\left[\sin i_{\mathrm{d}} \cos(f - \theta_H)\right].$$

C.3 The disc system K^{d}: determining the direction of $\hat{\mathbf{e}}_{\mathrm{obs}}$

The polar angle of $\hat{\mathbf{e}}^{\mathrm{d}}_{\mathrm{obs}}$ in K^{d} is defined as φ, which is the angle between $\hat{\mathbf{e}}_H$ and $\hat{\mathbf{e}}_{\mathrm{obs}}$ in K (Figs. 7.7 & C.5). In the K system,

$$\hat{\mathbf{e}}_{\mathrm{obs}} = \begin{pmatrix} \sin i \cos\theta_{\mathrm{obs}} \\ \sin i \sin\theta_{\mathrm{obs}} \\ \cos i \end{pmatrix},$$

and therefore using the definition of $\hat{\mathbf{e}}_H$ given in equation (C.2), it can be shown that

$$\cos\varphi = \hat{\mathbf{e}}_{\mathrm{obs}} \cdot \hat{\mathbf{e}}_H = \sin i \sin i_H \cos\left(\theta_{\mathrm{obs}} - \theta_H\right) + \cos i \cos i_H.$$

This allows the polar angle of $\hat{\mathbf{e}}^{\mathrm{d}}_{\mathrm{obs}}$, φ, to be determined in K^{d} (Fig. 7.7), but the value of the azimuthal angle, ϕ, must still be found. In K^{d}, the unit vectors $\hat{\mathbf{e}}^{\mathrm{d}}_*$ and $\hat{\mathbf{e}}^{\mathrm{d}}_{\mathrm{obs}}$ can be defined by (Fig. 7.7)

$$\hat{\mathbf{e}}^{\mathrm{d}}_* = \begin{pmatrix} \sin\Theta\cos\pi \\ \sin\Theta\sin\pi \\ \cos\Theta \end{pmatrix} = \begin{pmatrix} -\sin\Theta \\ 0 \\ \cos\Theta \end{pmatrix} \quad \text{and} \quad \hat{\mathbf{e}}^{\mathrm{d}}_{\mathrm{obs}} = \begin{pmatrix} \sin\varphi\cos\phi \\ \sin\varphi\sin\phi \\ \cos\varphi \end{pmatrix},$$

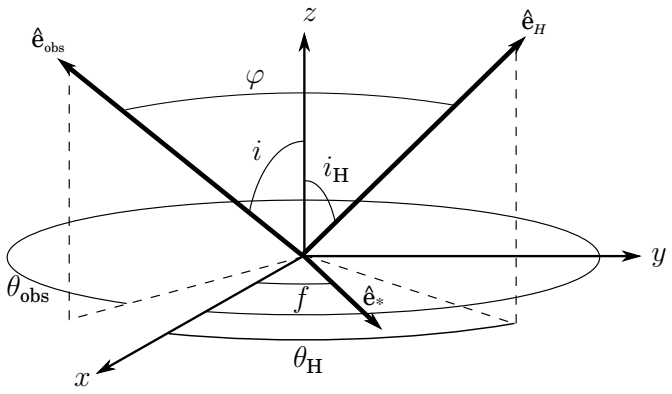

Figure C.5: Relative unit vectors for the disc coordinate system (K^{d}) shown in the orbital coordinate system (K).

where ϕ is the unknown azimuthal angle of $\hat{\mathbf{e}}^{\mathrm{d}}_{\mathrm{obs}}$, and therefore

$$\hat{\mathbf{e}}^{\mathrm{d}}_{*} \cdot \hat{\mathbf{e}}^{\mathrm{d}}_{\mathrm{obs}} = -\sin\Theta\sin\varphi\cos\phi + \cos\Theta\cos\varphi. \tag{C.3}$$

As shown in equation (7.12), in K, the angle between $\hat{\mathbf{e}}_{\mathrm{obs}}$ and $\hat{\mathbf{e}}_{*}$ is given by

$$\hat{\mathbf{e}}_{*} \cdot \hat{\mathbf{e}}_{\mathrm{obs}} = \cos\Psi' = \sin i\cos(f - \theta_{\mathrm{obs}}), \tag{C.4}$$

and, therefore, since $\hat{\mathbf{e}}_{*} \cdot \hat{\mathbf{e}}_{\mathrm{obs}}$ must be the same in K and K^{d}, by equating equations (C.3) and (C.4) it is possible to solve for the azimuthal angle, ϕ, which is given by (equation 7.15)

$$\phi = \cos^{-1}\left(\frac{\cos\Theta\cos\varphi - \cos\Psi'}{\sin\Theta\sin\varphi}\right),$$

or

$$\phi = \cos^{-1}\left(\frac{\cos\Theta\cos\varphi - \sin i\cos(f - \theta_{\mathrm{obs}})}{\sin\Theta\sin\varphi}\right).$$

While this solution for ϕ is not unique, since $\cos\phi = \cos(2\pi \pm \phi)$, the two possible solutions are symmetric and will produce the same scattering rate. Therefore, using the solution for φ and ϕ the direction of $\hat{\mathbf{e}}^{\mathrm{d}}_{\mathrm{obs}}$ can be defined in K^{d}.

C.4 The disc system K^{d}: Limits on the solid angle

This section expands the formulae given by equations (7.17)–(7.19) to calculate the solid angle over a disc with a finite half-opening angle θ_{disc}. Two conditions must be considered for $H > h_{\mathrm{disc}}$ and $H < h_{\mathrm{disc}}$ respectively, where H is the vertical height from the disc mid-plane and $h_{\mathrm{disc}} = R_{\mathrm{disc}}\tan\theta_{\mathrm{disc}}$ as is shown in Figs. C.6 and C.7 respectively.

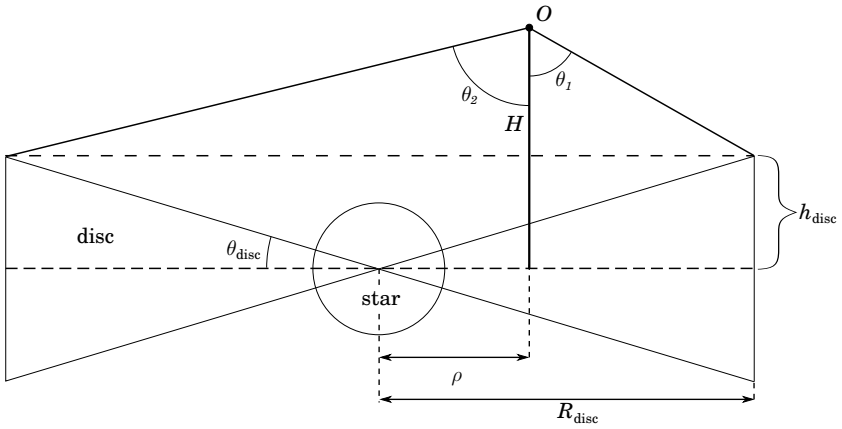

Figure C.6: Be star and disc with half-opening angle $\theta_{\rm disc}$, for $H > h_{\rm disc}$.

Condition $H > h_{\rm disc}$

For the condition $H > h_{\rm disc}$, it can be seen from Fig. C.6 that the new limits on the polar angles are given by

$$\theta_1 = \tan^{-1}\left(\left|\frac{\rho - R_{\rm disc}}{H - h_{\rm disc}}\right|\right), \tag{C.5}$$

$$\theta_2 = \tan^{-1}\left(\frac{R_{\rm disc} + \rho}{|H - h_{\rm disc}|}\right). \tag{C.6}$$

The limit on the azimuthal angles takes the same form as equation (7.19) where the "height" of the disc must be given by $H - h_{\rm disc}$, and therefore by defining

$$\tau_\phi(\theta) = \frac{R_{\rm disc}^2 - \rho^2 - (H - h_{\rm disc})^2 \tan^2\theta}{2\rho(|H - h_{\rm disc}|)\tan\theta},$$

the azimuthal angle is limited to

$$\cos^{-1}(\tau_\phi) \leq \phi \leq 2\pi - \cos^{-1}(\tau_\phi). \tag{C.7}$$

Condition $H < h_{\rm disc}$

For the condition $H < h_{\rm disc}$, it can be seen from Fig. C.7 that the values of the polar limits are given by

$$\theta_1 = \frac{\pi}{2} + \tan^{-1}\left(\frac{h_{\rm disc} - H}{R_{\rm disc} - \rho}\right) \tag{C.8}$$

$$\theta_2 = \frac{\pi}{2} + \tan^{-1}\left(\frac{h_{\rm disc} - H}{R_{\rm disc} + \rho}\right), \tag{C.9}$$

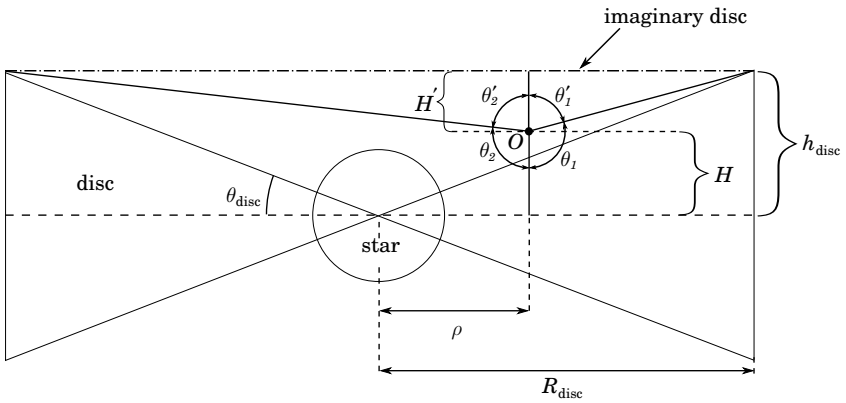

Figure C.7: Be star and disc with half-opening angle $\theta_{\rm disc}$, for $H < h_{\rm disc}$.

where now $\theta_1 > \theta_2$ and the integration is over the polar angle $0 \rightarrow \theta_1$. The solid angle is then given by the sum of $\Omega_1 + \Omega_2$ where

$$\begin{aligned} \Omega_1 &= \int_0^{2\pi} \int_0^{\theta_2} \sin\theta \, d\theta d\phi, \\ \Omega_2 &= \int_{\theta_2}^{\theta_1} \int_{\phi} \sin\theta \, d\phi d\theta. \end{aligned}$$

At polar angles $\theta < \theta_2$, there is no geometric limit on the azimuthal angle (i.e. $\phi \in [0, 2\pi]$), but above θ_2 a new limit must be imposed on the azimuthal angle. This is determined by considering an imaginary (flat) disc which lies above the Be disc and has the disc parameters (Fig. C.7)

$$\begin{aligned} \rho' &= \rho, \\ R'_{\rm disc} &= R_{\rm disc}, \\ H' &= h_{\rm disc} - H, \\ \theta' &= \pi - \theta \quad \text{and} \\ \phi' &= 2\pi - \phi. \end{aligned}$$

Any point (X', Y') on the imaginary disc is calculated by

$$\begin{aligned} X' &= H' \tan\theta' \cos\phi', \\ Y' &= H' \tan\theta' \sin\phi', \end{aligned}$$

and the circular disc constraint

$$(X' + \rho')^2 + (Y')^2 > (R'_{\rm disc})^2$$

can be applied, where all allowed point must now lie outside of a circle with radius $R_{\rm disc}$ and not within it. By substituting in the values for X' and Y', it can be shown that the limit on the azimuthal angle is determined by

$$\cos\phi' \geq \frac{R_{\rm disc}^2 - \rho'^2 - H'^2\tan^2\theta'}{2\rho' H'\tan\theta'},$$

or if written in the standard disc parameters, the limit is determined by

$$\cos\phi' \geq \cos\tau_\phi(\theta) = \cos\left(\frac{R_{\rm disc}^2 - \rho^2 - (h_{\rm disc}-H)^2\tan^2(\pi-\theta)}{2\rho(h_{\rm disc}-H)\tan(\pi-\theta)}\right).$$

The limits on ϕ' are therefore

$$0 \leq \phi' \leq \cos^{-1}(\tau_\phi) \quad \text{and} \quad 2\pi - \cos^{-1}(\tau_\phi) \leq \phi' \leq 2\pi,$$

which can be converted to the limits on ϕ as

$$0 \leq \phi \leq \cos^{-1}(\tau_\phi) \quad \text{and} \quad 2\pi - \cos^{-1}(\tau_\phi) \leq \phi \leq 2\pi, \tag{C.10}$$

since this results in the integration over the same. The solid angle over the circumstellar disc can therefore be found from equations (7.17) & (7.18) by determining ρ and H, and applying the correct limits for the angles (θ, ϕ), given by equations (C.5)–(C.10).

Condition $\Theta = 0$

The exception to this method is the limiting case of $\Theta = 0$, i.e. the disc is viewed face-on. In this case the solid angle reduces to

$$\Omega = 2\pi\int_0^{\alpha_{\rm disc}} \sin\theta\, d\theta,$$

where integration over the azimuthal angle is for $\phi \in [0, 2\pi]$, while the polar angle is defined by the radius of the disc. If the disc has a half-opening angle, $\theta_{\rm disc}$, the polar limit is determined by the line joining point O (the centre of the pulsar) with point P (the edge of the circumstellar disc) as shown in Fig. C.8. In the figure the length $PQ = R_{\rm disc}$ while the height $OQ = H - h_{\rm disc} = r - h_{\rm disc}$, where r is the binary separation. The limit on the polar angle is therefore

$$\begin{aligned}\alpha_{\rm disc} &= \tan^{-1}\left(\frac{PQ}{OQ}\right) \\ &= \tan^{-1}\left(\frac{R_{\rm disc}}{r - h_{\rm disc}}\right).\end{aligned}$$

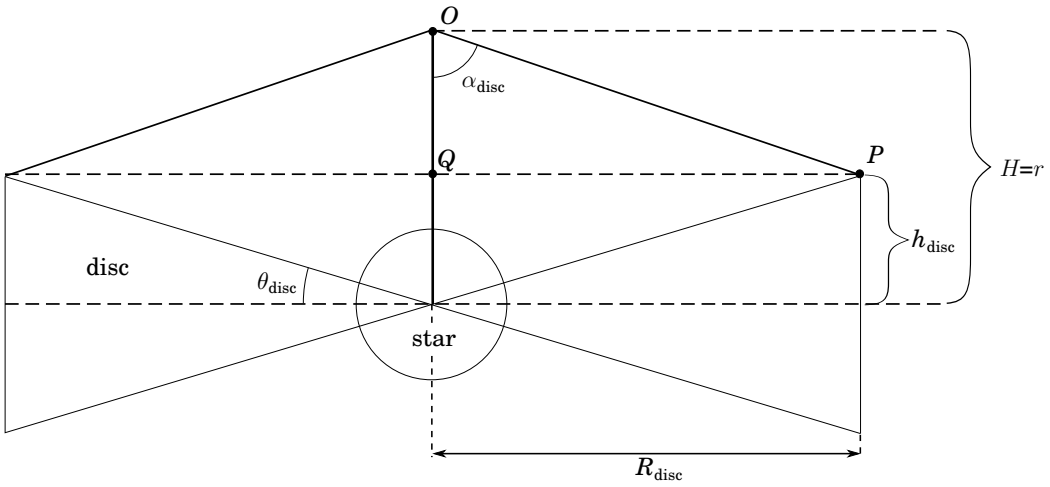

Figure C.8: Limit on polar angle for a disc of radius $R_{\rm disc}$ with a half-opening angle $\theta_{\rm disc}$ when $\Theta = 0$.

C.5 Constraints on the origin of the photons

This section will discuss how to determine, during the integration over the solid angle, whether a line-of-sight (i.e. the direction from which a photon arrives) intercepts with the star or the circumstellar disc. This will determine whether a photons originates from either the star or disc. The constraints are determined using the disc coordinate system, $K^{\rm d}$, shown in Fig. 7.7. When calculating the IC stellar contribution using the $K^{\rm s}$ coordinate system, the constraints can be determined by first converting the angles in $K^{\rm s}$ to those in the $K^{\rm d}$, as outlined in section C.6, and applying the same constraints discussed here.

Fig. C.9 shows the basic constraints that must be determined. In the figure the star, with radius R_*, is surrounded by a circumstellar disc with a half-opening angle $\theta_{\rm disc}$. Point O is the centre of the pulsar which lies a vertical height H above the mid-plane of the disc and a horizontal distance ρ from the centre of the disc (star) at point S. For certain lines-of-sight from the pulsar towards the star and disc, the star will obscured the disc and vice versa. Based on whether the line-of-sight intercepts the star or disc, the appropriate photon distribution must be chosen. The constraints are determined in terms of the polar angle, θ, and from the corresponding azimuthal angles ϕ. In the figure, for all lines-of-sight with angles less than θ_c and greater than $\Theta + \alpha_*$, (i.e. $\theta < \theta_c$ or $\theta > \Theta + \alpha_*$) photons will originate from the disc for all azimuthal angles. However, between these two angles (i.e. $\theta_{\rm c} \leq \theta \leq \Theta + \alpha_*$) it must be determined from the azimuthal angle whether the line-of-sight intercepts the star or disc.

Within this region there are two constraints that must be applied depending firstly on whether the disc is obscuring part of the star and secondly on the size of the star. The first constraint, which lies between $\theta_c < \theta < \theta_f$ in the figure, forms where the circumstellar disc forms a "ring" around the star.[i] For lines-of-sight which fall within this ring, the photons originate from the star,

[i]The star is actually obscured from angles slightly less than θ_c as shown, but the constraint only needs to be

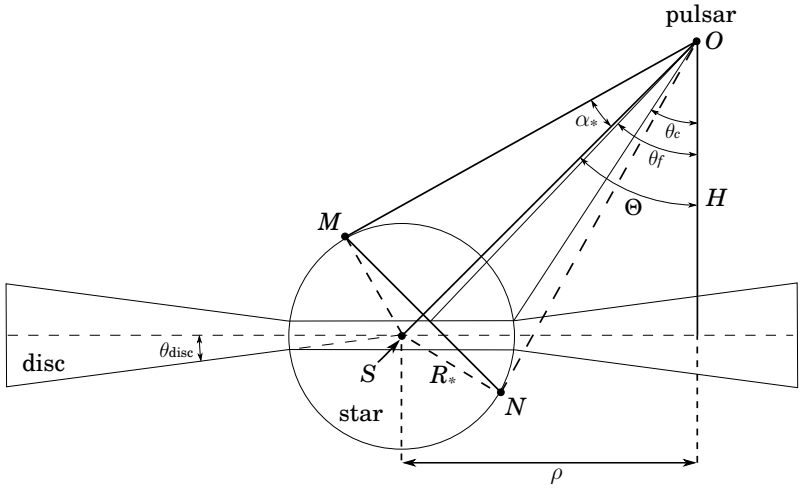

Figure C.9: Sketch of the angles that need to be calculated in order to determine whether a photon arrives from the star or the circumstellar disc.

while outside of the ring the photons arrive from the disc. This will be called the ring constraint and the appropriate azimuthal angles will be calculated using the same method that was used to determined solid angle over a disc (see equation 7.16). The second constraint is dependent on the maximum size of the star and is determined by the polar angle $\alpha_* = \sin^{-1}(R_*/r)$, as is shown in the K^{s} coordinate system (Fig. 7.6, p. 150). In other words, if a line-of-sight has an angle less than α_* relative to the line OS in Fig. C.9, it will intercept the star if it does not first intercept the disc. This will be referred to as the edge constraint and must be considered for angles $\theta_f < \theta < \Theta + \alpha_*$, in Fig. C.9.

The constraints need to be considered in two main cases, namely $\rho > R_*$ and $\rho \leq R_*$. These two scenarios, along with the appropriate angles and derivations are presented below.

C.5.1 Case: $\rho > R_*$

Fig. C.10 shows the star and disc with the associated angles, for the scenario of $\rho > R_*$; this is an expanded version of Fig. C.9 showing all the required angles to calculate the constraints on the line-of-sight.

considered within the given limits.

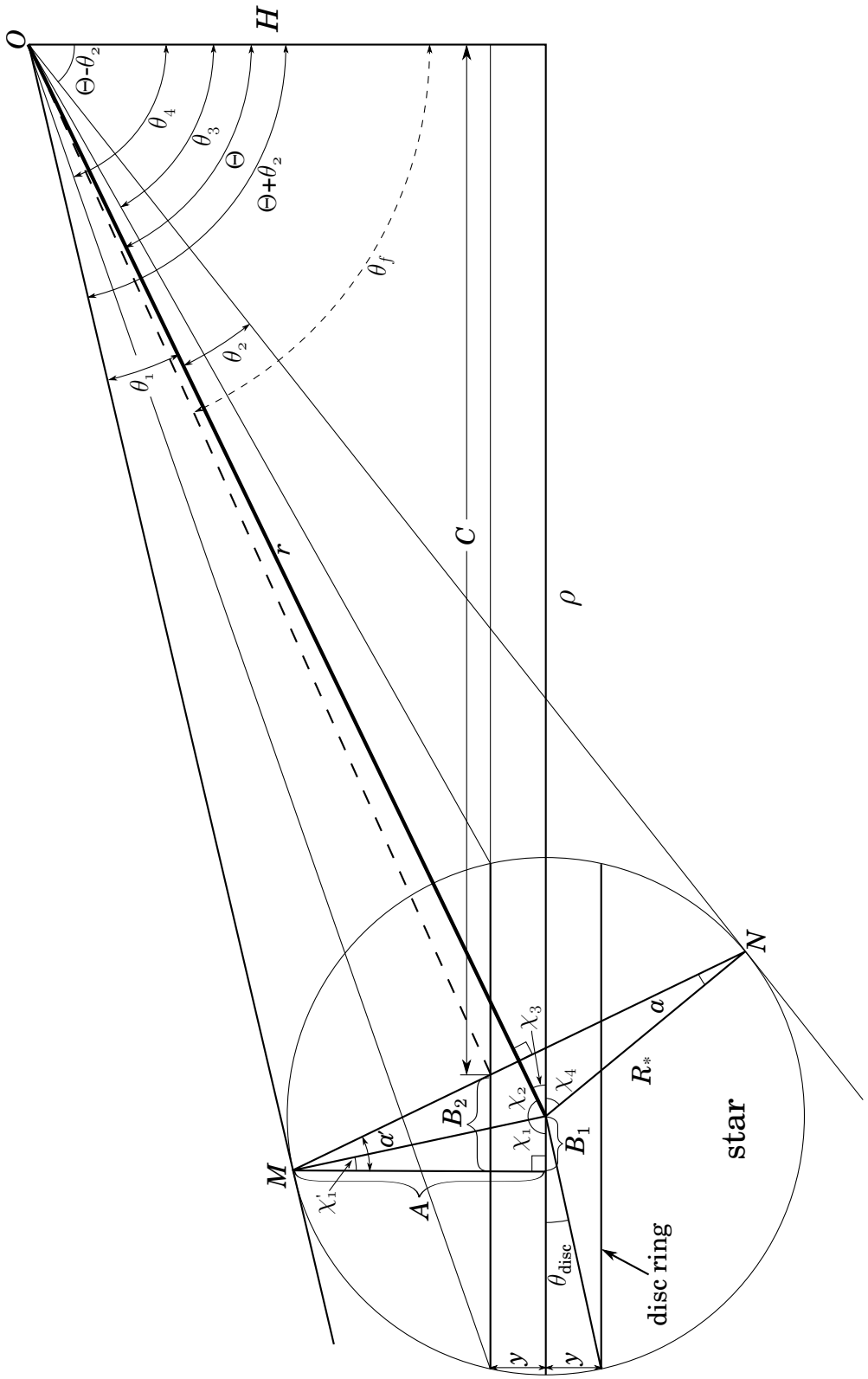

Figure C.10: Various angles needed to constrain the disc angle for $\rho > R_*$.

Calculation of the angles

The various angles in the figure are calculated as follows. The polar angles around point O are given by

$$\begin{aligned}
\theta_1 &= \theta_2 = \sin^{-1}\left(\frac{R_*}{r}\right), \\
\theta_3 &= \tan^{-1}\left(\frac{\rho - x}{H - y}\right), \quad \text{and} \\
\theta_4 &= \tan^{-1}\left(\frac{\rho + x}{H - y}\right),
\end{aligned}$$

where

$$\begin{aligned}
y &= R_* \sin\theta_{\rm disc}, \\
x &= R_* \cos\theta_{\rm disc},
\end{aligned} \tag{C.11}$$

where y is the height of the disc at the edge of the star. The angles around the centre of the star are calculated by

$$\begin{aligned}
\chi_3 &= \sin^{-1}\left(\frac{H}{r}\right), \\
\chi_2 &= \cos^{-1}\left(\frac{R_*}{r}\right) = (\chi_3 + \chi_4), \quad \text{and} \\
\chi_1 &= \pi - \chi_2 - \chi_3.
\end{aligned}$$

The remaining lengths and angles are calculated by

$$\begin{aligned}
a &= \frac{\pi}{2} - \chi_2 \\
B_1 &= R_* \cos\chi_1 \\
A &= R_* \sin\chi_1 \\
\chi_1' &= \frac{\pi}{2} - \chi_1 \\
a' &= \chi_1' + a \\
B_2 &= (A - y)\tan(a').
\end{aligned} \tag{C.12}$$

Therefore

$$\theta_f = \tan^{-1}\left(\frac{C}{H - y}\right),$$

where

$$C = \rho + B_1 - B_2.$$

Any line-of-sight that intercepts the star below y (equation C.11) is obscured by the circum-

stellar disc. Two separate conditions can be considered for the cases of $y \geq A$ and $y < A$, where A is defined in the figure (equation C.12).

Condition $y \geq A$

If $y > A$, the star is obscured by the disc at all polar angles and therefore only the ring constraint needs to be applied for angles between $\theta_3 < \theta < \theta_4$. This can be done by applying the constraint on ϕ which is given by equation (7.19) for a disc radius of $x = R_* \cos\theta_{\rm disc}$, a horizontal displacement ρ and a vertical height $H - y$ above the disc mid-plane. In other words, for polar angles that lie between $\theta_3 < \theta < \theta_4$ it is necessary to determine whether the azimuthal angles line within $\cos^{-1}(\tau_\phi) < \phi < 2\pi - \cos^{-1}(\tau_\phi)$, where τ_ϕ is the azimuthal limit, and is given by

$$\tau_\phi(\theta) = \frac{x^2 - \rho^2 - (H-y)^2 \tan^2\theta}{2\rho(H-y)\tan\theta}. \tag{C.13}$$

If the azimuthal angle is within this limit the line-of-sight intercepts the star, while if it is not, it intercepts the circumstellar disc.

Condition $y < A$

If $y < A$ the star is only partially obscured by the disc and it is necessary to consider both the limit due to the edge of the star and ring limit created by the disc. If the star was unobstructed by the disc, the polar limits would be define by the points M and N (Fig. C.10) and the surface of the star visible from point O point would lie in front of the line MN. The line-of-sight which intercepts with the point where the line MN intersects with the ring of the disc, is define to have a polar angle θ_f (Fig. C.9 & C.10). Therefore between $\theta_3 < \theta < \theta_f$ the limits on the azimuthal angle must be found using the same disc constraint discussed above (i.e. $\cos^{-1}(\tau_\phi) < \phi < 2\pi - \cos^{-1}(\tau_\phi)$), while between $\theta_f < \theta < (\Theta + \theta_1)$ the limits depend on whether the line-of-sight is beyond the edge of the stellar sphere.

In order to find the limits of the visible sphere surface in the $K^{\rm d}$ coordinate system, a change of coordinate system can be considered. A new coordinate system K'' can be created by rotating around the Y-axis in $K^{\rm d}$ by the angle Θ such that the polar angle in K'' points towards the centre of the star, similar to Fig. 7.6. The translation to the z'' coordinate in K'' is then made by

$$z'' = Z\cos\Theta - X\cos\Theta,$$

where X and Z are in the $K^{\rm d}$ frame. By making use of the standard conversion to polar coordinates

$$\begin{aligned} Z &= s\cos\theta \\ X &= s\sin\theta\cos\phi, \\ z'' &= s''\cos\alpha, \end{aligned}$$

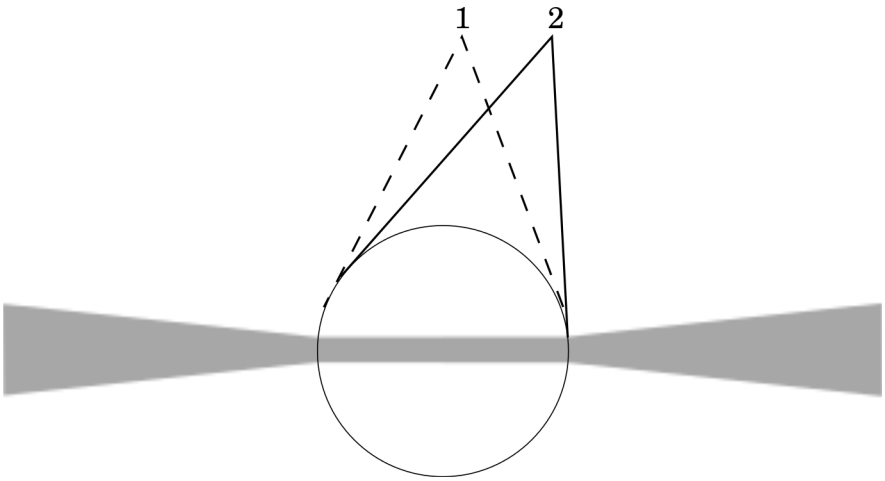

Figure C.11: Sketch of possible situations for $\rho \leq R_*$.

where θ and ϕ are the angles in $K^{\rm d}$, and $s = s''$ is the radial distance, it can be shown that the polar angle in K'' is calculated as

$$\cos\alpha = \cos\theta\cos\Theta - \sin\theta\cos\phi\sin\Theta. \tag{C.14}$$

Here the angle α is measured relevant to the line joining the centre of the star and the centre of the electron cloud and is equivalent to the polar angle in Fig. 7.6. The edge of the star then occurs at $\alpha = \alpha_* = \sin^{-1}(R_*/r)$ and, therefore, within the limit $\theta_f < \theta < (\Theta + \theta_1)$, if $\alpha \leq \alpha_*$ the line-of-sight intercepts the star, while if $\alpha > \alpha_*$ it intercepts the disc.

C.5.2 Case: $\rho \leq R_*$

For the second situation of $\rho \leq R_*$ it is possible that the star is not obscured by the disc. Consider the sketch in Fig. C.11 which shows the two possible situations; in situation 1 (dashed line) the star is not obscured by the disc and the limits depend on the edge of the star, while in situation 2 (solid line) the star is partly obscured by the disc on the right hand side. The full diagram of situation 1 is shown in Fig. C.12 and the full diagram for situation 2 is shown in Figs. C.13 & C.14 for two slightly different geometries. If $\rho \leq R_*$ additional constraints are required which were not applied to $\rho > R_*$, since the lines-of-sight with the same polar angle may require different constraints depending on the azimuthal angles.

Calculation of angles

The relevant angles in Figs. C.12, C.13 & C.14 are calculate as follows.

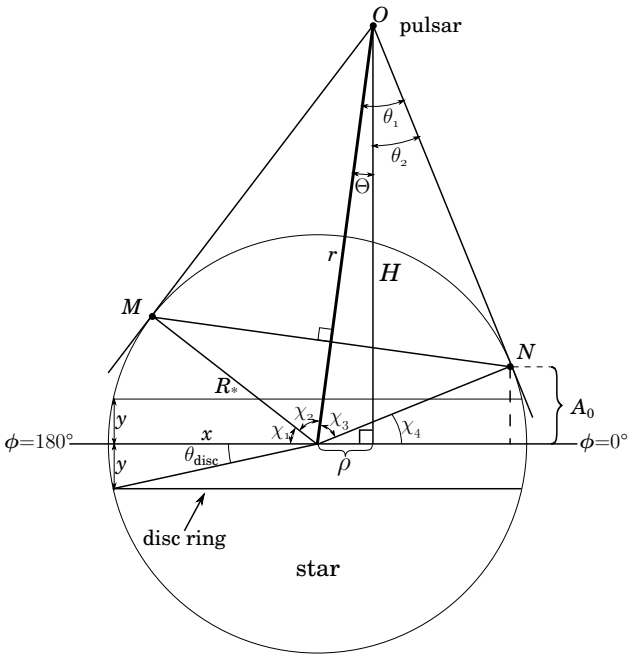

Figure C.12: Situation 1 in Fig C.11 with no obstruction of the star in the limit $\rho \leq R_*$. The various angles needed to calculate the limits are also shown.

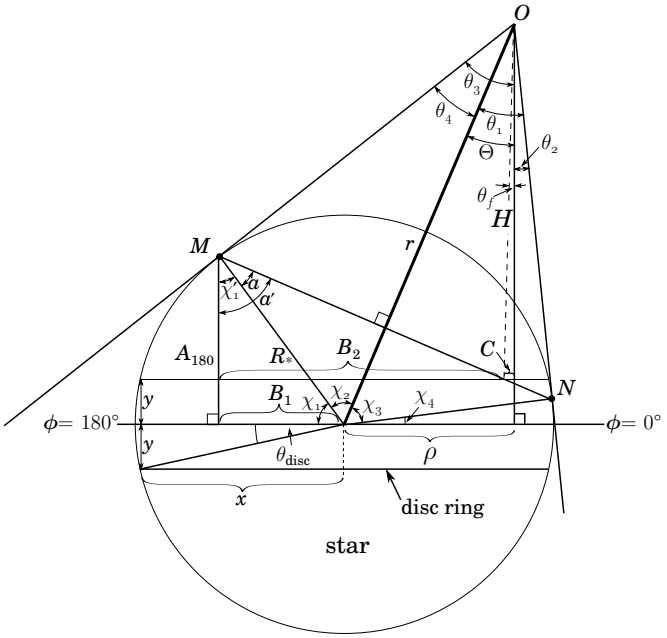

Figure C.13: Situation 2 in Fig C.11 with obstruction of the star in the limit $\rho \leq R_*$ with $B_2 < (B_1 + \rho)$. The various angles needed to calculate the limits are also shown.

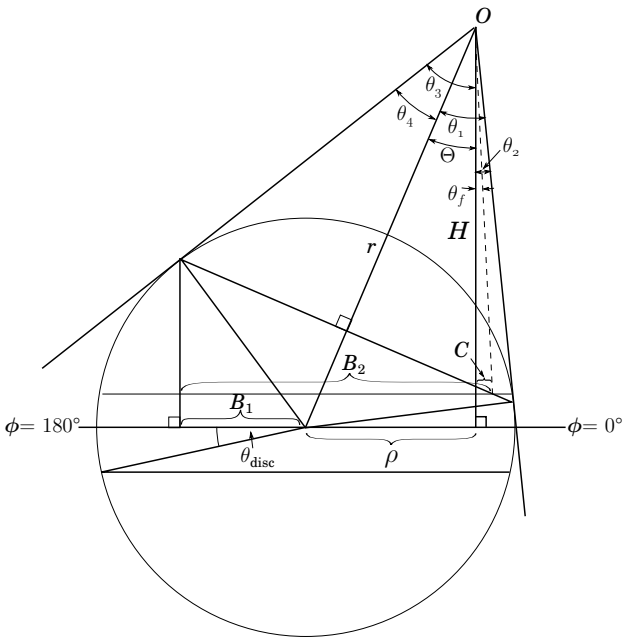

Figure C.14: Same as Fig. C.13, but with $B_2 > (B_1 + \rho)$. Only the relevant angles are shown.

In Fig. C.12 the polar angles around point O are given by

$$\theta_1 = \sin^{-1}\left(\frac{R_*}{r}\right)$$

and

$$\theta_2 = \theta_1 - \Theta,$$

where Θ is the angle between $\hat{\mathbf{e}}_*$ and $\hat{\mathbf{e}}_H$. The angles around the centre of the star are calculated by

$$\begin{aligned} \chi_2 &= \chi_3 = \cos^{-1}\left(\frac{R_*}{r}\right) \\ (\chi_3 + \chi_4) &= \sin^{-1}\left(\frac{H}{r}\right) \\ \chi_1 &= \pi - \chi_2 - (\chi_3 + \chi_4) \\ \chi_4 &= \pi - \chi_1 - 2\chi_2, \end{aligned}$$

where $\chi_2 = \chi_3$ due to the similarity of the triangles. Using χ_4 it is now possible to calculate the height A_0 defined in Fig. C.12 as

$$A_0 = R_* \sin\chi_4.$$

In Figs. C.13 & C.14 the polar angles around point O are defined as

$$\begin{aligned}\theta_1 &= \theta_4 = \sin^{-1}\left(\frac{R_*}{r}\right)\\ \theta_2 &= \theta_1 - \Theta,\end{aligned}$$

where

$$\begin{aligned}x &= R_* \cos\theta_{\rm disc}\\ y &= R_* \sin\theta_{\rm disc}.\end{aligned}$$

The angles around the centre of the star are calculated as

$$\begin{aligned}\chi_2 &= \chi_3 = \cos^{-1}\left(\frac{R_*}{r}\right)\\ (\chi_3+\chi_4) &= \sin^{-1}\left(\frac{H}{r}\right)\\ \chi_1 &= \pi - \chi_2 - (\chi_3+\chi_4)\chi_4 = \pi - \chi_1 - \chi_2 - \chi_3.\end{aligned}$$

The other lengths and angles in the figure are given by

$$\begin{aligned}a &= \pi/2 - \chi_2\\ \chi_1' &= \pi/2 - \chi_1\\ a' &= a + \chi_1'\\ A_{180} &= R_* \sin\chi_1\\ B_1 &= R_* \cos\chi_1,\end{aligned}$$

and

$$B_2 = R_*(A_{180} - y)\tan a'.$$

Thin disc: condition $A_0 > y$

Consider the case of a thin disc which does not obscures the star (situation 1 in Fig. C.11), i.e. $A_0 > y$ where A_0 is measured on the $\phi = 0°$ side of the X-axis in Fig. C.12. In this case the star is limited by its visible edge and this occurs when $\alpha \leq \alpha_* = \sin^{-1}(R_*/r)$ as shown in equation (C.14). Within the limit $\alpha \leq \alpha_*$ all photons originate from the star, while elsewhere the photons originate from the disc.

Thick disc: condition $A_{180} < y$

A second case can be considered where a thick disc obscures the whole star such that $A_{180} < y$, where A_{180} is measured on the 180° side of the X-axis, i.e. A_{180} in Fig. C.13. Therefore, if the

polar angle is between $0 < \theta < \theta_3$ the photon will originate from the star if the azimuthal angle is within the limit $\cos\phi \leq \cos\tau$, where τ_ϕ is defined by equation (C.13). Elsewhere the photons will originate from the disc.

Partially obscured star

The last case is for a partially obscured star where both the stellar edge constraint and the ring constraint must be consider. The first step is to determine the polar angle within which each of these limits must be considered by determining the angle θ_f.

If $B_2 < (B_1 + \rho)$ (Fig. C.13), the angle θ_f intercepts the disc on the $\phi = 180°$ side of the polar axis and

$$\begin{aligned} C &= B_1 + \rho - B_2 \\ \theta_f &= \tan^{-1}\left(\frac{C}{H-y}\right). \end{aligned}$$

Then the origin of the photons can be determined by applying the disc constraints $\cos\phi \leq \cos\tau$ (equation C.13) for polar angles $0 < \theta < \theta_f$, and by applying the condition $\alpha \leq \alpha_*$ (equation C.14) for polar angles $\theta_f < \theta < (\Theta + \theta_4)$.

If $B_2 > (B_1 + \rho)$, θ_f intercepts the disc on the $\phi = 0°$ side of the polar axis (Fig. C.14) and therefore

$$\begin{aligned} C &= B_2 - (B_1 + \rho) \\ \theta_f &= \tan^{-1}\left(\frac{C}{H-y}\right). \end{aligned}$$

Therefore to determine the origin of the photons, for polar angles between $0 < \theta < \theta_f$ and $\theta_2 < \theta < (\Theta + \theta_4)$ (see Figs. C.13 & C.14) the condition $\alpha \leq \alpha_*$ is applied, while for polar angles between $\theta_f < \theta < \theta_2$ the constraint $\alpha \leq \alpha_*$ is applied if $\pi/2 < \phi < 3\pi/2$, and if $\phi < \pi/2$ or $\phi > 3\pi/2$ the disc constraint ($\cos\phi \leq \cos\tau$) must be applied.

Using the geometry above it is then possible to determine, during the numerical integration, if a photon from a direction $\hat{\mathbf{e}}_{\rm ph}$ originates from the star or the disc. Since in practice the integration over the star and disc is treated separately the conditions above are applied to determine whether a photon from a given direction must be included in the calculation.

C.6 Converting from the $K^{\rm s}$ to $K^{\rm d}$ coordinate system

In order to be able to apply the constraints discussed in the previous section to the scattering that occurs in the stellar coordinate system, $K^{\rm s}$, a method must be derived to convert between $K^{\rm s}$ and $K^{\rm d}$. These two systems are shown in Fig. C.15 along with only the relevant angles. As has been defined previously, the unit vector $\hat{\mathbf{e}}_*$ points from the centre of the pulsar to the

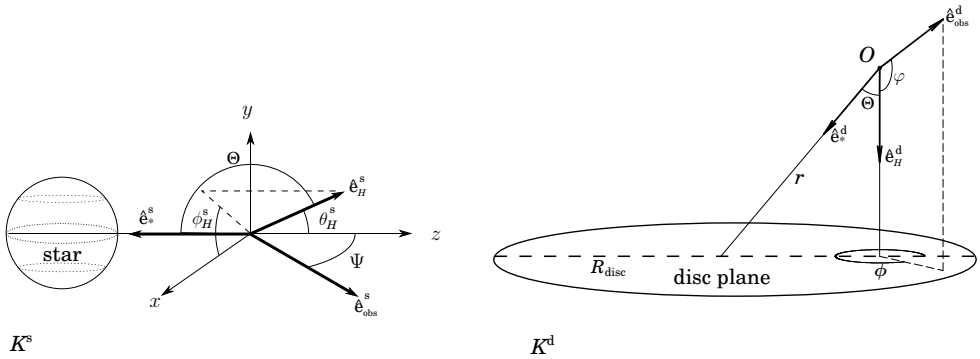

Figure C.15: The star ($K^{\rm s}$, left) and disc ($K^{\rm d}$, right) coordinate systems, showing only those angles which are relevant to the conversion between the two systems.

centre of the star, the unit vector $\hat{\mathbf{e}}_{\rm obs}$ points towards the observer and the unit vector $\hat{\mathbf{e}}_H$ points towards the normal of the disc. Variables with a superscript "s" are measured in $K^{\rm s}$, and those with a superscript "d" are measured in $K^{\rm d}$.

Since $\hat{\mathbf{e}}^{\rm d}_H$ defines the z'-axis in $K^{\rm d}$, by defining the direction in $K^{\rm s}$ as

$$\hat{\mathbf{e}}^{\rm s}_H = \begin{pmatrix} \sin\theta^{\rm s}_H \cos\phi^{\rm s}_H \\ \sin\theta^{\rm s}_H \sin\phi^{\rm s}_H \\ \cos\theta^{\rm s}_H \end{pmatrix},$$

a rotation can be made between the two systems if the values $\theta^{\rm s}_H$ and $\phi^{\rm s}_H$ are found. The angle between $\hat{\mathbf{e}}^{\rm s}_*$ and $\hat{\mathbf{e}}^{\rm s}_H$ is defined to be Θ (equation 7.13) in $K^{\rm d}$, and since $\hat{\mathbf{e}}^{\rm s}_*$ lies along the negative z-axis in $K^{\rm s}$, it follows that (Fig. C.15)

$$\theta^{\rm s}_H = \pi - \Theta$$

and

$$\hat{\mathbf{e}}^{\rm s}_H = \begin{pmatrix} \sin(\pi-\Theta)\cos\phi^{\rm s}_H \\ \sin(\pi-\Theta)\sin\phi^{\rm s}_H \\ \cos(\pi-\Theta) \end{pmatrix} = \begin{pmatrix} \sin\Theta\cos\phi^{\rm s}_H \\ \sin\Theta\sin\phi^{\rm s}_H \\ -\cos\Theta \end{pmatrix}.$$

The value of $\phi^{\rm s}_H$ can be found by requiring that $\hat{\mathbf{e}}_{\rm obs}\cdot\hat{\mathbf{e}}_H$ is the same in both the $K^{\rm d}$ and $K^{\rm s}$ coordinate systems. In $K^{\rm d}$,

$$\hat{\mathbf{e}}^{\rm d}_{\rm obs}\cdot\hat{\mathbf{e}}^{\rm d}_H = \cos\varphi,$$

where φ is given by equation (7.14), while in $K^{\rm s}$,

$$\hat{\mathbf{e}}^{\rm s}_{\rm obs}\cdot\hat{\mathbf{e}}^{\rm s}_H = \sin\Psi\sin\Theta\cos\phi^{\rm s}_H - \cos\Psi\cos\Theta,$$

where

$$\hat{\mathbf{e}}^{\mathrm{s}}_{\mathrm{obs}} = \begin{pmatrix} \sin\Psi \\ 0 \\ \cos\Psi \end{pmatrix},$$

and Ψ is given by equation (7.11). Therefore, by equating $\hat{\mathbf{e}}^{\mathrm{s}}_{\mathrm{obs}} \cdot \hat{\mathbf{e}}^{\mathrm{s}}_{H} = \hat{\mathbf{e}}^{\mathrm{d}}_{\mathrm{obs}} \cdot \hat{\mathbf{e}}^{\mathrm{d}}_{H}$, the azimuthal angle of $\hat{\mathbf{e}}^{\mathrm{s}}_{H}$ is given by

$$\phi^{\mathrm{s}}_{H} = \cos^{-1}\left(\frac{\cos\varphi + \cos\Psi\cos\Theta}{\sin\Psi\sin\Theta}\right).$$

In K^{s} the direction of $\hat{\mathbf{e}}^{\mathrm{s}}_{H}$ indicates the direction of the z'-axis of the K^{d} system. The conversion between two system due to rotation is given by

$$z' = lx + my + nz, \tag{C.15}$$

where l, m and n are the cosine directions defined as

$$\begin{aligned} l &= \cos A \\ m &= \cos B \\ n &= \cos C, \end{aligned}$$

where A, B and C are the angles between the z'-axis ($\hat{\mathbf{e}}^{\mathrm{s}}_{H}$) and the x, y and z-axes respectively. In K^{s}, if $\hat{\mathbf{e}}_x$, $\hat{\mathbf{e}}_y$ and $\hat{\mathbf{e}}_z$ are unit vectors along the x, y and z axis,

$$\begin{aligned} l = \quad \hat{\mathbf{e}}^{\mathrm{s}}_{H} \cdot \hat{\mathbf{e}}_x = \quad & \sin\Theta\cos\phi^{\mathrm{s}}_{H} \\ m = \quad \hat{\mathbf{e}}^{\mathrm{s}}_{H} \cdot \hat{\mathbf{e}}_y = \quad & \sin\Theta\sin\phi^{\mathrm{s}}_{H} \\ n = \quad \hat{\mathbf{e}}^{\mathrm{s}}_{H} \cdot \hat{\mathbf{e}}_z = \quad & -\cos\Theta. \end{aligned}$$

By substituting in the cosine directions and transforming from Cartesian to polar coordinates it can be shown from equation (C.15) that

$$\cos\theta^{\mathrm{d}} = \sin\Theta\sin\theta^{\mathrm{s}}\cos(\phi^{\mathrm{s}}_{H} - \phi^{\mathrm{s}}) - \cos\Theta\cos\theta^{\mathrm{s}},$$

where θ^{s} and ϕ^{s} are any polar and azimuthal angle in K^{s} and θ^{d} is the resulting polar angle in K^{d}. Then, if $\hat{\mathbf{e}}_{\theta,\phi}$ defines the direction considered in both systems, the appropriate azimuthal angle in K^{d} (ϕ^{d}) is found by requiring that $\hat{\mathbf{e}}^{\mathrm{s}}_{*} \cdot \hat{\mathbf{e}}^{\mathrm{s}}_{\theta,\phi} = \hat{\mathbf{e}}^{\mathrm{d}}_{*} \cdot \hat{\mathbf{e}}^{\mathrm{d}}_{\theta,\phi}$. In K^{s}

$$\hat{\mathbf{e}}^{\mathrm{s}}_{*} \cdot \hat{\mathbf{e}}^{\mathrm{s}}_{\theta,\phi} = -\cos\theta^{\mathrm{s}}$$

and in K^{d}

$$\hat{\mathbf{e}}^{\mathrm{d}}_{*} \cdot \hat{\mathbf{e}}^{\mathrm{d}}_{\theta,\phi} = \begin{pmatrix} -\sin\Theta \\ 0 \\ \cos\Theta \end{pmatrix} \cdot \begin{pmatrix} \sin\theta^{\mathrm{d}}\cos\phi^{\mathrm{d}} \\ \sin\theta^{\mathrm{d}}\sin\theta^{\mathrm{d}} \\ \cos\theta^{\mathrm{d}} \end{pmatrix} = \cos\Theta\cos\theta^{\mathrm{d}} - \sin\Theta\sin\theta^{\mathrm{d}}\cos\phi^{\mathrm{d}},$$

and, therefore, the azimuthal angle is found from

$$\cos\phi^{\mathrm{d}} = \frac{\cos\Theta\cos\theta^{\mathrm{d}} + \cos\theta^{\mathrm{s}}}{\sin\Theta\sin\theta^{\mathrm{d}}}.$$

Appendix D

Proceedings of IAUS 272

The isotropic inverse Compton modelling, utilizing the Johnston et al. (1994) stellar parameters was presented in part at the *IAU Symposium 272 – Active OB stars: structure, evolution, mass loss and critical limits* (editors C. Neiner, G. Wade, G. Meynet, G. Peters, Paris, France, 19-23 July 2010). This work was later incorporated in van Soelen and Meintjes (2011). The conference proceeding is included here.

Active OB stars: structure, evolution, mass loss, and critical limits
Proceedings IAU Symposium No. 272, 2010
C. Neiner, G. Wade, G. Meynet & G. Peters, eds.

doi:10.1017/S1743921311011677

γ-ray production via IC scattering of the infrared excess from the Be-type star in the binary system PSR B1259-63/SS2883

Brian van Soelen[1] and Pieter J. Meintjes[2]

Department of Physics, University of the Free State, Bloemfontein, Republic of South Africa
[1]email: vansoelenb@ufs.ac.za [2]email: MeintjPJ@ufs.ac.za

Abstract. Un-pulsed γ-ray emission has been detected close to periastron in the pulsar/Be-star binary system PSR B1259-63/SS 2883, believed to originate from the shock front that forms between the stellar and pulsar winds. A likely source of γ-ray production is the inverse Compton up-scattering of target photons from the Be star by relativistic electrons/positrons in the pulsar wind. In this study the influence of the infrared radiation, emanating from the circumstellar disc, on isotropic inverse Compton γ-ray production is investigated. It is shown that the scattering of infrared disc photons can increase the γ-ray flux by a factor ~ 2 in the 1–10 GeV range.

Keywords. stars: emission-line, Be, binaries: general, gamma rays: theory

1. Introduction

The Be X-ray Pulsar binary (Be-XPB) PSR B1259-63/SS 2883 consists of a 48 ms pulsar in orbit around a Be star (Johnston *et al.* 1992). The orbit is eccentric ($e \approx 0.87$) and un-pulsed TeV γ-ray emission has been detected around periastron (Aharonian *et al.* 2005). The system is powered by the spin-down luminosity of the pulsar and the un-pulsed radiation is believed to originate from a stand-off shock-front that forms between the pulsar and stellar wind. A likely production mechanism for the γ-rays is the inverse Compton (IC) scattering of target photons from the Be star (Tavani & Arons 1997). Previous models of IC scattering in PSR B1259-63/SS 2883 have not considered how the infrared (IR) excess from the circumstellar disc will influence the γ-ray production.

2. Modelling

2.1. *Curve of Growth Method*

The Curve of growth method (as outlined by Waters 1986) was used to model the IR excess associated with SS 2883. Under this model it is assumed that the Be star's circumstellar disc has a half-opening angle $\theta = 5°$, extends to a radius $R_{disc} = 50\ R_{star}$, and follows a power-law density profile $\rho \propto (r/R_{star})^{-n}$. A Kurucz atmosphere (Kurucz 1979) was fitted to the optical data (*UBV* from Westerlund & Garnier 1989), giving a temperature of $T_{star} = 25000$ K, while the IR excess was fitted to *2MASS* (Skrutskie *et al.* 2006) and *MSX* data (Price et al 2001) assuming $T_{disc} = 0.5\ T_{star}$.

2.2. *Inverse Compton Scattering*

As a first approximation of the effect of the IR excess on IC scattering the total number of scatters is calculated by integrating over the exact isotropic scattering rate equation given in Blumenthal & Gould (1970). The scattering rate is proportional to the photon distribution, $n(\epsilon)$, which is calculated by using the curve of growth method instead of a

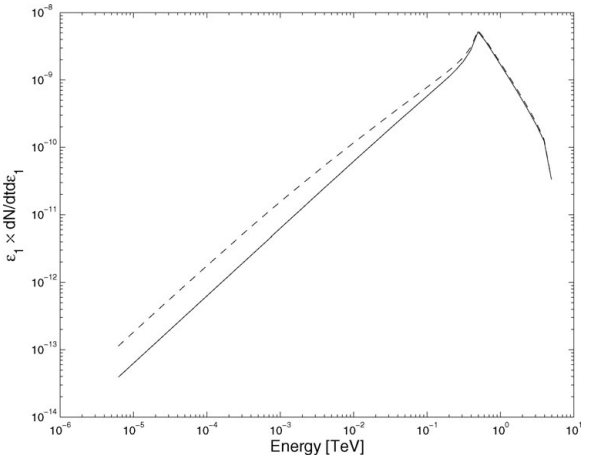

Figure 1. The predicted IC γ-ray flux in arbitrary unites for PSR B 1295-63/SS 2883. Dashed line includes the flux from the star and disc, while the solid line excludes the disc.

blackbody or mono-energetic photon distribution as was used in previous models. Fig. 1 shows the results of the IC scattering when only the flux from the star (solid line) and when the flux from the star plus the disc (dashed line) is considered, assuming a isotropic electron distribution, with a power index $p = 2.2$ between $\gamma = 10^6 - 10^7$. The modelled flux shows an increase of a factor ~ 2 in the 1–10 GeV range.

3. Conclusion

The predicted increase in the γ-ray flux is important for observations of γ-ray Be-XPB systems, especially given the observational range of *Fermi*. Future work will consider the anisotropic effects associated with a finite size star and disc.

Acknowledgements

This publication makes use of data from *2MASS*, a joint project of the University of Massachusetts and the Infrared Processing and Analysis Center/California Institute of Technology, funded by NASA and the NSF. This research made use of data from *MSX*; processing of the data was funded by the Ballistic Missile Defense Organization with additional support from the NASA Ofce of Space Science. This research has made use of the NASA/IPAC Infrared Science Archive, operated by the Jet Propulsion Laboratory, California Institute of Technology, under contract with NASA.

References

Aharonian, F., Akhperjanian, A. G., Aye, K.-M., Bazer-Bachi, A. R. *et al.* 2005, *A&A*, 442, 1
Blumenthal, G. R. & Gould, R. J. 1970, *Reviews of Modern Physics*, 42, 237
Johnston, S., Manchester, R. N., Lyne, A. G., Bailes, M. *et al.* 1992, *ApJ* (Letters), 387, L37
Kurucz, R. L. 1979, *ApJS*, 40, 1
Price, S. D., Egan, M. P., Carey, S. J., Mizuno, D. R. *et al.* 2001, *AJ*, 121, 2819
Skrutskie, M. F., Cutri, R. M., Stiening, R., Weinberg, M. D. *et al.* 2006, *AJ*, 131, 1163
Tavani, M. & Arons, J. 1997, *ApJ*, 477, 439
Waters, L. B. F. M. 1986, *A&A*, 162, 121
Westerlund, B. E. & Garnier, R. 1989, *A&AS*, 78, 203

Appendix E

Proceedings of HEPRO III

The anisotropic inverse Compton modelling, utilizing the Johnston et al. (1994) stellar parameters was presented in part at the High Energy Phenomena in Relativistic Outflows III (HEPRO III) conference (editors J.M. Paredes, M. Ribó, F.A. Aharonian and G.E. Romero, Barcelona, 27 June – 1 July, 2011). The peer-reviewed conference proceedings of this work has been accepted to appear in the International Journal of Modern Physics: Conference Series. The pre-print version of the conference proceedings is included here.

International Journal of Modern Physics: Conference Series

ANISOTROPIC SCATTERING FROM THE CIRCUMSTELLAR DISC IN PSR B1259-63

B. VAN SOELEN, P.J. MEINTJES

Department of Physics, University of the Free State, P.O. Box 339
Bloemfontein, Free State, 9300, Republic of South Africa
VanSoelenB@ufs.ac.za

Received Day Month Year
Revised Day Month Year

The gamma-ray binary system PSR B1259-63 has recently passed through periastron and has been of particular interest as it was observed by Fermi near the December 2010 periastron passage. The system has been detected at very high energies with H.E.S.S. The most probable production mechanism is inverse Compton scattering between target photons from the optical companion and disc, and relativistic electrons in the pulsar wind. We present results of a full anisotropic inverse Compton scattering model of the system, taking into account the IR excess from the extended circumstellar disc around the optical companion.

Keywords: Radiation mechanisms: non-thermal ; pulsars: individual: PSR B125963 ; X-rays: binaries.

PACS numbers: 11.25.Hf, 123.1K

1. Introduction

An important Be X-ray Pulsar binary (Be-XPB) example is the TeV gamma-ray system PSR B1259-63, which consists of a 48 ms pulsar orbiting the Be star LS 2883.[1] The orbit is eccentric ($e \approx 0.87$) and unpulsed TeV gamma-ray emission has been detected by the High Energy Stereoscopic System (H.E.S.S.) close to previous periastron passages.[2,3] The circumstellar disc is mis-aligned to the orbital plane and the pulsar passes through it twice, before and after periastron. Previous observations have also detected unpulsed radio emission near periastron,[4] and X-ray emission across the whole orbit.[5] The system is powered by the spin-down luminosity of the pulsar and the unpulsed radiation is believed to originate from a stand-off shock-front that forms between the pulsar and stellar winds. The X-ray emission is probably synchrotron radiation and gamma-rays are produced through inverse Compton (IC) scattering between target photons from the Be star-disc system and relativistic electrons ($\gamma \sim 10^6$).[6] In this study the anisotropic IC scattering in PSR B1259-63/LS 2883 has been investigated, focusing on the contribution of the infrared (IR) excess from the circumstellar disc to the IC scattering rate. The

additional effects of photon absorption through pair-production[7] or changes in the shock condition[7,8] have not been considered here. This study only presents the effect of the IR excess to investigate whether this a viable source of additional photons and whether this will have a significant influence on the gamma-ray production.

2. Modelling

In order to model the anisotropic IC spectrum from the circumstellar disc in PSR B1259-63 it is necessary to calculate the total number of scatterings, taking into account the anisotropic scattering rate and the photon contribution from the star and the circumstellar disc. The modelling presented here is dependent on the IR excess and curve of growth modelling calculated in Ref. 9 which assumed the stellar parameters presented by Ref. 10. For this reason a stellar mass and radius of $10M_{\odot}$ and $6R_{\odot}$, and a pulsar mass of $1.4M_{\odot}$ have been assumed and not the newer system parameters presented by Ref. 11.

2.1. *Anisotropic Scattering*

The anisotropic scattering rate[12,13] needs to take into account the scattering angle, θ_0, between the direction of the observer and the incoming photons over the full solid angle of the star and disc. The total anisotropic scattering rate is given by[14]

$$\frac{dN_{\rm tot}}{dtd\epsilon_1} = \int_{\Omega}\int_{\gamma}\int_{\epsilon_0} n_{\rm ph}(\epsilon_0) n_{\rm e}(\gamma) \frac{dN_{\gamma,\epsilon_0}}{dt\, d\epsilon_1} \cos\theta d\epsilon_0 d\gamma d\Omega \qquad (1)$$

where $n_{\rm ph}$ is the number of photons, $n_{\rm e}$ is the electron distribution, $dN/dtd\epsilon_0$ is the anisotropic scattering rate dependent on the scattering angle θ_0, and $\cos\theta$ is the angle to the normal of the photon source (star or disc). The star is assumed to have a black-body photon distribution ($T_* = 25\,000$ K), while the photon distribution from the disc is calculated using the curve of growth method.

The electron spectrum is assumed to have the form $n_{\rm e}(\gamma) = K_{\rm e}\gamma^{-p}$, where $K_{\rm e} = 1$ is used in this study as only the resulting change due to the IR excess is considered. The synchrotron radiative cooling time is $t_{\rm sync} \sim 770\ (\gamma/10^6)^{-1}(B/1\ {\rm G})^{-2}$ seconds, which is greater than the light crossing time of the disc. For this reason only a constant electron spectrum has been considered, appropriate for adiabatically cooled electrons.[15] Therefore, this study considers only whether the IR excess from the large circumstellar disc significantly influences the IC scattering. Additional effects due to radiative cooling have not been considered here.

2.2. *Disc photon spectrum - curve of growth method*

The intensity from the circumstellar disc depends on the free-free optical depth through the disc, from which the photon number density is calculated. The optical depth is determined by the curve of growth method[16] and the pulsar-disc orientation. It is assumed that the circumstellar disc has a half-opening angle $\theta_{\rm disc}$, extends

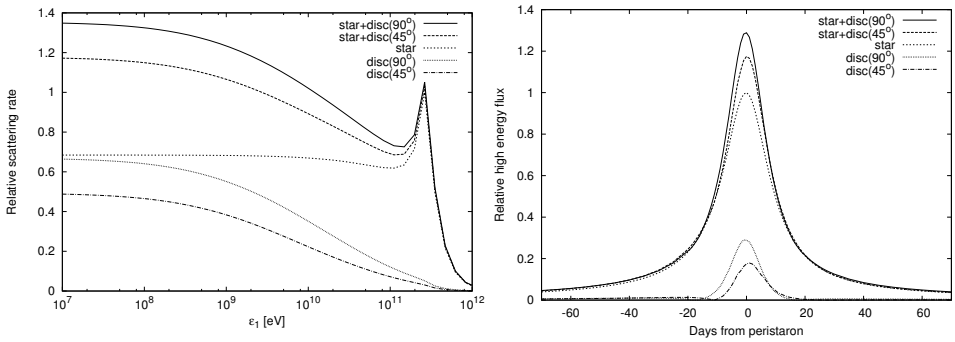

Fig. 1. (Left) Scattering rate for the disc and star contributions in PSR B1259-63 at periastron for a disc orientated 90° and 45° to the orbital plane, scaled to the peak stellar contribution. (Right) The corresponding light curve of the high energy contribution ($\sim 0.1 - 100$ GeV) of the star and disc around periastron considering only adiabatically cooled electrons.

to a radius $R_{\rm disc}$ and has a power-law density profile that decreases with distance as $\rho(r) = \rho_0 \, (r/R_*)^{-n}$.

3. Results

Two orientations of the disc have been considered; the first with a disc tilted 90° to the orbital plane with the normal lying along the semi-major axis ($T_{\rm disc} = 12\,500$ K & $\theta_{\rm disc} = 5°$), the second titled 45° to the orbital plane with the normal rotated 19° from the semi-major axis ($T_{\rm disc} = 15\,000$ K & $\theta_{\rm disc} = 0.7°$).[17,18] These disc temperatures and small half-opening angles are consistent with current modelling of the circumstellar discs of Be stars.[18,19] The disc is assumed to have a radius of $50R_*$, consistent with the binary separation at the time of the binary eclipse.[20,9] The parameters for the curve of growth method were taken from the fit to previous optical and IR observations[9] and the electron spectrum is modelled using an index of 2.4 between $\gamma = 2.54\times10^5$ and 2.54×10^7 (adopted from Ref. 15). Fig. 1 shows the relative scattering rate at periastron scaled to the peak of the stellar contribution for both disc orientations and the corresponding light curve at high energies ($\sim 0.1 - 100$ GeV). In both cases the contribution of the disc occurs towards high energies (as opposed to very high energies) where it results in an increase in the scattering rate by a factor ~ 2. The light curves show a peak in the disc contribution near periastron and less contribution near the disc crossing where the IC scattering is dominated by the scattering of stellar photons. The rotation of the disc from the semi-major axis results in a slightly higher flux before periastron and the shifting of the peak away from periastron, while the post-periastron flux is lower because of unfavourable scattering angles. In both cases the flux increases after the disc crossing as head-head scattering readily occurs in this region.

4. Conclusion

The IC scattering from the circumstellar disc in PSR B1259-63 is shown to increase the flux at high energies by a factor of ~ 2 during periastron. Due to the large size of the disc and the increase in the photon density at IR wavelength (increasing by ~ 1000 at mid-IR wavelengths)[9] it was possible that the increased solid angle could have a major influence. However, the flux from the circumstellar disc drops off rapidly with radial distance and the low flux from the disc at the point of the disc crossing mitigates the influence of the disc. This approximation, considering only adiabatically cooled electrons, shows that the influence of the IR excess does not dramatically increase the scattering rate during the disc crossing. In particular, this simplified model does not explain the flare observed by Fermi after the second disc crossing.[21] It should be noted that a simplified approximation was used to calculate the photon spectrum from the disc and a more detailed model may result in a higher photon density at the outer edges of the disc. Additional shock heating effects may also increase the brightness of the circumstellar disc during the pulsar passage. Such an effect could increase the scattering rate near the disc crossing and IC scattering of pre-shock $\gamma = 10^4$ electrons may explain the Fermi flare.[22]

Acknowledgments

BvS is funded by the South African Square Kilometre Array Project. The numerical calculations made use of the UFS High Performance Computation division.

References

1. S. Johnston, *et al.*, *ApJ*, **387**, L37 (1992)
2. F. Aharonian, *et al.*, *A&A*, **442**, 1 (2005)
3. F. Aharonian, *et al.*, *A&A*, **469** , L1 (2007)
4. S. Johnston, *et al.*, *MNRAS*, **302**, 277 (1999)
5. M. Chernyakova, *et al.*, *MNRAS*, **397**, 2123 (2009)
6. M. Tavani and J. Arons, *ApJ*, **477**, 439 (1997)
7. D. Khangulyan, *et al.*, *ApJ*, **742**, 98 (2011)
8. G. Dubus, *A&A*, **451**, 9 (2006)
9. B. van Soelen and P.J. Meintjes, *MNRAS*, **412**, 1721 (2011)
10. S. Johnston, *et al.*, *MNRAS*, **268**, 430 (1994)
11. I. Negueruela, *et al.*, *ApJ*, **732**, L11 (2011)
12. F.A. Aharonian and A.M. Atoyan, *Ap&SS*, **79**, 321 (1981)
13. D. Fargion, R.V. Konoplich and A. Salis, *Z. Phys. C.*, **74**, 571 (1997)
14. G. Dubus, B. Cerutti and G. Henri, *A&A*, **477**, 691 (2008)
15. J.G. Kirk, L. Ball and O. Skjaeraasen, *Astroparticle Phys.*, **10**, 31 (1999)
16. L.B.F.M. Waters, *A&A*, **162**, 121 (1986)
17. M. Chernyakova, *et al.*, *MNRAS*, **367**, 1201 (2006)
18. A.T. Okazaki, *et al.*, *PASJ*, **63**, 893 (2011)
19. J.H. Telting, *et al.*, *MNRAS*, **296**, 785 (1998)
20. S. Johnston, *et al.*, *MNRAS*, **358**, 1069 (2005)
21. A.A. Abdo, *et al.*, *ApJ*, **736**, L11 (2011)
22. D. Khangulyan, *et al.*, pre-print, astro-ph/1107.4833 (2011)